TECHNISCHE UNIVERSITÄT WIEN

An Investigation into Low-Frequency Aero-Vibro-Acoustic Mechanisms in Vehicles

Dissertation

Dipl.-Ing. Rafael ENGELMANN

In der Wissenschaft gleichen wir alle nur den Kindern, die am Rande des Wissens hie und da einen Kiesel aufheben, während sich der weite Ozean des Unbekannten vor unseren Augen erstreckt.

Isaac Newton

TECHNISCHE UNIVERSITÄT WIEN

DISSERTATION

An Investigation into Low-Frequency Aero-Vibro-Acoustic Mechanisms in Vehicles

ausgeführt zum Zwecke der Erlangung
des akademischen Grades eines Doktor der technischen Wissenfchaften
unter der Leitung von

Univ.-Prof. Dipl.-Ing. Dr.techn. Manfred Kaltenbacher
Institut für Mechanik und Mechatronik, E325 A4

eingereicht an der Technischen Universität Wien
Fakultät für Maschinenwesen und Betriebswissenschaften
von

Dipl.-Ing. Rafael Josef ENGELMANN
[redacted]

und begutachtet von

Prof. Stefan Becker
Lehrstuhl für
Strömungsmechanik
Cauerstraße 4
91058 Erlangen
Deutschland

Prof. Steffen Marburg
Lehrstuhl für
Akustik mobiler Systeme
Boltzmannstr. 15/I
85748 Garching
Deutschland

Eidesstattliche Erklärung

Ich erkläre an Eides statt, dass ich meine Dissertation mit dem Titel *An Investigation into Low-Frequency Aero-Vibro-Acoustic Mechanisms in Vehicles* selbständig und ohne Benutzung anderer als der angegebenen Hilfsmittel angefertigt habe und dass ich alle Stellen, die ich wörtlich oder sinngemäß aus Veröffentlichungen entnommen habe, als solche kenntlich gemacht habe. Die Arbeit hat bisher in gleicher oder ähnlicher Form oder auszugsweise noch keiner Prüfungsbehörde vorgelegen.

Wien, am 28.2.2023

Rafael Engelmann

Danksagung

Da diese Arbeit im Zuge des *ProMotion* Doktorandenprogramms der *BMW AG* entstanden ist, möchte ich mich zuallererst für die Finanzierung des Projektes und die äußerst lehrreiche und spannende Erfahrung, im Windkanal der *BMW AG* zu wirken, zu lernen und zu verstehen, bedanken. Es war mir eine stete Freude, mich die letzten Jahren mit den äußerst vielseitigen und spannenden Themen der Aerodynamik, der Akustik, der Stukturdynamik, der Signalverarbeitung und all den anderen Themenbereichen zu beschäftigen die mit meinem Dissertationsthema auf die eine oder andere Weise in Verbindung stehen. Geweckt wurde mein Interesse schon vor einigen Jahren von Prof. Manfred Kaltenbacher, der mir mit seiner ansteckenden Begeisterung für sein (und gefühlsweise auch alle anderen) Fachgebiete eine stete Inspiration war. Lieber Manfred, vielen, vielen Dank für all deine Ratschläge, die (nächtlichen?) Korrekturen, deine Motivation, dein Vertrauen in meine (meist unausgegorenen) Ideen und natürlich die Korrektur dieser Arbeit. Als zweiten im Bunde möchte ich mich bei Christoph Gabriel für die ausgezeichnete und freundschaftliche Betreuung, die guten Ratschläge und überhaupt, den Anstoß für dieses Promotionsthema bedanken.

Bei der *BMW AG* möchte ich mich insbesondere bei Thomas Neitzsch, Peter Kalinke und Bodo Durst für die organisatorische und fachliche Unterstützung und die Ermöglichung meines Projekts (und meiner persönlichen Freiheit im Umgang damit) bedanken. Auch bei meinen Teamkollegen und insbesondere dem *Operator*-Team im Windkanal möchte ich mich herzlich für Ratschläge, Anregungen und tatkräftige Hilfe bedanken. Ein besonderer Dank geht an Thomas Betzenbichler und das Werkstatt-Team für die praktische Anfertigung des Testkörpers, an Marinus Luegmair für die vielen freundschaftlichen Unterhaltungen und all die zusätzlich zu deiner eigentlichen Arbeit erfolgten Unterstützungen und an Sophie Cram für die Generierung der Strukturmoden.

An der *TU Wien* gilt mein besonderer Dank Florian Toth für die initiale Idee der Verwendung gekoppelter vibro-akustischer Moden und den vielen inhaltlichen Vorschlägen und Korrekturen am JSV Paper sowie Stefan Schoder für die vielen guten Ideen. Auch bei meinen Kollegen an der *TU Wien* möchte ich mich für die interessanten Gespräche und den freundschaftlichen Austausch bedanken.

Ein besonderer Dank geht an Prof. Steffen Marburg und an Prof. Stefan Becker für die Erstellung der Gutachten.

Für alles, aber insbesondere für die Weckung meiner Neugierde und meines Wissensdranges möchte ich mich bei meinen Eltern, Waltraud und Kurt Engelmann bedanken und natürlich bei meinem Bruder David Engelmann.

Vielen Dank, liebe Gloria, für die vielen schönen vergangenen und kommenden Jahre.

Abstract

The ubiquitous presence of noise in modern societies causes a significant amount of psychological strain and stress in individuals, and since this is especially true for transportation vehicles, engineers in the automotive industry are strongly interested in identifying the sources of noise and the critical transmission mechanisms. The issue is further exacerbated by the continuous exploitation of lightweight construction potentials. Since body modifications in the late development phase are associated with high effort and costs, early optimisation on the grounds of virtual models is crucial. Due to the transition to e-mobility, the engine is no longer a source of noise and wind noise excitation can now become crucial even at low driving speeds. The thesis at hand aims to delevop a foundation for the early assessment of wind-induced noise in vehicles by identifying and quantifying the essential physical mechanisms of the complex aero-vibro-acoustic problem. A detailed theoretical introduction explains the basic principles and methods for dealing with the various physical mechanisms by collecting relevant research and literature from a wide range of disciplines. Then a hybrid method is developed, with which experimental or computational acoustic or mechanical modes on arbitrary grids can be used as a basis for further calculations. A generic test body with clearly defined transmission paths is constructed to validate the developed method. The fluctuating surface pressure distribution on the structure is calculated by numerical simulation and the results are compared with wind tunnel measurements. Then, based on the hybrid method, a computational algorithm is developed that allows to calculate flow-induced interior noise on behalf of computational or experimental mechanical and acoustical modes and a transient simulation of the vehicle flow, and the method is extensively validated using wind tunnel measurements.

Kurzfassung

Die ständige Präsenz von Lärm in modernen Gesellschaften führt zu einem signifikanten Ausmaß von individueller psychischer Belastung und Stress und da dies in besonderem Maße für Fahrzeuge gilt, haben Ingenieure in der Automobilindustrie großes Interesse an der Identifikation der Lärmquellen und der kritischen Übertragungsmechanismen. Die Problematik wird zusätzlich durch die stetige Ausnutzung von Leichtbaupotentialen verschärft und da in der späten Entwicklungsphase Karosserieänderungen mit hohem Aufwand und Kosten verbunden sind, ist eine frühzeitige Optimierung auf Basis mathematischer Modelle erforderlich. Durch den Wandel zur E-Mobilität entfällt der Motor als Geräuschquelle und die Anregung durch Windgeräusche kann nun auch bei niedrigeren Geschwindigkeiten kritisch sein. Das Ziel der vorliegenden Arbeit ist es, die wesentlichen physikalischen Mechanismen der komplexen aero-vibro-akustischen Problemstellung zu identifizieren, zu quantifizieren und somit eine Grundlage für die frühzeitige Bewertung von windangeregtem Lärm in Fahrzeugen zu generieren. Hierzu werden in einer ausführlichen theoretischen Einleitung die Grundlagen und Methoden für die Behandlung der unterschiedlichen physikalischen Mechanismen erläutert und ein Bezug zu bestehender Forschung und Literatur aus den unterschiedlichsten Fachgebieten hergestellt. Danach wird eine hybride Methode für die Behandlung des vibro-akustischen Systems entwickelt, mit der experimentell oder computergestützt ermittelte akustische bzw. mechanische Moden auf beliebigen Gittern als Basis für die weitere Berechnung verwendet werden können. Anschließend wird ein generischer Testkörper entwickelt, der es erlaubt anhand klar definierter Übertragungspfade die Gültigkeit der entwickelten Methode zu überprüfen. Zur Berechnung der instationären Oberflächendrücke an der Struktur wird eine numerische Berechnung durchgeführt und die Ergebnisse dieser Berechnung werden mit Windkanalmessungen verglichen. Dann wird auf Basis der hybriden Methode ein, durch Windkanalmessungen validiertes, Simulationsprogramm entwickelt, das es erlaubt, den wind-induzierten Lärm innerhalb des Fahrzeug sowohl auf Basis computergestützter Modelle als auch auch experimenteller Messungen zu ermitteln.

Abbreviations

FE	Finite element
TPS	Thin-plate-spline
WPF	Wall pressure fluctuations
EMA	Experimental modal analysis
LB	Lattice boltzmann
TPA	Transfer path analysis
MA	Modal analysis
CMS	Component mode synthesis
NVH	Noise Vibration Harshness
BE	Boundary element
BC	Boundary condition
LV	Laser vibrometry
OMA	Operational Modal Analysis
PDE	Partial differential equation
DOF	Degree-of-Freedom
SEA	Statistical energy analysis
PTF	Patch transfer function
CFD	Computational fluid dynamics
SPL	Sound pressure level
FRF	Frequency response function
DL	Displacement level
APSD	Auto-power spectral density
avAPSD	Arithmetically averaged auto-power spectral density
CPSD	Cross-power spectral density
lonCPSD	Longitudinal cross-power spectral density
latCPSD	Lateral cross-power spectral density
MSC	Magnitude-squared coherence
lonMSC	Longitudinal magnitude-squared coherence
latMSC	Lateral magnitude-squared coherence

General notation

Symbol	Description
b	Scalar
$\boldsymbol{b}$	Vector
$\boldsymbol{B}$	Matrix
$b(x)$	Scalar valued Function
$\boldsymbol{b}(x)$	Vector valued function
$\boldsymbol{b}^T$	Hermitian transpose (complex transpose)
b_k	Entry of vector $\boldsymbol{b}$ at index k
$b_{\mathrm{a}\|k}$	Entry of vector $\boldsymbol{b}_\mathrm{a}$ at index k
b_{ij}	Entry of matrix $\boldsymbol{B}$ at index ij
$b_{(i)}$	Realization of b
$\left\{b_{(i)}\right\}$	Ensemble average over $b_{(i)}$
$\hat{b}(\omega)$	Temporal Fourier transformation of b(t)
$\breve{b}(k,\omega)$	Spatial Fourier transformation of $\hat{b}(x,\omega)$
$\tilde{b}_\mathrm{n}(\omega)$	Eigenvalue transformation of $\hat{b}(x,\omega)$
$\hat{S}_\mathrm{b}(\omega)$	Power spectrum of $b(t)$
$\hat{S}_\mathrm{b}(x,\omega)$	Auto power spectrum of $b(x,t)$
$\hat{S}_{\overline{\mathrm{b}}}(x,\omega)$	Auto power spectrum of arithmetic average of $b(x,t)$
$\hat{S}_\mathrm{b}(x,y,\omega)$	Cross power spectrum of $b(x,t)$
$\breve{\Phi}_\mathrm{b}(k_1,k_2,\omega)$	Wavenumber-frequency spectrum of $b(x,t)$
$\hat{\gamma}_\mathrm{b}(x,y,\omega)$	Magnitude-squared coherence of $b(x,t)$

General variables

Symbol	Description
$t, \delta t$	Time, Time shift
ω, f	Angular frequency, Frequency
$x, y, z, \boldsymbol{x} = [x,y,z], \boldsymbol{x}_1, \boldsymbol{x}_2, \boldsymbol{y}$	Space Coordinates
$\zeta, \eta, \boldsymbol{\zeta} = [\zeta, \eta]$	Relative coordinates
$k_\mathrm{x}, k_\mathrm{y}, k_\mathrm{z}, \boldsymbol{k} = [k_\mathrm{x}, k_\mathrm{y}, k_\mathrm{z}], \boldsymbol{k}_1, \boldsymbol{k}_2$	Angular wavenumber coordinates
κ	Trace wavenumber
Γ	Surface
V, Ω	Volume
$\boldsymbol{\Psi}, \psi$	Mode shape matrix, mode shape
c_ph	In-plane phase velocity $c_\mathrm{ph} = \omega/\kappa$
i	Imaginary unit
s	Pole
λ, ω, ζ	Eigenvalue, eigenfrequency, modal damping
$N(x), \boldsymbol{N} = diag([N(x), N(x), N(x)])$	Ansatz function, Ansatz matrix
$\wedge$	Assembly operator
$\boldsymbol{P}$	Point cloud
$\mathfrak{D}$	Delaunay triangulation
$\partial b/\partial x$	Partial derivative of b
∇	Gradient
$\nabla\times$	Curl
$\otimes$	Dyadic product
b_ic	Incompressible quantity
b'	Quantity with zero temporal mean

Transformations

Symbol	Formula	Description
$\mathcal{F}\left\{b(\boldsymbol{x},t)\right\}$	$\hat{b}(\boldsymbol{x},\omega) = \int_{\mathbb{R}} b(\boldsymbol{x},t)\mathrm{e}^{-\omega t}\mathrm{d}t$	Temporal Fourier transformation
$\mathcal{F}^{\mathrm{i}}\left\{\hat{b}(\boldsymbol{x},\omega)\right\}$	$b(\boldsymbol{x},t) = \int_{\mathbb{C}} \hat{b}(\boldsymbol{x},\omega)\mathrm{e}^{\omega t}\mathrm{d}\omega$	Inverse temporal Fourier transformation
$\mathcal{F}_{\mathrm{x}}\left\{\hat{b}(\boldsymbol{x},\omega)\right\}$	$\breve{b}(\boldsymbol{k},\omega) = \int_{\mathbb{R}^n} \hat{b}(\boldsymbol{x},\omega)e^{-\mathrm{i}\boldsymbol{k}\cdot\boldsymbol{x}}\mathrm{dx}$	Spatial Fourier transformation (wavenumber transformation)
$\mathcal{F}_{\mathrm{x}}^{\mathrm{i}}\left\{\breve{b}(\boldsymbol{k},\omega)\right\}$	$\hat{b}(\boldsymbol{x},\omega) = \int_{\mathbb{C}^n} \breve{b}(\boldsymbol{k},\omega)e^{\mathrm{i}\boldsymbol{k}\cdot\boldsymbol{x}}\mathrm{dx}$	Inverse spatial Fourier transformation
$\mathcal{E}_{\mathrm{a}}\left\{\hat{b}(\boldsymbol{x},\omega)\right\}$	$\tilde{b}_{\mathrm{n}}(\omega) = \int_{\mathbb{R}^n} \hat{b}(\boldsymbol{x},\omega)\psi^*_{\mathrm{a\|n}}(\boldsymbol{x})\boldsymbol{dx}$	Acoustical Eigenvalue transformation (same for Mechanical ($\mathcal{E}_{\mathrm{m}}$,$\psi_{\mathrm{m\|n}}$) and Coupled ($\mathcal{E}_{\mathrm{c}}$,$\psi_{\mathrm{c\|n}}$))
$\mathcal{E}_{\mathrm{a}}^{\mathrm{i}}\left\{\tilde{b}_{\mathrm{n}}(\omega)\right\}$	$\hat{b}(\boldsymbol{x},\omega) = \sum_{\mathrm{n}=0}^{N} \tilde{b}_{\mathrm{n}}(\omega)\psi_{\mathrm{a}}(\boldsymbol{x})$	Acoustical Eigenvalue transformation (same for Mechanical ($\mathcal{E}_{\mathrm{m}}$,$\psi_{\mathrm{m\|n}}$) and Coupled ($\mathcal{E}_{\mathrm{c}}$,$\psi_{\mathrm{c\|n}}$)

Acoustical field

Symbol	Description
p_{a}	Pressure
v_{a}	Particle velocity
q_{a}	Volume velocity
q_{b}	Boundary volume velocity
c_0	Speed of sound
ρ_0	Density
y_{a}	Acoustic admittance ($v_{\mathrm{a}}/p_{\mathrm{a}}$)
z_{a}	Acoustic dynamic stiffness($p_{\mathrm{a}}/v_{\mathrm{a}}$)
$z_{\Gamma\mathrm{a}}$	Acoustic dynamic boundary stiffness($p_{\mathrm{a}}/v_{\mathrm{a}}$)
s_{a}	Acoustic transmissibility ($p_{\mathrm{a}}/p_{\mathrm{f}}$)
$m_{\mathrm{a}}, c_{\mathrm{a}}, k_{\mathrm{a}}$	Mass/damping/stiffness (Open cavity formulation)
$\underline{m}_{\mathrm{a}}, \underline{c}_{\mathrm{a}}, \underline{k}_{\mathrm{a}}$	Mass/Damping/Stiffness (Closed cavity formulation)
G	Green's free space function $G(r,\omega) = e^{i\omega r/c_0}/(4\pi r)$

Mechanical field

Symbol	Description
u_{s}	Displacement
v_{s}	Velocity
f_{s}	Mechanical force
f_{b}	Boundary force
σ_{s}	Mechanical stress
z_{s}	Mechanical dynamic Stiffness ($f_{\mathrm{s}}/u_{\mathrm{s}}$)
y_{s}	Mechanical admittance ($u_{\mathrm{s}}/f_{\mathrm{s}}$)
$m_{\mathrm{s}}, c_{\mathrm{s}}, k_{\mathrm{s}}$	Mass/damping/stiffness
k_{b}	Bending wavenumber
D_{s}	Flexural rigidity
ρ_{s}	Density
ν	Poisson ratio
h_{s}	Plate thickness

Coupled vibro-acoustic field

Symbol	Description
d_{c}	Generalized displacement
f_{c}	Generalized force
y_{c}	Coupled admittance ($d_{\mathrm{s}}/f_{\mathrm{c}}$)
z_{c}	Coupled impedance ($f_{\mathrm{c}}/d_{\mathrm{s}}$)

Flow field

Symbol	Description
ρ_0	Ambient density
ρ	Density
p'_f	Pressure fluctuation (aerodynamic only, subsonic phase velocity)
p_a	Pressure fluctuation (acoustic)
p_0	Temporal mean pressure
p	Pressure (temporal mean + aerodynamic + acoustic)
v_f,	Velocity
ω_f	Vorticity
v_conv	Mean shear Velocity
v_∞	Free stream velocity
M_c	Convective wavenumber $M_\mathrm{c} = V_\mathrm{c}/c_0$
M_∞	Free stream wavenumber $M_\infty = V_\infty/c_0$
ν	Kinematic viscosity
μ	Dynamic viscosity $\mu = \rho_0\nu$
Re	Free stream Reynolds Number $Re = V_\infty l_\mathrm{char}/\nu$
St	Strouhal Number $St = f_\mathrm{st}D/v_\infty$
$\gamma_\zeta, \gamma_\eta$	Longitudinal and lateral Corcos parameters
τ_ij	Wall shear stress
δ	Boundary layer thickness
L	Lighthill stress tensor
π	Momentum flux tensor

Contents

1 Introduction

1.1 Motivation

Since the early days of automotive history, the objective of reducing noise in the interior of vehicles through design measures has always been an integral part of the development process. The complexity, multifaceted and sometimes contradictory demands placed on modern vehicles, such as reducing noise transmission while simultaneously reducing vehicle mass, requires a great amount of in-depth knowledge on the physical mechanisms involved. Over the past years, achieving exceptional acoustic comfort has become a high priority goal among the many requirements imposed. Depending on vehicle speed, engine load, and road conditions, three distinct primary noise sources can be distinguished: engine noise, road-induced noise and wind noise. The relative weighting of these noise sources is strongly related to engine load, vehicle speed and road conditions. In electric vehicles, the combustion noise of the engine is no longer a contributing factor and thus, only the latter two sources must be considered. At low speeds, structural vibrations induced by road surface irregularities excite the vehicle body, resulting in audible noise in the driver's compartment. Aeroacoustic noise related to turbulent structures in the exterior flow becomes more prominent at higher speeds. These turbulent structures induce structural vibrations that in turn induce noise inside the vehicle. At very low frequencies, the interior cavity may also be excited directly via holes and openings. Understanding wind-induced noise in vehicles at low frequencies is the overall goal of this dissertation. Owing to the high perceptibility of mid-to high-frequency noise, topics such as side mirror noise or noise generated by small cavity gaps have received significant attention [1]. Nevertheless, although less perceptible and annoying, low frequency noise can seriously affect driving comfort. Studies on the effect of low frequency noise on people generally reveal an annoying feeling of ear pressure accompanied by headache, fatigue and performance losses [2]. In recent years, research on the low frequency region has principally been conducted to address structure-borne noise from road roughness and engine vibration [3–5]. Although its significance has been emphasized by research like Lemaitre's [6] inquiry into the psychoacoustical perception of wind buffeting noise, the physical mechanisms of flow-induced low-frequency noise in the vehicle cabin remain poorly understood. The distinction between low and high frequency mechanisms is of fundamental importance for the mechanical and acoustical wave propagation patterns in the vehicle structure and the interior cavity. Standing waves, also known as modes, predominate at low frequencies, while high frequency wave patterns are a superposition of a wide variety of waves with different wavelengths, therefore requiring a statistical description. It is therefore evident that the terms low- or high-frequency can be defined either by a frequency threshold determined by human perception or by distinguishing between deterministic or modal low-frequency and rather statistical high-frequency patterns in the medium. The former allows an absolute definition of the frequency threshold while the latter interpretation is particularly important with regard to the application of mathematical and computer-aided methods. Due to the later use of a geometrically scaled testbody, it is not meaningful to precisely set frequency limits for low and high-frequency range; however, in a broad sense, the thesis will mainly concern a frequency range between 0 and 300 Hz. Somewhat counterintuitively, it is precisely because of the statistical descriptiveness that the high frequency range is comparatively easy to treat, while the low frequency region requires very accurate and sophisticated

models and techniques that may even go so far as to include the effect of structural uncertainties associated with the manufacturing process [4, 7, 8]. Experimental techniques are equally more challenging at low frequencies, as even small deviations in the measurement position can lead to significant deviations in the measured acoustic pressure or, analogously, the measured mechanical displacement. For the treatment of noise induced by the flow around the vehicle, a numerical description of the unsteady flow is required and, similar to acoustic and mechanic fields, it is especially at low frequencies where large-scale topological features, such as vortex shedding in the recirculation region behind the vehicle can be critical. As we will see in greater depth throughout the course of this work, the calculation of flow-induced noise in vehicles is a challenge that necessitates a synthesis of the most diverse fields, including most naturally fluid mechanics, acoustics and structural dynamics, but also sophisticated experimental, numerical and statistical methods. Regarding low-frequency vibroacoustics, a great deal of research has been conducted in recent years. For example, the topic of structural uncertainties [4, 9, 10] and the influence of openings in the package tray on the acoustic properties of the cavity have been addressed [11], but also vibro-acoustic substructuring methods such as normal mode coupling [4, 7, 12] and, in more recent contributions, the patch transfer method (PTF) [13, 14]. There is also considerable effort devoted to experimental modal analysis (EMA) [**?**,15], vibro-acoustic modal analysis [16] and operational modal analysis (OMA) [17,18]. Hybrid methods based on a mixture of experimental and numerical techniques are frequently employed as a result of the high effort required to produce a reliable numerical model for the vehicle structure [3, 13, 19]. Vibro-acoustic coupling effects are also regularly investigated, frequently on behalf of simple vibro-acoustic boxes [20] or academic structures [21] but also on real vehicles [3]. At this point, it is important to mention that the acoustic properties of the interior cavity can be significantly altered by the presence of flexible body components, especially at low frequencies [3]. Recent years have also seen a consistent progress regarding the prediction of wind-induced interior noise. In order to generate reliable and reproduceable knowlege, it is benefical to employ specifically designed academic structures and among the many structures employed in aerodynamic research only the SAE body employed in [1, 22–24] and the more recently developed Drivaer model [25–28] also allow to investigate aero-vibro-acoustic mechanisms. Based on a simplified vehicle geometry, the SAE body has e.g. been used to investigate the interior noise associated with the side window [22] and the underbody [29]. On the contrary, the Drivaer model is actually a real vehicle with specific insulation treatments that up to date has only been employed to investigate the transmission of noise via the side window [26, 28]. Apart from these test specimens, investigations were carried out either on real vehicles [30–34] or on less well-known generic models [35, 36], for which experimental validation is often not available. While a large part of the investigations deals with the transmission of flow-induced noise via the side window [22, 25–28, 31, 37], there are also investigations concerning wind-induced noise via the windshield [30], the underbody [32–34,38] and the side door [39]. Due to the distinct transmission properties associated with different wavelengths, the aerodynamic and acoustic components of wall pressure fluctuations are frequently studied [22, 24–27, 36, 37]. It can be assumed, however, that the acoustic component only contributes significantly at high frequencies [22, 26, 40, 41] and can thus be neglected at low frequencies. Only a small fraction of the literature concerning flow-induced noise in vehicles also addresses the low-frequency range. Due to the additional acoustic boundary flexibility associated with the mechanical structure at low frequencies [42], unwanted transmission paths must be blocked for an investigation. This is challenging at low frequencies, which is the reason for the frequent 100 Hz lower limit of investigations on the SAE body (explicitly noted by Hartmann [23]) and the DrivAer body (not explicitly noted). Although this allows for the investigation of the respective transmission mechanisms via various components, and the low-frequency excitation via the side window [37], the underbody [32, 33, 38], the side door [39], or the windshield [30] has been adressed, the reduction to a single transmission path precludes the evaluation of real vehicles. One of the few papers that consider

the entire vehicle body is that of Wang [35], but no experimental validation is available here. The role of different excitation regions (such as the windshield, underbody, or recirculation region behind the vehicle) and the interaction of vibrating mechanical structures via the interior cavity has not been studied yet, but is considered to be critical to achieve a proper understanding of low-frequency flow-induced noise in vehicles.

1.2 Aim of this thesis

Based on the previous explanations, it can be concluded that, despite the great amount of research currently conducted regarding noise inside vehicles, a great number of topics remain unexplored or have only received limited attention, particularly regarding low-frequency wind-induced noise. Since the validity of many simplifications applicable in the high-frequency domain and discussed in detail throughout this work appear at least questionable for the special case of low-frequency noise in real vehicles, it is crucial to establish a context between low- and higher-frequency mechanisms thoroughly treated in terms of e.g. wavenumber-frequency spectra in literature [43]. In particular, validating numerically obtained low-frequency wall pressure fluctuations (WPF) with wind tunnel measurements requires taking into account the effects of spatial coherence. To the best of the author's knowledge, no study has been conducted that thoroughly investigates and compares aerodynamic and aeroacoustic excitation in various areas of the vehicle, such as the underbody or the recirculation area behind the vehicle. Furthermore, with the exception of a few studies without experimental validation, the aero-vibro-acoustic investigations carried out so far are limited to a specific transmission path while other transmission paths are intentionally blocked. However, real vehicles contain a wide range of flexible components that may transmit noise inside the cabin and the associated vibro-acoustic coupling mechanisms are of great interest for aero-vibro-acoustic optimisation procedures. In summary, the aim of this work is, on the one hand, to combine existing knowledge from a wide range of disciplines for developing a theoretical framework for the treatment of low-frequency wind-induced noise, and, on the other hand, to develop a reliable method for assessing relevant problems. Particular emphasis is placed on the experimental validation of the different acoustical, mechanical and aerodynamical phenomena with appropriate measurement methods.

1.3 Content

Chapter 2: Vibro-acoustic mechanisms and techniques

This chapter sets a theoretical framework for the investigation of vibro-acoustic mechanisms in vehicles. Beginning with the transmission of waves through an infinite plate, the complexity is successively extended to a finite vibro-acoustic box with natural and inhomogeneous boundary conditions, then to general, strongly coupled vibro-acoustic systems, and finally to actual vehicles. The chapter also provides an extensive summary of available numerical, experimental and hybrid techniques for assessing the issue.

Chapter 3: Aero-vibro-acoustic mechanisms in vehicles

This chapter begins with the physical principles of aerodynamics and aeroacoustics and then discusses statistical methods for the description of wall pressure fluctuations and the transmission into a vibro-acoustic box. Then, a literature review of aerodynamic, aeroacoustic, and aero-vibro-acoustic publications pertinent to the topic is presented by isolating four distinct excitation mechanisms: convectively excited surfaces, the recirculation area, the underbody, and direct excitation via openings.

Chapter 4: Hybrid strategy for coupling experimental and numerical normal modes

This chapter presents a method for assesing vibro-acoustic problems based on arbitrary experimental or numerical modes. The method is based on a modal formulation extended with non-conforming grids that allows to coupled arbitrary mechanical or acoustical modes defined on point clouds. Extensive numerical validation using a coupled vibro-acoustic system shows, that the computational error can be greatly reduced if the discretization of the structural modes is refined via thin-plate-spline (TPS) interpolation.

Chapter 5: A generic Testbody for assesing flow-induced noise in vehicles

In this chapter, a generic test specimen designed and fabricated specifically for this thesis is presented and the mechanical structural modes required for the subsequent treatment are extracted via EMA. Furthermore, the acoustic modes of the cavity are calculated via the finite element (FE) method and validated by acoustical Frequency Response Functions (FRF's).

Chapter 6: Flow topology and wall pressure fluctuations

In this chapter, the numerical calculation of the transient WPF is presented and analysed. After identifying the relevant statistical quantities, a detailed validation with wind tunnel measurements is performed. It turns out that the excitation ranking of the different surfaces cannot be correctly reproduced due to an incorrectly predicted flow separation at the roof. Consequently, the excitation via the roof predominates in the numerical calculation, whereas in the experimental case, the strongest aerodynamic excitation appears at the windshield.

Chapter 7: Flow-induced noise inside the generic structure

This chapter represents the unification of all the previous investigations to finally address the transfer of flow-induced noise inside the testbody. The displacement and pressure spectra of the wind-excited structure are calculated using an especially designed custom program for investigating aero-vibro-acoustic issues. The direct excitation of the acoustic cavity via an idealized rear vent is also considered. The results are analyzed and compared with extensive wind tunnel measurements.

1.4 My main contributions

The primary novel contributions of this dissertation work are essentially contained in Chapters 4-7.
Chapter 4 presents a hybrid method that allows the solution of coupled vibro-acoustic problems based on uncoupled mechanical and acoustical modes. These modes can be calculated using either experimental methods (such as EMA) or numerical methods (such as FE), which can then be combined using a modal formulation to describe the dynamics of the coupled vibro-acoustic system. The main innovation compared with the original method proposed by Kim [44] is that arbitrary grids can be handled using the technique of non-conforming grids which greatly expands the method's range of applications.
Chapter 5 presents a novel test body specifically designed for the investigation of low-frequency aero-vibro-acoustic mechanisms. Common test bodies, such as the SAE test body [1, 22, 23] or the Drivaer model [25, 27, 45–47] are specifically designed to study noise transmission through the side window. The innovative test body, on the other hand, allows the investigation of vibro-acoustic coupling mechanisms between a variety of flexible panels, and particularly the investigation of the underbody and the trunk partition, which are of great interest in the low-frequency range.
In Chapter 6, a comprehensive evaluation of the WPF on the test body is performed. For this purpose, the results of a numerical simulation based on the lattice Boltzmann (LB) method are compared with wind tunnel measurements. Previous investigations have e.g. investigated the auto-power spectral density (APSD) over the hull of the vehicle [32] or the cross-power spectral density (CPSD) on certain surfaces [1, 22] but in order to understand and validate the low-frequency excitation of the vehicle both CPSD and APSD have to be investigated and compared on all surfaces which is a difficult task due to the high dimensionality of the statistical data sets. To the best of the author's knowledge, no such investigation has yet been conducted. The analysis reveals that there are typical characteristics for regions excited by convected turbulence, leeward components, and regions on the underbody. More specifically, the acoustic cavity modes at the underbody could be identified experimentally and numerically using the CPSD, which is a novel finding. The most representative statistical quantities are identified and finally allow for a tabular comparison of excitation via the various surfaces.
In Chapter 7, the full aero-vibro-acoustic workflow is carried out based on experimentally determined structural modes, computational acoustic modes and wall pressure excitation from a transient LB simulation. The results are then validated using extensive wind tunnel measurements. This approach differs from earlier contributions discussed in Chapter 3 in that it considers a wide variety of flexible surfaces, focuses on the low frequency range, accounts for the Helmholtz excitation via openings, and is thoroughly validated with wind tunnel measurements.

2 Vibro-acoustic mechanisms and techniques

2.1 State of art

Since the earliest days of industry, vibro-acoustic topics have been of great importance for developing mechanical devices and transportation vehicles such as aircraft, trains, and automobiles. Lord Rayleigh provided the first theoretical treatment on the propagation of acoustic waves in his 1877 book *The Theory of Sound* [49]. With the advent of modern computers in the 1970s and the resulting new possibilities related with advanced experimental and numerical methods, the importance of vibroacoustics in the modern industries soared and it is now a paramount concern of automotive manufacturers to prevent noise and vibration in an early phase of the development process. Nefske provided an early and influential overview of the state of research on vibro-acoustic effects in automobile cabins in 1980 [3]. Several techniques and methods, such as the finite element (FE) method, transfer path analysis (TPA), modal analysis (MA), and component mode synthesis (CMS), have been professionalized and are now an integral part of the development process. After many years of intensive research, assessing vibro-acoustic issues remains a challenging subject necessitating considerable understanding in a variety of cross-sectional fields encompassing mechanical engineering, electrical engineering, and computer science disciplines. Since a complete discussion of relevant mechanisms and techniques is much beyond the scope of this thesis, the interested reader is recommended to contemporary and exhaustive literature on the topic. The acronym NVH (Noise Vibration Harshness) is often used to identify related work. Anders Brandt's 2011 book, *Noise and Vibration Analysis* [50], provides an in-depth investigation of vibro-acoustic methods with a special emphasis on signal processing. Regarding the Fourier transform, the outstanding lecture notes by Brad Osgood are recommended [51]. Regarding the numerous strategies for simulative treatment of automotive issues, the 2016 book by Stephen A. Hambric [8] is also proposed. In addition, Jian Pang's 2019 book [52] offers a comprehensive and well-written discussion of vibro-acoustic and aero-vibro-acoustic topics. Other excellent resources for vibroacoustic topics are the classical books of Cremer [53] and Fahy [54]. The reader is directed to the book by Kaltenbacher [55] for a comprehensive introduction of the FE method. The terminology employed throughout this thesis is given in Tab. 2.1 as a precursor for later discussions. The specific mention of the domain (space-frequency, wavenumber-frequency, modal) is generally omitted for the sake of brevity. The context will tell whether an e.g. mechanical admittance is a spatially resolved admittance defined in the frequency domain $\hat{y}_\mathrm{s}$, a wave admittance $\breve{y}_\mathrm{s}$ defined in the wavenumber frequency domain or a modal admittance $\tilde{y}_\mathrm{s}$.

2.2 Transmission of waves through a flexible plate into an acoustic cavity

To aid comprehension, the reader is cordially invited to begin with the derivations in Appendix A and the simple 1D vibro-acoustic system consisting of a piston and a cavity in Appendix B before coming back to this, more challenging, example. In order to establish a foundation for the mathematical concepts, the physical mechanisms and the terminology used throughout the thesis at hand, we begin by investigating the transmission of plane acoustic (or aerodynamic) waves via a mechanical plate into an acoustical

Domain	Term	Space-Frequency	Wavenumber-Frequency	Modal
mechanical	admittance	$\hat{u}_\mathrm{s}/\hat{f}_\mathrm{s} = \hat{y}_\mathrm{s}$	$\breve{u}_\mathrm{s}/\breve{p}_\mathrm{s} = \breve{y}_\mathrm{s}$	$\tilde{u}_\mathrm{s}/\tilde{f}_\mathrm{s} = \tilde{y}_\mathrm{s}$
	dynamic stiffness	$\hat{f}_\mathrm{s}/\hat{u}_\mathrm{s} = \hat{z}_\mathrm{s}$	$\breve{p}_\mathrm{s}/\breve{u}_\mathrm{s} = \breve{z}_\mathrm{s}$	$\tilde{f}_\mathrm{s}/\tilde{u}_\mathrm{s} = \tilde{z}_\mathrm{s}$
acoustic	admittance	$i\omega\hat{q}_\mathrm{a}/\hat{p}_\mathrm{a} = \hat{y}_\mathrm{a}$	$i\omega\breve{v}_\mathrm{a}/\breve{p}_\mathrm{a} = \breve{y}_\mathrm{a}$	$i\omega\tilde{q}_\mathrm{a}/\tilde{p}_\mathrm{a} = \tilde{y}_\mathrm{a}$
	dynamic stiffness	$\hat{p}_\mathrm{a}/i\omega\hat{q}_\mathrm{a} = \hat{z}_\mathrm{a}$	$\breve{p}_\mathrm{a}/i\omega\breve{v}_\mathrm{a} = \breve{z}_\mathrm{a}$	$\breve{p}_\mathrm{a}/i\omega\tilde{q}_\mathrm{a} = \breve{z}_\mathrm{a}$
coupled	admittance	$\hat{d}_\mathrm{c}/\hat{f}_\mathrm{c} = \hat{y}_\mathrm{c}$	$\breve{d}_\mathrm{c}/\breve{f}_\mathrm{c} = \breve{y}_\mathrm{c}$	$\tilde{d}_\mathrm{c}/\tilde{f}_\mathrm{c} = \tilde{y}_\mathrm{c}$
	dynamic stiffness	$\hat{f}_\mathrm{c}/\hat{d}_\mathrm{c} = \hat{z}_\mathrm{c}$	$\breve{f}_\mathrm{c}/\breve{d}_\mathrm{c} = \breve{z}_\mathrm{c}$	$\tilde{f}_\mathrm{c}/\tilde{d}_\mathrm{c} = \tilde{z}_\mathrm{c}$

Table 2.1: Terminology for direct and inverse formulations. The coupled variables are related to the uncoupled variables as $\hat{d}_\mathrm{c} = [\hat{u}_\mathrm{s}, \hat{p}_\mathrm{a}]$ and $\hat{f}_\mathrm{c} = [\hat{f}_\mathrm{s}, i\omega\hat{q}_\mathrm{a}]$. Note that compared to other literature, such as [15], the ambient density is already included in the acoustic FRF's. This creates closer resemblance to the wavenumber-frequency formulation. The negative sign in $\hat{q}_\mathrm{a}$ is omitted for simplicity, thus inducing an additional phase change of π.

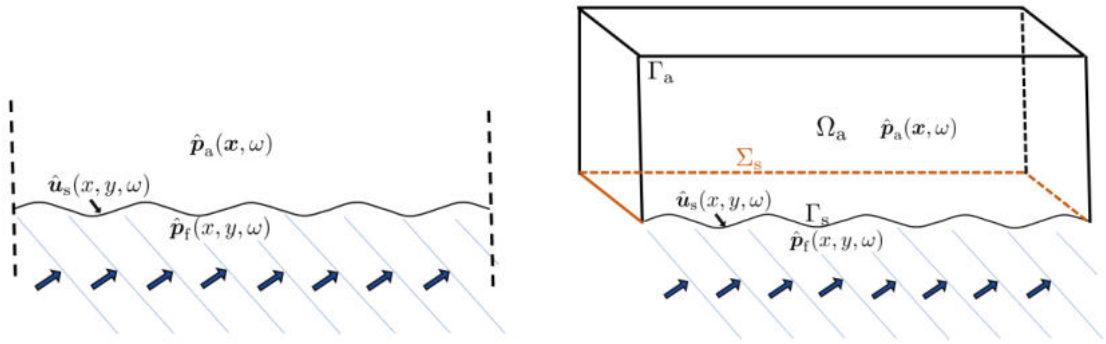

Figure 2.1: Transmission of waves through (a) infinite plate into semi-infinite cavity (b) finite plate defined on area Γ_s with boundary conditions along line Σ_s into finite cavity defined in domain Ω_a with cavity walls Γ_a.

cavity. Particular emphasis is placed on presenting the modal treatment of the mechanical, acoustic, or vibroacoustic issue as a generalization of the Fourier transform, thereby facilitating comprehension of the theoretical ideas perceived. Starting with the relatively simple vibro-acoustic setup in Fig. 2.1, we study the transmission of waves through an infinite Timoshenko-Mindlin plate with $[x_\mathrm{s}, y_\mathrm{,s}] \in \mathbb{R}^2$ into a semi-infinite space $\boldsymbol{x}_\mathrm{a} \in \mathbb{R}^3$, we gradually raise the complexity of the issue by first setting finite dimensions for plate $[x_\mathrm{s}, y_\mathrm{s}] \in \Gamma_\mathrm{s}$ and cavity $\boldsymbol{x}_\mathrm{a} \in \Omega_\mathrm{a}$, by allowing for general boundary conditions at the plate edges $[x_\mathrm{s}, y_\mathrm{,s}] \in \Sigma_\mathrm{s}$ and cavity walls $\boldsymbol{x}_\mathrm{a} \in \Gamma_\mathrm{a}$ (thus introducing the normal mode coupling procedure) and by finally addressing the modal decomposition of the strongly coupled vibro-acoustic system.

2.2.1 A semi-infinite cavity excited by boundary motion

The following derivation is based on the 2D example given in [54]. The propagation of acoustic waves in a (possibly infinite) cavity with mean speed of sound c_0 and mean density ρ_0 can be described by the wave equation for the acoustic pressure $\hat{p}_\mathrm{a}(\boldsymbol{x},\omega)$ in frequency domain as

$$(-\frac{\omega^2}{c_0^2} - \Delta)\hat{p}_\mathrm{a}(\boldsymbol{x},\omega) = 0\,. \tag{2.1}$$

Details on the derivation may be found in Sec. 3.1. The plate vibrations in terms of normal velocity $i\omega\hat{u}_\mathrm{s}(x,y,\omega)$ induced by the aerodynamic pressure distribution $\hat{p}_\mathrm{f}(\boldsymbol{x},\omega)$ represent a boundary source for the acoustical cavity. By satisfying the continuity of normal velocity at the boundary, the balance of

momentum allows to recast the boundary condition for the acoustic cavity according to

$$\boldsymbol{n} \cdot \nabla \hat{p}_{\mathrm{a}}(\boldsymbol{x}, \omega) = \omega^2 \rho_0 \hat{u}_{\mathrm{s}}(x, y, \omega) \quad \text{for} \quad \boldsymbol{x} \in \mathbb{R}^2 \,. \tag{2.2}$$

Assuming plane bending waves and plane acoustical waves, the velocity and pressure fields can be represented in terms of their inverse spatial Fourier transforms [56] and the angular wavenumber vector $\boldsymbol{k} = [k_{\mathrm{x}}, k_{\mathrm{y}}, k_{\mathrm{z}}]$ as

$$\hat{v}_{\mathrm{s}}(x, y, \omega) = \mathcal{F}_{\mathrm{x}}^{\mathrm{i}} \left\{ \breve{v}_{\mathrm{s}}(\mathbf{k}, \omega) \right\} = \frac{1}{(\sqrt{2\pi})^2} \int_{\mathbb{R}^2} \breve{v}_{\mathrm{s}}(\mathbf{k}, \omega) e^{i\mathbf{k}\cdot\mathbf{x}} d\mathbf{k} \quad \text{and} \tag{2.3}$$

$$\hat{p}_{\mathrm{a}}(\mathbf{x}, \omega) = \mathcal{F}_{\mathrm{x}}^{\mathrm{i}} \left\{ \breve{p}_{\mathrm{a}}(\mathbf{k}, \omega) \right\} = \frac{1}{(\sqrt{2\pi})^3} \int_{\mathbb{R}^3} \breve{p}_{\mathrm{a}}(\mathbf{k}, \omega) e^{i\mathbf{k}\cdot\mathbf{x}} d\mathbf{k} \,. \tag{2.4}$$

By applying the spatial Fourier transformation over $\mathbb{R}^3$ on Eq. (2.1) as

$$\mathcal{F}_{\mathrm{x}} \left\{ (-\frac{\omega^2}{c_0^2} - \Delta) \hat{p}_{\mathrm{a}}(\boldsymbol{x}, \omega) \right\} = \frac{1}{(\sqrt{2\pi})^3} \int_{\mathbb{R}^3} (-\frac{\omega^2}{c_0^2} - \Delta) \hat{p}_{\mathrm{a}}(\boldsymbol{x}, \omega) e^{-i\mathbf{k}\cdot\mathbf{x}} d\mathbf{x} = 0 \,, \tag{2.5}$$

we obtain the wave equation in $\boldsymbol{k} - \omega$ domain as

$$(-\frac{\omega^2}{c_0^2} + |\mathbf{k}|^2) \breve{p}_{\mathrm{a}}(\mathbf{k}, \omega) = 0 \,. \tag{2.6}$$

A physical solution is therefore only possible if $\omega^2/c_0^2 = |\mathbf{k}_0|^2$ is satisfied, which is the well known dispersion relation. The boundary condition given in Eq. (2.2) can be incorporated by obtaining the spatial derivative normal to the wall as

$$\mathcal{F}_{\mathrm{x}} \left\{ (\partial \hat{p}_{\mathrm{a}}(\boldsymbol{x}, \omega)/\partial z)_{z=0} \right\} = \left\{ -ik_z \breve{p}_{\mathrm{a}}(\mathbf{k}, \omega) \right\}_{z=0} = \omega^2 \rho_0 \breve{u}_{\mathrm{s}}(k_{\mathrm{x}}, k_{\mathrm{y}}, \omega) \,. \tag{2.7}$$

Evaluation at $z = 0$ can be performed by applying inverse Fourier transformation. Doing so yields

$$\frac{1}{(\sqrt{2\pi})^3} \int_{\mathbb{R}^3} \left\{ -ik_z \breve{p}_{\mathrm{a}}(\mathbf{k}, \omega) e^{-i(k_{\mathrm{x}}x + k_{\mathrm{y}}y + k_z z)} \right\} d\mathbf{k} = \frac{1}{(\sqrt{2\pi})^3} \int_{\mathbb{R}^3} \left\{ \omega^2 \rho_0 \breve{u}_{\mathrm{s}}(k_{\mathrm{x}}, k_{\mathrm{y}}, \omega) e^{-i(k_{\mathrm{x}}x + k_{\mathrm{y}}y)} \right\} d\mathbf{k} \,, \tag{2.8}$$

and therefore, $z = 0$ gives

$$\breve{p}_{\mathrm{a}}(\mathbf{k}, \omega) = \frac{i\omega^2 \rho_0 \breve{u}_{\mathrm{s}}(k_{\mathrm{x}}, k_{\mathrm{y}}, \omega)}{k_z} \,. \tag{2.9}$$

The 3-dimensional field can thus be synthesized according to

$$\hat{p}_{\mathrm{a}}(\mathbf{x}, \omega) = \mathcal{F}_{\mathrm{x}}^{\mathrm{i}} \left\{ \breve{p}_{\mathrm{a}}(\mathbf{k}, \omega) \right\} = \frac{1}{(\sqrt{2\pi})^3} \int_{\mathbb{R}^3} \frac{i\omega^2 \rho_0 \breve{u}_{\mathrm{s}}(k_{\mathrm{x}}, k_{\mathrm{y}}, \omega)}{k_z} e^{i\mathbf{k}\cdot\mathbf{x}} d\mathbf{k} \,. \tag{2.10}$$

By employing the dispersion relation it is clear that the normal wavenumber k_{z} is related to frequency and trace wavenumber $\kappa = \sqrt{k_{\mathrm{x}}^2 + k_{\mathrm{y}}^2}$ as

$$k_{\mathrm{z}}(k_{\mathrm{x}}, k_{\mathrm{y}}, \omega) = \sqrt{(\omega^2/c_0^2) - k_{\mathrm{x}}^2 - k_{\mathrm{y}}^2} = \sqrt{|\mathbf{k}_0|^2 - \kappa^2}. \tag{2.11}$$

The triple integral in Eq. (2.10) can therefore be transformed into a double integral

$$\hat{p}_{\mathrm{a}}(\mathbf{x}, \omega) = \frac{1}{(\sqrt{2\pi})^2} \int_{\mathbb{R}^2} \frac{i\omega^2 \rho_0 \breve{u}_{\mathrm{s}}(k_{\mathrm{x}}, k_{\mathrm{y}}, \omega)}{k_z} e^{iz\sqrt{|\mathbf{k}_0|^2 - \kappa^2}} e^{ik_{\mathrm{x}}x + ik_{\mathrm{y}}y} dk_{\mathrm{x}} dk_{\mathrm{y}} \,. \tag{2.12}$$

It follows that the 3D acoustic pressure field in the cavity can be directly inferred from the boundary vibrations. Note that the trace wavenumber at the boundary can be related to the phase speed as $c_{\mathrm{ph}} = \omega/\kappa$. It follows immediately from Eq. (2.9) that the acoustic dynamic boundary stiffness $\breve{z}_{\mathrm{a}\Gamma}(\mathbf{k},\omega)$ can be expressed according to

$$\breve{z}_{\mathrm{a}\Gamma}(\mathbf{k},\omega) = \frac{\breve{p}_{\mathrm{a}}(\mathbf{k},\omega)}{-\omega^2\breve{u}_{\mathrm{s}}(k_{\mathrm{x}},k_{\mathrm{y}},\omega)} = \frac{-i\rho_0}{\sqrt{|\mathbf{k}_0|^2-\kappa^2}} = \frac{\rho_0 c_0}{i\omega\sqrt{1-(\kappa/|\mathbf{k}_0|)^2}} = \frac{\rho_0 c_0}{i\omega\sqrt{1-(c_0/c_{\mathrm{ph}})^2}}\,. \tag{2.13}$$

A more intrinsic formulation can be obtained by introducing a cut-on angular frequency $\omega_{\mathrm{c}} = \kappa c_0$ representing a lower frequency limit for acoustically propagating waves at a given trace wavenumber. It follows that

$$\breve{z}_{\mathrm{a}\Gamma}(\mathbf{k},\omega) = \frac{\rho_0 c_0}{i\omega}\frac{1}{\sqrt{1-(\omega_{\mathrm{c}}/\omega)^2}}\,. \tag{2.14}$$

If the boundary (or trace) wavenumber κ is less than the acoustic wavenumber ($\kappa^2 < |\mathbf{k}_0|^2$, $c_{\mathrm{ph}} > c_0$, $\omega > \omega_{\mathrm{c}}$), then the z-component of the wavenumber is real (Eq. (2.11)) and the dynamic boundary stiffness given by $\breve{z}_{\mathrm{a}\Gamma}(\mathbf{k},\omega) \approx \rho_0 c_0/i\omega$ is imaginary, and inversely proportional to frequency (resistive). In contrast, if ($\kappa^2 > |\mathbf{k}_0|^2$, $c_{\mathrm{ph}} < c_0$, $\omega < \omega_{\mathrm{c}}$) then the z-component of the wavenumber is imaginary and $\breve{z}_{\mathrm{a}\Gamma}(\mathbf{k},\omega) \approx -\rho_0 c_0/\omega_{\mathrm{c}}$ is real and independent of frequency, which indicates a mass response of the fluid. In this case, exponentially decaying waves are observed at positive imaginary wavenumbers. Since negative imaginary wavenumbers would indicate exponentially growing waves, they are physically impossible (Sommerfeld radiation condition [54]). The acoustic dynamic boundary stiffness is useful for e.g. investigating the dynamics of a one-way coupled vibro-acoustic box. Such a one-way coupling can be computed by first obtaining the boundary displacement from the uncoupled mechanical structure's partial differential equation (PDE) and then calculating the pressure inside the cavity using the acoustic dynamic boundary stiffness. Employing $\breve{z}_{\mathrm{a}\Gamma}(\mathbf{k},\omega)$ takes into account that the mechanical structure represents a flexible boundary for the acoustical system (one-way coupling). Although one-way coupling is frequently presumed, it may be necessary to account for two-way coupling by including feedback from the acoustical system to the mechanical structure (more on that in Sec. 2.4). A possibility to account for two-way coupling is to describe both systems with Neumann boundary conditions (i.e. sound hard in acoustics and zero-force in mechanics) and account for the coupling conditions by adding them as an additional forcing on the right-hand side of both mechanic and acoustic system. The modal coupling technique that will be a major topic in this thesis relies on this principle to couple acoustical systems with sound hard walls and mechanical systems with free boundaries. To later be able to relate this technique to the theoretical foundations in this chapter we shall now derive the acoustic impedance of a semi-infinite cavity forced by an impressed volume acceleration related to the displacements of the adjacent mechanical structure. The reader is reminded that the difference to employing the dynamic boundary stiffness is that the wall, previously assumed to represent a flexible boundary to the acoustic cavity, is now sound hard but subject to impressed forcing. For this purpose we follow the derivation given in [55] but consider only a momentum source $\boldsymbol{q}_{\mathrm{mo}}(\boldsymbol{x},\omega)$ on the right-hand side. By introducing the acoustic particle velocity $\boldsymbol{v}_{\mathrm{a}}(\boldsymbol{x},\omega)$ the conservation of mass and momentum are given by

$$\frac{1}{\rho_0 c_0^2}\frac{\partial p_{\mathrm{a}}}{\partial t} + \nabla\cdot\boldsymbol{v}_{\mathrm{a}} = 0 \tag{2.15}$$

and

$$\frac{\partial \boldsymbol{v}_{\mathrm{a}}}{\partial t} + \frac{1}{\rho_0}\nabla p_{\mathrm{a}} = \frac{1}{\rho_0}\boldsymbol{q}_{\mathrm{mo}}\,. \tag{2.16}$$

Performing $\partial/\partial t$ on Eq. 2.15 and $\nabla\cdot$ on Eq. 2.16, subtracting the results, assuming constant speed of sound c_0, dividing by c_0^2 and applying temporal Fourier transformation allows to formulate the inhomoge-

nous wave equation with momentum source $\boldsymbol{q}_{\mathrm{mo}}(\boldsymbol{x},\omega)$ as

$$(-\frac{\omega^2}{c_0^2}-\Delta)\hat{p}_{\mathrm{a}}(\boldsymbol{x},\omega)=-\nabla\cdot\boldsymbol{q}_{\mathrm{mo}}(\boldsymbol{x},\omega)\,. \tag{2.17}$$

By considering Eq. (2.16) it becomes clear that the momentum source due to an impressed velocity perturbation $\hat{\boldsymbol{v}}_{\mathrm{s}}(\boldsymbol{x},\omega)$ is given by $\hat{\boldsymbol{q}}_{\mathrm{mo}}(\boldsymbol{x},\omega)=i\omega\rho_0\hat{\boldsymbol{v}}_{\mathrm{s}}(\boldsymbol{x},\omega)$ or (as a function of displacement) as $\hat{\boldsymbol{q}}_{\mathrm{mo}}=-\omega^2\rho_0\hat{\boldsymbol{u}}_{\mathrm{s}}(\boldsymbol{x},\omega)$. Performing the spatial Fourier transformation and recalling that the excitation is considered to be normal to z-plane as $\hat{u}_{\mathrm{s}}(\boldsymbol{x},\omega)=[0,0,\hat{u}_{\mathrm{s}}(\boldsymbol{x},\omega)]$ yields

$$\left(-\frac{\omega^2}{c_0^2}+|\mathbf{k}|^2\right)\breve{p}_{\mathrm{a}}(\mathbf{k},\omega)=ik_{\mathrm{z}}\omega^2\breve{u}_{\mathrm{s}}\,, \tag{2.18}$$

which in turn allows to define the acoustic impedance to a momentum source according to

$$\breve{z}_{\mathrm{a}}(\mathbf{k},\omega)=\frac{\breve{p}_{\mathrm{a}}(\mathbf{k},\omega)}{-\omega^2\breve{u}_{\mathrm{s}}\left(k_{\mathrm{x}},k_{\mathrm{y}},\omega\right)}=\frac{-ik_{\mathrm{z}}}{-\frac{\omega^2}{c_0^2}+|\mathbf{k}|^2}\,. \tag{2.19}$$

It is now possible to reformulate Eq. (2.19) as

$$\breve{p}_{\mathrm{a}}(\mathbf{k},\omega)-\omega^2\breve{z}_{\mathrm{a}}(\mathbf{k},\omega)\breve{u}_{\mathrm{s}}(\mathbf{k},\omega)=0 \tag{2.20}$$

or, by incorporating the acoustic wave mobility $\breve{y}_{\mathrm{a}}=1/\breve{z}_{\mathrm{a}}$, as

$$\breve{y}_{\mathrm{a}}(\mathbf{k},\omega)\breve{p}_{\mathrm{a}}(\mathbf{k},\omega)-\omega^2\breve{u}_{\mathrm{s}}(\mathbf{k},\omega)=0\,. \tag{2.21}$$

Note once again that the momentum source impedance $\breve{z}_{\mathrm{a}}$ allows to describe the pressure in an infinitely large cavity with sound hard walls excited by a momentum source. Provided the excitation occurs near the boundary, the boundary is still considered to be sound hard, which is the main difference from a formulation based on the boundary impedance $\breve{z}_{\mathrm{a}}$, where the boundary is flexible.

2.2.2 The Timoshenko-Mindlin plate

The propagation of mechanical bending waves in an infinite rectangular plate with constant flexural rigidity D_{s} subject to a distributed surface pressure excitation $\hat{p}_{\mathrm{f}}(x,y,\omega)$, owing to the presence of unsteady WPF as well as an induced pressure field $\hat{p}_{\mathrm{a}}(x,y,\omega)$ from the acoustical cavity, can be described using the Timoshenko-Mindlin plate differential equation

$$(-\omega^2+\frac{D_{\mathrm{s}}}{\rho_{\mathrm{s}}h_{\mathrm{s}}}\nabla^4)\hat{u}_{\mathrm{s}}(x,y,\omega)=\hat{p}_{\mathrm{f}}(x,y,\omega)-\hat{p}_{\mathrm{a}}(x,y,\omega)\,, \tag{2.22}$$

with $D_{\mathrm{s}}=\frac{E_{\mathrm{s}}h_{\mathrm{s}}^3}{12(1-\nu^2)}$, the biharmonic operator $\nabla^4=\frac{\partial^4}{\partial y_1^4}+2\frac{\partial^4}{\partial y_1^2\partial y_3^2}+\frac{\partial^4}{\partial y_3^4}$, theYoung's modulus E_{s}, the Poisson ratio ν, thickness h_{s} and density ρ_{s} [8, 53, 56]. By applying the 2-D Fourier-transformation over $\mathbb{R}^2$ and by introducing the bending wavenumber $k_{\mathrm{b}}^4=\omega^2\left(\rho_{\mathrm{s}}h_{\mathrm{s}}/D_{\mathrm{s}}\right)$ it follows that

$$-\omega^2\rho_{\mathrm{s}}h\left(1-\frac{\left(k_x^2+k_y^2\right)^2}{k_{\mathrm{b}}^4}\right)\breve{u}_{\mathrm{s}}=\breve{p}_{\mathrm{f}}-\breve{p}_{\mathrm{a}}\,, \tag{2.23}$$

which, in the case of vanishing acoustic feedback, allows to define the mechanical dynamic stiffness $\breve{z}_\mathrm{s}\left(k_\mathrm{x}, k_\mathrm{y}, \omega\right)$ as

$$\breve{z}_\mathrm{s}\left(k_\mathrm{x}, k_\mathrm{z}, \omega\right) = \frac{\breve{p}_\mathrm{f}}{\breve{u}_\mathrm{s}} = -\omega^2 \rho_\mathrm{s} h \left(1 - \frac{\left(k_x^2 + k_y^2\right)^2}{k_\mathrm{b}^4}\right) . \tag{2.24}$$

This in turn allows to recast Eq. (2.23) as

$$\breve{z}_\mathrm{s}\breve{u}_\mathrm{s} = \breve{p}_\mathrm{f} - \breve{p}_\mathrm{a} . \tag{2.25}$$

2.2.3 Transmission of waves through an infinite plate

After having completed the individual descriptions, the coupled vibro-acoustic issue can be formulated by simultaneously resolving Eq. (2.21) and Eq. (2.25) according to

$$\breve{z}_\mathrm{s}\breve{u}_\mathrm{s} + \breve{p}_\mathrm{a} = \breve{p}_\mathrm{f} \tag{2.26}$$

$$\breve{y}_\mathrm{a}\breve{p}_\mathrm{a} - \omega^2\breve{u}_\mathrm{s} = 0 . \tag{2.27}$$

The interaction between the two systems is described by the additional pressure loading $\breve{p}_\mathrm{a}$ from the acoustical system to the mechanical system and in turn, the mechanical normal acceleration $\omega^2\breve{u}_\mathrm{s}$ that drives the pressure fluctuations in the acoustical cavity. The system of equations can now be assembled, by either employing Eqs. (2.26) and (2.27) (furthermore called direct formulation) or on behalf of the respective reciprocal system variables $\breve{y}_\mathrm{s} = 1/\breve{z}_\mathrm{s}$ (mechanical wave admittance) and $\breve{z}_\mathrm{a} = 1/\breve{y}_\mathrm{a}$ (acoustical dynamic stiffness) in an inverse formulation. Assembling the corresponding equations results in

$$\begin{bmatrix} \breve{z}_\mathrm{s} & 1 \\ -\omega^2 & \breve{y}_\mathrm{a} \end{bmatrix} \begin{bmatrix} \breve{u}_\mathrm{s} \\ \breve{p}_\mathrm{a} \end{bmatrix} = \begin{bmatrix} \breve{p}_\mathrm{f} \\ 0 \end{bmatrix} \quad \text{and} \quad \begin{bmatrix} 1 & \breve{y}_\mathrm{s} \\ -\omega^2\breve{z}_\mathrm{a} & 1 \end{bmatrix} \begin{bmatrix} \breve{u}_\mathrm{s} \\ \breve{p}_\mathrm{a} \end{bmatrix} = \begin{bmatrix} \breve{y}_\mathrm{s}\breve{p}_\mathrm{f} \\ 0 \end{bmatrix} . \tag{2.28}$$

These formulations are intended as a precursor for Chap. 2.5, where it will be shown that the direct formulation results from a numerical discretization of the Helmholtz equation, whereas a conceptually similar inverse formulation is employed in experimental procedures based on vibro-acoustic TPA. The equations demonstrate that a direct connection between the aerodynamic excitation of the structure ($\breve{p}_\mathrm{f}$) and the acoustic pressure in the cavity ($\breve{p}_\mathrm{a}$) can be obtained from Eqs. (2.26) and (2.27). The resulting vibro-acoustic joint wavenumber admittance $\breve{y}_\mathrm{c} = \breve{p}_\mathrm{a}/\breve{p}_\mathrm{f}$ (that is actually a transmissibility but will still be referred to as admittance to keep the notation straight) becomes $\breve{y}_\mathrm{c} = \omega^2/(\omega^2 + \breve{y}_\mathrm{a}\breve{z}_\mathrm{s})$ or $\breve{y}_\mathrm{c} = \omega^2\breve{z}_\mathrm{a}/(\omega^2\breve{z}_\mathrm{a} + \breve{z}_\mathrm{s})$. If the feedback from the acoustic cavity to the mechanical structure is ignored, the vibro-acoustic joint wavenumber admittance can be formulated using the boundary admittance and becomes simply $\breve{y}_\mathrm{c} = \omega^2\breve{z}_{\mathrm{a}\Gamma}\breve{y}_\mathrm{s}$.

2.2.4 Finite domains

We will now demonstrate that these formulations equally apply to finite mechanical and acoustical domains. For this purpose, we assume that natural boundary conditions are satisfied for the mechanical structure, which means that the first three spatial derivatives of the displacements (resp. the velocities) must be zero and accordingly both inclination angle, shear force and bending moment at Γ_s identically vanish. The walls of the cavity are assumed sound hard, which corresponds to the natural boundary conditions of the wave equation in pressure formulation. By doubling the geometric dimensions L_x and L_y (and thus the wavelengths) of the plate, the natural plate boundary conditions can be transformed into the boundary conditions of the simply supported plate. Since the normal velocity of the plate enters

the acoustic field as a boundary condition, it is clear that only acoustic waves with matching wavelengths can propagate in the acoustic field. Due to the geometrical dimensions and boundary conditions, it is evident that only a finite number of acoustic and mechanical waves can exist. This can be described mathematically by transitioning from the Fourier transform to the Fourier series. Thus, we assume that the finite spatial pressure field $\hat{p}_{\mathrm{a}\Omega}(\boldsymbol{x},\omega)$ can be represented by a number of basis functions according to

$$\hat{p}_{\mathrm{a}\Omega}(\boldsymbol{x},\omega) = \frac{1}{\sqrt{N_\mathrm{x}N_\mathrm{y}N_\mathrm{z}}} \sum_{m,n,l=0}^{N_\mathrm{x},N_\mathrm{y},N_\mathrm{z}} \breve{p}_{\mathrm{a}|\mathrm{mnl}}(\omega) e^{i(\Delta k_\mathrm{x} m + \Delta k_\mathrm{y} n + \Delta k_\mathrm{z} l)} \tag{2.29}$$

with $[N_\mathrm{x}, N_\mathrm{y}, N_\mathrm{z}] \in \mathbb{N}^3$ and in-plane wavenumber spacing $\Delta k_\mathrm{x} = \pi/L_\mathrm{x}$ and $\Delta k_\mathrm{y} = \pi/L_\mathrm{y}$ to satisfy the plate (and cavity) boundary conditions and out-of-plane wavenumber spacing $\Delta k_\mathrm{z} = 2\pi/L_\mathrm{z}$ to ensure zero particle velocity at the opposing cavity wall. Then, by evaluating Eq. (2.6) for a discrete wavenumber vector $\boldsymbol{k} = [k_\mathrm{m}, k_\mathrm{n}, k_\mathrm{l}]$ with components $k_\mathrm{m} = m\Delta k_\mathrm{x}$, $k_\mathrm{n} = n\Delta k_\mathrm{y}$, $k_\mathrm{l} = l\Delta k_\mathrm{z}$ and by zeroing the expression in brackets, the angular eigenfrequencies of the cavity become

$$\omega_{\mathrm{a}|\mathrm{mnl}} = c_0\sqrt{k_\mathrm{m}^2 + k_\mathrm{n}^2 + k_\mathrm{l}^2} = 2\pi c_0 \sqrt{\left(m/2L_\mathrm{x}\right)^2 + \left(n/2L_\mathrm{y}\right)^2 + \left(l/L_\mathrm{z}\right)^2}\,. \tag{2.30}$$

The three indices used here can be combined into a new index which then gives a one-dimensional set of angular frequencies combined with a three-dimensional set of basis functions. These then correspond to the usual formulation of one-dimensional angular frequencies combined with their multidimensional eigenmodes. For the following, however, the three-index notation is advantageous. Similar to Eq. (2.30), the displacement field satisfying the natural mechanical boundary conditions can be represented by

$$\hat{u}_{\mathrm{s}\Omega}(\boldsymbol{x},\omega) = \frac{1}{\sqrt{N_\mathrm{x}N_\mathrm{y}}} \sum_{m,n}^{N_\mathrm{x},N_\mathrm{y}} \breve{u}_{\mathrm{s}|\mathrm{mn}}(\omega) e^{i(\Delta k_\mathrm{x} m + \Delta k_\mathrm{y} n)}\,, \tag{2.31}$$

and hence, by discretizing and zeroing the dynamic stiffness of the Kirchhoff plate in Eq. (2.24) it turns out that only a limited set of bending wavenumbers $k_{\mathrm{b}|\mathrm{mn}}$ satisfies the geometric boundary conditions. These bending wavenumbers can be evaluated according to $k_{\mathrm{b}|\mathrm{mn}}^2 = k_\mathrm{m}^2 + k_\mathrm{n}^2$ with k_n and k_m defined with the same wavenumber spacing as for the acoustic cavity and the corresponding natural frequencies become

$$\omega_{\mathrm{s}|mn} = \sqrt{\frac{D_\mathrm{s}}{\rho_\mathrm{s} h}} k_{\mathrm{b}|\mathrm{mn}}^2 = 4\pi^2 \sqrt{\frac{D_\mathrm{s}}{\rho_\mathrm{s} h}} \left(\left(\frac{m}{2L_\mathrm{x}}\right)^2 + \left(\frac{n}{2L_\mathrm{y}}\right)^2 \right)\,, \tag{2.32}$$

with discrete bending wave numbers

$$k_{\mathrm{b}|\mathrm{mn}} = 2\pi\sqrt{\left(m/2L_\mathrm{x}\right)^2 + \left(n/2L_\mathrm{y}\right)^2}\,. \tag{2.33}$$

By evaluating Eq. (2.24) and Eq. (2.19) for a finite set of trace or bending wavenumbers κ_{mnl} and $k_{\mathrm{b}|\mathrm{mn}}$ and by substituting the discrete sets of wavenumbers with the corresponding set of discrete natural frequencies $\omega_{\mathrm{a}|\mathrm{mnl}}$ and $\omega_{\mathrm{s}|\mathrm{mn}}$ it is possible to obtain a set of frequency-dependent relations for acoustical and mechanical dynamic stiffness. By introducing the acoustical and mechanical eigenvalues according to $\lambda = \omega^2$ these relations become

$$\breve{y}_{\mathrm{s}|\mathrm{mn}}(\omega) = \frac{1}{\rho_\mathrm{s} h} \frac{\omega^2 \left(\rho_\mathrm{s} h_\mathrm{s}/D_\mathrm{s}\right)}{\omega^2 \left(\rho_\mathrm{s} h_\mathrm{s}/D_\mathrm{s}\right) - \left(k_m^2 + k_n^2\right)^2} = \frac{1}{\rho_\mathrm{s} h} \frac{\omega^2}{\omega^2 - \omega_{s|mn}^2} = \frac{1}{\rho_\mathrm{s} h} \frac{\omega^2}{\omega^2 - \lambda_{s|mn}}\,, \tag{2.34}$$

and, by recalling that the wavenumbers in z-direction have corresponding eigenfrequencies $\omega_{00\mathrm{l}}$ and eigenvalues $\lambda_{a|00l}$ for which the relation $k_{\mathrm{z}|\mathrm{l}} c_0 = \omega_{00\mathrm{l}} = i\sqrt{\lambda_{a|00l}}$ holds, the acoustical dynamic stiffness

becomes

$$\breve{z}_{\mathrm{a|mnl}}(\omega) = \frac{ik_{\mathrm{z}}}{k_m^2 + k_n^2 + k_l^2 - \frac{\omega^2}{c_0^2}} = -\frac{c_0^2 ik_{\mathrm{z}}}{\omega^2 - \lambda_{a|mnl}} = \frac{c_0\sqrt{\lambda_{a|00l}}}{\omega^2 - \lambda_{a|mnl}}\,. \tag{2.35}$$

The acoustic dynamic boundary stiffness can also be obtained by replacing the continuous set of wavenumbers in Eq. (2.14) with a finite set of wavenumbers. It follows that

$$\breve{z}_{\mathrm{a\Gamma|mnl}}(\omega) = \frac{\rho_0 c_0}{\sqrt{1 - (k_m^2 + k_n^2)\, c_0^2/\omega^2}} = \frac{\rho_0 c_0}{\sqrt{1 - \omega_{a|mn0}^2/\omega^2}} = \frac{\rho_0 c_0}{\sqrt{1 - \lambda_{a|mn0}/\omega^2}}\,. \tag{2.36}$$

Therefore, the considerations discussed in Sec. 2.2.3 equally apply to finite vibro-acoustic systems. Note that in case that the excitation cannot be expressed in terms of the harmonic functions in Eq. (2.29), spectral leakage occurs. The harmonic basis functions of the discrete Fourier transform match the eigenfunctions of the investigated vibro-acoustic system, and thus the discrete Fourier transform is equivalent to an eigenvalue decomposition of the vibro-acoustic system. This leads to the important conclusion that the description of the vibro-acoustic system based on wave numbers, which is common in the literature and also used here, can be directly extended to finite-vibro-acoustic systems.

2.2.5 From Fourier transformation towards Eigenvalue transformation

The assumptions made in the previous chapter regarding the propagation of plane waves are only valid for a limited set of geometries and boundary conditions. Owing to the limited phase shift induced by boundary conditions ($\pm\pi$), the influence of the boundary conditions is particularly strong at low frequencies. The ratio between induced phase jump and overall phase change in a full cycle decreases with increasing frequency, and so does the influence of the boundary conditions [54]. In the general case, one can proceed similarly to Eq. (2.4), but instead of employing an (in)-finite set of plane waves it is presumed that the spatial fields can be represented as a superposition of a suitably chosen set of functions (namely the acoustic and mechanical modes $\psi_{\mathrm{a|n}}(\boldsymbol{x})$ and $\psi_{\mathrm{s|m}}(x,y)$ with frequency dependent weighting $\tilde{p}_{\mathrm{a|n}}(\omega)$ and $\tilde{v}_{\mathrm{s|m}}(\omega)$ (the modal participation factors). Compared to the spatial Fourier transformation, the difference is that instead of choosing a multi-dimensional set of one-dimensional orthonormal trigonometric basis functions weighted with a multi-dimensional set of coefficients, we choose a set of multi-dimensional orthonormal basis functions weighted with one-dimensional coefficients. An orthonormal multi-dimensional basis for a given pressure or displacement field is then given by the corresponding set of eigenfunctions. Consequently, similar to Eq. (2.4) or Eq. (2.29) (which is a discrete inverse Fourier transform), it is assumed that the acoustic and mechanical fields can be derived from the modal variables by employing inverse Eigenvalue transformations $\mathcal{E}_{\mathrm{a}}^{\mathrm{i}}$ and $\mathcal{E}_{\mathrm{s}}^{\mathrm{i}}$ as

$$\hat{p}_{\mathrm{a}}(\boldsymbol{x},\omega) = \sum_{n=0}^{N} \tilde{p}_{\mathrm{a|n}}(\omega)\psi_{\mathrm{a|n}}(\boldsymbol{x}) = \mathcal{E}_{\mathrm{a}}^{\mathrm{i}}\left\{\tilde{p}_{\mathrm{a|n}}\right\} \tag{2.37}$$

and

$$\hat{u}_{\mathrm{s}}(x,y,\omega) = \sum_{m=0}^{M} \tilde{u}_{\mathrm{s|m}}(\omega)\psi_{\mathrm{a|m}}(x,y) = \mathcal{E}_{\mathrm{s}}^{\mathrm{i}}\left\{\tilde{v}_{\mathrm{s|m}}\right\}\,. \tag{2.38}$$

We presume that the mode shapes are normalised to unity modal mass and satisfy the orthogonality relationship $\int_\Omega \psi_{\mathrm{a|n}}(\boldsymbol{x})\psi_{\mathrm{a|n'}}(\boldsymbol{x})dx = \delta_{nn'}$. These modes can be obtained by solving the related Eigenvalue problems that, in the given case can be formulated by incorporating e.g. additional acoustical Diriclet

(pressure release) boundary conditions at $\Gamma_\mathrm{D} \in \Omega_\mathrm{a}$ as

$$\text{Wave equation} \begin{cases} (-\frac{\omega_{\mathrm{a|n}}^2}{c_0^2} - \Delta)\psi_{\mathrm{a|n}}(\boldsymbol{x}) = 0\,. & \text{in } \Omega \\ \psi_{\mathrm{a|n}}(\boldsymbol{x}) = 0 & \text{on } \Gamma_\mathrm{D} \in \Omega_\mathrm{a} \end{cases} \tag{2.39}$$

with the corresponding Eigenvalues $\lambda_{\mathrm{a|n}} = \omega_{\mathrm{a|n}}^2$ and similarly, by incorporating e.g. additional mechanical Diriclet (zero displacement) boundary conditions at $\Sigma_\mathrm{D} \in \Gamma_\mathrm{s}$ as

$$\text{Timoshenko-Mindlin plate} \begin{cases} (-\omega_{\mathrm{s|m}}^2 + \frac{D}{\rho_\mathrm{s} h_\mathrm{s}}\nabla^4)\psi_{\mathrm{a|m}}(x,y) = 0 & \text{in } \Gamma_\mathrm{s} \\ \psi_{\mathrm{a|m}}(x,y) = 0 & \text{on } \Sigma_\mathrm{D} \in \Gamma_\mathrm{s} \end{cases} \tag{2.40}$$

with the corresponding Eigenvalues $\lambda_{\mathrm{s|m}} = \omega_{\mathrm{s|m}}^2$. Similar to the Fourier transform, Eigenvalue transformations can be defined for the structural and acoustical field, that allow to obtain the modal variables (i.e. the participation factors) from an existing or presumed field by projecting the field on each individual eigenfunction by means of a scalar product as

$$\mathcal{E}_\mathrm{a}\left\{\hat{p}_\mathrm{a}(\boldsymbol{x},\omega)\right\} = \int_{\Omega_\mathrm{a}} \hat{p}_\mathrm{a}(\boldsymbol{x},\omega)\psi_{\mathrm{a|n}}(\boldsymbol{x})dx = \tilde{p}_{\mathrm{a|n}}(\omega) \tag{2.41}$$

and

$$\mathcal{E}_\mathrm{s}\left\{\hat{u}_\mathrm{s}(x,y,\omega)\right\} = \int_{\Gamma_\mathrm{s}} \hat{u}_\mathrm{s}(x,y,\omega)\psi_{\mathrm{s|m}}(x,y)dx = \tilde{u}_{\mathrm{s|m}}(\omega) \tag{2.42}$$

The modal aerodynamic forcing on the mechanical plate can be obtained according to

$$\tilde{p}_{\mathrm{f|n}}(\omega) = \mathcal{E}_\mathrm{s}\left\{\hat{p}_\mathrm{f}(x,y,\omega)\right\}\,. \tag{2.43}$$

The ratio between modal mechanic displacement and modal aerodynamic forcing is the modal structural dynamic stiffness $\tilde{z}_{\mathrm{s|nm}}(\omega) = \tilde{p}_{\mathrm{f|n}}/\tilde{u}_{\mathrm{s|m}}$. Hence, each modal pair of displacement and aerodynamic forcing represents an individual spring-mass-damper system and the spatial variables are just a superposition of all these individual systems weighted with their individual eigenfunctions. The eigenvalues are the roots of the characteristic equation and contain all necessary informations to describe a 1-DOF structure with unity mass (see e.g. [57]), which is fulfilled here due to mass normalization. It follows that the modal structural dynamic stiffness to distributed pressure loading as $\tilde{z}_{\mathrm{s|m}}(\omega)$ and the modal structural admittance $\tilde{y}_{\mathrm{s|m}}(\omega)$ can be reproduced from the eigenvalues as

$$\tilde{z}_{\mathrm{s|m}}(\omega) = \omega^2 - \lambda_{\mathrm{s|m}} \quad \text{and} \quad \tilde{y}_{\mathrm{s|m}}(\omega) = \frac{1}{\omega^2 - \lambda_{\mathrm{s|m}}}\,. \tag{2.44}$$

The same holds for the acoustical system and thus the modal acoustic dynamic stiffness $\tilde{z}_{\mathrm{a|m}}(\omega)$ and the modal acoustic admittance $\tilde{y}_{\mathrm{a|m}}(\omega)$ become

$$\tilde{z}_{\mathrm{a|n}}(\omega) = \frac{1}{\omega^2 - \lambda_{\mathrm{a|n}}} \quad \text{and} \quad \tilde{y}_{\mathrm{a|n}}(\omega) = \omega^2 - \lambda_{\mathrm{a|n}}\,. \tag{2.45}$$

The reciprocal excitations can be incorporated on behalf of uncoupled structural and acoustic modes by additionally considering modal coupling matrices $\tilde{\boldsymbol{H}}_\mathrm{sa}$ and $\tilde{\boldsymbol{H}}_\mathrm{as}$ that contain the projection of the vibro-acoustic coupling loads (represented by the original modal formulation of pressure and displacement) on

the loaded systems given by

$$\tilde{\boldsymbol{H}}_{\mathrm{sa}} = \mathcal{E}_{\mathrm{s}}\left\{\mathcal{E}_{\mathrm{a}}^{\mathrm{i}}\left\{\tilde{p}_{\mathrm{a|n}}\right\}\right\} \quad \text{and} \quad \tilde{\boldsymbol{H}}_{\mathrm{as}} = \mathcal{E}_{\mathrm{a}}\left\{\mathcal{E}_{\mathrm{s}}^{\mathrm{i}}\left\{\tilde{u}_{\mathrm{a|n}}\right\}\right\} . \tag{2.46}$$

This definition is more commonly expressed in a discrete formulation and may e.g. be found in [58]. In the end, we can proceed similar to Sec. 2.2.3 to obtain the modal equations for normal mode coupling in

$$\text{direct}\left\{\begin{bmatrix}\tilde{\boldsymbol{Z}}_{\mathrm{s}} & \tilde{\boldsymbol{H}}_{\mathrm{sa}}\\ -\omega^2\tilde{\boldsymbol{H}}_{\mathrm{as}} & \tilde{\boldsymbol{Y}}_{\mathrm{a}}\end{bmatrix}\begin{bmatrix}\tilde{\boldsymbol{u}}_{\mathrm{s}}\\ \tilde{\boldsymbol{p}}_{\mathrm{a}}\end{bmatrix} = \begin{bmatrix}\tilde{\boldsymbol{p}}_{\mathrm{f}}\\ \boldsymbol{0}\end{bmatrix}\right. \quad \text{and inverse} \left\{\begin{bmatrix}\boldsymbol{I} & \tilde{\boldsymbol{Y}}_{\mathrm{s}}\tilde{\boldsymbol{H}}_{\mathrm{sa}}\\ -\omega^2\tilde{\boldsymbol{H}}_{\mathrm{as}}\tilde{\boldsymbol{Z}}_{\mathrm{a}} & \boldsymbol{I}\end{bmatrix}\begin{bmatrix}\tilde{\boldsymbol{u}}_{\mathrm{s}}\\ \tilde{\boldsymbol{p}}_{\mathrm{a}}\end{bmatrix} = \begin{bmatrix}\tilde{\boldsymbol{Y}}_{\mathrm{s}}\tilde{\boldsymbol{p}}_{\mathrm{f}}\\ \boldsymbol{0}\end{bmatrix}\right. \tag{2.47}$$

formulation for each frequency. In case of a unique set of spatial harmonics that describe acoustical and mechanical systems the modal coupling matrices become unity and we arrive at Eq. (2.28). This representation can now be employed to highlight a critical aspect of modal coupling. On the basis of Eq. (2.47) it is clear that the pressure distribution induced by a single mode is confined to a specific mechanical mode only if acoustic and mechanic mode shapes coincide. If the orthogonality condition is not satisfied, leakage occurs resulting in the distribution of excitation among all mechanical modes. The most critical case occurs if mechanical and acoustical modes are shifted by 180° indicating a vibro-acoustic shortcut. As long as the coupling is weak, which means that the feedback mechanism from the acoustic field does not significantly alter the structural modes of the plate this effect can be neglected. However, in the case of strong coupling, the acoustic pressure loading on the structure causes leakage in the modal displacements, followed by leakage induced from the boundary sources on the acoustic system. This process causes numerical artifacts and as a result, the application of modal coupling techniques is restricted to vibro-acoustic systems with sufficiently weak coupling effects (more on that in Chap. 4). For a detailed investigation of cross coupling effects see the recent publication by Sum (2021) [59]. However, if applicable, modal coupling is a powerful technique because it allows to describe coupled systems via individual uncoupled mode shapes. The first actual application of normal mode coupling by solving the uncoupled systems using the FE method dates back to Craggs (1973) [60].

2.2.6 Diagonalization via coupled vibro-acoustic modes

Analogous to the uncoupled acoustical and mechanical Eigenvalue transformations, such a transformation can also be defined for the coupled vibro-acoustic system. For this purpose, it is required to define the generalized displacement $\hat{d}_{\mathrm{c}}(\boldsymbol{x},\omega)$ incorporating both velocity and pressure and correspondingly the modal generalized displacement $\tilde{d}_{\mathrm{c}}(\boldsymbol{x},\omega)$ with generalized left and right eigenvectors $\psi_{\mathrm{cL|r}}(\boldsymbol{x})$ and $\psi_{\mathrm{c|r}}(\boldsymbol{x})$ to express the spatial field in terms of an inverse Eigenvalue transformation $\mathcal{E}_{\mathrm{c}}^{\mathrm{i}}$ as

$$\hat{d}_{\mathrm{c}}(\boldsymbol{x},\omega) = \mathcal{E}_{\mathrm{c}}^{\mathrm{i}}\left\{\tilde{d}_{\mathrm{c|r}}\right\} = \sum_{n=0}^{N}\tilde{d}_{\mathrm{c|r}}(\omega)\psi_{\mathrm{cL|r}}(\boldsymbol{x}) \quad \text{with} \quad \hat{d}_{\mathrm{c}}(\boldsymbol{x},\omega) = \hat{u}_{\mathrm{s}}(\boldsymbol{x},\omega) \quad \text{for} \quad \boldsymbol{x}\in\Gamma_{\mathrm{s}} \tag{2.48}$$

$$\text{and} \quad \hat{d}_{\mathrm{c}}(\boldsymbol{x},\omega) = \hat{p}_{\mathrm{a}}(\boldsymbol{x},\omega) \quad \text{for} \quad \boldsymbol{x}\in\Omega_{\mathrm{a}} \tag{2.49}$$

as well as a generalized forcing function $\hat{f}_{\mathrm{c}}(\boldsymbol{x},\omega)$ incorporating both mechanical and acoustical excitation as

$$\hat{f}_{\mathrm{c}}(\boldsymbol{x},\omega) = \mathcal{E}_{\mathrm{c}}^{\mathrm{i}}\left\{\tilde{f}_{\mathrm{c|r}}\right\} = \sum_{n=0}^{N}\tilde{f}_{\mathrm{c|r}}(\omega)\psi_{\mathrm{cL|r}}(\boldsymbol{x}) \quad \text{with} \quad \hat{f}_{\mathrm{c}}(\boldsymbol{x},\omega) = \hat{p}_{\mathrm{f}}(\boldsymbol{x},\omega) \quad \text{for} \quad \boldsymbol{x}\in\Gamma_{\mathrm{s}} \tag{2.50}$$

$$\text{and} \quad \hat{f}_{\mathrm{c}}(\boldsymbol{x},\omega) = i\omega\hat{q}_{\mathrm{a}}(\boldsymbol{x},\omega) \quad \text{for} \quad \boldsymbol{x}\in\Omega_{\mathrm{a}}\,. \tag{2.51}$$

Here it must be noted that the generalized functions at the interface are defined twice, once in the acoustic domain as an acoustic variable and once in the mechanical domain as a mechanical variable. In a discrete assembly, this corresponds to a dual substructuring method (more on that in Sec. 2.5). We furthermore employ $\boldsymbol{x}_\mathrm{a}$ and $x_\mathrm{s}, y_\mathrm{s}$ to identify the respective acoustical and mechanical variables. It is then possible to substitute the individual fields by their generalized counterparts and then to discretize and simultaneously solve the set of equations that describe the

$$\text{coupled eigenvalue problem} \begin{cases} D_\mathrm{s}\left(\nabla^4 - \omega_{\mathrm{c|r}}^2 m_\mathrm{s}/D_\mathrm{sb}\right)\psi_{\mathrm{c|r}}(x_\mathrm{s}, y_\mathrm{s}) + \psi_{\mathrm{c|r}}(x_\mathrm{a}, y_\mathrm{a}) = 0 & \text{in } \Gamma \\ \psi_{\mathrm{c|r}}(x_\mathrm{s}, y_\mathrm{s}) = 0 & \text{on } \Sigma_\mathrm{f} \\ (-\frac{\omega_{\mathrm{c|r}}^2}{c_0^2} - \Delta)\psi_{\mathrm{c|r}}(\boldsymbol{x}_\mathrm{a}) = 0\,. & \text{in } \Omega \\ \psi_{\mathrm{c|r}}(\boldsymbol{x}_\mathrm{a}) = 0 & \text{on } \Gamma_\mathrm{o} \\ \nabla\psi_{\mathrm{c|r}}(x_\mathrm{a}, y_\mathrm{a}) \cdot \boldsymbol{n} + i\omega\rho_0\psi_{\mathrm{c|r}}(x_\mathrm{s}, y_\mathrm{s}) = 0 & \text{on } \Gamma\,. \end{cases} \tag{2.52}$$

Here, the first line represents the mechanical structure defined in Eq. 2.2 with the additional acoustic forcing $\psi_{\mathrm{c|r}}(x_\mathrm{a}, y_\mathrm{a})$ from the cavity, the second line enforces the mechanical zero displacement boundary conditions, the third line represents the propagation of waves in the cavity (Eq. 2.1), the fourth line represents possible pressure release boundary conditions in the acoustic cavity and the fifth line enforces the continuity of normal velocity across the boundary (Eq. (2.2)). The result is naturally a set of coupled eigenvectors with associated eigenvalues $\lambda_{\mathrm{c|r}} = \omega_{\mathrm{c|r}}^2$. Due to the asymmetric nature of the problem the left and right eigenvectors do not coincide (unlike the uncoupled mechanical and acoustic formulations). To determine the left eigenvectors $\psi_{\mathrm{cL|n}}$ required for $\mathcal{E}_\mathrm{c}^\mathrm{i}$, the adjoint problem must be solved, which is not done here explicitly (more on that in Sec. 4.2.1). The coupled Eigenvalue transformation can then be defined to obtain the generalized modal displacements from the generalized displacements as

$$\mathcal{E}_\mathrm{c}\left\{\hat{d}_\mathrm{c}(\boldsymbol{x}, \omega)\right\} = \int_{\Omega_\mathrm{a}} \hat{d}_\mathrm{c}(\boldsymbol{x}, \omega)\psi_{\mathrm{cL|n}}(\boldsymbol{x})dx = \tilde{d}_{\mathrm{c|n}}(\omega)\,. \tag{2.53}$$

As was done in Eqs. (2.44) and (2.45), we can define a coupled modal dynamic stiffness $\tilde{z}_{\mathrm{c|r}}(\omega)$ and a coupled modal admittance $\tilde{y}_{\mathrm{c|r}}(\omega)$

$$\tilde{z}_{\mathrm{c|r}}(\omega) = \omega^2 - \lambda_{\mathrm{c|r}} \quad \text{and} \quad \tilde{y}_{\mathrm{c|r}}(\omega) = \frac{1}{\omega^2 - \lambda_{\mathrm{c|r}}} \tag{2.54}$$

relating generalised modal displacement and excitation as $\tilde{d}_{\mathrm{c|n}}(\omega) = \tilde{y}_{\mathrm{c|r}}(\omega)\tilde{f}_{\mathrm{c|r}}(\omega)$.

2.3 General plate-cavity systems

Following this brief introduction to the theoretical foundations of coupled plate-cavity systems, a brief overview of the historical and current developments in this area of research is provided. In 1963, Lyon [61] was one of the first to investigate the propagation of sound waves via a flexible panel into a closed rectangular box. In the same year, Dowell [62] published an influential contribution in which he expressed the mechanical displacements of a clamped panel in terms of its uncoupled mechanical and acoustic modes quite similar to what was presented previously but with a wave equation for particle velocity instead of acoustic pressure. A short time later, Pretlove [63] provided an exact solution to the coupled vibro-acoustic issue with a single simply supported plate. The article by Dowell (1977) [64] provides an excellent overview of the early work regarding vibro-acoustic boxes. In his publication [65], Pan described the more recent studies that had been done up until 1989. For an up-to-date survey, see Shahraeeni et al.

(2015) [66]. Analytical or semi-analytical models that explicitly contain a reduced set of parameters have been established in recent years (Chen (2014) [67] or Du (2012) [68]). Regarding the physical effects, it is worth mentioning in particular that with stronger coupling, the coupled eigenfrequencies are shifted with respect to the uncoupled ones, as such that the frequency difference between the neighboring uncoupled modes increases (e.g. if $f_s < f_a$ then $f_{c|s} < f_s$ and $f_{c|a} > f_a$ [3]). Regarding the effect of various parameters of vibro-acoustic systems, such as thickness, cavity length, influence of boundary conditions, and aspect ratio of the panel, as well as the influence of boundary conditions on the vibro-acoustic coupling effects, the interested reader is directed to Xue's 2018 paper [20]. Few contributions have been found regarding the vibro-acoustic implications of multiple flexible panels. For instance, Wang's (2017) research on the optimization of a vibro-acoustic system with flexible plates is worth mentioning [69]. Cavities with openings have also been studied by e.g. Kim (2002) [70] and Pàmies (2011) [71].

2.4 Automotive vibroacoustics

The transition from simple plate-cavity systems to complex vehicle bodies is comparatively simple regarding the physical phenomena, but obtaining a reliable structural model for the vehicle body, as well as deducing a meaningful interpretation is incomparably more challenging. The strength of the vibro-acoustic coupling effects is of utmost importance for the mathematical-experimental treatment, especially regarding the applicability of normal mode coupling but also for deducing a reliable interpretation of measurement or simulation data. In this context, the review of Nefske (1982) [3] has to be mentioned, who investigated the influence of a flexible tailgate on the coupled modes using the FE method and normal mode coupling. Significant coupling effects were found, the resulting frequency shifts in the mechanical and acoustic modes being in the range of a few Hz. To investigate the effects of the flexible boundary on the acoustic cavity modes, the vibrating surfaces of the vehicle must be blocked, which is practically impossible; hence, only generic test bodies, such as the one developed by Wyckaert (1996) [21], have been used for such studies. Here, it is shown experimentally that for structural excitation, the effects of coupling on the interior sound pressure are less pronounced than for interior acoustic excitation. A detailed investigation can be found in the review by Marburg (2002) [42], where it is concluded that the feedback effect of the mechanical system on the acoustic system can be neglected in case of structural excitation. Naturally, the validity of such a simplification depends on the specific structure employed and is difficult to estimate a priori. However, considering the many publications based on normal-mode coupling [3, 7, 12, 72], it seems safe to assume that the relaxation of boundary conditions is generally admissible. It will be investigated in this thesis that small openings, especially the rear vent opening can be a significant contributor to very low-frequency noise. This was also confirmed by Pan (1998) [73], who investigated the effect of openings on the sound pressure inside a helicopter. Although the influence of openings is of great importance, no investigation into direct aerodynamic excitation at low frequencies is known to the author. Clearly, the interior cavity shapes the dynamics of the acoustic system. More precisely, the trunk cavity acts as an acoustical mass that drives a Helmholtz resonance as investigated by Octav (2017) [74]. Due to the inherent uncertainties related with the manufacturing process, the opinion that these uncertainties must also be taken into account for adequate modeling has increasingly gained ground in recent years. The contribution by Durand (2008) [72], in which the influence of uncertainties in vehicle production was addressed on the basis of experimental measurements on a selection of 20 vehicles, was particularly interesting. Here, significant scatter of engine-related booming noise could be shown. Durand also notes that the influence of acoustic uncertainties is small compared to mechanical uncertainties.

2.5 Engineering techniques in automotive vibroacoustics

Since a great number of techniques for assessing interior noise in vehicles has been established in recent years, but no scholarly publication has been identified that places these methods within a common framework and elaborates on their applicability, advantages and disadvantages, an attempt will be made to fill that void in the next chapter. Owing to the specific physical effects in the low-frequency region, we will confine ourselves to suitable strategies (topics like e.g. statistical energy analysis (SEA) will therefore not be discussed). Before delving into the specifics of the various vibro-acoustic strategies, we will examine some fundamental ideas regarding direct and inverse formulations. Similar to the wavenumber-frequency and the modal formulations in Eqs. (2.28) and (2.47), a spatial discretization of the respective acoustic (wave equation in pressure formulation) and mechanic equations (Navier's equation in displacement formulation) and the boundary conditions allows to assemble a discrete system relating mechanical dynamic stiffness $\hat{\boldsymbol{Z}}_\mathrm{s}$, acoustic admittance $\hat{\boldsymbol{Y}}_\mathrm{a}$ or coupled dynamic stiffness $\hat{\boldsymbol{Z}}_\mathrm{c}$ with unknown solution vectors for displacement $\hat{\boldsymbol{u}}_\mathrm{s}$, pressure $\hat{\boldsymbol{p}}_\mathrm{a}$ and generalized displacement $\hat{\boldsymbol{d}}_\mathrm{c}$ subject to external excitation via force $\hat{\boldsymbol{f}}_\mathrm{s}$, volume flux $\hat{\boldsymbol{q}}_\mathrm{a}$ and generalized force $\hat{\boldsymbol{f}}_\mathrm{c}$ as

$$\begin{cases} \hat{\boldsymbol{Z}}_\mathrm{s}\hat{\boldsymbol{u}}_\mathrm{s} = \hat{\boldsymbol{f}}_\mathrm{s} \\ \hat{\boldsymbol{Y}}_\mathrm{a}\hat{\boldsymbol{p}}_\mathrm{a} = i\omega\hat{\boldsymbol{q}}_\mathrm{a} \\ \hat{\boldsymbol{Z}}_\mathrm{c}\hat{\boldsymbol{d}}_\mathrm{c} = \hat{\boldsymbol{f}}_\mathrm{c} \end{cases} \quad \text{and the corresponding inverse formulations} \quad \begin{cases} \hat{\boldsymbol{u}}_\mathrm{s} = \hat{\boldsymbol{Y}}_\mathrm{s}\hat{\boldsymbol{f}}_\mathrm{s} \\ \hat{\boldsymbol{p}}_\mathrm{a} = \hat{\boldsymbol{Z}}_\mathrm{a}i\omega\hat{\boldsymbol{q}}_\mathrm{a} \\ \hat{\boldsymbol{d}}_\mathrm{c} = \hat{\boldsymbol{Y}}_\mathrm{c}\hat{\boldsymbol{f}}_\mathrm{c} \end{cases} . \tag{2.55}$$

The inverse or FRF-matrices can directly be obtained from measurements, i.e. the displacements due to impressed force $\hat{y}_{\mathrm{s|ij}} = \hat{u}_{\mathrm{s|i}}/\hat{f}_{\mathrm{s|j}}$, the pressure due to an impressed volume source $\hat{z}_{\mathrm{a|ij}} = \hat{p}_{\mathrm{a|i}}/i\omega\hat{q}_{\mathrm{a|j}}$, and the generalized displacements due to an impressed generalized force $\hat{y}_{\mathrm{c|ij}} = \hat{d}_{\mathrm{c|i}}/\hat{f}_{\mathrm{c|j}}$. The reason for the opposite designations of the acoustic system matrices (dynamic stiffness - mobility) compared to the mechanical formulation follows from the historical definition of dynamic stiffness for the treatment of networks with sound soft boundaries (e.g. pipes, channels with open ending). For these networks, employing the volume velocity as a primal variable is more efficient. The discrete equations can directly be employed for the investigation of vibro-acoustic systems, either within the framework of the FE method or by investigating the critical paths via TPA [75]). However, in this work we are specifically interested in how the directly or inversely described acoustic or mechanical subsystems can be employed to investigate the behaviour of the coupled vibro-acoustic system. The fundamental concepts of assembling dynamic systems from subsystems are rooted in the concept of dynamic substructuring; consequently, we will outline the related theory briefly.

2.5.1 Overview of vibro-acoustic substructuring techniques

An introduction to dynamic substructuring may be found in the comprehensive book by Allen [76] or in the thesis of Davidsson [58]. To assemble a coupled system from decoupled subsystems, two conditions must generally be satisfied at the interface: compatibility of the primal or system variables (displacement, pressure) and equilibrium of the flow or dual variables (force, volume flux). Mathematically equivalent but practically distinct substructuring procedures can be derived by combining the subsystem matrices with the (discrete) coupling conditions. The main difference is if the boundary conditions arising from the coupling procedure are directly incorporated (primal coupling) or if they are enforced by adding additional interface forces (in general: Lagrange multiplier) to fullfill the coupling conditions. Consequently, modal reduction may be applied in either formulation to assemble the substructures from modal properties via CMS. The CMS techniques correspond to primal or dual coupling assemblies depending on if the modes are derived from the subsystems with Diriclet (primal, blocked-interface CMS) or Neumann (dual, free-

interface CMS) boundary conditions [76]. If the coupling conditions are incorporated by adding additional static component-modes derived by adding the static response of the substructure by progressively setting the displacement of every interface Degree-of-Freedom (DOF) to unity while zeroing all other DOFs to the fixed-displacement modes one speaks of the Hurty/Craig-Bampton Method [58,76]. Correspondingly, the free-displacement modes can be enriched by additional static modes obtained by evaluating the response of the subsystems due to unit force at the boundary nodes while keeping the other interface DOF's free [58]. It follows straight from Eq. (2.55) that these techniques may equally be applied to assemble acoustical systems from individual subsystems. Note however, that in the pressure-based formulation the Dirichlet and Neumann boundary conditions correspond to sound soft and sound hard walls alike. Thus, the behavior of a cavity can either be described by coupling two half-sized open (primal) or closed (dual) cavities (in inverse formulation: [77]). It is equally possible to assemble the inverse formulations to explore the behavior of a coupled system via admittance matrices measured on the uncoupled systems. These techniques are then referred to as FRF-based substructuring [78], component-based TPA [79,80] or admittance modeling [78] (for mechanical systems). If one examines transfer paths within an assembled system, one speaks of classical TPA [79]. Methods that can be used to infer the individual subsystems from an assembled system are called inverse methods [78,81]. For the coupling of vibro-acoustic systems in pressure-displacement formulation only the dual coupling by means of Lagrange multipliers can be considered due to the incompatibility of the primal variables in the formulation employed. Here, the coupled dynamic stiffness matrix $\hat{\boldsymbol{Z}}_\mathrm{c}$ of a coupled vibro-acoustic system can be calculated on the basis of the uncoupled mechanical ($\hat{\boldsymbol{Z}}_\mathrm{s}$) or acoustic subsystems ($\hat{\boldsymbol{Y}}_\mathrm{a}$) discretized under Neumann boundary conditions by additionally incorporating the coupling conditions. A detailed derivation of the coupled vibro-acoustic system matrix from the uncoupled FE systems will later be shown in Chap. 4. Suffice to say at this point that the resulting matrix incorporates the boundary conditions via coupling matrices $\hat{\boldsymbol{H}}_\mathrm{sa}$ and $\hat{\boldsymbol{H}}_\mathrm{as}$ and that the final matrix of the coupled system becomes

$$\begin{bmatrix} \hat{\boldsymbol{Z}}_\mathrm{s} & \hat{\boldsymbol{H}}_\mathrm{sa} \\ -\omega^2\hat{\boldsymbol{H}}_\mathrm{as} & \hat{\boldsymbol{Y}}_\mathrm{a} \end{bmatrix} \begin{bmatrix} \hat{\boldsymbol{u}}_\mathrm{s} \\ \hat{\boldsymbol{p}}_\mathrm{a} \end{bmatrix} = \begin{bmatrix} \hat{\boldsymbol{f}}_\mathrm{s} \\ \mathrm{i}\omega\hat{\boldsymbol{q}}_\mathrm{a} \end{bmatrix} \quad \text{or} \quad \hat{\boldsymbol{Z}}_\mathrm{c}\hat{\boldsymbol{d}}_\mathrm{c} = \hat{\boldsymbol{f}}_\mathrm{c}\,. \tag{2.56}$$

This formulation was originally presented by Cragg [82] and is used frequently in the literature although mostly by employing explicit mass, damping and stiffness matrices instead of structural dynamic impedance and acoustic admittance (e.g. [21,42,58,83]). The interested reader is encouraged to compare Eq. (2.56) to the wavenumber-frequency formulation in Eq. (2.28). Since the coupling matrices are nonzero only between interface nodes, the system of equations can be reassambled using the variables $\hat{\boldsymbol{u}}_\Gamma$ and $\hat{\boldsymbol{p}}_\Gamma$ at the interface, the dense coupling matrices $\hat{\boldsymbol{H}}_{\mathrm{sa}|\Gamma}$ and $\hat{\boldsymbol{H}}^\mathrm{T}_{\mathrm{sa}|\Gamma}$ and the submatrices $\hat{\boldsymbol{Z}}_{\mathrm{s}|11}$ ($\hat{z}_{\mathrm{s}11|\mathrm{ij}} = \hat{f}_{\Omega|\mathrm{i}}/\hat{u}_{\Omega|\mathrm{j}}$), $\hat{\boldsymbol{Z}}_{\mathrm{s}|12}$ ($\hat{z}_{\mathrm{s}12|\mathrm{ij}} = \hat{f}_{\Omega|\mathrm{i}}/\hat{u}_{\Gamma|\mathrm{j}}$, $\hat{\boldsymbol{Z}}_{\mathrm{s}|21}$ ($\hat{z}_{\mathrm{s}21|\mathrm{ij}} = \hat{f}_{\Gamma|\mathrm{i}}/\hat{u}_{\Omega|\mathrm{j}}$ and $\hat{\boldsymbol{Z}}_{\mathrm{s}|22}$ ($\hat{z}_{\mathrm{s}22|\mathrm{ij}} = \hat{f}_{\Gamma|\mathrm{i}}/\hat{u}_{\Gamma|\mathrm{j}}$). By similarly splitting the acoustical matrix $\hat{\boldsymbol{Z}}_\mathrm{s}$ into its submatrices, the system in Eq. (2.56) can be rewritten as

$$\begin{bmatrix} \hat{\boldsymbol{Z}}_{\mathrm{s}|11} & \hat{\boldsymbol{Z}}_{\mathrm{s}|12} & \boldsymbol{0} & \boldsymbol{0} \\ \hat{\boldsymbol{Z}}_{\mathrm{s}|21} & \hat{\boldsymbol{Z}}_{\mathrm{s}|22} & \boldsymbol{0} & \hat{\boldsymbol{H}}_{\mathrm{sa}|\Gamma} \\ \boldsymbol{0} & \boldsymbol{0} & \hat{\boldsymbol{Y}}_{\mathrm{s}|11} & \hat{\boldsymbol{Y}}_{\mathrm{s}|12} \\ \boldsymbol{0} & -\omega^2\hat{\boldsymbol{H}}_{\mathrm{as}|\Gamma} & \hat{\boldsymbol{Y}}_{\mathrm{s}|21} & \hat{\boldsymbol{Y}}_{\mathrm{s}|22} \end{bmatrix} \begin{bmatrix} \hat{\boldsymbol{u}}_\Omega \\ \hat{\boldsymbol{u}}_\Gamma \\ \hat{\boldsymbol{p}}_\Omega \\ \hat{\boldsymbol{p}}_\Gamma \end{bmatrix} = \begin{bmatrix} \hat{\boldsymbol{f}}_\Omega \\ \boldsymbol{0} \\ \mathrm{i}\omega\hat{\boldsymbol{q}}_\Omega \\ \boldsymbol{0} \end{bmatrix}. \tag{2.57}$$

Recent years have shown increasing interest in the PTF technique in order to directly assemble vibro-acoustic systems from decoupled inverse FRF-matrices $\hat{\boldsymbol{Y}}_\mathrm{s}$ and $\hat{\boldsymbol{Z}}_\mathrm{a}$ (e.g. [77]). To provide a common framework of vibro-acoustic substructuring techniques, an alternative to the original derivation provided by Rejlek in [13] is given below. For this purpose, an inverse formulation is obtained by multiplying the subsystems with the uncoupled inverse matrices. Because $\hat{\boldsymbol{Z}}_\mathrm{s}\hat{\boldsymbol{Y}}_\mathrm{s} = \boldsymbol{I}$ (and similarly $\hat{\boldsymbol{Y}}_\mathrm{a}\hat{\boldsymbol{Z}}_\mathrm{a} = \boldsymbol{I}$) , it is more easily to incorporate the matrices $\hat{\boldsymbol{Z}}_\mathrm{s}$ and $\hat{\boldsymbol{Y}}_\mathrm{a}$ instead of the corresponding upper and lower block

matrices in Eq. (2.57). Premultiplying with the horizontally concatenated inverse matrices can therefore be performed according to

$$\left[\begin{array}{cc|cc} & \hat{\boldsymbol{Z}}_\mathrm{s} & \boldsymbol{0} & \boldsymbol{0} \\ & & \boldsymbol{0} & \hat{\boldsymbol{H}}_{\mathrm{sa}\vert\Gamma} \\ \hline \boldsymbol{0} & \boldsymbol{0} & & \\ \boldsymbol{0} & -\omega^2\hat{\boldsymbol{H}}_{\mathrm{as}\vert\Gamma} & & \hat{\boldsymbol{Y}}_\mathrm{a} \end{array}\right] \left[\begin{array}{c} \hat{\boldsymbol{u}}_\Omega \\ \hat{\boldsymbol{u}}_\Gamma \\ \hat{\boldsymbol{p}}_\Omega \\ \hat{\boldsymbol{p}}_\Gamma \end{array}\right] = \left[\begin{array}{c} \hat{\boldsymbol{f}}_\Omega \\ \boldsymbol{0} \\ \mathrm{i}\omega\hat{\boldsymbol{q}}_\Omega \\ \boldsymbol{0} \end{array}\right] \Bigg| \left[\hat{\boldsymbol{Y}}_\mathrm{s} \quad \hat{\boldsymbol{Z}}_\mathrm{a}\right] . \tag{2.58}$$

By splitting the identity matrices into submatrices and performing the remaining matrix multiplications it follows that

$$\left[\begin{array}{cc|cc} \boldsymbol{I}_{\Omega_\mathrm{s}} & \boldsymbol{0} & \boldsymbol{0} & \hat{\boldsymbol{Y}}_{\mathrm{s}\vert 12}\hat{\boldsymbol{H}}_{\mathrm{sa}\vert\Gamma} \\ \boldsymbol{0} & \boldsymbol{I}_{\Gamma_\mathrm{s}} & \boldsymbol{0} & \hat{\boldsymbol{Y}}_{\mathrm{s}\vert 22}\hat{\boldsymbol{H}}_{\mathrm{sa}\vert\Gamma} \\ \hline \boldsymbol{0} & -\omega^2\hat{\boldsymbol{Z}}_{\mathrm{a}\vert 12}\hat{\boldsymbol{H}}_{\mathrm{as}\vert\Gamma} & \boldsymbol{I}_{\Omega_\mathrm{a}} & \boldsymbol{0} \\ \boldsymbol{0} & -\omega^2\hat{\boldsymbol{Z}}_{\mathrm{s}\vert 22}\hat{\boldsymbol{H}}_{\mathrm{as}\vert\Gamma} & \boldsymbol{0} & \boldsymbol{I}_{\Gamma_\mathrm{a}} \end{array}\right] \left[\begin{array}{c} \hat{\boldsymbol{u}}_\Omega \\ \hat{\boldsymbol{u}}_\Gamma \\ \hat{\boldsymbol{p}}_\Omega \\ \hat{\boldsymbol{p}}_\Gamma \end{array}\right] = \left[\begin{array}{c} \hat{\boldsymbol{Y}}_{\mathrm{s}\vert 11}\hat{\boldsymbol{f}}_\Omega \\ \hat{\boldsymbol{Y}}_{\mathrm{s}\vert 12}\hat{\boldsymbol{f}}_\Omega \\ \hat{\boldsymbol{Z}}_{\mathrm{s}\vert 11}\mathrm{i}\omega\hat{\boldsymbol{q}}_\Omega \\ \hat{\boldsymbol{Z}}_{\mathrm{s}\vert 12}\mathrm{i}\omega\hat{\boldsymbol{q}}_\Omega \end{array}\right] . \tag{2.59}$$

Contrary to the direct formulation in Eq. (2.56), this system can be solved in a two-step procedure by first determining the interface displacement and pressure from

$$\left[\begin{array}{cc} \boldsymbol{I}_{\Gamma_\mathrm{s}} & \hat{\boldsymbol{Y}}_{\mathrm{s}\vert 12}\hat{\boldsymbol{H}}_{\mathrm{sa}\vert\Gamma} \\ -\omega^2\hat{\boldsymbol{Z}}_{\mathrm{a}\vert 12} & -\omega^2\hat{\boldsymbol{Z}}_{\mathrm{s}\vert 22}\hat{\boldsymbol{H}}_{\mathrm{as}\vert\Gamma} \end{array}\right] \left[\begin{array}{c} \hat{\boldsymbol{u}}_\Gamma \\ \hat{\boldsymbol{p}}_\Gamma \end{array}\right] = \left[\begin{array}{c} \hat{\boldsymbol{Y}}_{\mathrm{s}\vert 12}\hat{\boldsymbol{f}}_\Omega \\ \hat{\boldsymbol{Z}}_{\mathrm{s}\vert 12}\mathrm{i}\omega\hat{\boldsymbol{q}}_\Omega \end{array}\right] . \tag{2.60}$$

and then determine the displacement and pressure in the respective fields according to

$$\left[\begin{array}{cc|cc} \boldsymbol{I}_{\Omega_\mathrm{s}} & \boldsymbol{0} & \boldsymbol{0} & \hat{\boldsymbol{Y}}_{\mathrm{s}\vert 12}\hat{\boldsymbol{H}}_{\mathrm{sa}\vert\Gamma} \\ \hline \boldsymbol{0} & -\omega^2\hat{\boldsymbol{Z}}_{\mathrm{a}\vert 12}\hat{\boldsymbol{H}}_{\mathrm{as}\vert\Gamma} & \boldsymbol{I}_{\Omega_\mathrm{a}} & \boldsymbol{0} \end{array}\right] \left[\begin{array}{c} \hat{\boldsymbol{u}}_\Omega \\ \hat{\boldsymbol{u}}_\Gamma \\ \hat{\boldsymbol{p}}_\Omega \\ \hat{\boldsymbol{p}}_\Gamma \end{array}\right] = \left[\begin{array}{c} \hat{\boldsymbol{Y}}_{\mathrm{s}\vert 11}\hat{\boldsymbol{f}}_\Omega \\ \hat{\boldsymbol{Z}}_{\mathrm{s}\vert 11}\mathrm{i}\omega\hat{\boldsymbol{q}}_\Omega \end{array}\right] . \tag{2.61}$$

Considering that the displacements of the uncoupled mechanical system due to the external loads $\hat{\boldsymbol{f}}_\Omega$ can be calculated according to $\hat{\boldsymbol{u}}_{\mathrm{suc}\vert\Omega} = \hat{\boldsymbol{Y}}_{\mathrm{s}\vert 11}\hat{\boldsymbol{f}}_\Omega$ (and analogously for the acoustic system $\hat{\boldsymbol{p}}_{\mathrm{auc}\vert\Omega} = \hat{\boldsymbol{Z}}_{\mathrm{s}\vert 11}\hat{\boldsymbol{q}}_\Omega$), then it is possible to additionally define the relative displacement $\hat{\boldsymbol{\delta}}_\mathrm{u}$ and pressure $\hat{\boldsymbol{\delta}}_\mathrm{p}$ at the interface induced solely by the respective coupling forces or the volume flux as

$$\hat{\boldsymbol{\delta}}_\mathrm{u} = \hat{\boldsymbol{Y}}_{\mathrm{s}\vert 12}\boldsymbol{H}_{\mathrm{sa}\vert\Gamma}\hat{\boldsymbol{p}}_\Gamma \quad \text{and} \quad \hat{\boldsymbol{\delta}}_\mathrm{p} = -\omega^2\hat{\boldsymbol{Z}}_{\mathrm{a}\vert 12}\boldsymbol{H}_{\mathrm{as}\vert\Gamma}\hat{\boldsymbol{u}}_{\mathrm{s}\vert\Gamma} . \tag{2.62}$$

Equivalently to solving Eq. (2.61), it is therefore also possible to obtain the total displacement and pressure at the nodes in the whole domain by recognizing that the total displacement or pressure fields $\hat{\boldsymbol{u}}_\Omega$ and $\hat{\boldsymbol{p}}_\Omega$ are a superposition of the uncoupled primal variables $\hat{\boldsymbol{u}}_{\mathrm{suc}\vert\Omega}$ and $\hat{\boldsymbol{p}}_{\mathrm{auc}\vert\Omega}$ and the relative displacement and pressure induced by the coupling procedure as

$$\hat{\boldsymbol{u}}_\Omega = \hat{\boldsymbol{u}}_{\mathrm{suc}\vert\Omega} - \hat{\boldsymbol{\delta}}_\mathrm{u} \quad \text{and} \quad \hat{\boldsymbol{p}}_\Omega = \hat{\boldsymbol{p}}_{\mathrm{auc}\vert\Omega} - \hat{\boldsymbol{\delta}}_\mathrm{p} . \tag{2.63}$$

This form of coupling is very similar to the patch transfer method (PTF) originally presented by Rejlek [13]. The differences are solely limited to the definition of the mechanical (there: velocity/pressure, here: displacement/force) and acoustical (there: pressure/velocity, here: pressure/volume acceleration) system matrices. Accordingly, arithmetic averaging is performed instead of integration. Theoretically, this variant can also be employed to estimate uncoupled systems from a coupled system, although the ill-posedness of the inversion problem is a major complication [14]. Similar to the methods employed in CMS, it is also possible to describe the respective subsystems via modes obtained by applying homogenous

Neumann boundary conditions (free-displacement, sound hard cavity). Under the assumption of weak coupling, the additional static interface modes can be neglected to arrive at the modal coupling technique given in Eq. (2.28). As with the free-displacement CMS mentioned earlier, pseudostatic corrections can also be employed, especially if strong coupling occurs [83]. Finally three main possibilities are available for coupling vibro-acoustic systems, being either direct via $\hat{\boldsymbol{Z}}_\mathrm{s} \Leftrightarrow \hat{\boldsymbol{Y}}_\mathrm{a}$ as in Eq. (2.55) or inverse via $\hat{\boldsymbol{Y}}_\mathrm{s} \Leftrightarrow \hat{\boldsymbol{Z}}_\mathrm{a}$ as in Eq. (2.60) or, if the vibro-acoustic coupling mechanisms are sufficiently weak by coupling solely the normal modes of the uncoupled system via $\boldsymbol{\Psi}_\mathrm{s} \Leftrightarrow \boldsymbol{\Psi}_\mathrm{a}$ as in Eq. (2.47). In addition, the various system descriptions can be converted into one another through the use of appropriate procedures. However, the determination of a direct description from an inverse description (by measurements) is only feasible in a least-squares sense due to the ill-posedness of the identification problem. The potential relations between direct and inverse descriptions, as well as the corresponding substructuring techniques are depicted in Fig. 2.2. System matrices $\hat{\boldsymbol{Z}}_\mathrm{s}$ and $\hat{\boldsymbol{Y}}_\mathrm{a}$ obtained by discretizing the respective differential equations via, for example, the FE method can be coupled via the direct formulation given in Eq. (2.56) ($\hat{\boldsymbol{Z}}_\mathrm{s} \Leftrightarrow \hat{\boldsymbol{Y}}_\mathrm{a}$). The inverse matrices $\hat{\boldsymbol{Y}}_\mathrm{s}$ and $\hat{\boldsymbol{Z}}_\mathrm{a}$ obtained from measurements can be coupled via the inverse method given in Eq. (2.60) (or the very similar PTF method). The coupled system can also be discretized directly ($\hat{\boldsymbol{Z}}_\mathrm{c}$) or analyzed via measured vibro-acoustic admittances $\hat{\boldsymbol{Y}}_\mathrm{c}$ to obtain the generalized displacements $\hat{\boldsymbol{d}}_\mathrm{c}$ due to impressed forces [80]. If only a limited frequency range is of interest and, in particular, only weak coupling is expected, coupling via normal modes is advantageous. The required mechanical and acoustic modes $\boldsymbol{\Psi}_\mathrm{s}$ and $\boldsymbol{\Psi}_\mathrm{a}$ can be obtained either by solving an eigenvalue problem using the discrete mass, damping and stiffness matrices in $\hat{\boldsymbol{Z}}_\mathrm{s}$ and $\hat{\boldsymbol{Y}}_\mathrm{a}$ or by applying EMA to the measured matrices of the form $\hat{\boldsymbol{Y}}_\mathrm{s}$ and $\hat{\boldsymbol{Z}}_\mathrm{a}$ [78]. In the same way, coupled vibro-acoustic modes $\boldsymbol{\Psi}_\mathrm{c}$ can be obtained from the matrices of the discretized coupled system $\hat{\boldsymbol{Z}}_\mathrm{c}$ by solving the non-symmetric eigenvalue problem or by experimental vibro-acoustic modal analysis using the vibro-acoustic transfer functions $\hat{\boldsymbol{Y}}_\mathrm{c}$. Alternatively, by (partial) inversion according to $\hat{\boldsymbol{Y}}_\mathrm{s} = \hat{\boldsymbol{Z}}_\mathrm{s}^{-1}$, $\hat{\boldsymbol{Z}}_\mathrm{a} = \hat{\boldsymbol{Y}}_\mathrm{a}^{-1}$ or $\hat{\boldsymbol{Y}}_\mathrm{c} = \hat{\boldsymbol{Z}}_\mathrm{c}^{-1}$ the inverse matrices are obtained from the discretized system (eg. to use the PTF or the TPA based on simulation data). Techniques for obtaining the system matrices from the inverse matrices according to $\hat{\boldsymbol{Z}}_\mathrm{c} \approx \hat{\boldsymbol{Y}}_\mathrm{c}^{-1}$, $\hat{\boldsymbol{Z}}_\mathrm{s} \approx \hat{\boldsymbol{Y}}_\mathrm{s}^{-1}$ or $\hat{\boldsymbol{Y}}_\mathrm{a} \approx \hat{\boldsymbol{Z}}_\mathrm{a}^{-1}$ are always ill-conditioned and subject to measurement errors. Such methods (and EMA techniques) belong to the realm of system identification methods. Both the direct and inverse matrices can be synthesized from experimentally or numerically deduced modes. Another possibility is to apply model-updating techniques, by obtaining objective functions $\hat{\boldsymbol{Y}}_\mathrm{c} = \hat{\boldsymbol{Z}}_\mathrm{c}^{-1}$ from the simulation and subsequently minimizing the error between objective and measurements by updating the system matrix [84]. In principle, hybrid formulations are also conceivable, in which measured FRF matrices are coupled with numerical systems. It follows that three groups of approaches are possible for the description of vibro-acoustic mechanisms. To tackle complex problems, *computational* approaches such as the FE or BE method are most frequently employed. However, creating a realistic computational model is a tedious and time-consuming task which is why experimental techniques are also frequently used to asses already existing structures. *Experimental* approaches either make use of experimentally determined transfer functions or deduce the system description from the measured data by solving an ill-conditioned inverse problem. The last category are *hybrid* approaches consisting of a combination of numerical, experimental and even analytical techniques.

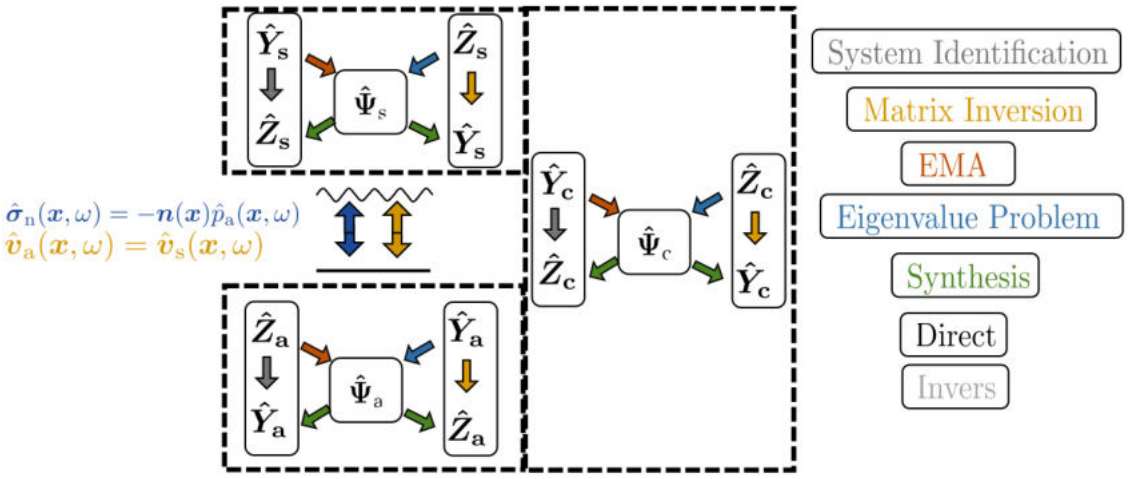

Figure 2.2: Possibilities for vibro-acoustic substructuring.

2.5.2 Numerical methods

We begin with techniques that can be applied to asses vibro-acoustic issues by discretizing the respective mechanical or acoustical differential equations. The name of each technique, at least a single associated paper and the employed incorporation of the coupling effects are listed in Table 2.2. For the simplified treatment of vibro-acoustic systems, lumped parameter modeling can be used [85]. The most commonly used methods in the industrial context are, however, based on direct discretization of the mechanical system using the FE method and of the acoustic system using the FE or BE method ($\hat{\boldsymbol{Z}}_{\mathrm{s}} \Leftrightarrow \hat{\boldsymbol{Y}}_{\mathrm{a}}$). The strongly coupled FE- method presented in Eq. (2.56) ($\hat{\boldsymbol{Z}}_{\mathrm{s}} \Leftrightarrow \hat{\boldsymbol{Y}}_{\mathrm{a}}$) has been used, for example, by Wang [38] to calculate the sound pressure induced by underbody vibrations of a real vehicle, or by Cameron [86] to evaluate the vibro-acoustic properties associated with the roof-cavity system. Ying-jie [87] also employed this method to calculate aero-vibro-acoustic noise in vehicles. The Boundary Element Method (BEM) can also be employed to describe the interior cavity as perceived by Wang [35] or Citarella [88]. Note that the vibro-acoustic formulation in Eq. (2.56) is not symmetric causing significant drawbacks in computational efficiency (Choi [89]) although a symmetric formulation can be derived by employing the velocity potential instead of the pressure (e.g. Olson [90]). Computational efficiency and numerical methods are not a focus of this thesis, the interest reader will find relevant information in the extensive review by Marburg [42]. A logical choice to speed up the solution of the strongly coupled procedure would be to use coupled modes to solve the coupled problem at the modal level ($\hat{\boldsymbol{Z}}_{\mathrm{c}} \Rightarrow \hat{\boldsymbol{\Psi}}_{\mathrm{c}}$), but no application to automotive problems could be found. First work on modal analysis of vibro-acoustic systems goes back to Bokil et al. (1992) [91]. The reader is reminded that for the case of numerically discretized system matrices, the mechanical, acoustic and vibro-acoustic structural modes are obtained by solving the corresponding

$$\text{Eigenvalue Problems} \begin{cases} \hat{\boldsymbol{Z}}_{\mathrm{s|n}} \boldsymbol{\Psi}_{\mathrm{s|n}} = \boldsymbol{0} \\ \hat{\boldsymbol{Y}}_{\mathrm{a|m}} \boldsymbol{\Psi}_{\mathrm{a|m}} = \boldsymbol{0} \\ \hat{\boldsymbol{Z}}_{\mathrm{c|r}} \boldsymbol{\Psi}_{\mathrm{c|r}} = \boldsymbol{0}\,. \end{cases} \tag{2.64}$$

Regarding the practical calculation of vibro-acoustic modes, the interested reader is referred to Arjmandi [92]. Coupled modes also allow to directly obtain coupled vibro-acoustic sensitivities (Ma [93]). If the feedback effect of the acoustic fluid on the mechanical structure is entirely neglected as proposed by Marburg [94], the mechanical displacement can be set as a boundary condition for the acoustic system

(i.e. by setting the upper right coupling matrix to zero in the direct formulation given in Eq. (2.47)). Under the presumption of weak coupling, coupling via normal modes ($\mathbf{\Psi}_s \Leftrightarrow \mathbf{\Psi}_a$) can be employed. The use of normal-mode coupling has the additional advantage that both structural and acoustic damping can be considered at the modal level. This strategy was perceived by e.g. Nefske [3], Xu [95] but also in [96] or [58]. It must be noted in general that the correct consideration of damping mechanisms in numerical descriptions is extremely challenging. In the general case, complex damping modes will occur but frequently, modal damping may already yield reasonable results [50]. The existence of normal modes in damped systems has been investigated by Phani (2002) [97]. While complex modes are in principle not a problem regarding numerical treatment, the method of Fullekrug [98], by which complex modes can be reduced to real modes appears interesting. An interesting review has also been given by Srikantha [99]. The treatment of uncertainties is beyond the scope of this paper. Note however that the stochastic models used for the treatment either resort to normal mode substructuring of the vibro-acoustic system [7, 72], or solve the full, non-symmetric FE model [9].

Description	Papers	BC treatment
Lumped parameter modelling $\hat{p}_a$-$\hat{u}_s$	[85]	Coupling Conditions
Strong FE coupling $\hat{p}_a$-$\hat{u}_s$	[38, 86, 87]	Strong constraints
Strong FE-BE coupling $\hat{p}_a$-$\hat{u}_s$	[35, 88]	Strong constraints
Structural BC from FE (uncoupled) on FE acoustic (uncoupled)	[94]	Fluid loading from cavity neglected for mechanical structure
Structural modes (FE, uncoupled) and acoustic modes (FE, uncoupled)	[3, 58, 95, 96]	Relaxed Interface constraints

Table 2.2: Computational Approaches in Vehicle NVH

2.5.3 Experimental methods

Since the creation of an acceptable simulation model of a complex real structure frequently requires tremendous effort as well as intensive knowledge of the mechanisms at play, it is often more appropriate to investigate the dynamics of an existing model on behalf of measured FRF's. The corresponding FRF data ($\hat{y}_{s|ij} = \hat{u}_{s|i}/\hat{f}_{s|j}$, $\hat{z}_{a|ij} = \hat{p}_{a|i}/\hat{q}_{a|j}$, $\hat{y}_{c|ij} = \hat{p}_{c|i}/\hat{f}_{c|j}$) based on mechanical-, acoustical- or vibro-acoustical measurements are recorded by applying suitable excitation and can then be assembled into a discrete matrix for each frequency. For details regarding the required signal processing procedures, the reader is referred to [50] and for practical considerations to the book of Avitabile [100]. Due to the fact that only a limited number of FRF's can be determined, great care must be taken when selecting (one or more) excitation points; otherwise, mechanisms essential to the specific problem may be hidden in the FRF data set. Note that, following the ubiquitous presence of noise in measurements, the FRF's are obtained by ensemble averaging of the normalized CPSD. Using the example of mechanical admittance, the averaging process can be formulated according to

$$\hat{Y}_{s|ij}(\omega) = \left\{ \frac{\hat{u}_{s_{(i)}}}{\hat{f}_{s_{(i)}}} \right\} = \left\{ \frac{\hat{u}_{s_{(i)}} \hat{f}^*_{s_{(i)}}}{\hat{f}_{s_{(i)}} \hat{f}^*_{s_{(i)}}} \right\} . \tag{2.65}$$

Thus, the admittances converge to the ensemble averaged admittance when an increasing number of measurements are made. Here, it is referred to the already mentioned review by Sejs [101] for details on TPA. Applications of vibro-acoustic TPA on vehicles can be found in Lee [102], Plunt [75] but also in [80, 103–105]. In the case of spatially distributed excitation (such as wind loads), the vibro-acoustic FRF must be determined for a vast number of excitation points, which is why the application of reciprocal techniques is beneficial. Via vibro-acoustic reciprocity, coupled FRF's can be obtained by exciting the

interior cavity with a single (or few) volume sources and measuring the induced acoustical pressure in the cavity and the mechanical displacements (Wyckaert [21]). The approach employed by Glandier [32] to calculate the internal sound pressure using observed surface pressures and reciprocally computed FRF's is an example of an intriguing contribution to this field. Owing to the otherwise large number of excitation points required to obtain coupled FRF's, this seems to be the most interesting procedure to investigate wind-induced interior noise based on coupled FRF's. The extraction of experimental mode shapes and eigenfrequencies from experimental FRF's is a sophisticated, but well established method to investigate the dynamics of mechanical and acoustic systems for which appropriate FE models do not exist. A detailed description of the technique may be found in [100]. In EMA, it is presumed that the FRF's in the inverse formulations in Eq. (2.55) can be expressed as a superposition of N_m partial fractions composed of residue vectors $\hat{\boldsymbol{a}}_\mathrm{r}$ related to the mass-normalized mode shapes $\boldsymbol{\psi}_\mathrm{r}$ according to $\hat{\boldsymbol{a}}_\mathrm{r} = \boldsymbol{\psi}_\mathrm{r}\boldsymbol{\psi}_\mathrm{r}^\mathrm{T}$, upper and lower residuals ($\hat{\boldsymbol{a}}_\mathrm{u}$, $\hat{\boldsymbol{a}}_\mathrm{l}$) and poles $s_{\mathrm{s|r}}$ related to undamped eigenfrequency $\omega_{\mathrm{s|r}}$ and modal damping $\zeta_{\mathrm{s|r}}$ as

$$s_{\mathrm{s|r}} = -\zeta_{\mathrm{s|r}}\omega_{\mathrm{s|r}} \pm j\omega_{\mathrm{s|r}}\sqrt{1-\zeta_{\mathrm{s|r}}^2}\,. \tag{2.66}$$

and that a single column of these FRF's obtained by measurements and stored in vectors $\hat{\boldsymbol{y}}_\mathrm{s}$ or $\hat{\boldsymbol{z}}_\mathrm{a}$ allows to obtain the modal description by iteratively solving (e.g. mechanical system)

$$\hat{\boldsymbol{y}}_\mathrm{s}(\omega) = \sum_{\mathrm{r}=1}^{N_\mathrm{m}} \frac{\hat{\boldsymbol{a}}_{\mathrm{s|r}}}{\mathrm{i}\omega - \mathrm{s}_{\mathrm{s|r}}} + \frac{\hat{\boldsymbol{a}}^*_{\mathrm{s|r}}}{\mathrm{i}\omega - \mathrm{s}^*_{\mathrm{s|r}}} + \frac{\hat{\boldsymbol{a}}_\mathrm{u}}{\omega^2} + \hat{\boldsymbol{a}}_\mathrm{l}\,. \tag{2.67}$$

For more details, the reader is referred to the book of Avitabile [100]. For the experimental determination of coupled vibro-acoustic modes, it must (as mentioned in Sec. 2.2.6) be taken into account that left and right eigenvectors have to be determined (for details, see Wyckaert [21]). While mechanical modal analysis is frequently employed, experimental acoustic modal analysis is a time-consuming and challenging task due to the large number of microphones required in 3D. Several articles on the use of acoustic modal analysis to automotive issues have been published in recent years. Accardo et al. [15, 15], recovered the acoustic modes of a vehicle using an acoustic shaker (LMS QSource) and the Polymax method [100]. Owing to the flexibility of the mechanic structure (see Sec. 2.4), the experimentally obtained natural frequencies cannot be directly compared to acoustic FE models with sound hard boundaries. Tsuji also wrote a relevant article in 2013 [106]. Vibro-acoustic modal analysis has been employed by Hermann [16] to investigate booming noise in a vehicle and by Wyckaert [21] in her remarkable investigation on low-frequency vibroacoustics on a simplied vehicle. Techniques for OMA have also received increasing interest [12,18,107]. Xu [107] employed acoustic excitation and laser vibrometry (LV) measurements to establish the operating modes of a rectangular plate. Vibro-acoustic OMA was also successfully implemented to investigate an acoustically excited wind turbine [17]. Pierro [18] employed both OMA and EMA in his study on the vibro-acoustic behavior of a helicopter. Note that, regarding the transmission of wind noise through automotive structures, performing OMA directly in a wind tunnel and scaling the results with a reduced set of FRF's (similar to Brandt [108]) appears a promising idea. The findings are summarized in Tab. 2.3.

Description	Papers
Vibro-acoustic TPA	[32, 75, 80, 102–105]
Acoustic modal analysis	[15, 15, 106]
Coupled modes from in situ Meas, volume source excitation	[16, 21]
Coupled modes from OMA	[12, 18, 107, 108]

Table 2.3: Experimental approaches in automotive NVH

2.5.4 Hybrid methods

Description	Papers	BC treatment
Vibro-acoustic PTF with structural FRF from measurement and acoustic FRF from simulation	[13]	Interface constraints enforced patch-wise, fluid excitation overestimated
Structural BC from Measurement (coupled) on FE acoustic (uncoupled)	[12]	Interface constraints enforced
Volume acceleration from Measurement (coupled) on FE acoustic (uncoupled)	[19]	Structural flexibility neglected for acoustic fluid
Structural modes (in situe Meas, coupled) and acoustic modes (FE,uncoupled)	[3]	Modal relaxed Interface constraints
Semi-Analytical Method of Herpe	[41]	Modal relaxed Interface constraints
Structural modal updating	[110]	Acoustic excitation neglected for mechanical structure
Vibro-acoustic modal updating	[84]	Interface constraints enforced

Table 2.4: Hybrid approaches in automotive NVH

Due to the comparatively reliable simulative description of the acoustic cavity (see the comparison between experimental and numerical modes in Accardo [15]) combined with the tremendous effort to generate a valid structural model (see Sec. 2.4), hybrid methods in which a combination of experimental and simulative data is used to assemble and investigate the dynamics of the coupled model are of special interest. Essentially, the complete set of methods depicted in Fig. 2.2 is now available, whereas in the important case of a simulatively (i.e. via $\hat{\boldsymbol{Y}}_\mathrm{a}$) described acoustic cavity combined with an experimentally (i.e. via $\hat{\boldsymbol{Y}}_\mathrm{s}$) described structure one of the two systems has to be inverted (partly or in a least-squares sense). Thus, for the direct coupling ($\hat{\boldsymbol{Y}}_\mathrm{a} \Leftrightarrow \hat{\boldsymbol{Z}}_\mathrm{S}$) according to Eq. (2.56) the dynamic stiffness matrix must be obtained from $\hat{\boldsymbol{Y}}_\mathrm{s}$ via a system identification algorithm while, if the inverse (or similar, the PTF) method is employed according to Eq. (2.60), the (partial) inversion of the acoustic system matrix $\hat{\boldsymbol{Y}}_\mathrm{a}$ is required. Given that weak coupling is usually valid for automotive problems, the coupling of mechanical modes determined via EMA from experimental data and acoustic modes via a numerical eigenvalue decomposition appears especially promising ($\boldsymbol{\Psi}_\mathrm{s} \Leftrightarrow \boldsymbol{\Psi}_\mathrm{a}$). This was first recognized by Kim in his seminal work on a generic testbody [44]. Here, the nodes of an acoustic FE model were localized directly at the measurement nodes of the experimental structure. The feedback effect of the acoustic cavity on the structural model was neglected during experimental acquisition. Herpe [41] proposed a similar idea, in which the acoustic fluid is simplified as a rectangular box and the coupling properties are then considered at a modal level (also in [26]). This method is rather not suitable for the low-frequency range due to the strong spatial variability of the acoustic field. Furthermore, the influence of seats or the influence of the package tray, which is important for the low-frequency range, cannot be considered [74]. Another possibility is to directly apply measured displacement spectra as a boundary condition for an acoustic simulation (Lee [12]). Brandstätter [19] used a method in which the acoustic model was idealized as

sound-hard and the mechanical displacement field (and accordingly, the associated volume acceleration) was used as an acoustic source . Strong deviations from the experimental measurements were found, further supporting the conclusion that the acoustic boundary flexibility associated with the mechanical structure must be taken into account during the coupling process. Furthermore, Rejlek [13] used the PTF method in an academic example to couple experimental mechanical with computational acoustical FRF's. Here, all boundary conditions are strongly satisfied in a patch-wise manner, overestimating the acoustic feedback due to the in-situ measurements of the mechanical FRF's. Finally, modal-updating methods should be mentioned, in which the properties of a numerical model are modified using measured data. Here, assuming negligible acoustic feedback, the mechanical model can be updated by in-situ measurements to be then coupled with a numerical model for the cavity (Meggit [111]), or the coupled FE model can be modified by measurements on a coupled cavity as (Nehete [84]). Publications on the subject can also be found from Xu [95] or Plunt [80, 112].

3 Aero-vibro-acoustic mechanisms in vehicles

In addition to a physical description of the vibro-acoustic behavior of the vehicle, a description of the acting external loads is required to predict the flow-induced interior noise in a vehicle. These loads are composed of the WPF acting on on the body (referred to as indirect excitation) or via air leakages and openings between the acoustic cavity and the flow around it (referred to as direct excitation), The fundamental theoretical concepts that govern aerodynamic (and aeroacoustic) WPF are introduced at the beginning of this chapter. After describing the statistical methods necessary for characterizing the WPF, the previous example of a vibro-acoustic box subject to wind-induced excitation is expanded to include a model for the convective component of the wall pressure CPSD. The transmission into the cavity is then analyzed, along with the more general case of an arbitrary vibro-acoustic system described by its eigenmodes. The topological characteristics of flow around vehicles and the associated noise-generating mechanisms are described, and relevant literature is collected. The noise-generating mechanisms are then classified into four groups and discussed along with recent research: excitation by convected turbulence, excitation from leeward components, excitation from the underbody and direct acoustic excitation via openings.

3.1 Aerodynamics and the generation of sound by flow

The considerations presented in the following are a short summary of the relevant topics treated in the book of Kaltenbacher [55] or the two comprehensive textbooks by Blake [43, 56]. Note that, if not stated otherwise, all variables in this section are in the space-time domain. The additional label $*_\mathrm{f}$ to distinguish flow variables from structural or acoustical variables is omitted in the following. In an Eulerian approach (i.e. in a space-fixed coordinate system), the continuum equation of a fluid element with location- and time-dependent density ρ and velocity $\boldsymbol{v}$ can be written with or without consideration of compressibility according to

$$\frac{\partial \rho}{\partial t} + \nabla \cdot (\rho \boldsymbol{v}) = 0 \quad \text{(compressible fluid) or } \nabla \cdot \boldsymbol{v} = \nabla \cdot \boldsymbol{v}_\mathrm{ic} \quad = 0 \quad \text{(incompressible fluid)}\,. \tag{3.1}$$

Furthermore, using the static pressure p, the viscous stress tensor $\boldsymbol{\tau}$ and the identity tensor $\boldsymbol{I}$ and neglecting any additional external forces, the momentum equation is given by

$$\frac{\partial \rho \boldsymbol{v}}{\partial t} + \nabla \cdot (\rho \boldsymbol{v} \otimes \boldsymbol{v}) = -\nabla p + \nabla \cdot \boldsymbol{\tau}\,, \tag{3.2}$$

or

$$\frac{\partial \rho \boldsymbol{v}}{\partial t} + \nabla \cdot (\rho \boldsymbol{v} \otimes \boldsymbol{v} + p\boldsymbol{I} - \boldsymbol{\tau}) = \boldsymbol{0} \tag{3.3}$$

or, using index notation, by

$$\frac{\partial \rho v_\mathrm{i}}{\partial t} + \frac{\partial}{\partial x_\mathrm{j}} \left(\rho v_\mathrm{j} v_\mathrm{i} + p\delta_\mathrm{ij} - \tau_\mathrm{ij}\right) = 0\,. \tag{3.4}$$

The momentum flux contributions can be collected in a momentum flux tensor $\boldsymbol{\pi}$ as

$$\pi_\mathrm{ij} = \rho v_\mathrm{i} v_\mathrm{j} + p\delta_\mathrm{ij} - \tau_\mathrm{ij}, \tag{3.5}$$

which simplifies the momentum equation to

$$\frac{\partial \rho \boldsymbol{v}}{\partial t} + \nabla \cdot \boldsymbol{\pi} = 0\,. \tag{3.6}$$

By employing a suitable model for the viscous stresses, such as a linear relationship via the dynamic viscosity μ and the distortion rate tensor according to $\tau_{\mathrm{ij}} = \mu \partial v_{\mathrm{i}} / \partial x_{\mathrm{j}}$, the coupled compressible system of equations in Eq. (3.1) and (3.3) can in principle be solved subject to suitable boundary and initial conditions within the framework of a compressible direct numerical simulation (DNS) to obtain the fluctuating wind loads on the vehicle [113]. At low Mach numbers $M_\infty = v_\infty / c_0 \ll 1$ the fluid can be assumed incompressible ($\rho = \rho_0$). The pressure $p(t)$ determined on a virtual microphone on a non-slip wall in an incompressible turbulent simulation then corresponds to a superposition of a location-dependent static pressure p and flow-induced (but nevertheless static, not to be confused with dynamic pressure) pressure fluctuation p_{f} according to $p = p_0(\boldsymbol{x}) + p'(\boldsymbol{x}, t)$, with the induced pressure fluctuations being a result of the turbulent structures in the flow. Since a real medium is always compressible, real flows will always contain density fluctuations $\rho_{\mathrm{a}}(\boldsymbol{x}, t)$ with associated acoustic pressure fluctuations $p_{\mathrm{a}}(\boldsymbol{x}, t) = \rho_{\mathrm{a}}(\boldsymbol{x}, t) c_0^2$ which propagate as acoustic waves in the medium. Thus, the pressure (at a no-slip wall) in a real fluid is actually a superposition of a location-dependent static pressure p_0, aerodynamic pressure fluctuations p'_{f} propagating with subsonic phase speed v_{conv} owing to the convective nature of the flow and acoustic pressure fluctuations p_{a} propagating with the speed of sound c_0 as

$$p(\boldsymbol{x}, t) = p_0(\boldsymbol{x}) + \underbrace{p'_{\mathrm{f}}(\boldsymbol{x}, t) + p_{\mathrm{a}}(\boldsymbol{x}, t)}_{p'(\boldsymbol{x}, t)}\,. \tag{3.7}$$

Only acoustic waves propagate in the far-field while aerodynamic waves with subsonic phase speed decay rapidly with increasing distance from the source. It is within the scope of the discipline of aeroacoustics to investigate the propagation of acoustic (sound) and aerodynamic (pseudo-sound) waves in flows. The foundations of aeroacoustics were laid by Lighthill in 1951 when, by a clever manipulation, he represented the compressible flow equations as a conventional wave equation in an ambient fluid with additional external source terms [114]. For the derivation, we follow the discussion given in [55]. Start by noting that the momentum flux tensor π^0_{ij} in an ideal, linear acoustic medium without flow becomes

$$\pi_{\mathrm{ij}} \to \pi^0_{\mathrm{ij}} = \underbrace{(p - p_0)}_{p'(\boldsymbol{x}, t)} \delta_{\mathrm{ij}} = c_0^2 \underbrace{(\rho - \rho_0)}_{\rho'(\boldsymbol{x}, t)} \delta_{\mathrm{ij}}\,, \tag{3.8}$$

where the ambient pressure p_0 was subtracted (this is possible because of the divergence operator in Eq. (3.6)) to be able to exploit the isentropic equation of state given by $p' = c_0^2 \rho'$. Lighthill's idea was esentially, that adding $\nabla \cdot \boldsymbol{\pi}^0$ to (3.6), rewriting the result and introducing the tensor $\boldsymbol{L}$ yields

$$\frac{\partial \rho \boldsymbol{v}}{\partial t} + \nabla \cdot \boldsymbol{\pi}^0 = -(\nabla \cdot \boldsymbol{\pi} - \nabla \cdot \boldsymbol{\pi}^0) = -\nabla \cdot \boldsymbol{L}\,. \tag{3.9}$$

The left-hand side of Eq. (3.9) now corresponds to the momentum equation in a medium at rest while the right-hand side contains a modified forcing tensor $\boldsymbol{L}$. It is now possible to derive an inhomogenous wave equation of a medium *at rest* that nevertheless reflects the pressure or density perturbations *within the flow*. For this purpose, the ambient density is first subtracted from the temporal derivative of the conservation of mass given in Eq. (3.1) to arrive at

$$\frac{\partial}{\partial t} \underbrace{(\rho - \rho_0)}_{\rho'} + \frac{\partial \rho v_{\mathrm{i}}}{\partial x_i} = 0\,. \tag{3.10}$$

Substituting $\boldsymbol{\pi}^0$ in Eq. (3.9) yields

$$\frac{\partial \rho v_\mathrm{i}}{\partial t} + \frac{\partial}{\partial x_i}(c_0^2 \underbrace{(\rho - \rho_0)}_{\rho'}) = -\frac{\partial L_\mathrm{ij}}{\partial x_i} \,. \tag{3.11}$$

The wave equation can now derived by performing a temporal derivative on Eq. (3.10), a spatial derivative on Eq. (3.11) and then eliminating the momentum density ρv_i. The resulting wave equation becomes

$$\left(\frac{1}{c_0^2}\frac{\partial^2}{\partial t^2} - \nabla \cdot \nabla\right)\left(c_0^2 \rho'\right) = \frac{\partial^2 L_\mathrm{ij}}{\partial x_i \partial x_j} \,, \tag{3.12}$$

and is nowadays referred to as Lighthill's equation. It can thus be concluded that the waves propagating in the flow correspond to those caused in an undisturbed fluid when excited by a stress distribution equal to the difference between the true momentum flux tensor and the momentum flux tensor in an ambient medium. This stress distribution is the famous Lighthill stress tensor, which, as can be seen from the previous analysis, is given by

$$L_\mathrm{ij} = \pi_\mathrm{ij} - \pi_\mathrm{ij}^0 = \rho v_\mathrm{i} v_\mathrm{j} + \Big(\underbrace{(p - p_0)}_{p'_\mathrm{f}} - c_0^2 \underbrace{(\rho - \rho_0)}_{\rho'}\Big)\delta_\mathrm{ij} - \tau_\mathrm{ij} \,. \tag{3.13}$$

Here, it should be noted that the density perturbation ρ' no longer corresponds to a physical density but to a virtual density related to the flow-induced pressure fluctuations in the flow according to $p_\mathrm{f} = c_0^2 \rho'$. The first term in Lighthill's stress tensor describes the well-known Reynolds stress tensor $\rho v_\mathrm{i} v_\mathrm{j}$, the second term represents the excess terms and the third term represents the viscous stress tensor. The unique feature of Lighthill's equation is that the nonlinear compressible flow equations can be represented as an inhomogeneous wave equation. This equation is the foundation of the heavily studied field of aeroacoustic analogies, in which wave propagation in compressible flows can be described by combining a linear acoustic wave equation with sources from an (often incompressible) aerodynamic simulation. The reason why wave propagation phenomena can be described on the basis of an incompressible flow simulation is that $\boldsymbol{L}$ can be described to first order on the basis of the incompressible velocity fluctuations $L_\mathrm{ij} = \rho v_{\mathrm{ic|i}} v_{\mathrm{ic|j}}$ [55]. Since it was not possible to discretize Lighthill's equation at that time, and the solution to the above differential equation by using Green's free space function is only valid for open regions free of diffraction and refraction, a further refinement was presented by Curle which takes into account the effects induced by an additional (virtual or rigid) surface Γ_s [115]. The integral representation proposed by Curle employs Green's free space function and thus only accounts for waves propagating at the speed of sound. This however excludes aerodynamic waves, such as those encountered in wall pressure measurements underneath a TBL. The investigations presented below are therefore (for now) concerned only with acoustic radiation from a compact turbulent source region without additional motion between the source and the observer, as it occurs in the convection of turbulent patterns in the context of turbulent WPF theory. As will be discussed in more detail in Sec. 3.5 the effects occurring in vehicles can be grouped into four different categories, namely, excitation via a TBL, excitation via direct openings to the surroundings, and excitation via the turbulent recirculation region and the underbody. For convectively excited surfaces, the aerodynamic pressure fluctuations represent the critical quantity that can directly be taken from an incompressible flow simulation. However, acoustic excitation may well dominate at other surfaces, especially at the underbody [29]. For this reason, and as a theoretical foundation for the interpretation of turbulent WPF as imprints of a variety of turbulent vortex structures in the flow, we will briefly review the integral representations of Lighthill's equation. Note however, that the far-field assumption frequently employed in aeroacoustics appears unjustified for low frequencies.

For the description via Green's free space functions in the time domain, the time shift $\delta t = |\boldsymbol{x} - \boldsymbol{y}|/c_0$ required to overcome the distance between source at position $\boldsymbol{y}$ and receiver at position $\boldsymbol{x}$ must be taken into account by evaluating the Lighthill tensor at a retarded time $\tau = t - \delta t$. We will furthermore denote quantities evaluated at a retarted time with square brackets (i.e. $\boldsymbol{L}(\tau, \boldsymbol{y}) = [\boldsymbol{L}(t, \boldsymbol{y})]$). For solid surfaces without slip, assuming incompressible flow simulation and using the components e_j of the normal vector, a simplified form of Curle's equation given in [56] is obtained as a superposition of a volume contribution of quadrupole sources and a surface contribution of dipole sources to

$$4\pi c_0^2 \left(\rho(\boldsymbol{x}, t) - \rho_0\right) = \frac{\partial^2}{\partial x_\mathrm{i} \partial x_\mathrm{j}} \int_V \frac{\left[L_\mathrm{ij}\right]}{r} dV(y) \quad + \frac{\partial}{\partial x_\mathrm{i}} \int_\sum \frac{e_\mathrm{j}}{r} \left[\rho v_\mathrm{i} v_\mathrm{j} - \tau_\mathrm{ij} + p\delta_\mathrm{ij}\right] d\Gamma_\mathrm{s}(\boldsymbol{y}) \,. \tag{3.14}$$

Later it was shown by Powell that the additional dipole sources in Curle's equation are simply a result of the reflection of quadrupole sources in the flow. It is expedient to cite this famous reflection theorem at this point:

"The pressure dipole distribution on a plane, infinite and rigid surface accounts for the reflection in that surface of the volume distribution of acoustic quadrupole generators of a contiguous inviscid fluid flow, and for nothing more, when these distributions are determined in accordance with Lighthill's concept of aerodynamic noise generation and its natural extension." [116] .

Although the formulation of the Lighthill source term based on the velocity fluctuations is useful for computations and for experimentally determining the WPF based on measured velocity fluctuations (as originally intended by Lighthill [56]), it provides little insight into the actual mechanisms leading to the generation of pressure fluctuations in the fluid. The decisive contribution regarding the sound generating mechanisms was later made by Powell in his *Theory of Vortex Sound* [117]. His major contribution was to show that Lighthill's (or Curle's) equation can also be represented in an alternative form given in [56], stating that (with additional considerations of no-slip boundaries at a stationary wall and free-field radiation, no source convection, and neglect of viscous stresses) the acoustic pressure in the free field can be obtained by employing the vorticity $\boldsymbol{\omega}(\boldsymbol{y}, t)$ according to

$$4\pi p_\mathrm{a}(\boldsymbol{x}, t) = \frac{\partial}{\partial x_\mathrm{i}} \iiint_V \frac{\left[\rho(\boldsymbol{\omega} \times \boldsymbol{v})\right]}{r} dV(\boldsymbol{y}) \quad + \frac{\partial}{\partial x_n} \int_\Sigma \frac{[p]}{r} dS(\boldsymbol{y}) \,. \tag{3.15}$$

The acoustic field can thus be described as a superposition of a volume distribution of dipoles proportional to $(\boldsymbol{\omega} \times \boldsymbol{v})$ and a surface distribution of dipoles proportional to the pressure at the solid surface. The Reynolds stresses are therefore strongly related to vorticity fluctuations. As previously mentioned, convection effects cannot be considered in the given integral formulations, they are however of great importance, particularly for the study of TBL. In this case, the sources can (in a simplified approach) be considered in terms of a frozen boundary layer that is convected over the vehicle (Taylor's frozen eddy hypothesis [118]). Considering only a main flow direction parallel to the surface results in a dominant contribution of hydrodynamic (or evanescent) waves propagating with a dominant subsonic phase velocity ($v_\mathrm{conv} < c_0$). A detailed treatment of the general subject of moving turbulent sources in the flow was presented by Ffowcs Williams and Hawkings [119]. By reversing Ffowcs Williams analogy, it is also possible to infer the source terms in the flow from the surface pressures on the wall provided that the velocity field is known (Gloerfelt [120]). The subject is extensive and will not be elaborated in detail here, but it should be noted that the physical effects are closely related to the well-known Doppler effect. Convected sources imply a set of mechanisms referred to as convected propagation (owing to the flow velocity relative to the observer), Doppler shift (owing to the source motion relative to the observer)

and convective amplification (owing to the source motion relative to the flow) [121]. With respect to the computational treatment of aero-acoustic problems, a variety of options are available. As mentioned earlier, the strongest, and most expensive, approach is the direct numerical solution of the compressible flow equations (Liang [113]). However, since the resolution of all turbulent scales of the compressible equations requires enormous computation time, in general only a part of the scales is resolved and smaller turbulent structures (so-called subgrid scales) are described via a turbulence model gauged with empirical parameters. Based on the Lighthill equation, the incompressible flow equations can also be solved in combination with an aeroacoustic analogy. Besides the flow equations, another fundamentally different method for computing e.g. the turbulent flow around the vehicle is available. This method is the lattice Boltzmann (LB) method, in which physical processes in fluids can be described on the basis of a microscale discretization of the Boltzmann equation. An introduction to the LB method can be found in the dissertation by Viggen (2014) [122]. While the LB method is easy to implement and, above all, highly parallelizable, for a long time especially the consideration of complex geometries as well as the implementation of a turbulence model to resolve the dissipative subgrid scales has caused great difficulties [123]. In recent years, however, the method has been professionalized and is now increasingly used to simulate complex multiphysics processes [124] and, in particular, to simulate complex flow around real vehicles (e.g. [125–127]).

3.2 Stochastic nature of turbulence and convected turbulence

The theory presented previously provides deep and important insights into the noise generating processes. However, the randomness inherently associated with the stochastic nature of turbulent flows only allows an averaged or statistical description to be reproducible. Any realization of a physical quantity in turbulent flows, whether by measurement or simulation, is subject to noise and is therefore different from any other measurement $\hat{p}_{\mathrm{f}_{(\mathrm{i})}}(\boldsymbol{x},\omega) \neq \hat{p}_{\mathrm{f}_{\mathrm{i}+1}}(\boldsymbol{x},\omega)$, a turbulent flow is therefore never strictly stationary. Weak stationarity can however be assumed, implying that the statistical properties of the flow remain the same during each realisation. Therefore, statistical methods must be employed to describe the turbulent processes in the flow (for details see [50]). This can be done, for example, by computing the temporal autocorrelation or, more interesting for our application, the Fourier transform of the autocorrelation, which is the CPSD already employed to estimate consistent and reproducible FRF's in impulse hammer measurements in Eq. (2.65). To obtain a formulation independent of the measurement duration, the resulting spectrum is divided by the measurement time T, such that for an infinite measurement duration the definition of the auto power spectral density (APSD) from a set of surface pressure measurements $\hat{p}_{\mathrm{f}_{(\mathrm{i})}}(\boldsymbol{x},\omega)$ becomes

$$\hat{S}_{\mathrm{pf}}(\boldsymbol{x},\omega) = \lim_{T\to\infty} \frac{1}{T}\{\hat{p}_{\mathrm{f}_{(\mathrm{i})}}(\boldsymbol{x},\omega)\hat{p}^{*}_{\mathrm{f}_{(\mathrm{i})}}(\boldsymbol{x},\omega)\}\,. \tag{3.16}$$

A suitable window must additionally be chosen to avoid leakage. This signal processing method is also known as Welch periodogram [128]. However, the APSD only provides information about the power of the spatial surface pressure distribution and not about the inherent phase relationship between different positions. This spatial phase relationship, however, is essential, especially at low frequencies. For illustration, the reader may imagine a plate excited by WPF with given APSD but various phase relationships. If the phase is the same everywhere, the plate will oscillate, while a surface pressure distribution with random phase will (in the limit of zero spatial correlation) not cause any vibration. Therefore, for a physically meaningful description of the WPF, the spatio-temporal statistics must also be considered. This requires an analysis of the CPSD between the individual signals at positions $\boldsymbol{x}_1$ and $\boldsymbol{x}_2$. The CPSD

of pressure $\hat{S}_{\mathrm{pf}}(\boldsymbol{x}_1, \boldsymbol{x}_2, \omega)$ accordingly becomes

$$\hat{S}_{\mathrm{pf}}(\boldsymbol{x}_1, \boldsymbol{x}_2, \omega) = \lim_{T\to\infty} \frac{1}{T}\{\hat{p}_{\mathrm{f_{(i)}}}(\boldsymbol{x}_1, \omega)\hat{p}^*_{\mathrm{f_{(i)}}}(\boldsymbol{x}_2, \omega)\}. \tag{3.17}$$

We furthermore employ $\hat{S}_{\mathrm{pf}}(\boldsymbol{x}_1, \boldsymbol{x}_2, \omega)$ to label the CPSD and $\hat{S}_{\mathrm{pf}}(\boldsymbol{x}, \omega)$ to label the APSD. The WFSDl density (WFSD) $\breve{\Phi}_{\mathrm{pf}}(\boldsymbol{k}_1, \boldsymbol{k}_2, \omega)$ is yet another method that can be used to describe the statistical properties of turbulent flows. The WFSD $\breve{\Phi}_{\mathrm{pf}}(\boldsymbol{k}_1, \boldsymbol{k}_2, \omega)$ relates to its CPSD $\hat{S}_{\mathrm{pf}}(\boldsymbol{x}_1, \boldsymbol{x}_2, \omega)$ in space via spatial Fourier transform, just as the CPSD relates to the cross-correlation in time via temporal Fourier transform. Accordingly, this spectrum can be obtained by spatial Fourier transform and normalisation with Length L and width B (to be independent of geometry) according to

$$\breve{\Phi}_{\mathrm{pf}}(\boldsymbol{k}_1, \boldsymbol{k}_2, \omega) = \frac{1}{LB}\mathcal{F}_{\mathrm{x_1}}\left\{\mathcal{F}_{\mathrm{x_2}}\left\{\hat{S}_{\mathrm{pf}}(\boldsymbol{x}_1, \boldsymbol{x}_2, \omega)\right\}\right\}. \tag{3.18}$$

Note that a double Fourier transform is employed to transform the CPSD into the $\boldsymbol{k}_1$-$\boldsymbol{k}_2$-ω space. If the assumption of stationarity would not hold, a double transformation into the ω-ω' space would similarly be required to obtain the APSD of the correlation between arbitrary signals measured at t and t'. However, owing to stationarity the autocorrelation can be represented purely by the time shift $\tau = t' - t$, which in turn allows to perform the usual reduction to a single time (or frequency) variable. The idea of stationarity can now be forwarded from temporal to spatial domain by assuming homogeneity. For the statistical description of homogeneous turbulence without pressure gradients, two simplifications are typically applied. First, it is assumed that the CPSD is spatially constant ($\hat{S}_{\mathrm{pf}}(\boldsymbol{x}, \omega) = \hat{S}_{\mathrm{pf}}(\omega)$), and in further tightening that the CPSD is displacement invariant, i.e. that $\hat{S}_{\mathrm{pf}}(\boldsymbol{x}_1, \boldsymbol{x}_2, \omega) = \hat{S}_{\mathrm{pf}}(\boldsymbol{x}_1, \boldsymbol{x}_1 + \boldsymbol{\zeta}, \omega) = \hat{S}_{\mathrm{pf}}(\boldsymbol{\zeta}, \omega)$ and thus both aerodynamic (evanescent) and acoustic (propagating) waves are represented solely by means of plane waves. The field is thus spatially homogeneous [56], allowing for a reduction in dimensionality. The corresponding shift-invariant spectrum is then obtained according to $\breve{\Phi}_{\mathrm{f}}(\boldsymbol{k}, \omega) = \mathcal{F}_{\boldsymbol{\zeta}}\{\hat{S}_{\mathrm{pf}}(\boldsymbol{\zeta}, \omega)\}$. At this point, let us examine the effect of convection of turbulent sources in a shear layer with convection velocity v_{conv} parallel to the wall on the CPSD or WFSD measured at the wall. A significant simplification can be made by assuming the turbulent sources to be stationary and by additionally considering the convection of a turbulent pattern with constant velocity v_{conv} according to the already mentioned Taylor hypothesis of frozen convection [118]. The shift-invariant **velocity** spectrum $\breve{\Phi}_{\mathrm{vf}}(\boldsymbol{k}, \omega)$ can then be represented as a superposition of a frozen turbulence pattern described in wavenumber domain as $\breve{\Phi}_{\mathrm{vf0}}(\boldsymbol{k})$ and a convection effect $\breve{S}_{\mathrm{vfc}}(\omega)$ as

$$\breve{\Phi}_{\mathrm{vf}}(\boldsymbol{k}, \omega) = \breve{\Phi}_{\mathrm{vf0}}(\boldsymbol{k})\breve{S}_{\mathrm{vfc}}(\omega). \tag{3.19}$$

To illustrate the convection effect, imagine a thin layer of alternatively rotating vortices with a characteristic distance l_{char} between two equally rotating vortices, moving along a plane with shear velocity v_{conv}. If one then measures the velocity deviations $v(t)$ at any point within the plane, the velocity fluctuations $v'(t)$ will appear in terms of a harmonic oscillation with convection-dependent angular frequency ω_{c} and can therefore be expressed as $v'(t) = Re\{e^{i\omega_{\mathrm{c}}t}\}$. This angular frequency can then be determined from aerodynamic wavelength ($\lambda_{\mathrm{char}} = l_{\mathrm{char}}$) or convective wavenumber ($k_{\mathrm{conv}} = 2\pi/\lambda_{\mathrm{char}}$) and the convection velocity v_{conv} according to $\omega_{\mathrm{c}} = k_{\mathrm{conv}}v_{\mathrm{conv}}$. Due to the displacement invariance, we proceed similar to Eq. (3.16) and by remembering the assumption of homogenous turbulence and constant convection velocity, the power spectral density becomes $\hat{S}_{\mathrm{vfc}}(\omega) = \hat{S}_{\mathrm{vfc0}}(\omega)\,\delta(\omega - \omega_{\mathrm{c}}) = \hat{S}_{\mathrm{vfc0}}(\omega)\,\delta(\omega - k_{\mathrm{conv}}v_{\mathrm{conv}})$. Based on the contributions of Pope [129] and Taylor [118, 130] and in a form similar to that given in [56] the

WFSD of convected turbulence finally becomes

$$\breve{\Phi}_{\mathrm{vf}}(\boldsymbol{k},\omega) = \breve{\Phi}_{\mathrm{vf0}}(\boldsymbol{k})\hat{S}_{\mathrm{vfc0}}\left(\omega\right)\delta(\omega - k_{\mathrm{conv}}v_{\mathrm{conv}})\,. \tag{3.20}$$

Now, by considering the velocity field $v(\boldsymbol{k},\omega)$ (or the corresponding WFSD by multiplying with the complex conjugate) as a boundary condition for an acoustic cavity with infinitely far sound hard boundaries (i.e. a semi-free field) as in the example given in Sec. 2.2.1, much can be deduced about the nature of the induced WFSD of pressure $\breve{\Phi}_{\mathrm{pf}}(\boldsymbol{k},\omega)$ at the wall. The velocity field actually represents a wavy wall and therefore, the considerations below Eq. (2.13) regarding the nature of the acoustic dynamic boundary stiffness equally apply to the propagation of waves induced by convected turbulent patterns. Subsonic convection produces aerodynamic waves with subsonic phase velocities, and unsteady turbulent sources in the flow produce acoustic waves. As the wave dynamic stiffness of acoustic waves (with acoustic wavenumber) approaches infinity, this part is transmitted very effectively, manifesting itself in a clear maximum in the WFSD of the pressure at the wall (being however typically hidden under the high amplitude contribution of the convective part with dominant wavenumber k_{conv}, more in Sec. 3.5.1). The physics equally apply to finite domains by recurring to the ideas presented in Sec. 2.2.4.

3.3 Transmission of wall pressure fluctuations into a cavity

Now that we have investigated the statistical methods for describing convective turbulent WPF, we can rely on the foundations laid from Sec. 2.2 to Sec. 2.2.4 to examine the examples of the infinite and, respectively, finite vibro-acoustic box Sec. 2.2 forced by turbulent WPF. For this purpuse, the vibro-acoustic joint wavenumber admittance $\breve{y}_{\mathrm{c}}$ defined in Sec. 2.2.3 is employed to express the acoustic pressure $\breve{p}_{\mathrm{a}}$ in the cavity as the product of aerodynamic forcing $\breve{p}_{\mathrm{f}}$ and admittance $\breve{y}_{\mathrm{c}}$ as $\breve{p}_{\mathrm{a}} = \breve{y}_{\mathrm{c}}\breve{p}_{\mathrm{f}}$. As already explained in Sec. 2.2.3, there are two different possibilities to obtain an analytic expression for $\breve{y}_{\mathrm{c}}$. The first possibility is to consider the full, two-way coupling by employing $\breve{y}_{\mathrm{c}} = \omega^2\breve{z}_{\mathrm{a}}/\left(\omega^2\breve{z}_{\mathrm{a}} + \breve{z}_{\mathrm{s}}\right)$. A power-based description is required to be independent of background noise. For an infinitely long measurement duration no ensemble averaging is required and thus a power-based formulation can be obtained by multiplying with the complex conjugate as

$$\breve{p}_{\mathrm{a}} = \breve{y}_{\mathrm{c}}\breve{p}_{\mathrm{f}} \quad \Rightarrow \quad \breve{p}_{\mathrm{a}}\breve{p}_{\mathrm{a}}^{*} = \breve{y}_{\mathrm{c}}\breve{y}_{\mathrm{c}}^{*}\breve{p}_{\mathrm{f}}\breve{p}_{\mathrm{f}}^{*}\,. \tag{3.21}$$

The complex conjugate products can then be combined to the respective WFSD $\breve{\Phi}_{\mathrm{pa}}$, $\breve{\Phi}_{\mathrm{yc}}$ and $\breve{\Phi}_{\mathrm{pf}}$ to arrive at

$$\breve{\Phi}_{\mathrm{pa}}(\boldsymbol{k},\omega) = \breve{\Phi}_{\mathrm{yc}}(\boldsymbol{k},\omega)\breve{\Phi}_{\mathrm{pf}}(\boldsymbol{k},\omega)\,. \tag{3.22}$$

The WFSD of the two-way coupling vibro-acoustic joint admittance becomes

$$\breve{\Phi}_{\mathrm{yc}} = \frac{\omega^2\breve{z}_{\mathrm{a}}}{\breve{z}_{\mathrm{s}} + \omega^2\breve{z}_{\mathrm{a}}}\left(\frac{\omega^2\breve{z}_{\mathrm{a}}}{\breve{z}_{\mathrm{s}} + \omega^2\breve{z}_{\mathrm{a}}}\right)^{*} = \frac{\omega^4\breve{z}_{\mathrm{a}}\breve{z}_{\mathrm{a}}^{*}}{\omega^4\breve{z}_{\mathrm{a}}\breve{z}_{\mathrm{a}}^{*} + 2\omega^2\breve{z}_{\mathrm{a}}\breve{z}_{\mathrm{s}}^{*} + \breve{z}_{\mathrm{s}}\breve{z}_{\mathrm{s}}^{*}} = \frac{\omega^4\breve{\Phi}_{\mathrm{za}}}{\breve{\Phi}_{\mathrm{zs}} + 2\omega^2\breve{\Phi}_{\mathrm{sa}} + \omega^4\breve{\Phi}_{\mathrm{za}}}\,. \tag{3.23}$$

which can then be combined with the WFSD of convected turbulence given in Eq. (3.20) to obtain the desired relation between the WFSD of pressure in the cavity and the TBL excitation to

$$\breve{\Phi}_{\mathrm{pa}}(\boldsymbol{k},\omega) = \breve{\Phi}_{\mathrm{yc}}(\boldsymbol{k},\omega)\breve{\Phi}_{\mathrm{pf}}(\boldsymbol{k},\omega) = \frac{\breve{\Phi}_{\mathrm{za}}}{\breve{\Phi}_{\mathrm{zs}} + 2\breve{\Phi}_{\mathrm{sa}} + \breve{\Phi}_{\mathrm{za}}}\breve{\Phi}_{\mathrm{pf0}}(\boldsymbol{k})\breve{\Phi}_{\mathrm{pfc0}}(\omega)\delta(\omega - k_{\mathrm{conv}}v_{\mathrm{conv}})\,. \tag{3.24}$$

The interested reader may note that the similar derivation for assessing sound transmission via partitions given in [54] is actually the Fourier-based substructuring method in Eq. (2.28). It has been discussed

in Sec. 2.4 that the feedback effect from the acoustic system to the mechanic structure can, in a first approximation, be neglected in case of vehicles. However, this approximation depends strongly on the particular design of the mechanical structure and the size of the acoustic cavity, and at least for the generic structure studied in this work, two-way coupling does occur. However, the case of one-way coupling is interesting from a didactic point of view and will therefore be investigated as well. Deriving a power-based formulation of $\breve{y}_\mathrm{c} = \omega^2 \breve{z}_{\mathrm{a}\Gamma} \breve{y}_\mathrm{s}$ and substituting the WPF model similar to Eqs. (3.21) and (3.22) yields

$$\breve{\Phi}_{\mathrm{pa}}(\boldsymbol{k},\omega) = \omega^4 \breve{\Phi}_{\mathrm{za}\Gamma}(\boldsymbol{k},\omega) \breve{\Phi}_{\mathrm{ys}}(\boldsymbol{k},\omega) \breve{\Phi}_{\mathrm{pf0}}(\boldsymbol{k}) \breve{\Phi}_{\mathrm{pfc0}}(\omega) \delta(\omega - k_\mathrm{conv} v_\mathrm{conv}) \,. \tag{3.25}$$

The case of a finite plate and a finite cavity is more interesting and, as explained in section 2.2.4, the expressions for the infinite case can straightforwardly be applied to the finite case by evaluating the continuous expressions only for a reduced set of wavenumbers (or eigenvalues) as it was done in Eq. (2.34) and (2.36). The power-based formulation of the WFSD of the one-way coupled finite system can then be obtained according to

$$\breve{p}_{\mathrm{a}|\mathrm{mnl}} = \breve{y}_{\mathrm{c}|\mathrm{mnl}} \breve{p}_{\mathrm{f}|\mathrm{mnl}} \quad \Rightarrow \quad \breve{p}_{\mathrm{a}|\mathrm{mnl}} \breve{p}^*_{\mathrm{a}|\mathrm{mnl}} = \breve{y}_{\mathrm{c}|\mathrm{mnl}} \breve{y}^*_{\mathrm{c}} \breve{p}_{\mathrm{f}|\mathrm{mnl}} \breve{p}^*_{\mathrm{f}|\mathrm{mnl}} \,, \tag{3.26}$$

and

$$\breve{\Phi}_{\mathrm{pa}|\mathrm{mnl}}(\omega) = \breve{\Phi}_{\mathrm{yc}|\mathrm{mnl}}(\omega) \breve{\Phi}_{\mathrm{pf}|\mathrm{mnl}}(\omega) \,. \tag{3.27}$$

Substituting the expressions in Eqs. (2.36) and (2.34) yields

$$\breve{\Phi}_{\mathrm{yc}|\mathrm{mnl}}(\omega) = \frac{\omega^4}{\rho_\mathrm{s}^2 h^2} \frac{\rho_0^2 c_0^2}{\sqrt{1-\lambda_{a|mn0}/\omega^2} \left(\sqrt{1-\lambda_{a|mn0}/\omega^2}\right)^*} \frac{1}{(\omega^2 - \lambda_{s|mn})^2} \,. \tag{3.28}$$

The excitation of the finite system can be obtained by applying an inverse Fourier transform on Eq. 3.20 according to

$$\hat{S}_{\mathrm{pf}}(\boldsymbol{\zeta},\omega) = \mathcal{F}^{\mathrm{i}}_{\boldsymbol{\zeta}} \left\{ \breve{\Phi}_{\mathrm{pf}}(\boldsymbol{k},\omega) \right\} = \mathcal{F}^{\mathrm{i}}_{\boldsymbol{\zeta}} \left\{ \breve{\Phi}_{\mathrm{pf0}}(\boldsymbol{k}) \delta(\omega - k_\mathrm{conv} v_\mathrm{conv}) \right\} = \hat{S}_{\mathrm{pf0}}(\boldsymbol{\zeta},\omega) e^{-ik_\mathrm{conv}\zeta} \,, \tag{3.29}$$

from which the discrete loading on a finite number of modes may then be obtained by projecting on a finite set of harmonic functions (see Sec. 2.2.4) as

$$\breve{\Phi}_{\mathrm{pf}|\mathrm{mnl}}(\omega) = \int_{\mathbb{R}^2} \hat{S}_{\mathrm{pf0}}(\boldsymbol{\zeta},\omega) e^{-ik_\mathrm{conv}\zeta} e^{-i(\zeta k_{x|m} + \eta k_{y|n})} d\zeta d\eta \tag{3.30}$$

and the final equation describing the response of a finite rectangular cavity with sound hard walls coupled with a Kirchhoff plate with simply supported edges and subject to convected excitation of frozen turbulence becomes

$$\breve{\Phi}_{\mathrm{pa}|\mathrm{mn}}(\omega) = \breve{\Phi}_{\mathrm{yc}|\mathrm{mnl}}(\omega) \breve{\Phi}_{\mathrm{pf}|\mathrm{mnl}}(\omega) \,, \tag{3.31}$$

from which the spatial field can simply be assembled by weighting with the respective harmonic functions and summation. The result of this analysis is that the interior SPL increases (quadratically) proportional to acoustic density ρ_0 and speed of sound c_0 and decreases inversely proportionally to mechanical density ρ_s and plate thickness h. In the absence of structural and acoustical damping, the SPL becomes infinite near the mechanical natural frequencies $\omega_{s|mn}$ and the acoustical in-plane natural frequencies $\omega_{a|mn0}$ but not on those natural frequencies associated with out-of-plane modes l. This becomes clear when considering the low-frequency limit case, in which the 1-DOF acoustic system is excited by a normal boundary motion and thus the pressure in the cavity is proportional to the product of the density and the time derivative of the particle velocity at the boundary. The most critical case occurs if there exists a

frequency ω being both a mechanical and acoustical eigenfrequency $\omega = \omega_{\mathrm{a|mn}}$ and $\omega = \omega_{\mathrm{s|mn}}$ for which the related convective wavenumber k_{conv}, the mechanical trace wavenumber $\kappa_{s|mn} = \sqrt{k_{s|m}^2 + k_{s|n}^2}$ and the acoustic trace wavenumber $\kappa_{a|mn} = \sqrt{k_{a|m}^2 + k_{a|n}^2}$ coincide (aero-vibro-acoustic coincidence). However, this is only possible if both the convection and bending wave velocities are equal to the speed of sound, which will not be the case in the typical speed range of motor vehicles. However, the case of aerodynamic coincidence, in which mechanical and convective wavenumber match ($\kappa_{a|mn} = k_{\mathrm{conv}}$) can occur during high-speed motion in vehicles as investigated by Businger [131]. Regardless of excitation, strong damping-controlled amplitudes occur at the coupled natural frequencies of the system (those at which the entire denominator of $\breve{\Phi}_{\mathrm{yc}}(\boldsymbol{k}, \omega)$ vanishes). If the convective wavenumber k_{conv} does not coincide with a resonant wavenumber $\kappa_{a|mn}$, spectral leakage occurs and the energy is redistributed among all other harmonics due to to the violation of the orthogonality condition. Generalizing to the case of an arbitrarily supported coupled plate-cavity system affords to transition from the discrete Fourier decomposition to a coupled eigenvalue decomposition. Clearly, the corresponding considerations apply equally to the discrete systems presented in Sec. 2.4, but for the sake of simplicity we will leave it at a functional description. If the spatially continuous but temporally bounded i-th realisation of the pressure distribution $\hat{p}_{\mathrm{f}_{(\mathrm{i})}}(\boldsymbol{x}, \omega)$ is established, for example, by means of a numerical simulation, the question emerges how an ensemble averaging can be realised to avoid incorporating the ubiquituous background noise. The most obvious approach would be to compute N-solutions by first imposing the i-th pressure distribution $\hat{p}_{\mathrm{f}_{(\mathrm{i})}}(\boldsymbol{x}, \omega)$ to obtain the i-th generalized displacements according to

$$\hat{z}_{\mathrm{c}}(\boldsymbol{x}, \omega)\hat{d}_{\mathrm{c}_{(\mathrm{i})}}(\boldsymbol{x}, \omega) = \hat{p}_{\mathrm{f}_{(\mathrm{i})}}(\boldsymbol{x}, \omega)\,, \tag{3.32}$$

and to subsequently perform ensemble averaging of the generalised displacements according to

$$\hat{S}_{\mathrm{dc}}(\boldsymbol{x}, \omega) = \lim_{T\to\infty} \frac{1}{T} \left\{ \hat{d}_{\mathrm{c}_{(i)}}(\boldsymbol{x}, \omega)\hat{d}^*_{c_{(i)}}(\boldsymbol{x}, \omega) \right\}\,. \tag{3.33}$$

However, this approach has the major disadvantage that, especially in the case of real automotive problems, an enormous amount of computation time may be required. A significant improvement can be realised by solving the coupled eigenvalue problem and subsequently averaging on a modal basis. Thus, if one solves the problem given in Eq. (2.52) to determine the eigenvalues and eigenmodes required and then applies the corresponding vibro-acoustic eigentransformation according to

$$\tilde{f}_{\mathrm{c}_{(\mathrm{i})}}(\omega) = \mathcal{E}_{\mathrm{c}} \left\{ \hat{p}_{\mathrm{f}_{(\mathrm{i})}}(\boldsymbol{x}, \omega) \right\}\,, \tag{3.34}$$

then, one can obtain a modal formulation according to

$$\tilde{d}_{\mathrm{c}_{(\mathrm{i})}}(\omega) = \frac{1}{\omega^2 - \lambda_{\mathrm{c|n}}} \tilde{f}_{\mathrm{c}_{(\mathrm{i})}}(\omega) \tag{3.35}$$

and from that, by inverse eigentransformation according to $\hat{d}_{\mathrm{c}_{(\mathrm{i})}}(\boldsymbol{x}, \omega) = \mathcal{E}_{\mathrm{c}}{}^{\mathrm{i}} \left\{ \tilde{d}_{\mathrm{c}_{(\mathrm{i})}}(\omega) \right\}$, one can synthesise the spatial displacements and pressures. Note that the resulting equation only needs to be evaluated for each mode and therefore requires only decent computation time. Thus, an ensemble-averaged APS for broadband excitation can be determined simple and rapidly on the basis of the modal formulation by projecting the excitation into the modal space and averaging only on the basis of the synthesised displacements (see also Glandier [32]. This procedure can however cause high effort if the spectral averaging has to be carried out over a large number of positions. We will therefore examine a second variant for calculating the power spectra. Considering that the modal formulation is exactly deterministic when determined from experimental data via EMA, a power formulation can be derived by multiplying the

individual relations between the coupled modal impedance of the n-th mode $\tilde{z}_{\mathrm{c|n}}(\omega)$ and the generalized displacement $\tilde{d}_{\mathrm{c_{(i)}|m}}$ related to the i-th forcing $\tilde{f}_{\mathrm{c_{(i)}|m}}(\omega)$ in the ensemble average as

$$\tilde{z}_{\mathrm{c|n}}(\omega)\tilde{d}_{\mathrm{c_{(i)}|m}}(\omega) = \tilde{f}_{\mathrm{c_{(i)}|m}}(\omega)\,. \tag{3.36}$$

Multiplying with the conjugate functions and performing ensemble averaging as

$$\tilde{z}_{\mathrm{c|n}}\tilde{z}^{*}_{\mathrm{c|m}}\{\tilde{d}_{\mathrm{c_{(i)}|n}}\tilde{d}^{*}_{\mathrm{c_{(i)}|m}}\} = \{\tilde{f}_{\mathrm{c_{(i)}|n}}\tilde{f}^{*}_{\mathrm{c_{(i)}|m}}\}\,, \tag{3.37}$$

yields

$$\tilde{\Phi}_{\mathrm{zc|mn}}(\omega)\tilde{\Phi}_{\mathrm{dc|mn}}(\omega) = \tilde{\Phi}_{\mathrm{fc|mn}}(\omega)\,. \tag{3.38}$$

This formulation is particularly interesting because it allows to employ a statistical WFSD model to represent the aerodynamical excitation. For us it is of more interest that the APSD of the generalised displacements can, instead of averaging over the spatial field, be performed on a modal basis as

$$\hat{S}_{\mathrm{dc}}(\boldsymbol{x},\omega) = \{\hat{d}_{\mathrm{c_{(i)}|n}}(\omega)\hat{d}^{*}_{\mathrm{c_{(i)}|m}}(\omega)\} = \sum_{n=0}^{N}\sum_{m=0}^{M}\psi_{\mathrm{c|n}}(\boldsymbol{x})\psi_{\mathrm{c|m}}(\boldsymbol{x})\tilde{\Phi}_{\mathrm{dc|mn}}(\omega)\,. \tag{3.39}$$

The advantage of such a procedure is that the averaging is no longer conducted for all nodes, but only for all modes. Compared to the original formulation, the synthesis of the generalised APS only contains an additional summation over the modes. An application of modal averaging can be found in [132]. Of course, it is also possible to sum over the multi-dimensional CPSD [133] or to use a wavenumber formulation as in [134].

3.4 Automotive aerodynamics

Since the early days of the automobile industry, the flow around the vehicle has been an important concern due to its substantial effect on induced drag. The interested reader is directed to the works by Hucho [135] and Katz [136] as well as Ekmann's dissertation [137] or the recent article by Aleyasin (2021) [138]. Historically, research has strongly been driven by attempts to quantify and understand the effect of the large recirculation region behind the vehicle on the induced drag. For this reason, aerodynamic studies often deal with spatially averaged or spatiotemporally averaged quantities (e.g. lift coefficient). Recent years have seen an increasing focus on the temporal characteristics of automobile flow (e.g. [138–140]). Researchers commonly employ generic test bodies of various complexity to examine the flow topology. Over the years, a large number of test bodies have been developed in order to generate comparable and consistent simulation and measurement findings for scientific research. The Ahmed test body presented in [141] and employed in e.g. [125, 138, 139] is particularly noteworthy. However, owing to its blunt front face, the Ahmed test body is of limited use for investigating more realistic situations; for this purpose, the SAE [1, 22–24], the Windsor [127], Asmo [142], and more recently the Drivaer [25–28] model were later developed with increasing complexity. The SAE body and the Drivaer model were additionally developed for aeroacoustic applications, i.e. extensive acoustic treatment of the passenger compartment allows to investigate the transmission of pressure fluctuations at the side window to the driver's ear. For investigations in the wind tunnel a variety of experimental techniques are available, such as traditional oil film visualization [143], hot wire measurements [138] but also modern state-of-the art techniques like in particular Particle-Image-Velocimetry [138]. Alternatively, surface pressure microphones can be employed to measure WPF [139]. These experimental methods have played an increasing role in validating numerical methods based on the Navier-Stokes or Lattice-Boltzmann equations [124]. Although increas-

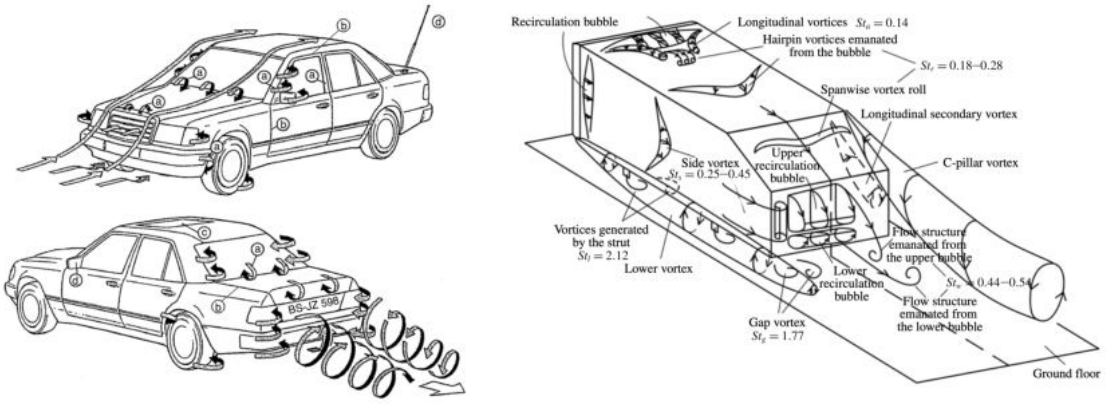

Figure 3.1: Topological features of flow around vehicles. (a) real vehicle [146] (b) Ahmed body [140].

ingly stable and powerful algorithms to numerically solve the governing differential equations have been brought into use recently, intensive physical knowledge is required to deduce the relevant information from the wealth of data produced. It is advantageous to describe the irrotational and incompressible potential flow that governs the overall behavior of the flow using potential theory, in terms of saddle points, bifurcation lines, and stable and unstable nodes. For this purpose, the excellent paper by Krajnovic on the flow around the Ahmed body is recommended [144]. To investigate the dynamic behavior of the potential flow, Proper Orthogonal Decomposion (POD) or Dynamic Mode Decomposition (DMD) may be applied [145]. For the spatial visualization of coherent regions, the Q-criterion (2nd invariant of velocity gradient tensor) may also be employed. In particular, the Q-criterion allows to discriminate vortical regions (with high Reynolds stresses) and viscous regions [127]. At sufficiently high frequencies, directly analyzing the spectral coherence of velocity [140] or pressure [139] is simple and allows to infer the essential statistical quantites from on a very reduced set of measurements. Zhang's extensive visualization of vehicle flow patterns shown in Fig. 3.1b will serve as a starting point for our investigation in vehicle aerodynamics [140]. The flow topology is complex, three-dimensional, and depends on geometry and Reynolds numbers, but key topographic features can be identified at common Reynolds numbers and velocities. The extended recirculation region behind the vehicle dominated by large-scale vortices is the most important area regarding the development of drag. The well-known C-pillar vortex forms symmetrically along the side edge of the roof (upper bubble), detaches at the rear and forms a symmetric roller vortex (for more details see [142]). Parallel to the ground, a symmetrical, steady recirculation region emerges [138]. The structure of the upper and lower recirculation bubbles strongly depends on the slant angle (the angle between the roof and the hatchback). The detailed study of Tunayetal [147] mentions that two major flow topologies can be distinguished based on a critical slant angle of 30°. At a slant angle of more than 30° the pressure gradients along the slant angle enforce an early flow separation at the upper edge of the roof implying a substantial increase in mean drag coefficient [125]. In contrast, with a smaller slope angle, the flow remains attached significantly longer and the lower recirculation bubble is concentrated close to the ground (as in Fig. 3.1b). Flow separation frequently occurs at the roof [148] (even with a slanted forebody [142]) or at the side [140]. At the nose of the vehicle (Fig. 3.1a), the incoming air is split at a stagnation point, with part of the air being directed under the vehicle (see also Wang [38]). The lifting portion of the air is distributed in various directions and frequently remains attached until the leading edge of the roof [137, 142]. A detachment bubble can also form between hood and windshield on non-streamlined bodies (especially in trucks [137]). The A-pillar vortex on the side window is frequently acoustically critical due to its proximity to the driver's ear [23, 149]. Vortex streets may form at the wheels (in this case: round supports, more in [38]). For further information concerning

the influence of geometric properties on the overall flow structure, the reader is referred to [138] and [140].

3.5 Automotive aeroacoustics

Owing to the high influence of vehicle noise to passenger comfort, recent years have shown a substantial amount of research in the field. Special attention has been paid to the higher frequency range ($f > 500\,\mathrm{Hz}$) and, consequently, to the identification of the critical contributors in the compressible (acoustic) part of the wall pressure spectrum (e.g. [39, 43]). Mechanisms in the low and mid frequency range ($f \approx 100 - 500\,\mathrm{Hz}$) have also been intensively studied; recent dissertations on the subject include those by Aucejo [150], Businger [39], Nusser [151] and Vadavalli [152]. Only very few papers also deal with the very low frequency range ($f < 100\,\mathrm{Hz}$), an overview of the relevant contributions will be provided in the course of this chapter. It will be exemplified later in Chapter 6 that an important contributor to interior noise are convectively transported turbulent sources. For this, as already explained in Sec. 3.2 and Sec. 3.3, the mean flow properties discussed in the previous section are of outstanding importance. The surface pressure spectra may be directly investigated experimentally in regions with relevant excitation [139], but as they are the imprint of a number of turbulent sources in the flow, they do not directly permit identification of the critical sources in the flow. WPF underneath a TBL have, however, been the subject of extensive research due to its exceptional importance for airplane cabin noise [43] and owing to the wealth of theoretical knowledge in the field, far-reaching conclusions can be drawn from a statistical description of the WPF at the wall. [153]. The indoor sound pressure fluctuations induced at very low frequencies $f < 100\,\mathrm{Hz}$ are often also referred to as booming [154–156] or buffeting noise [6, 31, 157]. A particular case is the well-known phenomenon of sunroof buffeting generated by an open sunroof or side window [158, 159]. This phenomenon is characterized by a strong aeroacoustic feedback mechanism and will not be discussed in this thesis. Preventing the transmission of noise in the very low frequency region is particularly challenging because it is strongly influenced by air-tightness and large scale low order structural modes. Therefore, the corresponding studies are frequently performed with a lower cut-off frequency of 100 Hz [22, 28]. Recent studies highlight the contribution of low-frequency noise transmitted through the underbody [29, 32, 32, 33]. The testbodies suitable for aero-vibro-acoustic investigations, namely the SAE body [1, 22, 23] and the drivaer model [25, 27, 45–47] have both been specifically designed to limit the possible aero-vibro-acoustic transmission paths to the side window.

It is now deemed beneficial to briefly and chronologically recall the most recent investigations (since 2010): Moron (2011) [33] investigated the influence of the underbody in a purely numerical approach. Hartmann (2012) [23] investigated aero-vibro-acoustic excitation via the side window on the SAE body and also compared a large number of commercial CFD solvers. His results also include the low frequency region contribution but he was more interested in the compressible part of the wall pressure spectrum. Glandier (2015) [32] published an interesting paper using a coupled vibro-acoustic FE model combined with a computational fluid dynamics (CFD) simulation to calculate low-frequency noise. In particular, he obtained interior SPL's via vibro-acoustic transfer functions combined with WPF measurements. Herpe (2018) [30] investigated aero-vibro-acoustic excitation across the windshield and the side window. He (2018) [28] investigated the transmission of WPF via the side window of the Drivaer model on behalf of a modal substructuring approach with experimentally fitted boundary conditions. In particular, he employed a Corcos model to describe the stochastic loading (more on that in Sec. 3.5.1). Yuan (2020) [37] investigated the statistical properties of the WPF at the side window by inverse determination from measured vibrations. He also investigated the coherence between the side window and the pressure inside and concluded that the low frequency component cannot be directly related to the side window and that the entire vibro-acoustic system must be investigated. Wang (2020) [38] investigated the influence of

the underbody using a generic vehicle and a real vehicle as examples and discovered that the thickness of the underbody has a significant impact on the SPL. Nusser (2021) [22] investigated the transmission of WPF through the side window into the interior of the vehicle using the SAE test body as an example. She used an incompressible large-eddy simulation (LES) to calculate the flow and a coupled structural-acoustic model to describe the vibro-acoustic setup. Boundary conditions and material parameters were determined based on experimental measurements. Schwertfirm (2022) [29] investigated the underbody excitation and concluded that the two-side coupling between vibration and flow can be neglected. Thus, while there are a number of studies on aero-vibro-acoustic mechanisms, there is no study that addresses the relative weighting of the various contributors, as WPF can theoretically be transmitted inward through any flexible vehicle component. Therefore, we will take a step back and investigate the overall physical mechanisms contributing to low-frequency interior noise. To do so, we identify four relevant excitation and transmission paths. First and foremost, there are regions where turbulent structures are convected at high velocity along the vehicle structure; these regions can be described on behalf of extensive knowledge concerning WPF under a TBL. If aerodynamic and structural wavelengths coincide, aerodynamic coincidence can produce exceptional noise levels in the cabin. Secondly, large-scale coherent vortex structures in the recirculation region behind the vehicle can either directly excite the trunk region via aerodynamic pressure fluctuations or produce acoustic waves that excite the entire vehicle structure, however this effect has not been addressed to date. The third mechanism is transmission of noise via the underbody. Due to the limited number of waves that can propagate in the underbody cavity, the associated modal acoustic field can generate considerable interior noise. These three processes can be categorized as indirect transmission processes—that is, noise is transmitted via structural vibrations. The fourth mechanism is the direct transmission of noise from the outside environment through openings and leakages. In the following paragraphs, these mechanisms will be examined in greater depth. Finally, it should be noted at this point that especially in the low frequency range, the psycho-acoustic evaluation of noise is challenging and much research work still needs to be done here. In the course of this work, we will only focus on the physical mechanisms and therefore examine the unweighted SPL. As an interesting starting point for low frequency psycho-acoustics the article written by Lemaitre [6] may be proposed.

3.5.1 Excitation by convected turbulence

WPF under a TBL have probably been one of the most thoroughly explored issues in aeroacoustics in recent decades, and as a result, a substantial degree of complexity and a profound understanding have been achieved. In addition to the book by Blake [43], which has been recommended several times and offers an excellent introduction to the field as well as several further reading suggestions, there is an older review by Bull [153], that may be proposed. This topic is a very vibrant area of research, an overview of current developments may be found in the thesis of Alaloui (2015) [160]. It is common practice to describe spatiotemporal statistics in the frequency domain by means of CPSD or in the wavenumber domain by means of the previously discussed WFSD (Sec. 3.2). Recalling to Eq. (3.20) and Eq. (3.29), it is clear that the CPSD for convected turbulence will be a product of a contribution $\hat{S}_{\mathrm{pf0}}(\boldsymbol{\zeta}, \omega)$ accounting for the spatial structure of the turbulence and a convective contribution that can be described via plane aerodynamic (evanescent) waves according to $e^{-ik_{\mathrm{conv}}\zeta}$. Regarding the spatial structure of the turbulence, it makes sense to assume that the coherence (the normalized CPSD) between a reference position and another position separated by in-flow distance ζ and cross-flow distance η may be represented by exponential decay with a decay rate that grows with frequency (smaller vortices) and gets smaller with mean shear velocity (faster decorrelation) and is thus proportional to the convective wavenumber $k_{\mathrm{conv}} = \omega / v_{\mathrm{conv}}$. The decay rate can therefore be expressed by employing longitudinal and lateral wavenumbers $k_{\gamma\zeta}$ and $k_{\gamma\eta}$ that are proportional to k_{conv} with additional parameters γ_ζ and γ_η as

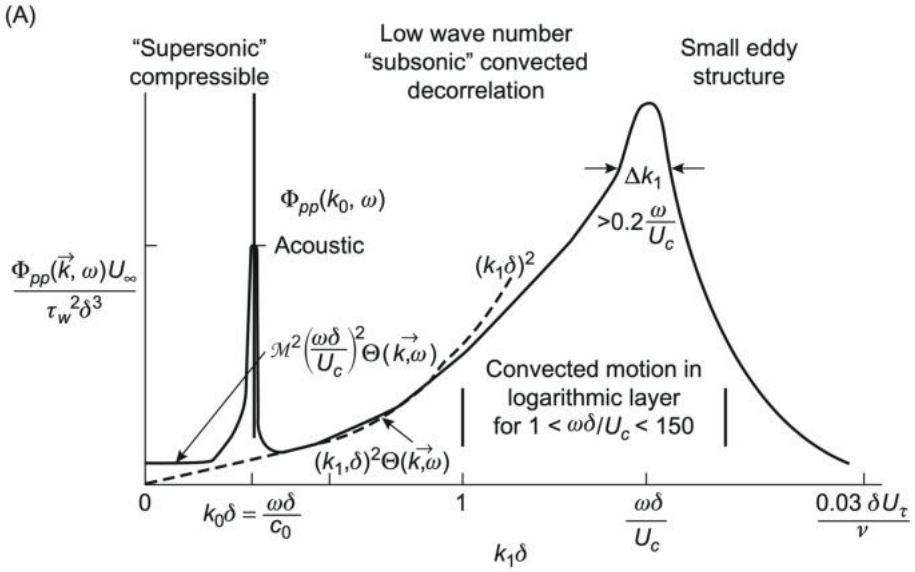

Figure 3.2: Chase wavenumber spectrum of homogenous turbulence (Illustration from [43]).

$k_{\gamma\zeta} = \gamma_\zeta k_{\mathrm{conv}}$ and $k_{\gamma\eta} = \gamma_\eta k_{\mathrm{conv}}$. A model for the statistical pattern may thus read

$$\hat{S}_{\mathrm{pf0}}(\boldsymbol{\zeta}, \omega) = e^{-|k_{\gamma\zeta}\zeta|}e^{-|k_{\gamma\eta}\eta|} = e^{-\gamma_\zeta|\omega\zeta/v_{\mathrm{conv}}|}e^{-\gamma_\eta|\omega\eta/v_{\mathrm{conv}}|}\,, \tag{3.40}$$

which in combination with an aerodynamic component in Eq. (3.29) allows to describe the whole spectrum according to

$$\hat{S}_{\mathrm{pf}}(\boldsymbol{\zeta}, \omega) = \breve{\Phi}_{\mathrm{pfc0}}(\omega)\hat{S}_{\mathrm{pf0}}(\boldsymbol{\zeta}, \omega)e^{-ik_{\mathrm{conv}}\zeta} = \hat{S}_{\mathrm{pfc0}}(\omega)e^{-\gamma_\zeta|\omega\zeta/v_{\mathrm{conv}}|}e^{-\gamma_\eta|\omega\eta/v_{\mathrm{conv}}|}e^{ik_{\mathrm{conv}}} = \hat{S}_{\mathrm{pfc0}}(\omega)\hat{\gamma}_{\mathrm{pf}}(\zeta, \eta, \omega)\,. \tag{3.41}$$

This is the well-known and frequently employed Corcos model for turbulent WPF initially presented in 1967 [161]. By using spatial Fourier transform, a WFSD may be readily produced [162]. This model is appropriate for describing fully developed equilibrium boundary layers on smooth and rough surfaces with no pressure gradient and assuming isotropic homogenous turbulence and negligible compressible spectrum components. Due of its simplicity, it is commonly used to simulate stochastic excitation [28,37, 132,163–165]. Businger showed the usefulness of this type of model for describing turbulent excitation on a car door [39]. On behalf of a more physical reasoning, assuming homogenous turbulence (and therefore only plane hydrodynamic and acoustic waves) allows to integrate Lighthill's equation and by additionally neglecting shear stresses and normal pressure gradients directly at the wall, it becomes evident, that the surface pressure spectrum is essentially composed of a nonlinear turbulence-turbulence component and a mean-shear-turbulence component [43]. The mean-shear-turbulence component represents the convection of a frozen pattern of turbulence indicated in Eq. (3.20) while the nonlinear turbulence-turbulence component accounts for the nonlinear processes related with eddy growth, mixing and decay. Apparently these nonlinear processes are the reason for the lateral and longitudinal decay of coherence employed in Eq. (3.42). Apart from the Corcos model, various semi-empirical models have been proposed to characterize the statistical features, most notably the extensive model of Chase [166] illustrated in Fig. 3.2. This model allows to deduce the WFSD $\breve{\Phi}_{\mathrm{vf}}(\boldsymbol{k}, \omega)$ on behalf of the wall shear stress τ_{w}, the boundary layer thickness δ, the convection velocity v_{conv} as well as kinematic viscosity ν and speed of sound c_0. The dominant part of the spectrum is the convective peak (or ridge) at $k_\zeta = k_{\mathrm{conv}}$. However, Taylor hypothesis is not strictly fulfilled (the turbulent pattern is not *frozen*) and therefore the WFSD is broadband and

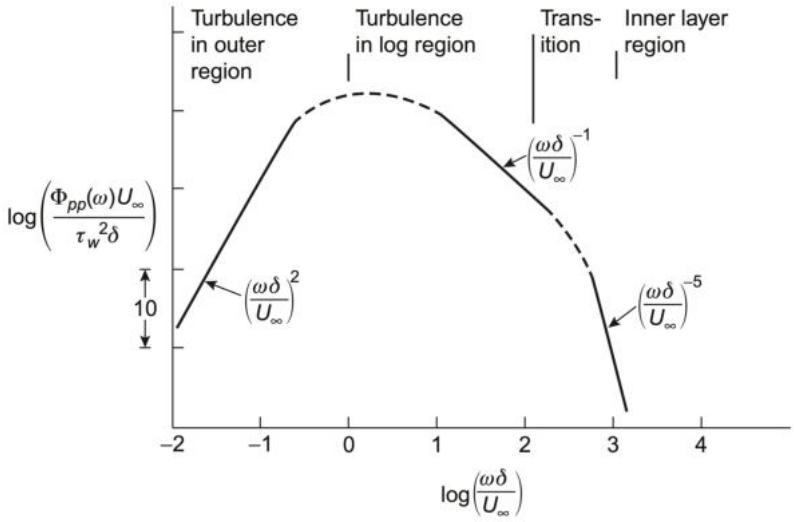

Figure 3.3: Principal contributors to wall pressure APSD (Illustration from [43]).

composed of a wide range of contributions originating throughout the boundary layer. These contributions can be identified on behalf of their trace wavenumber k_ζ and the associated phase speed $v_\zeta = \omega/k_\zeta$. At low wavenumbers $k_\zeta\delta < c_0$, an acoustic contribution with sonic or supersonic trace wavenumbers can be identified. As already indicated, this contribution may cause substantial excitation due to high coherence and is therefore intensively investigated. At low frequencies, however, this component is presumably negligible because the wavelengths of the structure are usually closer to the aerodynamic wavelength and although the acoustic component can efficiently excite lower order modes its level is far below that of the aerodynamic contribution. An estimate of the critical frequency above which compressible effects are important for a given wavenumber k_ζ is given in [43] and reads according to

$$\left(\frac{\omega_{\text{comp}}\delta}{v_{\text{conv}}}\right)^2 \sim (k\delta)^2 M_{\text{c}}^{-2}\,. \tag{3.42}$$

For a bending mode at the side door with a wavelength of $l \approx 1\,\text{m}$ ($k_{\text{x}} = 2\pi/l$), an incident flow velocity $v_{\text{conv}} \approx 40\,\text{m/s}$, a boundary layer thickness of $\delta \approx 0.02\,\text{m}$ [167] follows $f_{\text{comp}} \approx 343\,\text{Hz}$, which is significantly higher than usual natural frequencies for side doors [39]. The reader's attention is drawn to the fact that the abscissa in Fig. 3.2 may actually be read as a weighted (with 2π) Strouhal number $St = fl_{\text{char}}/v_\infty$ associated with the characteristic length scale of the turbulent vortices l_{char}. Due to the relation between wavenumber and characteristic vortex size, the different areas can be assigned to different regions in the TBL. A recommended paper on the subject is that by Farabee et al. [168]. Recalling the single-point APSD in [43] (shown in Fig. 3.3), we note that large-scale eddies cause the low-frequency part of the APS up to $log(\omega_{\text{low}}\delta/v_\infty) \approx -0.5$, while a dominant contribution in the mid frequency range up to $log(\omega_{\text{log}}\delta/v_\infty) \approx 0.5$ can be related to sources in the logarithmic region of the boundary layer. Sources in the transition layer are dominant at higher frequencies and above the high frequency cut-off at $log(\omega_{\text{inner}}\delta/v_\infty) \approx 2.5$ the sources are located within the inner layer. For the given example, the cut-off frequencies are $f_{\text{low}} \approx 100\,\text{Hz}$, $f_{\text{log}} \approx 3000\,\text{Hz}$ and $f_{\text{inner}} \approx 100\,\text{kHz}$. It follows that for the low- and mid frequency ranges of interest within this thesis, the sources are mostly located in the outer region and in the logarithmic region. Wood and Westphal [169] investigated the low-frequency components and found that this component arises from three mechanisms, namely unsteadiness in the free streem, free-stream turbulence and irrotational motion induced by the boundary layer. The low-frequency region is often difficult to measure because background acoustic noise often exists in this frequency range [168]. The

effect of pressure gradients on the WFSD has been investigated in [160] and it has been found that the convective ridge is either stretched or compressed depending on the sign of the pressure gradient. It is still unclear whether and which WFSD model can be used to describe low-frequency excitation of vehicles, particularly in the presence of strong pressure gradients and flow separation, and it is an important part of this work to investigate the statistical description of a complex vehicle flow on a simplified test body in order to further decide on the applicability of a simplified description. In particular, the assumption of homogeneous turbulence should be mentioned here, which is obviously violated in the case of flow separation or large-scale vortex shedding regions. Regarding the transmission of TBL induced noise in vehicles, the contribution via the side window was frequently investigated [28, 30, 31, 37, 170], but also via the windscreen [30] (here dominant under 100 Hz) and the side door [163].

3.5.2 Excitation from leeward components

It is possible to assign distinct vortex shedding frequencies to each of the different characteristic vortex structures shown in Fig. 3.1. The Strouhal number defined as $St = \frac{f_{\mathrm{st}} D}{v_\infty}$ can be employed to estimate the shedding frequency f_{st} of vortices and values of $St \approx 0.2 - 0.3$ are commonly found for large-scale vortex shedding, using the undisturbed velocity v_∞ and a characteristic length $D = \sqrt{A_{\mathrm{f}}}$ based on the square root of the blocking area A_{f} [140]. Zhang determined the Strouhal numbers for the different vortex structures of the Ahmed body (Fig. 3.1). To estimate the influence of the vortex regions on the acoustic spectrum, we can use the lower cut-off frequency of the hearing threshold at $f_{\mathrm{low}} \approx 16\,\mathrm{Hz}$, a blocking area of $A_{\mathrm{f}} \approx 2\,\mathrm{m}^2$, and a mean velocity of $v_\infty \approx 40\,\mathrm{m/s}$, to determine a lower limit of $St_{\mathrm{low}} \approx 0.55$ for the Strouhal number of acoustically relevant vortices on real vehicles. Thus, some of the vortex regions in Fig. 3.1 may well be acoustically relevant, especially the vortex street emerging from the wheels that seems particularly suitable to induce underbody noise. Note that the critical Strouhal number representing the hearing threshold will be reduced with increasing speed and decreasing vehicle cross section and thus, small vehicles at high speeds appear more likely to suffer from wake-induced low-frequency noise. Physically, it is clear that the WPF induced by large scale vortices will contain both an aerodynamic contribution due to the low-speed convection of turbulent structures and an acoustic contribution decaying with $1/r$ with increasing distance from the vortex core (see Eq. (3.14)). It is unclear, however, which of the two contributions is typically dominant, and no specific study on the acoustic pressure induced by WPF in the recirculation region of a closed cavity with flexible walls could be found by the author. Typically, the objective of investigations into the transient properties of the vehicle flow is to understand their impact on the overall vehicle forces. Several investigations can be found, most notably the previously mentioned examination by Zhang [140] and the investigation of Fares [125] on the Ahmed body but also the study of Islam [127] on the Windsor Body at a supercritical slant angle of $\alpha \approx 40\,^\circ$. Note, that a supercritical slant angle ($\alpha > 30\,^\circ$) has been found to generate considerably stronger low frequency WPF [125]. It is of special interest, that in [127] two dominant modes were found at $St \approx 0.46$ and $St \approx 0.79$, where the first mode was assigned to the shear layer at the bottom and the second can be calculated as the ratio v_∞ / H. Further investigations can be found in [125, 142, 171, 172].

3.5.3 Excitation from the underbody

The aero-vibro-acoustic excitation via the underbody region is a topic that has only received limited but growing interest in recent years. Here the works of Moron [33], Crouse [34] and the recent contributions by Wang [38] and Schwertfirm [29] may be mentioned. The underbody represents a cavity with sound-hard upper and lower surfaces with ground clearance g and sound-soft side surfaces separated by length L and width B respectively. Analogously to the treatment of the finite closed rectangular cavity in Sec. 2.2.4,

Lighthill's equation given in Eq. (3.12) can be adapted to a finite cavity by employing a suitable set of orthogonal harmonic functions with wavenumber spacing $\Delta k_\mathrm{x} = \pi/L$, $\Delta k_\mathrm{y} = \pi/B$ and $\Delta k_\mathrm{z} = 2\pi/g$, that fulfill the boundary conditions (as a precursor, check Fig. 6.12). The corresponding eigenfrequencies can then simply be obtained according to Eq. (2.30). Therefore, the excitation induced by the Lighthill tensor is distributed across a limited number of harmonic functions, and correspondingly high levels can be found in close proximity to natural frequencies. The source distribution can typically not be represented by this particular set of basis functions and therefore leakage occurs. The WPF at the underbody surfaces are therefore once again a superposition of aerodynamic waves due to the convection of turbulent structures and acoustic waves with significantly larger amplitudes than in the free-field due to the finite dimensions of the cavity. This has been investigated by Wang in [38] and he concludes that for his specific case, the aerodynamic component is dominant. Schwertfirm [29] has investigated the underbody of the SAE testbody and especially the effect of vibro-acoustic coupling between the underbody cavity and the flexible structure. In this study, coupling induces a slight shift of structural eigenmodes due to the additional acoustic mass of the cavity and a decrease in SPL within the cavity. It is important to note, that an experimental identification of the acoustic contribution of the WPF by assessing the CPSD between two microphones has not yet been performed. This however allows to separate acoustical and hydrodynamic component based on their respective wavelengths as will be shown in Sec. 6.

3.5.4 Direct acoustic excitation

The stochastic pressure fluctuations in the flow can directly excite the acoustic cavity if the fluid is in direct contact with the surrounding flow via openings. A classification of cavity types depending on opening length, cavity depth and opening width can be found in [52]. The two mechanisms relevant for low frequency vehicle noise is the case of a wide opening with a shallow depth cavity, which can occur if a window or sunroof is opened while driving, and the Helmholtz-resonator case in which openings act as acoustic masses of a low frequency Helmholtz-resonator. The former can create excessive noise levels [158, 173, 173] but shall not be treated in this thesis. The latter represents a direct and efficient transmission path for aerodynamic or aeroacoustic pressure fluctuations in the flow that contributes to the interior noise at very low frequencies. The topic has been mentioned by Brandstätter [19] and Nusser [**?**,151] but it has not been thoroughly explored. The elements of the Helmholtz resonator depicted in Fig 3.4a are the acoustic mass of the fluid in the neck $m_\mathrm{a} = \rho_0 L/A$ (with acoustic dynamic stiffness $\hat{z}_{\mathrm{a}|12} = -\omega^2 m_\mathrm{a}$) depending on the effective length L (including a length correction [54]) and cross section A of the opening and the acoustic stiffness of the fluid $k_\mathrm{a} = \rho_0 A^2 c_0^2/V_0$ (with acoustic admittance $\hat{z}_{\mathrm{a}|20} = k_\mathrm{a}$) depending additionally on the volume of the interior cavity V_0. The resonance of the simple oscillator follows most naturally to $f_\mathrm{H} = \sqrt{k_\mathrm{a}/m_\mathrm{a}}/(2\pi)$. To calculate the interior pressure $\hat{p}_{20}$ due to pressure excitation $\hat{p}_{10}$ from the exterior flow it makes sense to draw the corresponding circuit as shown in Fig. 3.4b The continuity of mass (and respectively: volume acceleration) in the system directly allows to calculate the acoustic transmissibility $\hat{s}_{\mathrm{a}|12} = \hat{p}_{20}/\hat{p}_{10}$ according to $\hat{s}_{\mathrm{a}|12} = \hat{z}_{\mathrm{a}|20}/(\hat{z}_{\mathrm{a}|20} + \hat{z}_{\mathrm{a}|12})$. Another Helmholtz-resonator mechanism can be attributed to the excitation of the passenger cabin through holes in the package tray as intensively investigated by Lee [11, 175, 176]. The contribution of Pan on the Helmholtz resonance effect in a helicopter cockpit is also worth mentioning [73].

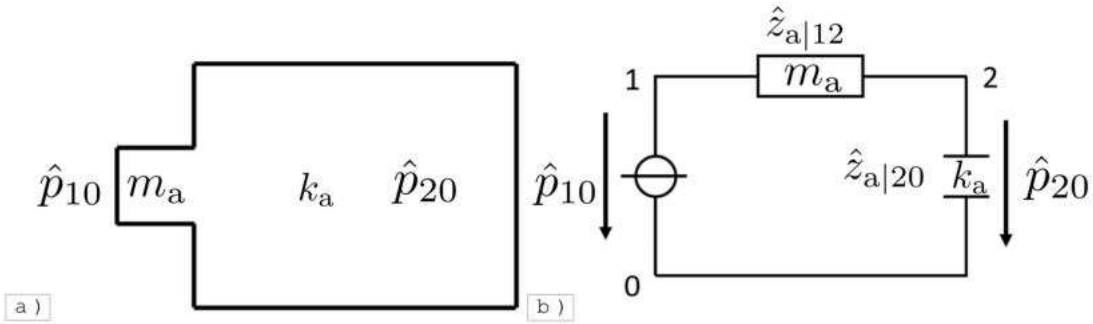

Figure 3.4: Helmholtz resonator in a vehicle. (a) Simplified system composed of rear vent with acoustical mass m_a and acoustical stiffness k_a (b) Equivalent circuit.

4 Hybrid strategy for coupling experimental and numerical normal modes

In this chapter, the most promising option for the investigation of aero-vibro-acoustic mechanisms in vehicles, particularly with regard to the low and medium frequency components, will be selected and improved. Please note that parts of this chapter have already been published in [48]. It is worth pointing out that the test body that was developed for this work and that will be discussed in detail in the following chapter was initially supposed to be dealt with strictly on the grounds of a numerical model presented in [177]. Due to the high computational effort as well as the expected practical effort for the generation of a reliable structural model, an alternative way to asses the issue has been sought (see also the experimental validation in [178]). Considering the explanations given in Sec. 2.4 and Sec. 2.5.3, and thus in accordance with the investigations in [178] or in Chap. 5, it is clearly apparent that the acoustic model can be represented fairly well by applying a FE model. Since experimental investigation of the acoustic cavity appears disadvantageous due to the high effort required to gain a sufficient number of acoustic FRF's, a hybrid variant consisting of a numerical model of the cavity and a mechanical model derived from measurement data appears optimal. In order to solve the aero-vibro-acoustic issue, it makes sense to investigate the hybrid methods described in Sec. 2.5.4 and Tab. 2.4 with regard to their individual advantages and disadvantages. The vibro-acoustic PTF method, which has been intensively explored in recent years, is in principle applicable for a hybrid formulation. However, it has a significant backdraw owing to the high computational effort and storage required to determine an acoustic dynamic stiffness matrix $\hat{\boldsymbol{Z}}_{\mathrm{a}}$ from the admittance matrix $\hat{\boldsymbol{Y}}_{\mathrm{a}}$. More specifically, the interior pressure at every node in the fluid must be determined for volume excitation at every coupling node (i.e. at every node at the interface between structure and fluid). Furthermore, the mechanical transfer functions determined according to Eq. (2.65) are only deterministic with a sufficiently large number of averages or a sufficiently long averaging time, and noise amplification can occur in the system due to the random character of the flow (Sec. 3.3). Thus, to avoid noise amplification, a power-based formulation relying on a 5D CPSD similar to Eq. (**??**) would be required, but this would involve enormous effort. It is also possible to use mechanical displacements as boundary conditions in the acoustic system, such as employed by Lee used in [12]. The method presented by Brandstätter in [19] considers the volume acceleration induced by the mechanical field as an acoustical volume source for the uncoupled acoustic system and thus neglects the considerable influence of mechanical flexibility on the acoustic cavity (compare with Sec. 2.5.3). Herpe's method [41] is not appropriate for the very low frequency range because of the geometric simplification of the interior cavity as a rectangular box. In addition, no geometric changes could be made to the acoustic field, and the significant influence of the rear bench [177] could not be taken into account. Modal-updating methods can be employed to improve an existing numerical mechanical or vibro-acoustic model, but this requires a great deal of effort and can only be used if a numerical model is already available [84, 110]. Finally, the method of modal coupling via numerically determined acoustic modes and experimentally determined mechanical modes presented by Kim [44] is available. This method combines the numerical advantages of the modal description (memory-saving and efficient due to diagonalised formulation) with the practical advantages of a hybrid formulation. Furthermore, the structural modes in the formulation

can be employed either by means of an experimental or numerical modal analysis. The applicability of modal substructuring for vehicle vibroacoustics is supported by numerous examples in the literature and therefore appears possible (see Sec. 2.4). A disadvantage of the method used by Kim is that here the nodes of the acoustic grid at the interface must correspond to the measuring points of the EMA. However, if one combines the method of normal-mode coupling with the method of non-conforming grids presented by Flemisch [179], the applicability of the method can be significantly extended. It hereby becomes possible to compute coupled modes from experimental or numerical uncoupled modes on arbitrary grids. These coupled modes provide a valuable diagonalization of the underlying system and can be employed to describe the vibro-acoustic response to internal (volume acceleration) or external (force, pressure) excitation.

4.1 Governing equations and finite element formulation

4.1.1 Mechanical system

The dynamical behavior of a mechanical system can be described using the temporally fourier transformed version of Navier's equations

$$-\rho_\mathrm{s}\omega^2\hat{\boldsymbol{u}}_\mathrm{s}(\boldsymbol{x},\omega) - \tilde{\boldsymbol{\nabla}}^T[\boldsymbol{c}]\tilde{\boldsymbol{\nabla}}\hat{\boldsymbol{u}}_\mathrm{s}(\boldsymbol{x},\omega) = \hat{\boldsymbol{f}}_\mathrm{s}(\boldsymbol{x},\omega), \tag{4.1}$$

where we have assumed a linear elastic material and small displacements. In Eq. (4.1), $\hat{\boldsymbol{u}}_\mathrm{s}(\boldsymbol{x},\omega)$ denotes mechanical displacement, ρ_s material density, $[\boldsymbol{c}]$ the stiffness tensor, ω angular frequency and $\hat{\boldsymbol{f}}_\mathrm{s}(\boldsymbol{x},\omega)$ the external volume force density. Strain tensor $[\hat{\boldsymbol{\epsilon}}_\mathrm{s}]$ and displacement vector $\hat{\boldsymbol{u}}_\mathrm{s}$ are related via $[\hat{\boldsymbol{\epsilon}}_\mathrm{s}] = \tilde{\boldsymbol{\nabla}}\hat{\boldsymbol{u}}_\mathrm{s} = ((\boldsymbol{\nabla}\hat{\boldsymbol{u}}_\mathrm{s}) + (\boldsymbol{\nabla}\hat{\boldsymbol{u}}_\mathrm{s})^T)/2$. We will start with an undamped mechanical system and incorporate damping on a modal basis later in the analysis. The weak formulation in Eq. (4.2) can be obtained by projecting on suitable test function $\boldsymbol{w}_\mathrm{s}(\boldsymbol{x})$. Note, that the weak formulation introduces the boundary traction $\hat{\boldsymbol{\sigma}}_\mathrm{n}(\boldsymbol{x},\omega)$ acting on the bounding surface Γ_s. The final weak form then reads

$$-\int_{\Omega_\mathrm{s}} \rho_\mathrm{s}\omega^2\boldsymbol{w}'(\boldsymbol{x})\hat{\boldsymbol{u}}_\mathrm{s}(\boldsymbol{x},\omega)d\Omega + \int_{\Omega_\mathrm{s}} \left(\tilde{\boldsymbol{\nabla}}\boldsymbol{w}'(\boldsymbol{x})\right)^T[\boldsymbol{c}]\tilde{\boldsymbol{\nabla}}\hat{\boldsymbol{u}}_\mathrm{s}(\boldsymbol{x},\omega)d\Omega = \int_{\Omega_\mathrm{s}} \boldsymbol{w}'(\boldsymbol{x})\hat{\boldsymbol{f}}_\mathrm{s}(\boldsymbol{x},\omega)d\Omega + \int_{\Gamma_\mathrm{s}} \boldsymbol{w}'(\boldsymbol{x})\hat{\boldsymbol{\sigma}}_\mathrm{n}(\boldsymbol{x},\omega)d\Gamma\,. \tag{4.2}$$

We define a matrix of N compactly supported (i.e. only on each element) node-centered ansatz functions $N_{\mathrm{s|j}}(\boldsymbol{x})$ centered at each node at position $\boldsymbol{x}_\mathrm{j}$ as

$$\boldsymbol{N}_{\mathrm{s|j}}(\boldsymbol{x}) = \begin{bmatrix} N_{\mathrm{s|j}}(\boldsymbol{x}) & 0 & 0 \\ 0 & N_{\mathrm{s|j}}(\boldsymbol{x}) & 0 \\ 0 & 0 & N_{\mathrm{s|j}}(\boldsymbol{x}) \end{bmatrix} \tag{4.3}$$

and by supposing that all variables can be expressed as a superposition of these node-centered ansatz functions with weighting vectors $\hat{\boldsymbol{u}}_{\mathrm{s|j}}$, $\hat{\boldsymbol{f}}_{\mathbf{s|j}}$ and $\hat{\boldsymbol{\sigma}}_{\mathbf{s|j}}$, it follows that

$$\hat{\boldsymbol{u}}_{\mathrm{s}}(\boldsymbol{x},\omega) = \sum_{j=1}^{N} \boldsymbol{N}_{\mathrm{s|j}}(\boldsymbol{x})\hat{\boldsymbol{u}}_{\mathrm{s|j}}\,, \tag{4.4}$$

$$\hat{\boldsymbol{f}}_{\mathrm{s}}(\boldsymbol{x},\omega) = \sum_{j=1}^{N} \boldsymbol{N}_{\mathrm{s|j}}(\boldsymbol{x})\hat{\boldsymbol{f}}_{\mathbf{s|j}} \tag{4.5}$$

and

$$\hat{\boldsymbol{\sigma}}_{\mathrm{n}}(\boldsymbol{x},\omega) = \sum_{j=1}^{N} \boldsymbol{N}_{\mathrm{s|j}}(\boldsymbol{x})\hat{\boldsymbol{\sigma}}_{\mathbf{s|j}}\,. \tag{4.6}$$

As typical for FE-formulations, the test function are equally assumed to be composed of ansatz functions alike with weights $\boldsymbol{w}_{\mathbf{s|k}}$ as

$$\boldsymbol{w}_{\mathrm{s}}(\boldsymbol{x}) = \sum_{k=1}^{N} \boldsymbol{N}_{\mathrm{s|k}}(\boldsymbol{x})\boldsymbol{w}_{\mathbf{s|k}}\,. \tag{4.7}$$

Substituting Eqs. (4.5) – (4.7) in Eq. (4.2) yields

$$\sum_{k=1}^{N} \boldsymbol{w}_{\mathbf{s|k}} \Bigg(\sum_{j=1}^{N} \int_{\Omega_{\mathrm{s}}} -\rho_{\mathrm{s}}\omega^2 \boldsymbol{N}_{\mathrm{s|k}}^{T}(\boldsymbol{x})\boldsymbol{N}_{\mathrm{s|j}}(\boldsymbol{x})\hat{\boldsymbol{u}}_{\mathrm{s|j}} d\Omega + \int_{\Omega_{\mathrm{s}}} \left(\tilde{\boldsymbol{\nabla}}\boldsymbol{N}_{\mathrm{s|k}}(\boldsymbol{x})\right)^{T}[\boldsymbol{c}]\tilde{\boldsymbol{\nabla}}\boldsymbol{N}_{\mathrm{s|j}}(\boldsymbol{x})\hat{\boldsymbol{u}}_{\mathrm{s|j}} d\Omega - \tag{4.8}$$

$$\int_{\Omega_{\mathrm{s}}} \boldsymbol{N}_{\mathrm{s|k}}^{T}(\boldsymbol{x})\hat{\boldsymbol{f}}_{\mathrm{s}}(\boldsymbol{x},\omega) d\Omega - \int_{\Gamma_{\mathrm{s}}} \sum_{j=1}^{N} \boldsymbol{N}_{\mathrm{s|k}}^{T}(\boldsymbol{x})\boldsymbol{N}_{\mathrm{s|j}}(\boldsymbol{x})\hat{\boldsymbol{\sigma}}_{\mathrm{n|j}} d\Gamma \Bigg) = 0\,. \tag{4.9}$$

Thanks to the compactly supported ansatz functions, the integrations can be performed over each element to arrive at element-wise mass and stiffness matrices $\boldsymbol{m}_{\mathrm{s|e}}$ and $\boldsymbol{k}_{\mathrm{s|e}}$ and element-wise forcing vectors $\hat{\boldsymbol{f}}_{\mathrm{s|e}}$ and $\hat{\boldsymbol{f}}_{\mathrm{b|e}}$ that can than be assembled in global mass and stiffness matrices $\boldsymbol{M}_{\mathrm{s}}$ and $\boldsymbol{K}_{\mathrm{s}}$ and global forcing vectors $\hat{\boldsymbol{f}}_{\mathrm{s}}$ and $\hat{\boldsymbol{f}}_{\mathrm{b}}$ as

$$\boldsymbol{M}_{\mathrm{s}} = \wedge_{e=1}^{n_{\mathrm{e}}} \boldsymbol{m}_{\mathrm{s|e}} \quad m_{\mathrm{s|ejk}} = \rho_{\mathrm{s}} \int_{\Omega_{\mathrm{s|e}}} \boldsymbol{N}_{\mathrm{s|k}}^{T}(\boldsymbol{x})\boldsymbol{N}_{\mathrm{s|j}}(\boldsymbol{x}) d\Omega\,, \tag{4.10}$$

$$\boldsymbol{K}_{\mathrm{s}} = \wedge_{e=1}^{n_{\mathrm{e}}} \boldsymbol{k}_{\mathrm{s|e}} \quad k_{\mathrm{s|ejk}} = \int_{\Omega_{\mathrm{s|e}}} \left(\tilde{\boldsymbol{\nabla}}\boldsymbol{N}_{\mathrm{s|k}}(\boldsymbol{x})\right)^{T}[\boldsymbol{c}]\tilde{\boldsymbol{\nabla}}\boldsymbol{N}_{\mathrm{s|j}}(\boldsymbol{x}) d\Omega\,, \tag{4.11}$$

$$\hat{\boldsymbol{f}}_{\mathrm{s}} = \wedge_{e=1}^{n_{\mathrm{e}}} \hat{\boldsymbol{f}}_{\mathrm{s|e}} \quad \hat{f}_{\mathrm{s|ek}} = \int_{\Omega_{\mathrm{s|e}}} \boldsymbol{N}_{\mathrm{s|k}}^{T}(\boldsymbol{x})\hat{\boldsymbol{f}}_{\mathrm{s}}(\boldsymbol{x},\omega) d\Omega \tag{4.12}$$

and

$$\hat{\boldsymbol{f}}_{\mathrm{b}} = \wedge_{e=1}^{n_{\mathrm{e}}} \hat{\boldsymbol{f}}_{\mathrm{b|e}} \quad \hat{f}_{\mathrm{b|ek}} = \int_{\Gamma_{\mathrm{s}}} \sum_{j=1}^{N} \boldsymbol{N}_{\mathrm{s|k}}^{T}(\boldsymbol{x})\boldsymbol{N}_{\mathrm{s|j}}(\boldsymbol{x})\hat{\boldsymbol{\sigma}}_{\mathrm{n|j}} d\Gamma\,. \tag{4.13}$$

The discretized mechanical system finally becomes

$$(-\boldsymbol{M}_{\mathrm{s}}\omega^2 + \boldsymbol{K}_{\mathrm{s}})\hat{\boldsymbol{u}}_{\mathrm{s}} = \hat{\boldsymbol{f}}_{\mathrm{s}} + \hat{\boldsymbol{f}}_{\mathrm{b}}\,. \tag{4.14}$$

A thorough investigation into the mechanical problem can be found in the book of Kaltenbacher [55] or the thesis of Davidsson [58].

4.1.2 Acoustical system

The distribution of acoustic pressure $\hat{p}_{\mathrm{a}}(\boldsymbol{x},\omega)$ in a cavity of speed of sound c_0 and mean density ρ_0 subject to external volume velocity sources $\hat{q}_{\mathrm{a}}(\boldsymbol{x},\omega)$ can be described through the Helmholtz-equation

$$(-\frac{\omega^2}{c_0^2}-\Delta)\hat{p}_{\mathrm{a}}(\boldsymbol{x},\omega)=\mathrm{i}\omega\rho_0\hat{q}_{\mathrm{a}}(\boldsymbol{x},\omega)\,. \tag{4.15}$$

Similarly to the mechanical system, we obtain the weak formulation by projecting on a continuous test function $w_{\mathrm{a}}(\boldsymbol{x})$

$$-\int_{\Omega_{\mathrm{a}}}\frac{\omega^2}{c_0^2}w_{\mathrm{a}}(\boldsymbol{x})\hat{p}_{\mathrm{a}}(\boldsymbol{x},\omega)d\Omega+\int_{\Omega_{\mathrm{a}}}\nabla w_{\mathrm{a}}(\boldsymbol{x})\nabla\hat{p}_{\mathrm{a}}(\boldsymbol{x},\omega)d\Omega= \int_{\Omega_{\mathrm{a}}}w_{\mathrm{a}}(\boldsymbol{x})\mathrm{i}\omega\rho_0\hat{q}_{\mathrm{a}}(\boldsymbol{x},\omega)d\Omega+\int_{\Gamma_{\mathrm{a}}}w_{\mathrm{a}}(\boldsymbol{x})\nabla\hat{p}_{\mathrm{a}}(\boldsymbol{x},\omega)\cdot\boldsymbol{n}d\Gamma\,. \tag{4.16}$$

Just as the boundary tractions in the mechanical formulation, an additional source term on the boundary surface Γ_{a} is introduced. The linearised conservation for momentum can be used to reformulate the boundary contribution in terms of the particle velocity $\hat{\boldsymbol{v}}_{\mathrm{a}}(\boldsymbol{x},\omega)$ as

$$\boldsymbol{n}\cdot\nabla\hat{p}_{\mathrm{a}}(\boldsymbol{x},\omega)=-\rho_0 i\omega\hat{\boldsymbol{v}}_{\mathrm{a}}(\boldsymbol{x},\omega)\cdot\boldsymbol{n} \tag{4.17}$$

and therefore

$$\int_{\Gamma_{\mathrm{a}}}w_{\mathrm{a}}(\boldsymbol{x})\nabla\hat{p}_{\mathrm{a}}(\boldsymbol{x},\omega)\boldsymbol{n}d\Gamma=-\int_{\Gamma_{\mathrm{a}}}w_{\mathrm{a}}(\boldsymbol{x})\rho_0 i\omega\hat{\boldsymbol{v}}_{\mathrm{a}}(\boldsymbol{x},\omega)\cdot\boldsymbol{n}d\Gamma=-\int_{\Gamma_{\mathrm{a}}}w_{\mathrm{a}}(\boldsymbol{x})\rho_0 i\omega\hat{v}_{\mathrm{an}}(\boldsymbol{x},\omega)d\Gamma\,. \tag{4.18}$$

By supposing that acoustic pressure, volume velocity, normal velocity and test function can be expressed as a superposition of node-centered ansatz functions $N_{\mathrm{a|j}}$ with weights $\hat{p}_{\mathrm{a|j}}$, $\hat{v}_{\mathrm{an|j}}$, $\hat{q}_{\mathrm{a|j}}$ and $w_{\mathrm{a|k}}$ as

$$\hat{p}_{\mathrm{a}}(\boldsymbol{x},\omega)=\sum_{j=1}^{N}N_{\mathrm{a|j}}(\boldsymbol{x})\hat{p}_{\mathrm{a|j}}\,, \tag{4.19}$$

$$\hat{q}_{\mathrm{a}}(\boldsymbol{x},\omega)=\sum_{j=1}^{N}N_{\mathrm{a|j}}(\boldsymbol{x})\hat{q}_{\mathrm{a|j}}\,, \tag{4.20}$$

$$\hat{v}_{\mathrm{an}}(\boldsymbol{x},\omega)=\sum_{j=1}^{N}N_{\mathrm{a|j}}(\boldsymbol{x})\hat{v}_{\mathrm{an|j}}\,, \tag{4.21}$$

and

$$w_{\mathrm{a}}(\boldsymbol{x})=\sum_{k=1}^{N}N_{\mathrm{a|k}}(\boldsymbol{x})w_{\mathrm{a|k}}\,, \tag{4.22}$$

then Eq. (4.16) can be rewritten according to

$$\sum_{k=1}^{N}w_{\mathrm{a|k}}\Bigg(\sum_{j=1}^{N}\Big(\int_{\Omega_{\mathrm{a}}}\frac{-\omega^2}{c_0^2}N_{\mathrm{a|k}}(\boldsymbol{x})N_{\mathrm{a|j}}(\boldsymbol{x})\hat{p}_{\mathrm{a|j}}d\Omega+\int_{\Omega_{\mathrm{a}}}\nabla N_{\mathrm{a|k}}(\boldsymbol{x})\nabla N_{\mathrm{a|j}}(\boldsymbol{x})\hat{p}_{\mathrm{a|j}}d\Omega\Big)- \tag{4.23}$$

$$\int_{\Omega_{\mathrm{a}}}N_{\mathrm{a|k}}(\boldsymbol{x})i\omega\rho_0\hat{q}_{\mathrm{a}}(\boldsymbol{x},\omega)d\Omega+\int_{\Gamma_{\mathrm{a}}}\sum_{j=1}^{N}N_{\mathrm{a|k}}(\boldsymbol{x})N_{\mathrm{a|j}}(\boldsymbol{x})\rho_0 i\omega\hat{v}_{\mathrm{an|j}}\boldsymbol{n}d\Gamma=0\Bigg)\,. \tag{4.24}$$

By element-wise integration and a FE assembling procedure the discrete matrices can be obtained according to

$$\underline{\boldsymbol{M}}_{\mathrm{a}} = \wedge_{e=1}^{n_{\mathrm{e}}} \underline{\boldsymbol{m}}_{\mathrm{a|e}} \quad \underline{m}_{\mathrm{a|ejk}} = \frac{1}{\rho_0} \int_{\Omega_{\mathrm{a|e}}} \frac{1}{c_0^2} N_{\mathrm{a|k}}(\boldsymbol{x}) N_{\mathrm{a|j}}(\boldsymbol{x}) d\Omega \tag{4.25}$$

$$\underline{\boldsymbol{K}}_{\mathrm{a}} = \wedge_{e=1}^{n_{\mathrm{e}}} \underline{\boldsymbol{k}}_{\mathrm{a|e}} \quad \underline{k}_{\mathrm{a|ejk}} = \frac{1}{\rho_0} \int_{\Omega_{\mathrm{a|e}}} \nabla N_{\mathrm{a|k}}(\boldsymbol{x}) \nabla N_{\mathrm{a|j}}(\boldsymbol{x}) d\Omega \tag{4.26}$$

$$\hat{\boldsymbol{q}}_{\mathrm{a}} = \wedge_{e=1}^{n_{\mathrm{e}}} \hat{\boldsymbol{q}}_{\mathrm{a|e}} \quad \hat{q}_{\mathrm{a|ek}} = \int_{\Omega_{\mathrm{a|e}}} N_{\mathrm{a|k}}(\boldsymbol{x}) \hat{q}_{\mathrm{a}}(\boldsymbol{x}, \omega) d\Omega \tag{4.27}$$

$$\hat{\boldsymbol{q}}_{\mathrm{b}} = \wedge_{e=1}^{n_{\mathrm{e}}} \hat{\boldsymbol{q}}_{\mathrm{b|e}} \quad \hat{q}_{\mathrm{b|ek}} = \int_{\Gamma_{\mathrm{a|e}}} \sum_{j=1}^{N} N_{\mathrm{a|k}}(\boldsymbol{x}) N_{\mathrm{a|j}}(\boldsymbol{x}) \hat{v}_{\mathrm{an}} d\Gamma \,, \tag{4.28}$$

to finally obtain the discretized acoustic system to

$$(-\underline{\boldsymbol{M}}_{\mathrm{a}} \omega^2 + \underline{\boldsymbol{K}}_{\mathrm{a}}) \hat{\boldsymbol{p}}_{\mathrm{a}} = i\omega \hat{\boldsymbol{q}}_{\mathrm{a}} - i\omega \hat{\boldsymbol{q}}_{\mathrm{b}} \,. \tag{4.29}$$

Note that the acoustic mass and stiffness matrices $\underline{\boldsymbol{M}}_{\mathrm{a}}$ and $\underline{\boldsymbol{K}}_{\mathrm{a}}$ have been divided by ambient density ρ_0 to express the acoustic pressure $\hat{\boldsymbol{p}}_{\mathrm{a}}$ subject to the volume velocity source $\hat{\boldsymbol{q}}_{\mathrm{a}}$ and the boundary source $\hat{\boldsymbol{q}}_{\mathrm{b}}$ (compare with Tab. 2.1). The system matrices are displayed in underlined fashion because they do not represent mass and stiffness coefficients in terms of acoustic dynamic stiffness ($\hat{\boldsymbol{Z}}_{\mathrm{a}} = -\omega^2 \boldsymbol{M}_{\mathrm{a}} + \boldsymbol{K}_{\mathrm{a}}$) but rather in terms of acoustic admittance ($\hat{\boldsymbol{Y}}_{\mathrm{a}} = -\omega^2 \underline{\boldsymbol{M}}_{\mathrm{a}} + \underline{\boldsymbol{K}}_{\mathrm{a}}$) (see [15] or App. A). This is the acoustic equivalent of mechanical systems, in which experimental data is obtained in terms of mechanical admittance $\hat{Y}_{\mathrm{s}}$ while the FE system is described in terms of mechanical dynamic stiffness $\hat{Z}_{\mathrm{s}}$.

4.1.3 Coupled vibro-acoustic system

A vibro-acoustic system contains a mechanical structure coupled to an acoustic domain through an interface Γ_{c}. Interface conditions are naturally enforced to satisfy continuity of momentum and displacement. These interface conditions can be described through mechanical normal stresses and pressure on the one hand, and mechanical velocity and acoustic particle velocity on the other hand

$$\hat{\boldsymbol{\sigma}}_{\mathrm{n}}(\boldsymbol{x}, \omega) = -\boldsymbol{n}(\boldsymbol{x}) \hat{p}_{\mathrm{a}}(\boldsymbol{x}, \omega) \quad \text{and} \tag{4.30}$$

$$\hat{\boldsymbol{v}}_{\mathrm{a}}(\boldsymbol{x}, \omega) = \hat{\boldsymbol{v}}_{\mathrm{s}}(\boldsymbol{x}, \omega) = i\omega \hat{\boldsymbol{u}}_{\mathrm{s}}(\boldsymbol{x}, \omega) \quad \text{for} \quad \mathrm{x} \in \Gamma_{\mathrm{c}} \,. \tag{4.31}$$

By replacing the boundary traction vector $\hat{\boldsymbol{\sigma}}_{\mathrm{n}}(\boldsymbol{x}, \omega)$ in Eq. (4.17) and the boundary velocities $\hat{\boldsymbol{v}}_{\mathrm{a}}(\boldsymbol{x}, \omega)$ in Eq. (4.16) via $\hat{p}_{\mathrm{a}}(\boldsymbol{x}, \omega)$ and $\hat{\boldsymbol{u}}_{\mathrm{s}}$ in Eq. (4.31), one may derive the weak formulation of the strongly coupled vibro-acoustic problem. Instead, we directly formulate the mechanical boundary source term $\hat{\boldsymbol{f}}_{\mathrm{c}}$ induced through counteracting acoustic pressure, as well as the acoustic boundary source term $\hat{\boldsymbol{q}}_{\mathrm{c}}$ induced by enforced mechanical displacement. To obtain the algebraic acoustic volume source vector $\hat{\boldsymbol{q}}_{\mathrm{c}}$, a few steps are required. To begin with, the continuous mechanical displacement vector $\hat{\boldsymbol{u}}_{\mathrm{s}}(\boldsymbol{x}, \omega)$ is expressed as a superposition of a matrix of node-centered mechanical test function $\boldsymbol{N}_{\mathrm{s|j}}(\boldsymbol{x})$ weighted with discrete nodal displacement vectors $\hat{\boldsymbol{u}}_{\mathrm{s|j}}$. The source contribution on node k of element e can then be obtained by projecting the normal component of displacement on an acoustic test function $N_{\mathrm{a|k}}(\boldsymbol{x})$ over the element area $\Gamma_{\mathrm{c|e}}$. The algebraic acoustic volume source vector $\hat{\boldsymbol{q}}_{\mathrm{c}}$ can then be obtained by assembling the element-wise components of $\hat{\boldsymbol{q}}_{\mathrm{c|e}}$

$$\hat{\boldsymbol{q}}_{\mathrm{c}} = \wedge_{e=1}^{n_{\mathrm{e}}} \hat{\boldsymbol{q}}_{\mathrm{c|e}} \quad \hat{q}_{\mathrm{c|ek}} = \int_{\Gamma_{\mathrm{c}|e}} \sum_{j=1}^{N} N_{\mathrm{a|k}}(\boldsymbol{x}) \boldsymbol{N}_{\mathrm{s|j}}(\boldsymbol{x}) \mathrm{i}\omega \hat{\boldsymbol{u}}_{\mathrm{s|j}} \cdot \boldsymbol{n}(\boldsymbol{x}) d\Gamma. \tag{4.32}$$

The algebraic boundary force vector $\hat{\boldsymbol{f}}_{\mathrm{c}}$ can be obtained in a similar fashion

$$\hat{\boldsymbol{f}}_{\mathrm{c}} = \wedge_{e=1}^{n_{\mathrm{e}}} \hat{\boldsymbol{f}}_{\mathrm{c|e}} \quad \hat{f}_{\mathrm{c|ek}} = -\int_{\Gamma_{\mathrm{c}}} \sum_{j=1}^{N} \boldsymbol{N}_{\mathrm{s|k}}^{T}(\boldsymbol{x}) N_{\mathrm{a|j}}(\boldsymbol{x}) \boldsymbol{n}(\boldsymbol{x}) \hat{p}_{\mathrm{a|j}} d\Gamma. \tag{4.33}$$

In practice, the terms in Eq. (4.32) and Eq. (4.33) are unknown at this stage. It makes therefore sense to explicitly assemble the coupling matrix $\boldsymbol{H}_{\mathrm{as}}$

$$\boldsymbol{H}_{\mathrm{as}} = \wedge_{e=1}^{n_{\mathrm{e}}} \boldsymbol{h}_{\mathrm{as|e}} \quad \boldsymbol{h}_{\mathrm{as|ejk}} = \int_{\Gamma_{\mathrm{c}}} N_{\mathrm{a|k}}(\boldsymbol{x}) \boldsymbol{N}_{\mathrm{s|j}}(\boldsymbol{x}) \boldsymbol{n}(\boldsymbol{x}) d\Gamma = \tag{4.34}$$

$$\int_{\Gamma_{\mathrm{c}}} \begin{bmatrix} N_{\mathrm{a|k}}(\boldsymbol{x}) N_{\mathrm{s|j}}(\boldsymbol{x}) n_{\mathrm{x}}(\boldsymbol{x}) \\ N_{\mathrm{a|k}}(\boldsymbol{x}) N_{\mathrm{s|j}}(\boldsymbol{x}) n_{\mathrm{y}}(\boldsymbol{x}) \\ N_{\mathrm{a|k}}(\boldsymbol{x}) N_{\mathrm{s|j}}(\boldsymbol{x}) n_{\mathrm{z}}(\boldsymbol{x}) \end{bmatrix} d\Gamma \tag{4.35}$$

to arrive at discrete relations between unknown variable $\hat{\boldsymbol{q}}_{\mathrm{c}}$ and boundary source $\hat{\boldsymbol{u}}_{\mathrm{s}}$

$$\hat{\boldsymbol{q}}_{\mathrm{c}} = \boldsymbol{H}_{\mathrm{as}} \mathrm{i}\omega \hat{\boldsymbol{u}}_{\mathrm{s}}. \tag{4.36}$$

Proceeding analogously for Eq. (4.33) yields $\boldsymbol{H}_{\mathrm{sa}}$. The mechanical force vector $\hat{\boldsymbol{f}}_{\mathrm{c}}$ due to acoustic pressure $\hat{\boldsymbol{p}}_{\mathrm{a}}$ may be expressed by

$$\hat{\boldsymbol{f}}_{\mathrm{c}} = \boldsymbol{H}_{\mathrm{sa}} \hat{\boldsymbol{p}}_{\mathrm{a}}. \tag{4.37}$$

By comparing Eq. (4.32) and Eq. (4.33) it can be shown that the coupling matrices are related according to

$$\boldsymbol{H}_{\mathrm{as}} = \boldsymbol{H}_{\mathrm{sa}}^{T} = \boldsymbol{H}. \tag{4.38}$$

We employ $\boldsymbol{H}$ to express the strongly coupled structural-acoustic equations

$$(-\boldsymbol{M}_{\mathrm{s}}\omega^2 + \boldsymbol{K}_{\mathrm{s}}) \hat{\boldsymbol{u}}_{\mathrm{s}} = \hat{\boldsymbol{f}}_{\mathrm{s}} + \boldsymbol{H} \hat{\boldsymbol{p}}_{\mathrm{a}} \tag{4.39}$$

$$(-\underline{\boldsymbol{M}}_{\mathrm{a}}\omega^2 + \underline{\boldsymbol{K}}_{\mathrm{a}}) \hat{\boldsymbol{p}}_{\mathrm{a}} = \mathrm{i}\omega \hat{\boldsymbol{q}}_{\mathrm{a}} + \omega^2 \boldsymbol{H}^{T} \hat{\boldsymbol{u}}_{\mathrm{s}} \tag{4.40}$$

and rearrange the equations to arrive at a matrix formulation

$$\begin{bmatrix} -\omega^2 \boldsymbol{M}_{\mathrm{s}} + \boldsymbol{K}_{\mathrm{s}} & -\boldsymbol{H} \\ -\omega^2 \boldsymbol{H}^{T} & -\omega^2 \underline{\boldsymbol{M}}_{\mathrm{a}} + \underline{\boldsymbol{K}}_{\mathrm{a}} \end{bmatrix} \begin{bmatrix} \hat{\boldsymbol{u}}_{\mathrm{s}} \\ \hat{\boldsymbol{p}}_{\mathrm{a}} \end{bmatrix} = \begin{bmatrix} \hat{\boldsymbol{f}}_{\mathrm{s}} \\ i\omega \hat{\boldsymbol{q}}_{\mathrm{a}} \end{bmatrix}. \tag{4.41}$$

The equation provided here is commonly used to handle strongly coupled vibro-acoustic problems numerically. However, as stated in the introduction, this study demonstrates a novel way for combining experimental and numerical modes using non-conforming grids. For the sake of completeness we briefly include the essential theory about modal decomposition.

4.1.4 Eigenvalue decomposition

The theory of eigenvalue decomposition is well established and may in detail be found in e.g [8]. For a given stiffness $\boldsymbol{K}$ and mass matrix $\boldsymbol{M}$ one can obtain the corresponding eigenvalues λ_{r} and eigenvectors $\boldsymbol{\psi}_{\mathrm{r}}$ by solving the eigenvalue problem

$$(\boldsymbol{K} - \lambda_{\mathrm{r}} \boldsymbol{M}) \boldsymbol{\psi}_{\mathrm{r}} = \boldsymbol{0}. \tag{4.42}$$

It is now possible to express the spatial unknown $\hat{\boldsymbol{x}}$ as a linear combination of modes weighted by corresponding participation factors. Collecting all modes column-wise in a mode matrix $\boldsymbol{\Psi}$ and the

participation factors in a participation vector $\tilde{\boldsymbol{x}}$ yields

$$\hat{\boldsymbol{x}} = \boldsymbol{\Psi}\tilde{\boldsymbol{x}}\,. \tag{4.43}$$

The discrete equation system containing mass and stiffness matrices as well as a forcing vector $\hat{\boldsymbol{f}}$ can be diagonalized by substituting $\hat{\boldsymbol{x}}$ and projecting on the set of modes through

$$\boldsymbol{\Psi}^T(-\boldsymbol{M}\omega^2 + \boldsymbol{K})\boldsymbol{\Psi}\tilde{\boldsymbol{x}} = \boldsymbol{\Psi}^T\hat{\boldsymbol{f}}\,. \tag{4.44}$$

We employ mass normalised eigenvectors to arrive at the normalized modal problem

$$(-\boldsymbol{I}\omega^2 + \boldsymbol{\Lambda})\tilde{\boldsymbol{x}} = \tilde{\boldsymbol{f}}, \tag{4.45}$$

where $\boldsymbol{\Lambda}$ is a diagonal matrix containing the corresponding eigenvalues. For each decoupled equation, modal damping ζ_i may be taken into account by adding a damping term according to

$$\tilde{m}_\mathrm{i}(-\omega^2 + 2\mathrm{i}\omega\zeta_\mathrm{i}\omega_\mathrm{i} + \omega_\mathrm{i}^2)\tilde{x}_\mathrm{i} = \tilde{f}_\mathrm{i}. \tag{4.46}$$

The procedure described above can be used to express the uncoupled mechanical problem in Eq. (4.14) (without boundary forces) in terms of modal displacements $\tilde{\boldsymbol{u}}_\mathrm{s}$, modal forcing $\tilde{\boldsymbol{f}}_\mathrm{s}$, mechanical eigenvalues $\boldsymbol{\Lambda}_\mathrm{s}$ and structural modal damping $\boldsymbol{\zeta}_\mathrm{s}$ by

$$(-\boldsymbol{I}\omega^2 + 2\boldsymbol{\zeta}_\mathrm{s}\sqrt{\boldsymbol{\Lambda}_\mathrm{s}}\mathrm{i}\omega + \boldsymbol{\Lambda}_\mathrm{s})\tilde{\boldsymbol{u}}_\mathrm{s} = \tilde{\boldsymbol{f}}_\mathrm{s}. \tag{4.47}$$

Similarly, the uncoupled acoustic problem in Eq. (4.29) can be written in terms of modal pressure $\tilde{\boldsymbol{p}}_\mathrm{a}$, modal volume sources $\tilde{\boldsymbol{q}}_\mathrm{a}$, acoustic eigenvalues $\boldsymbol{\Lambda}_\mathrm{a}$ and acoustic modal damping $\boldsymbol{\zeta}_\mathrm{a}$ by

$$(-\boldsymbol{I}\omega^2 + 2\boldsymbol{\zeta}_\mathrm{a}\sqrt{\boldsymbol{\Lambda}_\mathrm{a}}\mathrm{i}\omega + \boldsymbol{\Lambda}_\mathrm{a})\tilde{\boldsymbol{p}}_\mathrm{a} = \tilde{\boldsymbol{q}}_\mathrm{a}. \tag{4.48}$$

The coupled modes can be determined similarly to the approach outlined above for uncoupled mechanical or acoustic systems. For this purpose, the vibro-acoustic system shown in Eq. (4.41) can be formulated in terms of generalized displacements $\hat{\boldsymbol{d}}$ and generalized forces $\hat{\boldsymbol{f}}$ by concatenating the individual vectors to

$$\hat{\boldsymbol{d}} = \begin{bmatrix}\hat{\boldsymbol{u}}_\mathrm{s}\\ \hat{\boldsymbol{p}}_\mathrm{a}\end{bmatrix} \quad \text{and} \quad \hat{\boldsymbol{f}} = \begin{bmatrix}\hat{\boldsymbol{f}}_\mathrm{s}\\ \hat{\boldsymbol{q}}_\mathrm{a}\end{bmatrix}\,. \tag{4.49}$$

By additionally combining the submatrices in Eq. (4.41) to a generalized system matrix $\hat{\boldsymbol{T}}$, the coupled system reads

$$\hat{\boldsymbol{T}}\hat{\boldsymbol{d}} = \hat{\boldsymbol{f}}\,. \tag{4.50}$$

The usual eigenvalue decomposition in Eqs. (4.42)-(4.44) applies only in case of hermitian-symmetric matrices, which is not the case in Eq. (4.41). An eigenvalue decomposition of non-symmetric problems affords the solution of two related eigenvalue problems to obtain left and right eigenvectors $\boldsymbol{\psi}_{\mathrm{L|k}}$ and $\boldsymbol{\psi}_\mathrm{k}$. Regarding the structural-acoustic problem, it can be shown (e.g. [92]) that the left eigenvectors can be obtained from the corresponding right eigenvectors by scaling the acoustic components with the coupled eigenvalues λ_k as

$$\boldsymbol{\psi}_{\mathrm{cL|k}} = \begin{bmatrix}\boldsymbol{\psi}_{\mathrm{cLs|k}}\\ \boldsymbol{\psi}_{\mathrm{cLa|k}}\end{bmatrix} = \begin{bmatrix}1 & 0\\ 0 & 1/\lambda_\mathrm{k}\end{bmatrix}\begin{bmatrix}\boldsymbol{\psi}_{\mathrm{cs|k}}\\ \boldsymbol{\psi}_{\mathrm{ca|k}}\end{bmatrix}\,. \tag{4.51}$$

These left and right eigenvectors can now be assembled in mode shape matrices $\boldsymbol{\Psi}_{\mathrm{cL}}$ and $\boldsymbol{\Psi}_{\mathrm{c}}$ to diagonalize the original problem

$$\boldsymbol{\Psi}_{\mathrm{cL}}^{T}\hat{\boldsymbol{T}}\boldsymbol{\Psi}_{\mathrm{c}}\hat{\boldsymbol{d}} = \boldsymbol{\Psi}_{\mathrm{cL}}^{T}\hat{\boldsymbol{f}}\,. \tag{4.52}$$

The diagonal set of equations can now be written in terms of a generalized modal system matrix $\tilde{\boldsymbol{T}}$ relating generalized modal displacements $\tilde{\boldsymbol{d}}$ and forces $\tilde{\boldsymbol{f}}$ as

$$\tilde{\boldsymbol{T}}\tilde{\boldsymbol{d}} = \tilde{\boldsymbol{f}}\,. \tag{4.53}$$

In a subsequent step, mass-normalized mode shapes $\boldsymbol{\psi}_{\mathrm{s|i}}$ can be obtained and aligned column-wise in a mode shape matrix $\boldsymbol{\Psi}_{\mathrm{s}}$. We have now obtained a modal description of the mechanical system that can be processed analogously to modes obtained in a FE-framework. In case of acoustic modal extraction, the FRF vector contains measured dynamic stiffness spectra $\hat{z}_{\mathrm{i}}(\omega)$ relating measured pressure $\hat{p}_{\mathrm{i}}(\omega)$ and volume acceleration $i\omega\hat{q}_{\mathrm{f}}(\omega)$ (for more details, see [15]).

4.2 Normal mode coupling via non-conforming grids

The strong influence of boundary conditions complicates the treatment of vibro-acoustic problems at low frequencies. An appropriate representation of the boundary situation requires extensive modelling effort or the use of experimental measurement data to tune the simulation model towards desired physical behavior. The use of a modal method makes perfect sense given the numerous advantages of the modal system description in the low frequency range. In a low density medium, such as air, the coupled problem can usually be diagonalized using the uncoupled mechanical and acoustic modes. The concept of coupling experimentally measured mechanical modes with simulated acoustic modes presented here is based on an original work of Kim [44]. In this work, experimental structural modes were coupled with simulated acoustic modes by positioning the measurement points at the nodes of the acoustic grid. Generalizing this work to be able to deal with arbitrary measurement grids requires a reliable treatment of coarsely sampled non-conforming grids. After a brief review of modal substructuring theory, we demonstrate how radial basis functions can be used in combination with non-conforming grids to adress weakly coupled vibro-acoustic systems based on experimental or numerical modes discretized on point clouds.

4.2.1 Normal mode substructuring

Alternatively to the direct approach based on the coupled FE description shown in Eq. (4.41), vibro-acoustic modes can also be obtained by employing their respective uncoupled modes. This is only possible if the boundary constraints can be relaxed, i.e. if the coupled mechanical displacements and pressures can be adequately represented as a superposition of weighted uncoupled modes, which is often appropriate if air is the acoustic medium. Following this assumption each coupled mode can be expressed as a superposition of uncoupled structural and acoustic mode shape matrices scaled with coefficients of a modal eigenvector $\boldsymbol{\theta}_{\mathrm{i}}$. For that purpose we introduce the matrix of uncoupled modes $\boldsymbol{\Psi}_{\mathrm{sa}}$ by horizontally concatenating the uncoupled modes according to $\boldsymbol{\Psi}_{\mathrm{sa}} = [\boldsymbol{\Psi}_{\mathrm{s}}, \boldsymbol{\Psi}_{\mathrm{a}}]$. Note that acoustical degrees of freedom are zero for mechanical modes and vice versa. The aforementioned assumption indicates that each coupled mode shape $\boldsymbol{\psi}_{\mathrm{c|i}}$ can be expressed by weighting the uncoupled mode matrix with a modal eigenvector according to

$$\boldsymbol{\psi}_{\mathrm{c|i}} = \boldsymbol{\Psi}_{\mathrm{sa}}\boldsymbol{\theta}_{\mathrm{i}} \tag{4.54}$$

By introducing right and left modal shape matrices $\boldsymbol{\Theta}$ and $\boldsymbol{\Theta}_{\mathrm{L}}$ it follows that the vibro-acoustic modes can be expressed as

$$\boldsymbol{\Psi}_{\mathrm{c}} = \boldsymbol{\Psi}_{\mathrm{sa}}\boldsymbol{\Theta} \quad \text{and} \quad \boldsymbol{\Psi}_{\mathrm{cL}} = \boldsymbol{\Psi}_{\mathrm{sa}}\boldsymbol{\Theta}_{\mathrm{L}}\,. \tag{4.55}$$

Substituting Eq. (4.55) in Eq. (4.52) yields

$$\boldsymbol{\Theta}_{\mathrm{L}}^{T}\boldsymbol{\Psi}_{\mathrm{sa}}^{T}\hat{\boldsymbol{T}}\boldsymbol{\Psi}_{\mathrm{sa}}\boldsymbol{\Theta}\tilde{\boldsymbol{d}} = \boldsymbol{\Theta}_{\mathrm{L}}^{T}\boldsymbol{\Psi}^{T}\hat{\boldsymbol{f}}\,. \tag{4.56}$$

Now, we can introduce the modal coupling matrix $\tilde{\boldsymbol{H}}$ as

$$\tilde{\boldsymbol{H}} = \boldsymbol{\Psi}_{\mathrm{s}}^{T}\boldsymbol{H}\boldsymbol{\Psi}_{\mathrm{a}} \tag{4.57}$$

and the modal parameter matrix $\tilde{\boldsymbol{T}}$ as

$$\tilde{\boldsymbol{T}} = \boldsymbol{\Psi}_{\mathrm{sa}}^{T}\hat{\boldsymbol{T}}\boldsymbol{\Psi}_{\mathrm{sa}} = \begin{bmatrix} -\omega^2 + 2\boldsymbol{\zeta}_{\mathrm{s}}\sqrt{\boldsymbol{\Lambda}_{\mathrm{s}}}s + \boldsymbol{\Lambda}_{\mathrm{s}} & -\tilde{\boldsymbol{H}} \\ -\tilde{\boldsymbol{H}}^{T}\omega^2 & -\omega^2 + 2\boldsymbol{\zeta}_{\mathrm{a}}\sqrt{\boldsymbol{\Lambda}_{\mathrm{a}}}s + \boldsymbol{\Lambda}_{\mathrm{a}} \end{bmatrix}. \tag{4.58}$$

The mechanical and acoustic submatrices of $\tilde{\boldsymbol{T}}$ can either be obtained by solving the corresponding decoupled mechanical and acoustical eigenvalue problems computationally or via experimental modal analysis. The modal coupling matrix $\tilde{\boldsymbol{H}}$ can be acquired by computing the coupling matrices between adjacent surfaces and subsequent projection. Under the assumption of sufficiently small modal damping the postulated left and right modal shape matrices $\boldsymbol{\Theta}$ and $\boldsymbol{\Theta}_{\mathrm{L}}$ can indeed be evaluated by employing the modal mass and stiffness matrices

$$\tilde{\boldsymbol{M}} = \begin{bmatrix} \boldsymbol{I}_{\mathrm{s}} & \boldsymbol{0} \\ \tilde{\boldsymbol{H}}^{T} & \boldsymbol{I}_{\mathrm{a}} \end{bmatrix} \quad \text{and} \quad \tilde{\boldsymbol{K}} = \begin{bmatrix} \boldsymbol{\Lambda}_{\mathrm{s}} & -\tilde{\boldsymbol{H}} \\ \boldsymbol{0} & \boldsymbol{\Lambda}_{\mathrm{a}} \end{bmatrix} \tag{4.59}$$

to solve the right and left eigenvalue problems

$$(-\lambda_i\tilde{\boldsymbol{M}} + \tilde{\boldsymbol{K}})\boldsymbol{\theta} = \boldsymbol{0} \quad \text{and} \quad (-\lambda_i\tilde{\boldsymbol{M}}^{T} + \tilde{\boldsymbol{K}}^{T})\boldsymbol{\theta}_{\mathrm{L}} = \boldsymbol{0}\,. \tag{4.60}$$

and concatenating the resulting modes column-wise. The coupled right and left structural-acoustic modes $\boldsymbol{\Psi}_{\mathrm{c}}$ and $\boldsymbol{\Psi}_{\mathrm{cL}}$ can then be assembled according to Eq. (4.55). For a harmonic problem, it is convenient to solve

$$\tilde{\boldsymbol{T}}\tilde{\boldsymbol{d}} = \tilde{\boldsymbol{f}} \quad \text{with} \quad \tilde{\boldsymbol{f}} = [\tilde{\boldsymbol{f}}_{\mathrm{s}}; \boldsymbol{0}] \tag{4.61}$$

for every frequency and to reconstruct the displacement and pressure vector in $\hat{\boldsymbol{d}}$ according to

$$\hat{\boldsymbol{d}} = \boldsymbol{\Psi}_{\mathrm{c}}\tilde{\boldsymbol{d}}\,. \tag{4.62}$$

If the generalized modal displacements $\tilde{\boldsymbol{d}}$ are of interest, one can evaluate the undamped mode shape matrix $\boldsymbol{\Psi}$ and the generalized displacement vector $\hat{\boldsymbol{d}}$ first and obtain $\tilde{\boldsymbol{d}}$ through

$$\boldsymbol{\Psi}_{\mathrm{c}}\tilde{\boldsymbol{d}} = \hat{\boldsymbol{d}}\,. \tag{4.63}$$

The coupled modal damping factors can then be extracted from $\tilde{\boldsymbol{d}}$. The limitations of this approach lie in the assumption that the coupled modes need to be expressible as a superposition of undistorted mechanical and acoustic mode shapes. It has been shown by Davidsson [58], that the structural displacement error induced by normal mode coupling is most pronounced near acoustically dominated modes. This appears natural considering that the pressure distribution within the cavity is controlled by the shape of the

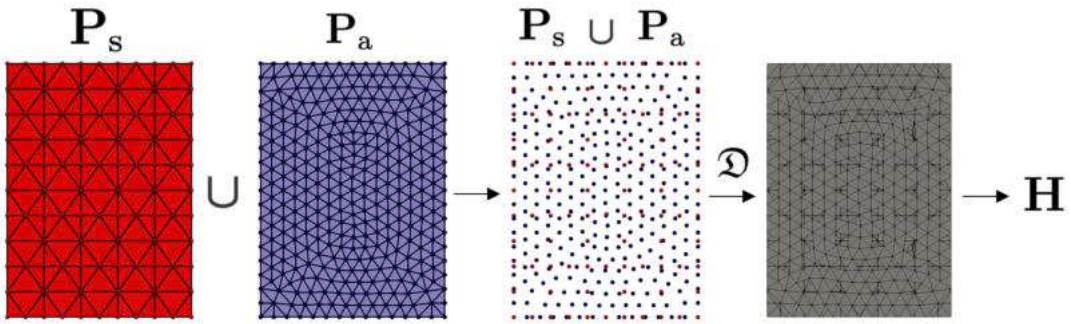

Figure 4.1: Calculation of coupling matrices on non-conforming interface via intersection grid.

acoustic mode and that the resultant mechanical stresses are only partially reproduced by the supplied mechanical modes. Due to the incomplete continuity of acoustic particle velocity across the interface, the acoustic pressure field near structurally dominated modes exhibits the opposite effect. However, when it comes to low-frequency noise in air-filled cavities, the many advantages of normal-mode coupling may frequently exceed the associated inaccuracies, particularly when it comes to numerical models of complex vibro-acoustic structures.

4.2.2 Determination of coupling matrices for non-conforming grids

Regarding a general setup with arbitrary measurement positions we investigate in the calculation of modal coupling matrices for acoustic and structural modes defined on a set of surface nodes $\boldsymbol{x}_\mathrm{a} \in \boldsymbol{P}_\mathrm{a} \subset \Gamma_\mathrm{a}$ and $\boldsymbol{x}_\mathrm{s} \in \boldsymbol{P}_\mathrm{s} \subset \Gamma_\mathrm{s}$ with corresponding (not necessarily predefined) grids. In order to obtain the coupling matrix $\boldsymbol{H}_\mathrm{i}$ between adjacent node sets $\boldsymbol{P}_{\mathrm{a|i}}$ and $\boldsymbol{P}_{\mathrm{s|i}}$ a continuous description in terms of suitable test functions $N_{\mathrm{a|k}}(\boldsymbol{x})$ and $\boldsymbol{N}_{\mathrm{s|j}}(\boldsymbol{x})$ on the respective grids is required. In case a suitable grid is not yet available (e.g. measurement positions), it can be obtained by employing a Delaunay-triangulation $\mathfrak{D}$ on the corresponding node set. Algorithms to obtain a 2D-Delaunay triangulation are available and sufficiently robust to obtain the connectivity matrix for a set of triangles covering the parent surface Γ [180]. In case the employed grids are non-conforming, the coupling matrix can be assembled by integrating on a so called intersection grid (see Fig. 4.1). In this approach, the union of the two point clouds $\boldsymbol{P}_\mathrm{s}$ and $\boldsymbol{P}_\mathrm{a}$ is formed. The resulting point cloud is then triangulated and the coupling integrals on the resulting conforming subgrid are evaluated according to Eq. (4.35). The non-conforming coupling matrix $\boldsymbol{H}_\mathrm{as}$ can then be obtained on each element by summing the contributions of the corresponding sub-elements. More details on the construction of intersection grids can be found in the publication by Flemisch et al. [179]. Note that the problem of solving the coupled vibro-acoustic equation in Eq. (4.41) via an intersection grid corresponds to a so-called mortar method [55]. The modal coupling matrices of the various modal pairings may now be computed according to Eq. (4.57). The procedure is illustrated in Fig. 4.2 on behalf of an exemplary mechanical and acoustical mode shape defined on the respective point clouds $\boldsymbol{P}_\mathrm{s}$ and $\boldsymbol{P}_\mathrm{a}$. Note, that the calculation of vibro-acoustic coupling forces is equivalent to the computation of nodal forces arising from aerodynamic excitation. It follows naturally that in the case of distributed aerodynamic pressure excitation $\hat{\boldsymbol{p}}_\mathrm{f}$, the mechanical force vector $\hat{\boldsymbol{f}}_\mathrm{s}$ can be obtained by employing an aerodynamic-structural coupling matrix $\boldsymbol{H}_\mathrm{sf}$ according to

$$\hat{\boldsymbol{f}}_\mathrm{s} = \boldsymbol{H}_\mathrm{sf} \hat{\boldsymbol{p}}_\mathrm{f} \,. \tag{4.64}$$

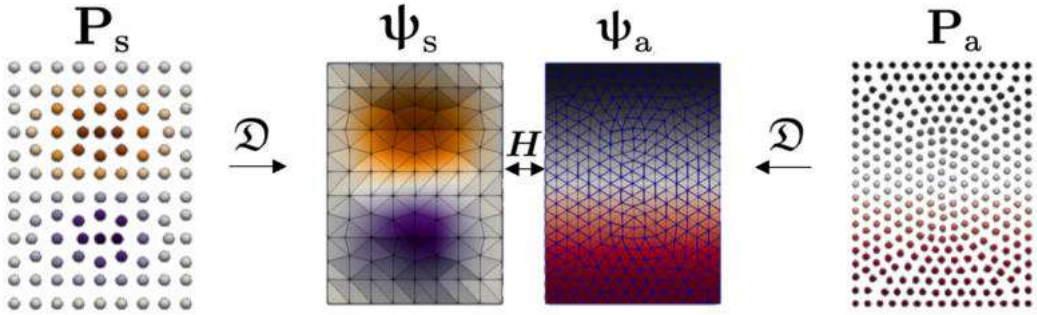

Figure 4.2: Calculation of modal coupling matrix on non-conforming grids ($\tilde{h}_{ij} = \boldsymbol{\psi}_{s|i}^T \boldsymbol{H} \boldsymbol{\psi}_{a|j}$).

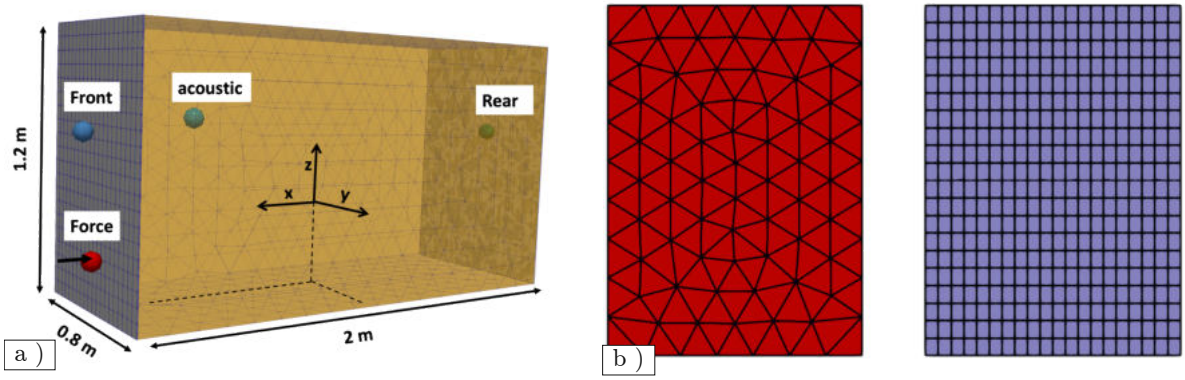

Figure 4.3: Acoustic box with flexible walls. (a) Geometry and positions (b) non-conforming interface with acoustic (left) and mechanic (right) grid.

4.3 Validation

The proposed method is validated on behalf of a reverberant acoustic box enclosed by flexible plates (Fig. 4.3a) with plate thickness $d = 0.005\,\mathrm{m}$ and clamped boundaries. The acoustic grid is discretized with quadratic tetrahedral elements whereas the mechanical domain is discretized using quadratic hexahedral elements. Fig. 4.3b illustrates the coupling surfaces involved in the numerical example. The mechanical structure is modelled as a homogeneous linear elastic structure with the mechanical properties of aluminium. The acoustic medium is air at 25° C. The plate designated *Front* is stimulated at the position illustrated in Fig. 4.3a $(-1.005, -0.22, -0.24)$ with a unit force in the frequency range 0 to 260 Hz. The mechanical normal displacements are obtained and compared at $(-1.005, 0.22, -0.08)$ (*Front*) and $(1.005, 0.22, -0.08)$ (*Rear*) while the acoustic pressure spectrum is synthesized at $(-0.7, 0.2, 0.2)$. The term coupled eigenmodes will further on be used to refer to the right eigenvectors of the vibro-acoustic system. We furthermore compute the sound pressure level (SPL) and the displacement level (DL) according to

$$\mathrm{SPL} = 20\log_{10}(|\hat{p}_a|/20 \cdot 10^{-6}) \quad \text{and} \quad \mathrm{DL} = 20\log_{10}(|\hat{u}_s|/10^{-12})\,. \tag{4.65}$$

4.3.1 Coupled vibro-acoustic modes

To validate the proposed approach, we compare the results obtained by modal substructuring with those resulting from a fully coupled FE simulation. We employ modes up to twice the frequency of interest (i.e. 500 Hz) resulting in 21 mechanical modes per plate and 41 acoustic modes. The same grids are incorporated in both approaches and no additional interpolation step is employed. Our first step in

addressing the issue is to study the vibro-acoustic modes obtained by solving the undamped modal eigenvalue problem Eq. (4.60). According to Eq. (4.55), the system's coupled eigenvectors $\boldsymbol{\psi}_{\mathrm{c|i}}$ can be synthesized from the modal eigenvectors $\boldsymbol{\theta}_{\mathrm{c|i}}$ as well as the uncoupled mechanical and acoustical modes $\boldsymbol{\psi}_{\mathrm{s|i}}$ and $\boldsymbol{\psi}_{\mathrm{a|i}}$. The transpose of the modal shape matrix $\boldsymbol{\Theta}$ is illustrated in Fig. 4.4. In this representation,

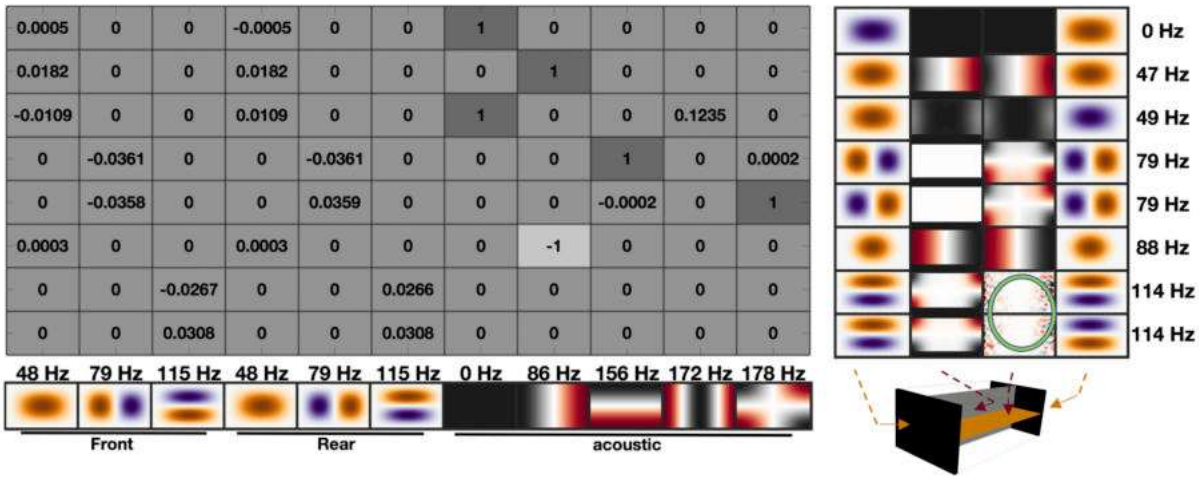

Figure 4.4: Entries of the modal shape matrix $\boldsymbol{\Theta}$ with the corresponding structural and acoustic modes in $\boldsymbol{\Psi}_{\mathrm{sa}}$ and the associated coupled modes $\boldsymbol{\psi}_{\mathrm{c|i}}$ according to Eq. (4.54). Numerical artefacts at 114 Hz (green ring) are caused by nearest neighbor mapping.

each row of the matrix contains the scaling of the relevant uncoupled mechanical and acoustic modes for each coupled mode. Therefore, the uncoupled mechanical and acoustic modes are displayed below the columns while the corresponding coupled modes are shown to the right of the respective mode. The mechanical modes show the normal displacement outwards of the acoustic domain (brown: positive, blue negative). The acoustic modes are displayed in the vertical and horizontal plane with positive acoustic pressure colored in red and negative acoustic pressure colored in black. As expected, the lowest coupled mode at 0 Hz is the pressure equalization mode, which implies that pushing the first plate in causes the rear plate to move in the opposite direction as a result of a spatially homogeneous increase in acoustic pressure. Modes dominated by the first acoustic mode, on the other hand, have a nodal line in the center and are thus in phase with outwards oriented structural modes. For the sake of brevity, we will not cover the remaining modes in detail. Regarding the eigenfrequencies of the coupled arrangement, it is well established that vibro-acoustic modes may be significantly shifted in frequency relative to uncoupled modes. In this case, the frequency shift of ± 1 Hz with respect to the initial uncoupled mechanical modes corresponds roughly to the coupling degree of common automotive problems (see also [3]). Finally, we note that the numerical variations at 114 Hz (green box) are caused by the nearest neighbor mapping of the tetrahedral grid nodes onto the horizontal plane.

4.3.2 Validation

Next, we compare the displacement and pressure at the selected positions obtained in the modal coupling procedure to those obtained by directly solving the strongly coupled vibro-acoustic problem Eq. (4.41). To account for the influence of modal damping on the coupled system, we set the acoustic damping to 5% and the mechanical damping to 2%. In order to compare the modal workflow to a direct, strongly coupled FE calculation, the discrete damping matrices must be assembled. This can be accomplished for the specified system by utilizing the relation $\boldsymbol{C} = \boldsymbol{\Psi} 2\boldsymbol{\zeta}\sqrt{\boldsymbol{\Lambda}}\boldsymbol{\Psi}^{\mathrm{T}}$. Regarding the modal workflow, modal displacement and pressure spectra can be obtained by solving the damped modal formulation Eq.

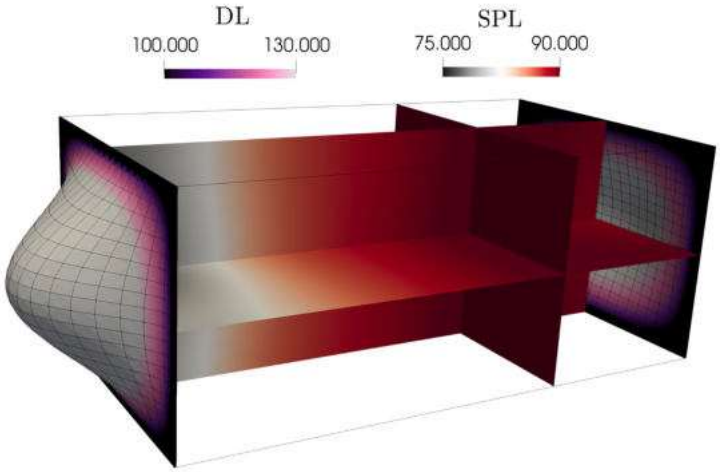

Figure 4.5: Synthesized pressure and displacement fields at 50 Hz.

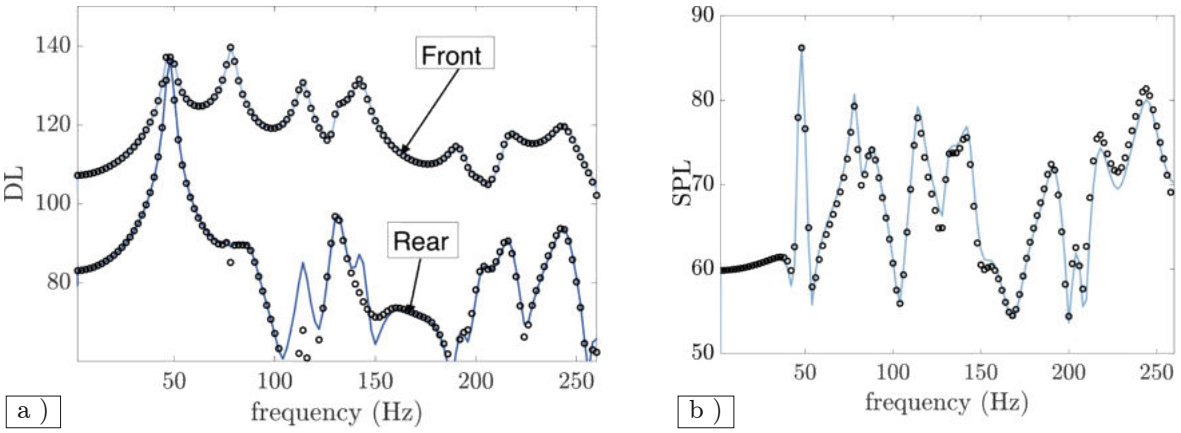

Figure 4.6: Comparison of results obtained by modal substructuring (solid line) with direct FE calculation (circles) (a) displacement level (b) pressure level.

(4.58). After solving the modal-harmonic problem for each frequency and scaling the components of each eigenvector at the desired point by its modal displacement, the spatial field variables can be retrieved at the relevant nodes. In addition to point-wise synthesis, it is feasible to synthesize three-dimensional fields, as exemplified in Fig. 4.5. The corresponding results can then be compared to those obtained using the strongly coupled FE solution. The mechanical displacement and acoustic pressure spectra shown in Fig. 4.5 are found to be very consistent with strongly coupled FE results. The tiny inaccuracy at the rear plate close to the 114 Hz mode stem from a violation of the weak coupling assumption stated above (see section 4.2). However, the corresponding error is more than 60 dB smaller than the displacements of the exciting plate and hence does not affect the internal pressure level.

4.3.3 Vibro-acoustic mode superposition

The following section will highlight how the dynamics of the system can beneficially be interpreted in terms of vibro-acoustic mode shapes. For this purpose, the generalized modal displacements of the coupled problem must be determined in order to be able to identify the dominant mechanisms of the system at hand. For this purpose, the modal generalized displacements must first be calculated according to Eq. (4.63) using the undamped coupled eigenvectors and the generalized displacements from Eq. (4.61). The

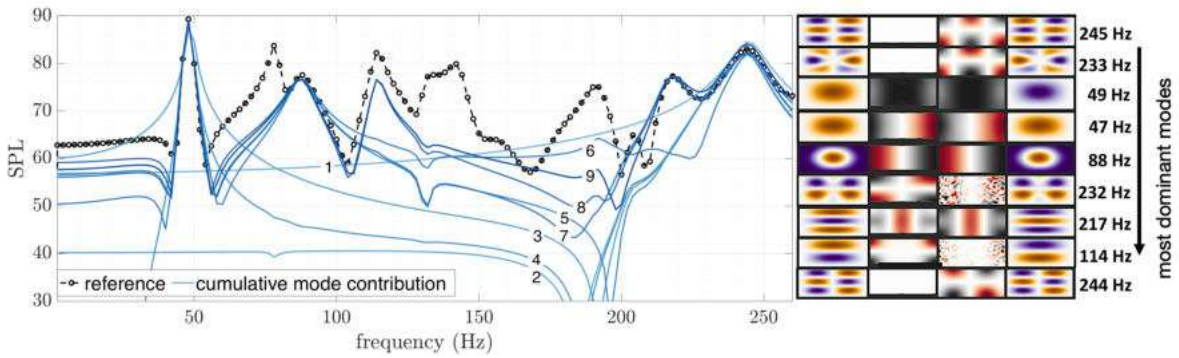

Figure 4.7: Cumulative sum of synthesized pressure spectra due to different coupled modes vs. reference solution (circles).

sound pressure spectrum originating from the j-th vibro-acoustic mode can then be determined according to

$$\hat{\boldsymbol{p}}_{\mathrm{j}} = \hat{\boldsymbol{\psi}}_{\mathrm{c|j}} \boldsymbol{p}_{\mathrm{j}} \,. \tag{4.66}$$

The resulting spectra can be ordered by scaling the mode-wise synthesized pressure spectra based on their contribution to the overall acoustic spectrum. For that purpose we calculate the complex coherence $\gamma_{\mathrm{k|j}}$ (i.e. the normalized complex scalar product) between the individual spectrum of mode j at position k ($\hat{\boldsymbol{p}}_{\mathrm{k|j}}$) and the total pressure spectrum $\hat{\boldsymbol{p}}_{\mathrm{k}}$ as

$$\gamma_{\mathrm{k|j}} = \frac{\hat{\boldsymbol{p}}_{\mathrm{k|j}}^{\mathrm{T}} \hat{\boldsymbol{p}}_{\mathrm{k}}}{\hat{\boldsymbol{p}}_{\mathrm{k}}^{\mathrm{T}} \hat{\boldsymbol{p}}_{\mathrm{k}}} \,. \tag{4.67}$$

Note that $\sum_{j=1}^{\mathrm{N_c}} \gamma_{\mathrm{k|j}} = 1$ and that $^{\mathrm{T}}$ herein denotes the hermitian (complex) transpose. We can then rank the different modes according to the norm of the complex coherence (Fig. 4.7). The modes depicted here constitute 50% of the total energy of the spectrum at location k. The total acoustic pressure spectrum as well as the cumulative sum of the respective modes is displayed in the graph. For example, the 1st line shows the acoustic pressure due to the most important mode at 246 Hz, whereas the 4th line represents the cumulative sum of modes 1 to 4. It is worth pointing out that conversely to most open domain problems, the symmetrical acoustic and mechanical modes account for the majority of acoustic sound pressure at the chosen position.

4.4 Discretization error regarding EMA

The approach proposed herein is novel in that it allows to directly incorporate experimental modes obtained from EMA and defined on arbitrary interface grids to address weakly coupled vibro-acoustic problems. Given the usually coarse spatial resolution of experimentally measured modes, the discretization error is a critical issue. The previously investigated non-conforming approach can be beneficially combined with a suitable interpolation procedure to overcome the associated limitations. After briefly discussing the theoretical ideas of RBF interpolation, we address the sensitivity of intersection based non-conforming coupling to discretization issues and how RBF interpolation may be employed to permit the application of modal substructuring on coarse, irregularly sampled, measurement grids.

4.4.1 Interpolation with radial basis functions

Name	Basis function $\phi(\boldsymbol{x})$
thin-plate spline (TPS)	$\lvert\boldsymbol{x}\rvert^2 \log(\lvert\boldsymbol{x}\rvert + 1)$
multiquadric	$\sqrt{1 + \lvert\boldsymbol{x}\rvert^2/\delta^2}$
Wendland	$(1 - (\lvert\boldsymbol{x}\rvert/\delta))^4(4\lvert\boldsymbol{x}\rvert/\delta + 1)$

Table 4.1: RBF interpolation kernels.

The interpolation of mechanical displacements is a prominent issue in aeroelasticity whenever an aerodynamic pressure distribution has to be interpolated onto a mechanical grid. Beckert, for example, has addressed the subject [181]. Different radial basis functions (RBF) are explored, and the compactly supported RBF (on behalf of the wendland kernel introduced in [182] and the euclid hat function) are deemed advantageous. A subsequent review by Boer [183] compares several methods for computing the coupling matrices including nearest neighbour interpolation, RBF interpolation on behalf of Wendland, multiquadric and thin-plate splines (TPS) and the weighted residual method employed herein (see Tab. 4.1). Cinquegrana [184] has also recently interpolated aerodynamic excitation onto a structural grid by employing compactly supported TPS. Compactly supported basis functions are non-zero only on a subset of nodes (e.g. Finite Elements) while global interpolation incorporates basis functions being non-zero throughout the domain. In case of TPS interpolation, the basis function $\phi(r)$ approaches zero as $r \to \infty$, hence global and compact interpolation differ only in the choice of a finite radius δ above which $\phi(r)$ is set to zero. Other basis functions, such as the multiquadric and Wendland kernels, afford the choice of a suitable parameter δ. In the interpolation procedure, we presume that the given normal displacements $\psi_{\mathrm{s|i}}(\boldsymbol{x})$ of each mode can be interpolated with a set of basis functions $G(\boldsymbol{x})$ evaluated at $\boldsymbol{x} - \boldsymbol{x}_\mathrm{i}$ and weighted with w_i as

$$\psi_{\mathrm{s|i}}(\boldsymbol{x}) = \sum_{i=1}^{N} w_\mathrm{i}\phi(\boldsymbol{x} - \boldsymbol{x}_\mathrm{i})\,. \tag{4.68}$$

The interpolation step solves the discrete set of equations and determines the appropriate weights to approximate the original data points in a continuous manner. This continouus description in terms of radial basis functions can then be numerically integrated by employing adequately discretized linear triangular elements in conjunction with the non-conforming grid technique to obtain the modal coupling coefficients between mechanical and acoustic modes. Based on the conclusions drawn in these articles, we compare several RBF methods to investigate their applicability for modal substructuring. The incorporated basis functions are shown in Table 4.1.

4.4.2 Discretization error of non-conforming method

To begin with, we explore the effect of grid spacing on the accuracy of the modal coupling procedure presented previously. Since triangulated grids are commonly employed in the automatic generation of meshes for experimental modes, we compare different variants of triangular grids to the original rectangular grid (Fig. 4.8). To investigate the applicability of the coupling procedure on experimentally extracted modes, we produce pseudo-experimental modes by extracting subsets of the original structural modes. The resulting modes could equally be obtained by applying an EMA procedure to a set of appropriate FRFs. After applying the modal coupling procedure and synthesizing the acoustic spectrum large variations from the reference solution for all triangulated grids are observed (Fig. 4.9). To identify the reasons for the considerable differences between the synthesized pressure spectra on coarse and fine grids, it is crucial to study the corresponding modal coupling coefficients $\tilde{h}_\mathrm{ij}$ between a set of structural modes $\boldsymbol{\psi}_{\mathrm{s|i}}$ and acoustic modes $\boldsymbol{\psi}_{\mathrm{a|j}}$ for the different variants (Fig. 4.10). The absolute discretization error in the energy norm of the modal coupling coefficients $\epsilon_{\gamma|\mathrm{ij}} = ||\tilde{h}_\mathrm{ij}|| - ||\tilde{h}^\mathrm{ref}_\mathrm{ij}||$ (with $\tilde{h}^\mathrm{ref}_\mathrm{ij}$ representing the coefficients on

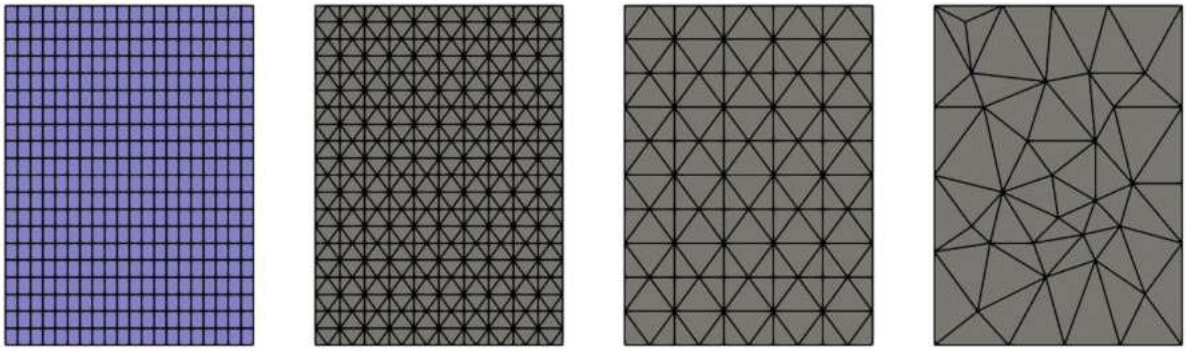

Figure 4.8: Different mechanical grids at the interface, left to right: structured grid (fine), structured grid (medium), structured grid (coarse), unstructured grid.

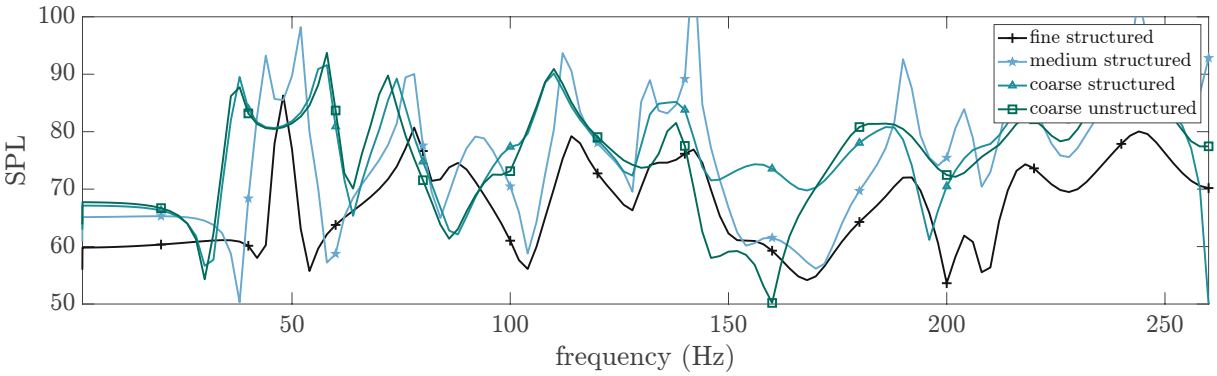

Figure 4.9: Effect of discretization on non-conforming coupling procedure.

the fine grid) turns out to be approximately linearly related to the characteristic discretization length γ. This is consistent with Wolmuth's work concerning error norms of mortar finite element techniques [185]. Concerning practical applications in terms of EMA, it is evident that the necessary grid resolution for a sufficiently accurate calculation of the modal coupling coefficients clearly limits the applicability of the methodology shown here. This issue can however be overcome by employing a suitable interpolation method to resample the coarsely discretized measurement grid onto a reasonably fine grid.

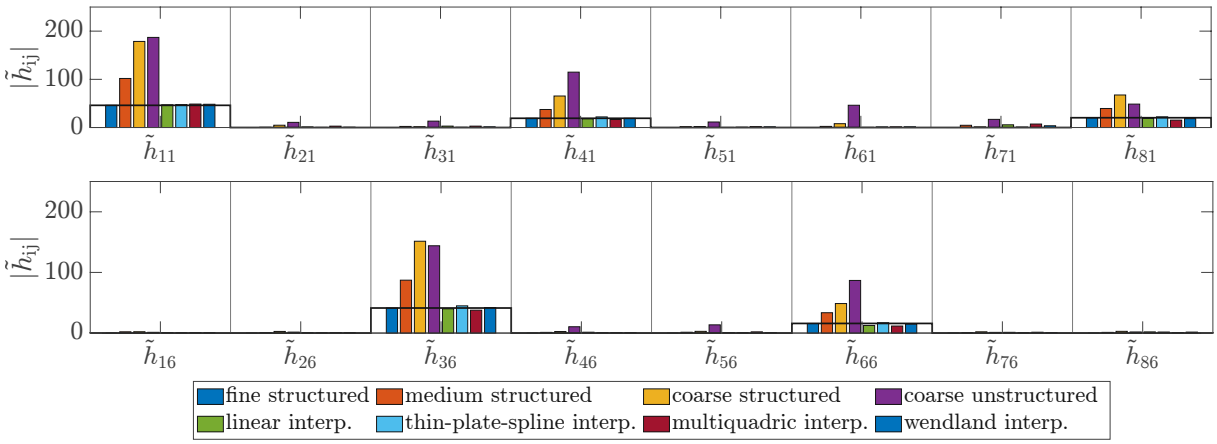

Figure 4.10: Comparison of modal coupling coefficients for first (top) and 6th (bottom) acoustical mode, black bar indicates reference on fine grid.

4.4.3 Discretization Error using Interpolation

To demonstrate the applicability of the presented strategy to deal with a wide range of experimental grids, the mode shapes on the coarse, unstructured grid are interpolated onto the fine grid using the RBF interpolation techniques summarized in Table 4.1. The finite radius δ is set to 0.1. Diagonal coefficients in the resulting matrix are set to zero. For completeness, element-wise linear interpolation has also been considered [186]. Several discretized or interpolated variations of the primary structural mode are shown in Fig. 4.11. In addition, the reference structural mode on the fine grid is shaded in grey. The structural modes determined via linear interpolation in Fig. 4.11b agree with the initial

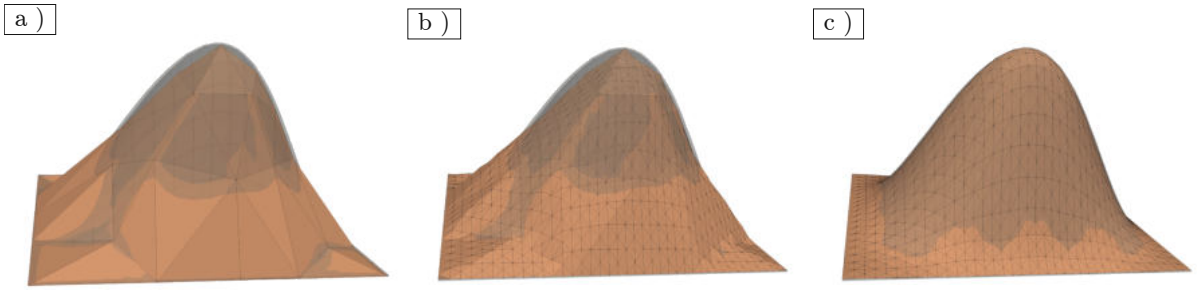

Figure 4.11: Displacement warp of principal structural mode at fine grid (grey) vs. different configurations (orange). (a) original at coarse grid (b) linear interpolation (c) TPS interpolation.

deformations at the coarse grid in Fig. 4.11a. In terms of the corresponding modal coupling coefficients in Fig. 4.10, it is however clearly evident that the linear interpolation already constitutes a substantial improvement when compared to the non-conforming approach using a coarse grid. This is because the reduced discretization length reduces the discretization error in calculating the coupling matrices. The RBF interpolation instead provides smooth approximations of the original structural mode, as can be seen in Fig. 4.11c on behalf of the Wendland interpolation. Given that the various interpolation variants are now discretized on the same grid, a detailed comparison of the error norm $\boldsymbol{\epsilon}_\psi$ with $\epsilon_{\psi|\mathrm{i}} = ||\boldsymbol{\psi}_{s|i} - \boldsymbol{\psi}_{s|i}^{\mathrm{ref}}||$ between interpolated $\boldsymbol{\psi}_{s|i}$ and original structural modes $\boldsymbol{\psi}_{s|i}^{\mathrm{ref}}$ lends itself to investigation (Fig. 4.12). It

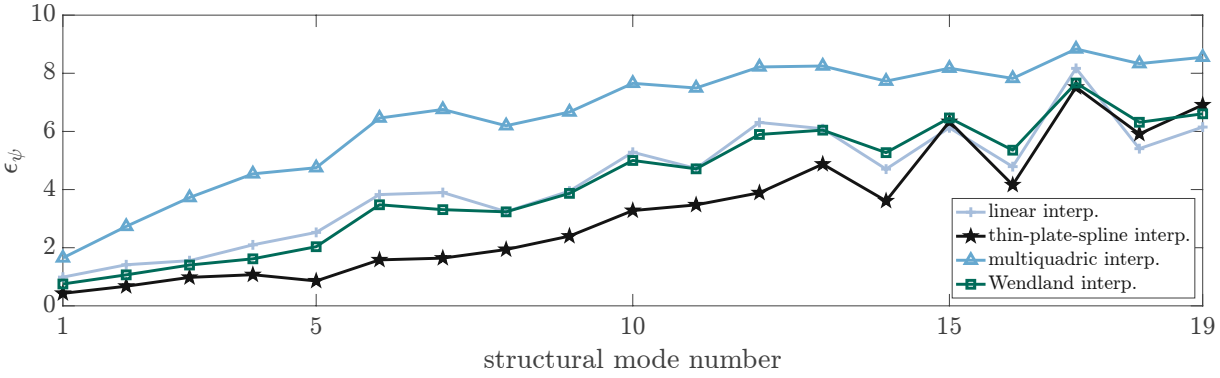

Figure 4.12: Absolute error norm during mode shape interpolation.

is apparent that the TPS interpolation provides the best approximation for the original deflections in the investigated setup. This is because the TPS basis functions employed here are solutions of the biharmonic equation $\nabla^4\phi(r) = \delta(r)$, which is also utilized in Kirchhoff-Love plate theory to calculate the displacement of isotropic, homogeneous plane plates [187]. While linear interpolation and interpolation based on the wendland kernel produce comparable results, interpolation based on the multiquadric kernel produces significant deviations from the reference solution for the given parameterization. This applies equally if the corresponding synthesized SPL displayed in Fig. 4.13 are investigated. By comparing

Fig. 4.13 with the original results obtained without interpolation (Fig. 4.9), it becomes evident that an additional interpolation procedure significantly reduces the error induced in the coupling procedure. The conclusion can be made here that, with the exception of multiquadric interpolation, satisfactory results can be obtained for all interpolation methods. While this statement cannot be generalized, it seems reasonable to suggest the TPS interpolation for dealing with vibroacoustically relevant structures which may frequently be idealized as vibrating plates. Regarding implementation, globally supported radial basis functions may be implemented with great ease for plane surfaces due to the absence of grids. It may also be beneficial to employ RBF interpolation to resample both acoustic and structural modes on an equidistant grid on which integration can easily be performed. Due to the practical constraints regarding EMA data collection, the computational effort associated with the interpolation procedure is of minor importance.

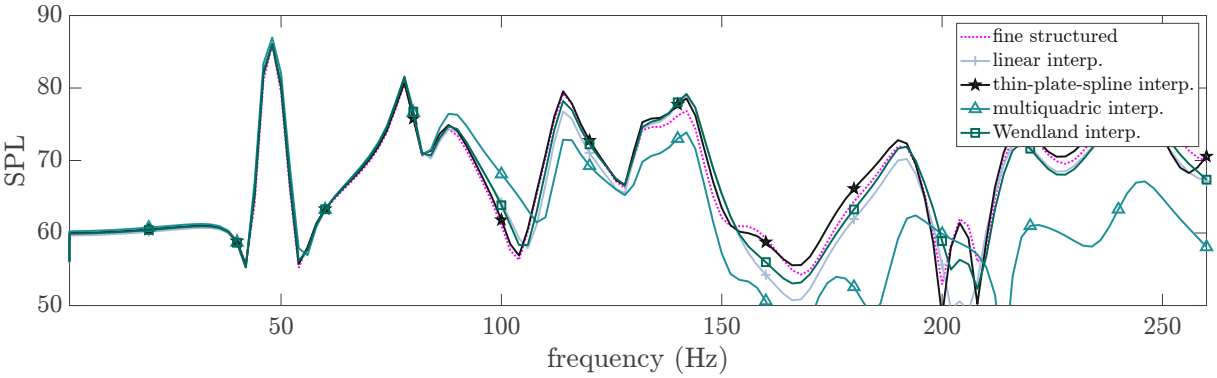

Figure 4.13: Synthesized pressure spectrum after interpolation.

4.4.4 Extraction of mechanical modes from a coupled arrangement

In terms of practical application, it should be noted that the experimental eigenmodes that may be employed in the course of this procedure can typically only be identified in a coupled setup (i.e. filled with air). For this purpose, the FRFs between an accelerometer and an exciting source (e.g. impulse hammer) are determined for all measuring positions. The mechanical modes may then be extracted via EMA. To examine the effect of extracting the mechanical modes in a coupled arrangement and thus the methodology's applicability to most practical problems, we compare the eigenvalues of the mechanical system recovered from the purely mechanical system to those obtained by measuring the FRFs within the coupled arrangement. The unity force displacement spectrum of *Front* is shown in Fig. 4.14. We recognize, that the acoustic feedback effect in this scenario is largely restricted to the first mechanical mode. The acoustic feedback causes an underestimation of mechanical displacement. Using a 2 Hz frequency resolution, this results in an overestimation of modal damping in the EMA ($\zeta_{\mathrm{sc}|1} = 2.8\,\%$ vs. $\zeta_{\mathrm{s}|1} = 2\,\%$). Refining the frequency resolution to 0.2 Hz clearly reveals the coupled eigenmodes at 47 Hz and 49 Hz (small box in Fig. 4.14) and therefore, the apparent damping stems from the resonance shifts induced by the coupling (small box in Fig. 4.14). Without drawing a broad generalization, we conclude that extracting mechanical modes from a coupled system results in an underestimate of the interior acoustic pressure levels. Compared to the overall uncertainty in mechanical mode extraction, this impact is probably insignificant (also stated by Marburg in [42]).

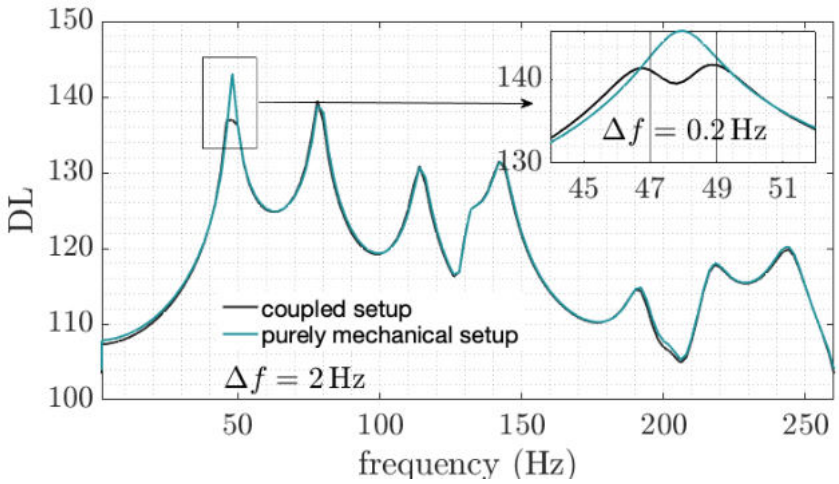

Figure 4.14: In-situ modal extraction (coupled setup) vs. in-vacuo modal extraction (purely mechanical setup). The fine frequency resolution reveals that the apparent damping stems from the resonance shifts induced by the coupling (small box).

5 A generic structure for assessing flow-induced noise in vehicles

5.1 Requirements

To investigate the physical mechanisms governing flow-induced noise in vehicles, it is preferable to employ a generic testbody that allows to control the number of potential transmission paths and is flexible enough to permit the subsequent investigation of optimization strategies. The most frequently employed aero-vibro-acoustic testbodies (i.e. the SAE [1, 22–24] or Drivaer [25–28] models) were especially designed such as to limit the possible transmission paths to the side window. This is especially difficult in the low-frequency range, which is why simulation or measurement results are frequently provided with a lower cut-off frequency of 100 Hz [22, 28]. In this particular investigation, however, we are especially interested in low-frequency mechanisms and as a result, it is not appropriate to employ a testbody with close similarities to the SAE or Drivaer models. For this purpose a new test body is sought that can be used to study the aero-vibro-acoustic behavior of a car-like structure with multiple flexible components. In light of this, the following design objectives have been established for the test body:

(a) The geometry must be chosen as such as to reproduce the global aerodynamic characteristics of a real vehicle (Fig. 3.1).

(b) The acoustic qualities of the interior cavity should be comparable to those of a passenger cabin. In this context, particular attention should be devoted to the effect of the rear bench on lower order acoustic mode shapes (see [11, 177]).

(c) The investigation of direct acoustic excitation via apertures and leakages should be possible (Sec. 3.5.4).

(d) It is essential that each of the vibro-acoustic relevant mechanical plates can be installed in a rigid or likewise flexible manner to be able to separately investigate the different contributions.

(e) The testbody should be designed as modular as possible to allow for a straightforward verification of optimization prodecures.

(f) It should be possible to investigate various ground clearings given that the underbody excitation is thought to produce significant interior noise in the low-frequency region (Sec. 3.5.3).

5.2 Realization

For the design of the new test body presented in [177] (2020) and shown in Fig. 5.1a, all of these considerations were taken into account. Its aluminium body is mainly composed of ITEM profiles (Fig. 5.2.b) with attached fasteners that allow to mount the various flexible plates. The geometrical dimensions are $L = 1.88\,\mathrm{m}$, $H = 0.6\,\mathrm{m}$ and $B = 0.7\,\mathrm{m}$. A supercritical slant angle ($\alpha > 30\,^\circ$) generates considerably

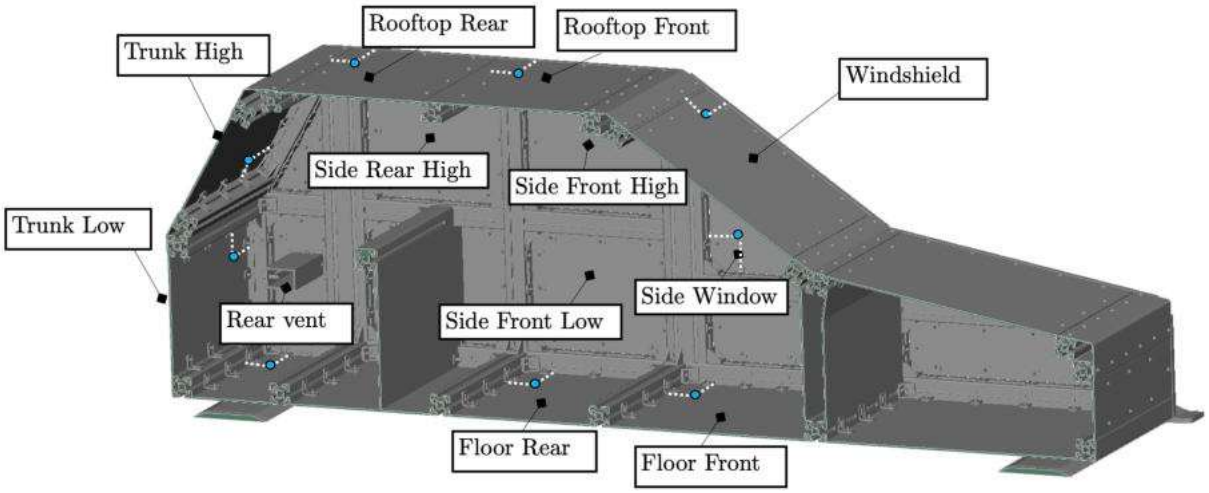

Figure 5.1: Newly developed test body with geometric dimensions and plate designations. The blue dots indicate accelerometer measurement positions. The dotted white lines with length of 8 cm indicate the exact positions.

stronger low frequency pressure fluctuations due to the large scale turbulent structures in the recirculation region, as was already mentioned in Sec. 3.5.2 and in [125]. A rather high slant angle of $\alpha = 60\,^\circ$ was chosen. The plates come in a variety of thicknesses (3 mm, 1 mm, 0.7 mm) to facilitate the investigation of a wide variety of vibro-acoustic systems, as well as to investigate or isolate individual regions. The designations of the different plates can be found in Fig. 5.1 (plates without designation are 3 mm thick and assumed rigid). The plates are attached to the rigid frame via fasteners, see Fig. 5.5a. An additional (slideable) rear bench was included and positioned as such, that the ensuing modes are comparable to those of a real vehicle [177]. As a side note, the plate separating the trunk from the main cavity was originally designed as a single 3 mm panel. However, the single plate turned out to be an efficient vibro-acoustic absorber that significantly reduced the interior SPL while at the same time inducing severe (tangible) vibration at the plate. The effect was suppressed by adding an additional 3 mm panel but may be of use for practical applications. The underbody mechanisms can be addressed by choosing one of three sets of struts (Fig. 5.2a.) for ground clearances $g = 4$, 9 or 12 cm. One of the two apertures is in practice used to feed in the required cable for the measurement system. Additionally, a ventilation aperture adjustable in length with the dimensions $l_{\text{vent}} = 32$, 52 or 136 mm was incorporated. Steel rails beveled in the flow direction can be used to install the test body in the wind tunnel at BMW AG in Munich.

5.3 Validation

A FE model was developed to assess both the structural (Fig. 5.3a) and the acoustic field (Fig. 5.3b.). The effect of the rear bench was considered by introducing a sound-hard boundary in the acoustic FE model. The interested reader can find a detailed description of the FE model in [177]. To incorporate the effect of leakages and openings a sound soft boundary was defined at the corresponding aperture (this solely affects the Helmholtz-resonance frequency of the acoustic system, see Sec. 3.5.4). For the verification of the full aero-vibro-acoustic problem of flow-induced cabin noise, a thorough validation of the different physical domains (acoustics, mechanics, fluid dynamics) is required. The decoupled acoustic and structural systems should be compared to experimental data for this purpose. Thanks to the modular design of the testbody, analyzing the decoupled systems is possible. We will begin by investigating the

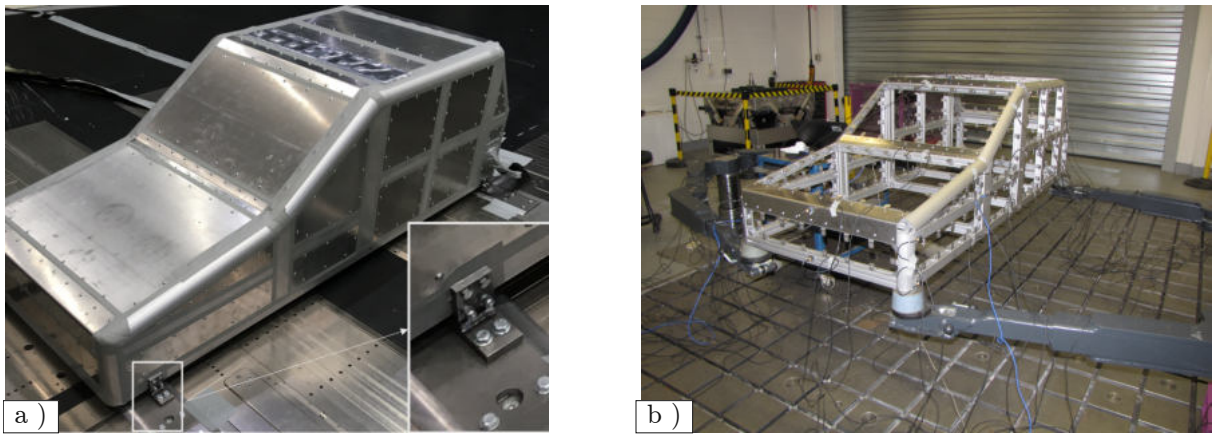

Figure 5.2: Test body during (a) wind tunnel measurements (b) EMA of the rigid frame (results not discussed in this thesis).

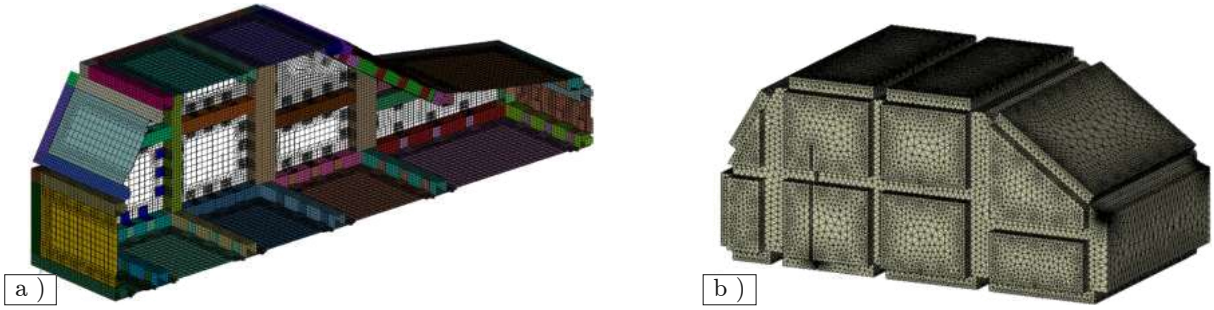

Figure 5.3: FE model (a) Middle cut through the structural FE model (b) acoustic FE model with soundhard boundary at the position of the simplified rear bench.

properties of the sound-hard acoustic cavity be applying additional masses on the 3 mm plates of the testbody such as to prevent any flux of acoustic energy through the mechanical structure.

5.3.1 Acoustical system

The acoustic modes are obtained by solving the eigenvalue problem of the acoustic FE system (taking into account the sound soft boundary condition at the rear vent) within the framework of the open source FEM code openCFS [188]. The lowest four modes are shown in Fig. 5.4 and compare well to those of a real vehicle [177]. To validate the acoustic FE model, acoustic FRF measurements were performed using an LMS Qsource source (Fig. 5.5a., see [15] for more information on the source) and a limited number of microphones at the microphone locations depicted in Fig. 5.5b. For the determination of the acoustic FRF functions, white noise volume acceleration was impressed at the source (position $\boldsymbol{x}_\mathrm{j}$) and the microphone pressures were measured at positions $\boldsymbol{x}_\mathrm{i}$. The dynamic stiffness FRF's were then

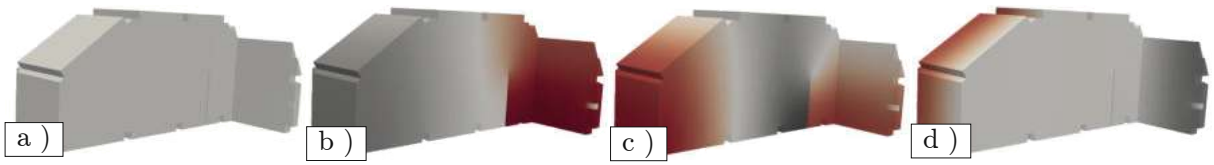

Figure 5.4: Acoustic cavity modes at (a) 10 Hz, (b) 128 Hz, (c) 222 Hz, (d) 231 Hz

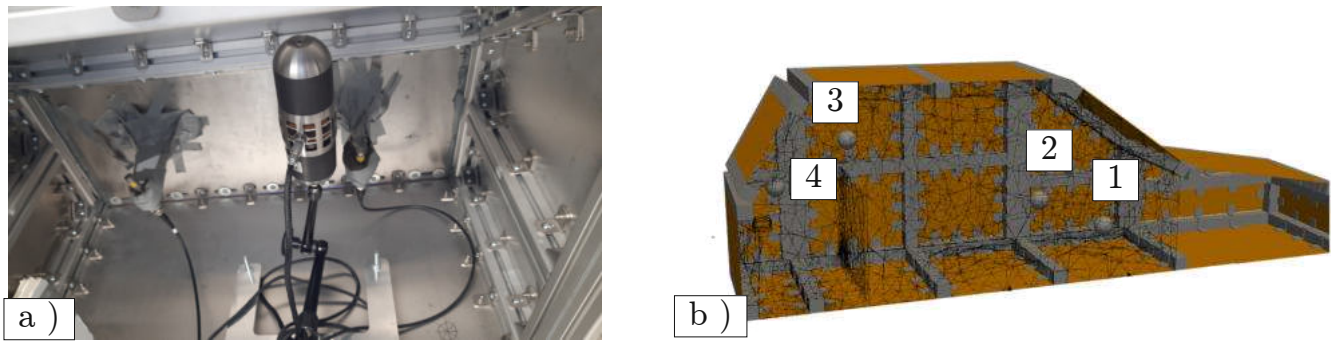

Figure 5.5: a) LMS QSource volume acceleration source at Position 1. (b) Measurement positions for acoustic validation.

obtained according to

$$\hat{Z}_{\mathrm{a|ij}}(\omega) = \left\{ \frac{\hat{p}_{\mathrm{a}_{(\mathrm{i})}}(\boldsymbol{x}_{\mathrm{i}}, \omega)}{i\omega \hat{q}_{\mathrm{a}_{(\mathrm{i})}}(\boldsymbol{x}_{\mathrm{j}}, \omega)} \right\} = \left\{ \frac{\hat{p}_{\mathrm{a}_{(\mathrm{i})}}(\boldsymbol{x}_{\mathrm{i}}, \omega) i\omega \hat{q}^{*}_{\mathrm{a}_{(\mathrm{i})}}(\boldsymbol{x}_{\mathrm{j}}, \omega)}{(i\omega \hat{q}_{\mathrm{a}_{(\mathrm{i})}}(\boldsymbol{x}_{\mathrm{j}}, \omega))(i\omega \hat{q}^{*}_{\mathrm{a}_{(\mathrm{i})}}(\boldsymbol{x}_{\mathrm{j}}, \omega))} \right\} \tag{5.1}$$

by ensemble averaging over a measurement period of 60 s with an additional Hamming window with $T = 1\,\mathrm{s}$ and hence a frequency resolution of $\Delta f = 1\,\mathrm{Hz}$. On the other hand, the computational FRF's could be obtained by idealising the volume source as a point source and applying modal synthesis on the uncoupled modes according to

$$\hat{Z}_{\mathrm{a|ij}}(\omega) = \frac{\hat{p}_{\mathrm{a}}(\boldsymbol{x}_{\mathrm{i}}, \omega)}{i\omega \hat{q}_{\mathrm{a}}(\boldsymbol{x}_{\mathrm{j}}, \omega)} = \sum_{n=0}^{N} \frac{\psi_{\mathrm{a|n}}(\boldsymbol{x}_{\mathrm{i}}) \psi_{\mathrm{a|n}}(\boldsymbol{x}_{\mathrm{j}})}{\omega^2 - \lambda_{\mathrm{a|n}}}\,. \tag{5.2}$$

The computational and numerical FRF's are displayed in Fig. 5.6 and naturally show maxima at the experimental and numerical natural frequencies of the cavity $\lambda_{\mathrm{a|n}} = \omega^2_{\mathrm{a|n}}$. The minima occur at frequencies at which the superposition of individual modal contributions vanishes due to opposing phases in the corresponding mode shapes (a comprehensive introduction may be found in [100]). The low-frequency drop in measured FRF's is associated with the cut-off frequency of the acoustic source. The low-frequency maximum in the computational FRF's (level out of range) is associated with the Helmholtz resonance of the system at $f_{\mathrm{n|0}} = 8\,\mathrm{Hz}$. There is a difference of approximately $\approx 10,\mathrm{Hz}$ between the experimental and simulated acoustic natural frequencies that is attributable to the not entirely rigid nature of the mechanical structure. Due to the mechanical natural frequencies being higher than the two acoustic natural frequencies shown here, the effect of the flexible mechanical boundary is similar to an additional acoustic mass, and therefore the coupled (actual) natural frequencies are shifted to lower values compared to the uncoupled ones. We will later on notice the opposite effect (upwards frequency shift) in case of a very flexible system with thin plates and structural eigenfrequencies below the lower natural frequencies of the cavity (Sec. 7.2). In order to achieve a better visualization, the numerical acoustic natural frequencies employed in Eq. (5.2) were modified to match the experimental natural frequencies. Apart from the slight frequency shift, the computational and experimental FRF's are essentially in good agreement.

5.3.2 Mechanical system

Initially, it was intended to conduct a validation of the mechanical FE model shown in Fig. 5.3a. However, the numerical model of the relatively simple 3 mm system has already shown unsatisfactory in the context of a previous inquiry [178]. Fitting the boundary condition using a simple model-updating method was tested but discarded. Due to the anticipated high modeling effort required to generate a reliable model and

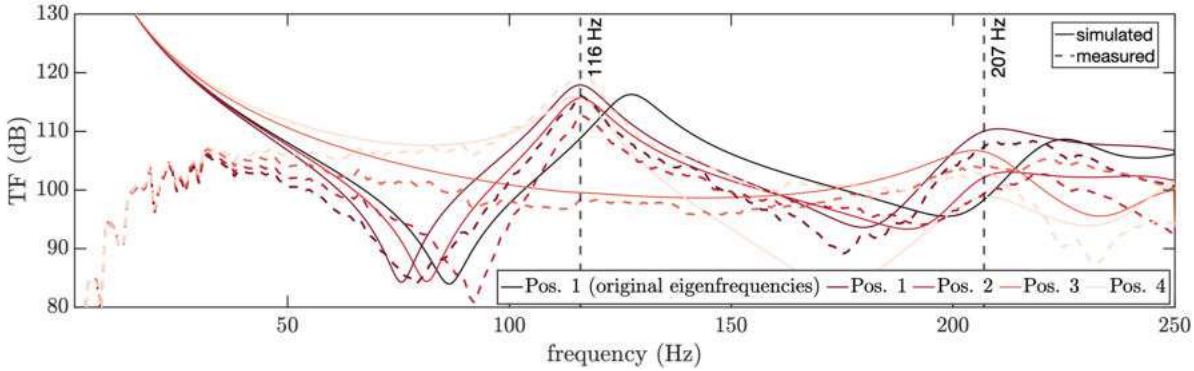

Figure 5.6: Simulated vs. measured acoustic transfer function between Position 1 and Position 4. The original numerical natural frequencies at 128 Hz and 220 Hz were modified to match the experimental natural frequencies at 116 Hz and 207 Hz in Eq. (5.2) for better visualization.

the straightforward handling of the aero-vibro-acoustic issue on behalf of experimental modes described in the previous chapter, the construction of a suitable model was not performed. The non-conforming approach was tested with a 3 mm structure in [178] and yielded good results. The effect of plate thickness on vibro-acoustic coupling effects is nontrivial even for simple structures (Xue [20]), but it is evident from Eq. (4.39) that high sound pressure levels cause stronger feedback to the mechanical structure. The one-way coupled admittance in Eq. (3.28) therefore suggests that the relative mechanical displacement induced solely by the acoustical feedback will increase with decreasing plate thickness. An arrangement with thinner plates was therefore chosen for further investigation. Since the turbulent structures on the windshield were the major source of excitation, a more complicated arrangement was chosen to pronounce excitation via other transmission paths. All plates designated in Fig. 5.1 were installed with a thickness of 1 mm except for *Floor Front* and *Windshield* (3 mm). Subsequently, the mechanical admittance FRF's were determined by impulse hammer measurements with spatial resolution of 4 cm and a fixed accelerometer at the positions indicated in Fig. 5.1 by averaging over three subsequently determined datasets according to

$$\hat{Y}_{\mathrm{s|ij}}(\omega) = \left\{ \frac{\hat{v}_{\mathrm{s_{(i)}}}(\boldsymbol{x}_\mathrm{i},\omega)}{\hat{f}_{\mathrm{s_{(i)}}}(\boldsymbol{x}_\mathrm{j},\omega)} \right\} = \left\{ \frac{\hat{v}_{\mathrm{s_{(i)}}}(\boldsymbol{x}_\mathrm{i},\omega)\hat{f}^*_{\mathrm{s_{(i)}}}(\boldsymbol{x}_\mathrm{j},\omega)}{\hat{f}_{\mathrm{s_{(i)}}}(\boldsymbol{x}_\mathrm{j},\omega)\hat{f}^*_{\mathrm{s_{(i)}}}(\boldsymbol{x}_\mathrm{j},\omega)} \right\} . \tag{5.3}$$

It is assumed that the feedback effect of the acoustic cavity on the mechanical plate is negligible. This assumption will later be verified by comparing the uncoupled and coupled mechanical eigenfrequencies (more information on this in Sec. 7.3). The mechanical modes are determined using the Polymax algorithm (details in [100]) and the mechanical admittances were in turn synthesized according to

$$\hat{Y}_{\mathrm{s|ij}}(\omega) = \frac{\hat{v}_\mathrm{s}(\boldsymbol{x}_\mathrm{i},\omega)}{\hat{f}_\mathrm{s}(\boldsymbol{x}_\mathrm{j},\omega)} = \sum_{n=0}^{N} \frac{\psi_{\mathrm{s|n}}(\boldsymbol{x}_\mathrm{i})\psi_{\mathrm{s|n}}(\boldsymbol{x}_\mathrm{j})}{\omega^2 - \lambda_{\mathrm{s|n}}} . \tag{5.4}$$

For a selection of flexible plates, the four lowest mechanical modes extracted on each plate are displayed in Fig. 5.7. Compared to the 3 mm plates, the flexible 1 mm plates are much more difficult to characterize and, in some cases, nonlinear effects occur (recognizable by a dip in the coherence but not shown here). It is clear that a mechanical shaker measurement would yield much better results, but this is not done due to the time and effort required, and it will be demonstrated later that the modes determined here can be used for the characterisation of the aero-vibro-acoustic mechanisms. We compare the FRF's synthesised via modal synthesis (Eq. (5.4)) with the original measurements. The energetic

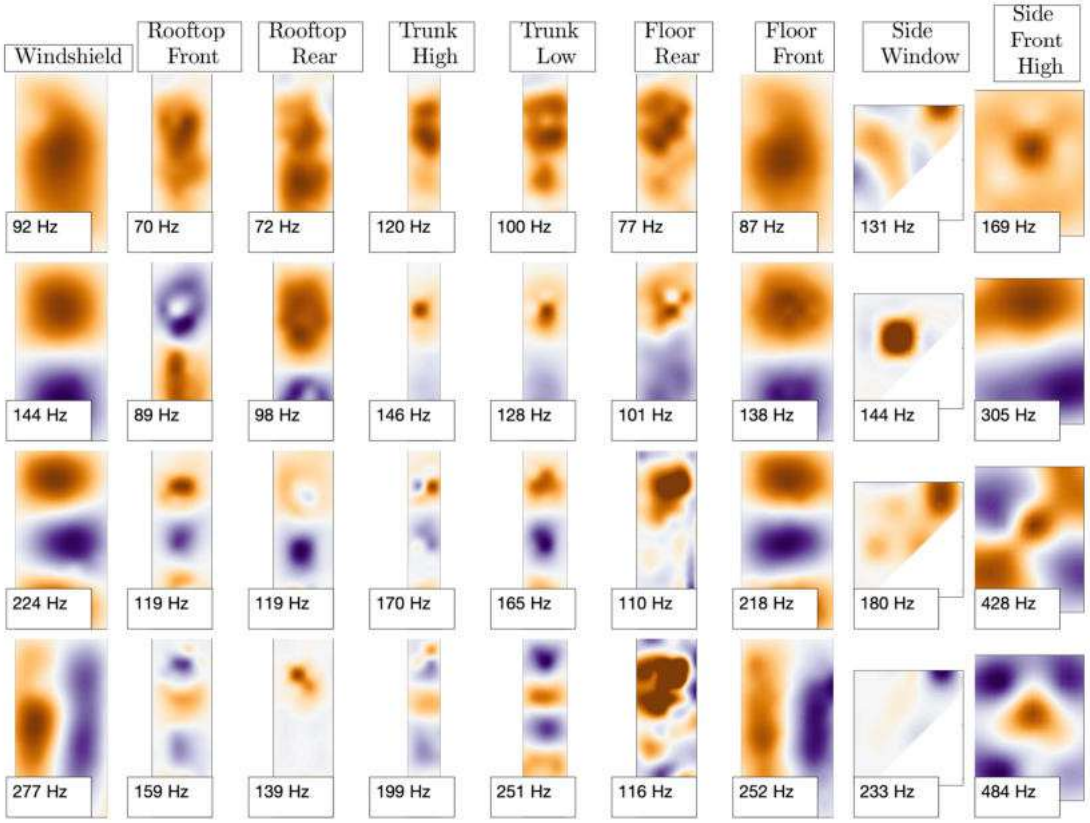

Figure 5.7: Set of four modes each for a set of flexible regions in ascending mode order from top to bottom.

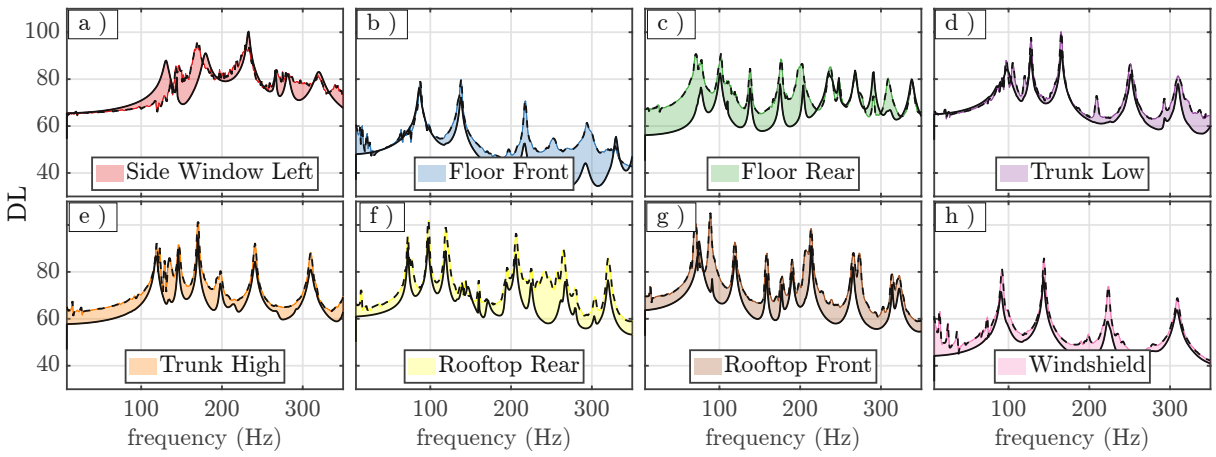

Figure 5.8: Energetically averaged displacement level (DL) to unity forcing (corresponding to the admittance $|\overline{\hat{Y}_s}|(\omega)$) from a set of FRF's between all positions at each surface (see [178]) and the reference position in Fig. 5.1 (solid- experimental, dashed- synthesized, color- deviation).

average $\overline{|\hat{Y}_\mathrm{s}|}(\omega) = 1/N\sqrt{\sum_{i=1}^{N}|\hat{Y}_{\mathrm{s|i}}(\omega)|^2}$ due to excitation at the accelerometer positions in Fig. 5.1 is obtained and shown in Fig. 5.8 (black lines, difference shaded). The majority of modes has been accurately detected. Significant deviations arise at *Floor Rear*; these faults are attributable to the fact that determining the right FRF functions at the very flexible 1 mm plate with impulse hammer excitation from below was practically challenging. It is also apparent that the second mode at *Rooftop Front* is severely underestimated. At higher frequencies, significant deviations occur at *Side Window Left* and *Floor Front*. In general, the errors are in the range of $\approx 5\,\mathrm{dB}$, thus we consider the extracted modes to be sufficiently accurate.

6 Flow topology and wall pressure fluctuations

The vibro-acoustic system is excited by both aerodynamic waves as a result of the convection of turbulent source terms and acoustic waves (particularly at the underbody, see Sec. 3). The exciting regions can be assigned to physically distinct regions (Chap. 3) and, at least for convection-dominated regions extensive models are available. Here, we are particularly interested in how far the simplifications of homogeneous turbulence discussed in Section 3.2, i.e. displacement invariance, constant pressure level over the respective excitation surface and the assumption of constant shear velocity v_{conv}, are fulfilled to determine the applicability of one of the available models for turbulent WPF's. A flow simulation is used to estimate the unsteady WPF and the relevant spectra are compared to wind tunnel measurements based on WPF measurements. The validation of the fluid dynamical simulation with regards to the vibro-acoustic excitation is a difficult task, since not only amplitudes but also the statistical properties of the field in the space-frequency domain have to be investigated and compared (see 3.2). The purpose of this chapter is therefore, to assess the validity of the flow simulation by comparing it with extensive wind tunnel measurement data on behalf of the most meaningful measures regarding aero-vibro-acoustic excitation. Furthermore, methods for identifying the critical excitation surfaces are identified, tested and compared.

6.1 Simulation setup

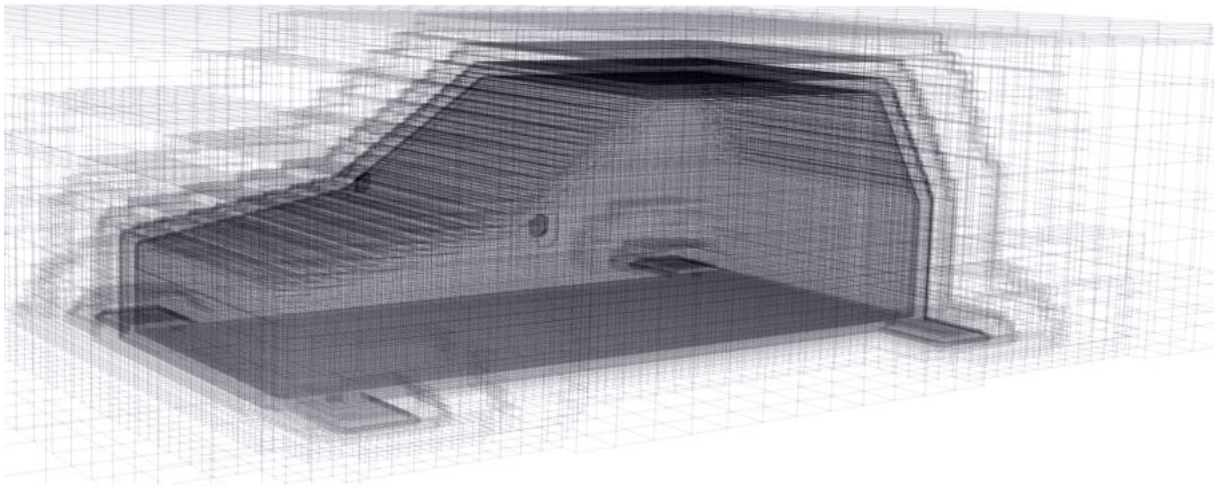

Figure 6.1: Distribution of voxels for the numerical simulation.

Various numerical methods are available for the transient calculation of the flow (see Sec. 3.1) and it is the widely used, LB-based environment *PowerFlow* (version 6-2019-R2), that is employed herein (details on the formulation in [124, 171], relevant papers in [124, 125, 127]). The formulation employed is also known as the VLES (Very Large Eddy Simulation) formulation because the dissipative and inertial subgrid scales are modeled using a two-equation model [171]. The discretization is done in PowerFlow

using a hex-based grid, that is incrementally increased with a refinement factor of 2 (Fig. 6.1). The grid includes 12 scales with grid lengths ranging from 3 mm to 6.144 m. In order to prevent reflections, the coarse grid is extended over a vast distance (≈ 600 m). A constant velocity boundary condition of $v_\infty = 120\,\mathrm{km/h} \approx 33\,\mathrm{m/s}$ is set at the inlet and constant ambient pressure at the outlet. All walls are idealized as smooth, no symmetry is exploited, and the true Mach number ($M = 0.097$) was used for the calculation. The simulation is performed with time step $\Delta t = 6.7 \cdot 10^{-6}$ s over a period of $T = 9$ s as part of an industrial workflow at BMW (special thanks go to Christoph Gabriel). The last 5 s are stored using an additional low pass filter with $f_\mathrm{g} = 500$ Hz.

6.2 Measurement setup

The measurements were carried out in the wind tunnel of the BMW Group in Munich. Details of the wind tunnel can be found in [189]. The length of the test area is 10 m, so with a cross-sectional area of the nozzle of 10 m^2 and a cross-sectional area of the test body of 0.47 m^2, the surface blocking ratio is approximately 1/20. To measure the WPF, *GRAS 40AF 1/2"* polarized free-field microphones were used. These surface microphones have lower and upper cutoff frequencies of $f_\mathrm{u} = 3$ Hz and $f_\mathrm{o} = 20$ kHz, respectively. Using 14 of these microphones, a two-row array (spacing 8 cm) was constructed for time-synchronous measurement of the WPF and, using this array, sequential measurement runs were performed at the locations indicated in Fig. 6.2a with a measurement duration of 60 s and a sampling rate of 96 kHz. Fig. 6.2b shows the test body in the wind tunnel with mounted surface pressure microphone array.

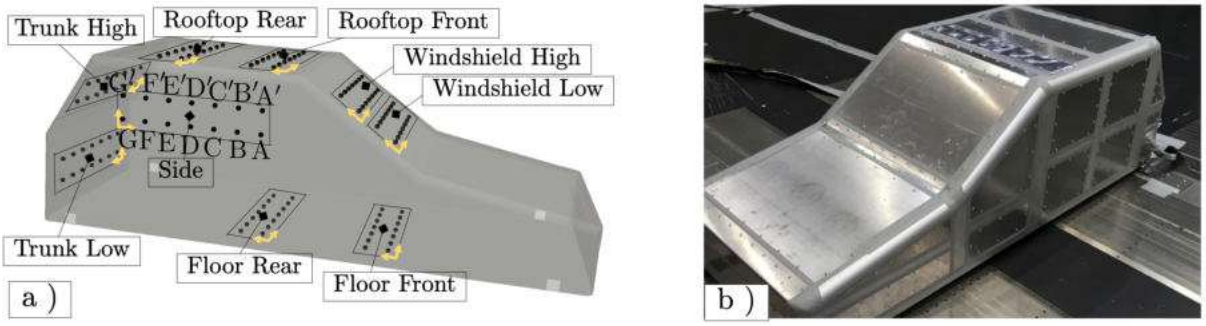

Figure 6.2: Experimental setup (a) Measurement positions of surface pressure array, axes origin in yellow (b) Installed test body.

6.3 Mean flow

The physical examination of the results of the flow simulation is a difficult task, since, regarding the excitation of the adjacent mechanical structure not only the spatial APSD (i.e. a 3D representation per frequency step) but also the CPSD that reflects information about the spatial coherence between each measurement point and all other measurement points have to be investigated. The result should then still be validated with the wind tunnel measurements. Because of this, it is of the utmost importance to select suitable criteria in order to reduce the dimensionality of the problem. The time-averaged properties of the flow are of great importance for assessing indirect excitation of the structure since the WPF at the wall can be considered, to a first approximation, to be an imprint of a frozen turbulent pattern convected at a mean flow velocity with horizontal and lateral correlation lengths (remember the Corcos model given in Eq. (3.41)). Due to the no-slip condition, the streamlines at the wall merge into the wall shear stress lines [190]. These wall shear stress lines provide important information about the flow

conditions near the wall. Note that it has been pointed out in Sec. 3.5.1 that the dominant sources for low-frequency excitation are expected to be located between the logarithmic layer of the TBL and the outer flow. As a result, we begin by analyzing the topology of the mean flow and by comparing the results with elaborations on other test bodies discussed in the literature (and in Sec. 3.4). For this purpose, suitably chosen streamlines are shown in Fig. 6.3 and Fig. 6.5 and the wall shear stress lines are shown in Fig. 6.4 and Fig. 6.6. A number in a circle is given to each respective region to allow to relate each pattern to the explanations in the paragraphs that follow. The reader is invited to compare the patterns mentioned here with those in Fig. 3.1.

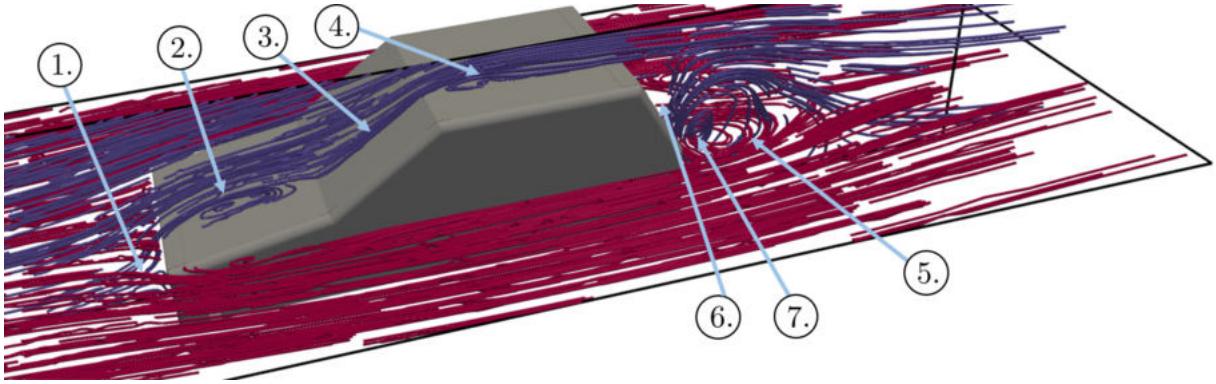

Figure 6.3: Visualization of mean flow streamlines (top view).

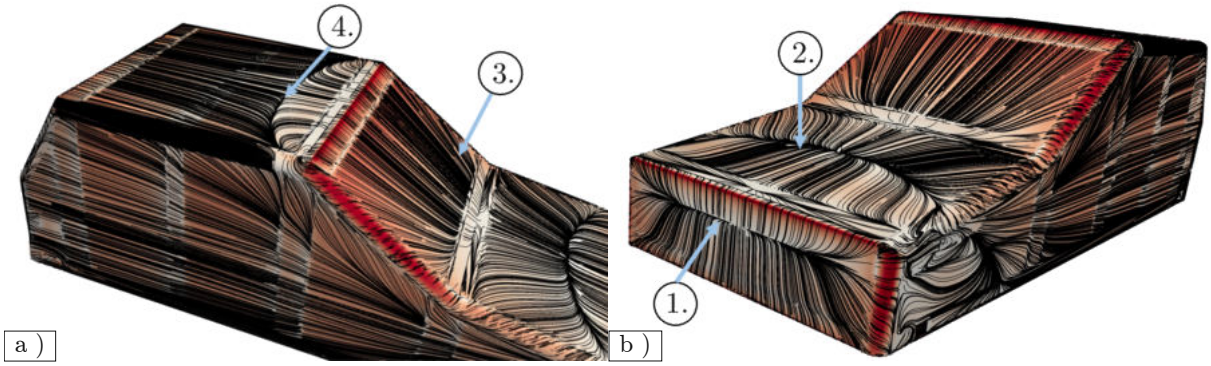

Figure 6.4: Visualization of wall shear lines (a) top left view (b) top right view.

(1) *Initial Stagnation Point*

At the leading edge of the vehicle, a stagnation point is formed that separates the incoming flow into overflow, underflow, and byflow. The location of the stagnation point indicates that a substantial portion of the flow is deflected beneath the underbody.

(2) *Hood Vortex*

A first detachment bubble forms due to the abrupt transition at the vehicle's leading edge. The wall shear stress lines in Fig. 6.4b indicate that the flow reattaches in the middle of the hood.

(3) *Windscreen*

Along the windshield, the fluid is accelerated and part of the flow is deflected sideways, colliding there with the upward flow from the side of the body, producing the A-Pillar vortex (9) shown in Fig. 6.5.

④ *Rooftop*

A second time, the flow separates at the roof and another, smaller recirculation bubble is formed (Fig. 6.3) with a stagnation line that is slightly tilted against the main flow direction (Fig. 6.4a).

⑤ *Horizontal Wake Vortex*

In the horizontal plane, the symmetrical recirculation region that is typical for the flow around blunt bodies is formed (Fig. 6.3). The incomplete symmetry indicates that the calculation has not yet fully converged.

⑥ *Vertical Recirculation Bubble*

The recirculation region is divided into two pairs of large counter-rotating vortices (Fig. 6.3). Whereas in the case of a subcritical slant angle (Fig. 3.1b), both vortices form below the rear partition and the flow remains attached until the trailing edge of the hatchback, the supercritical angle enforces early flow separation at the rear edge of the roof and the recirculation region extends much farther upwards.

⑦ *Vertical Lower Recirculation Bubble*

Another stagnation point appears on the underside of the tail due to the collision of the underbody flow with the lower recirculation bubble (Fig. 6.6b).

⑧ *Underbody*

The underbody flow is symmetric with streamlines increasingly heading outwards due to the pressure differences between the underbody and the surroundings (Fig. 6.6a).

⑨ *A-Pillar Vortex*

The A-pillar vortex in Fig. 6.5 emerges as a result of the upward flow at the side of the vehicle and the upward flow at the windshield (Fig. 6.4a). This contribution typically accounts for a large proportion of noise induced into the cabin, especially in the higher frequency range, (partly due to its close proximity to the driver's ear [149]).

⑩ (10) *Lower Vortex*

The flow emerging from the underbody generates a vortex at the side edge (Fig. 6.5). This vortex grows along the underbody and combines with the opposing vertex to form a large counter-rotating vortex pair as illustrated in [142].

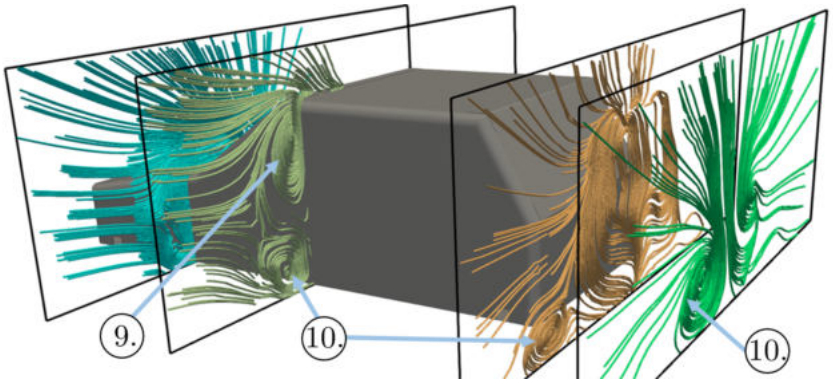

Figure 6.5: Visualization of mean flow streamlines in the plane normal to the mean flow (side view).

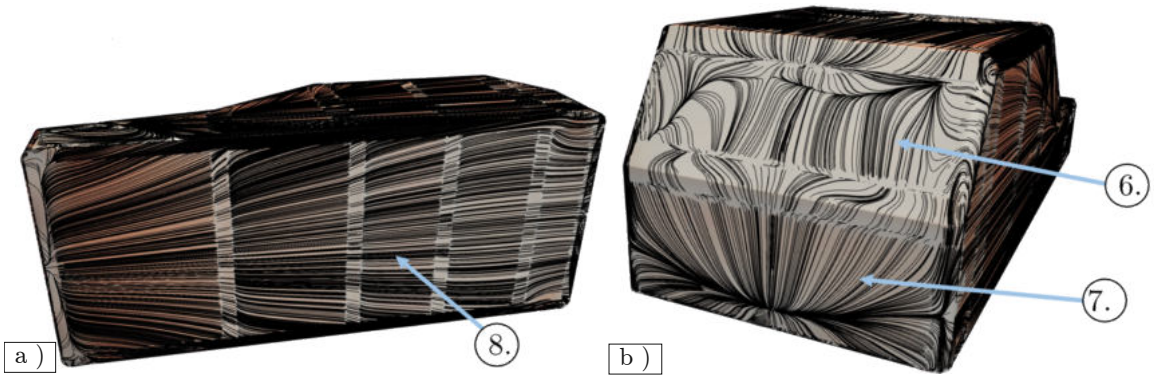

Figure 6.6: Visualization of wall shear lines (a) underbody view (b) rear view.

6.4 Instantaneous flow

Obviously, an evaluation of the unsteady processes associated with the turbulence is required to assess the induced excitation. The turbulence is filtered out by definition during averaging. In principle, unsteady processes can be analyzed in both the time and frequency domains; however, due to the large number of images required for frequency domain evaluation, we present only a randomly selected time step for illustration and perform the spectral evaluation based on the microphone positions in the next step. Naturally, it is possible to think of the instantaneous snapshot as a superposition of a large number of different periodic processes. The Q-criterion proposed by Hunt in [191] corresponds to the 2nd invariant

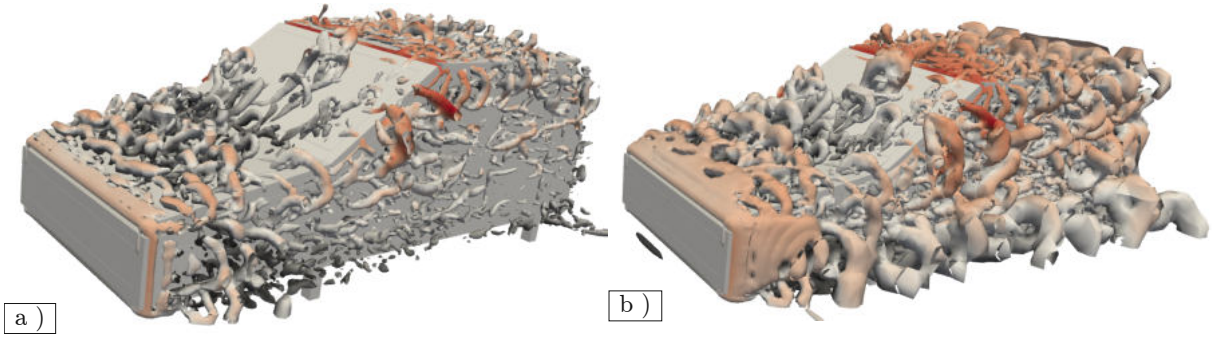

Figure 6.7: Q-Criterion with (a) $Q_{\mathrm{Iso}} = 6000$ (b) $Q_{\mathrm{Iso}} = 1000$

of the velocity gradient tensor. It can be rewritten in terms of norm of vorticity $\boldsymbol{\omega}_{\mathrm{f}}$ and shear strain rate $\boldsymbol{S}$ as $Q = 1/2\left(\|\boldsymbol{\omega}_{\mathrm{f}}\|^2 - \|\boldsymbol{S}\|^2\right)$ and therefore allows to visualize regions of high turbulent kinetic energy (positive Q) or regions with high visous stresses (negative Q, see [127]). Due to the relevance of vorticity as a source of noise, we are interested in the former. The corresponding isosurfaces for two chosen values are shown in Fig. 6.7. Different turbulent structures can be identified around the test body. On the one hand, these include longitudinal vortical structures that, when emitted, are aligned with the mean flow and hence become stretched during convection, but also u-shaped vortices that are initially oriented transverse to the mean flow and distorted during convection; these are well-known in fluid mechanics and referred to as horseshoe vortices [192]. The horseshoe vortex system is essentially a miniature version of the airfoil vortex created, for instance, during airplane takeoff, with the original lift-generating vortex parallel to the flow and vortex cores oriented in opposite directions along the flow. During convection, the vortices are stretched and, due to the lift generated at the leading part of the vortex system, it eventually lifts off the plane. If the legs are particularly long compared to the transverse vortex, the vortices are called hairpin vortices (more on this in [193]). A large part of these structures is already generated during

the initial separation at the front of the test body. The favorable velocity gradients at the windshield inhibit the production of turbulent structures and already existing vortex structures are deflected above the vehicle. At the roof, new vortices form, are transported to the rear, grow, and recombine with the initial vortices created during the initial flow separation. These turbulent vortices eventually lift off at the trailing edge and then contribute to the large-scale vortex structures behind the vehicle. In addition, large-scale vortices associated with the lower vortex in Fig. 6.5 (10) are clearly visible. Additionally, in Fig. 6.8, the physical quantities velocity norm $v_\mathrm{f} = |\boldsymbol{v}_\mathrm{f}|$, vorticity norm $\boldsymbol{\omega}_\mathrm{f} = |\omega_\mathrm{f}|$, and static pressure p_f are shown for the same time step in different planes in Fig. 6.8. Here we again see the lower vortex,

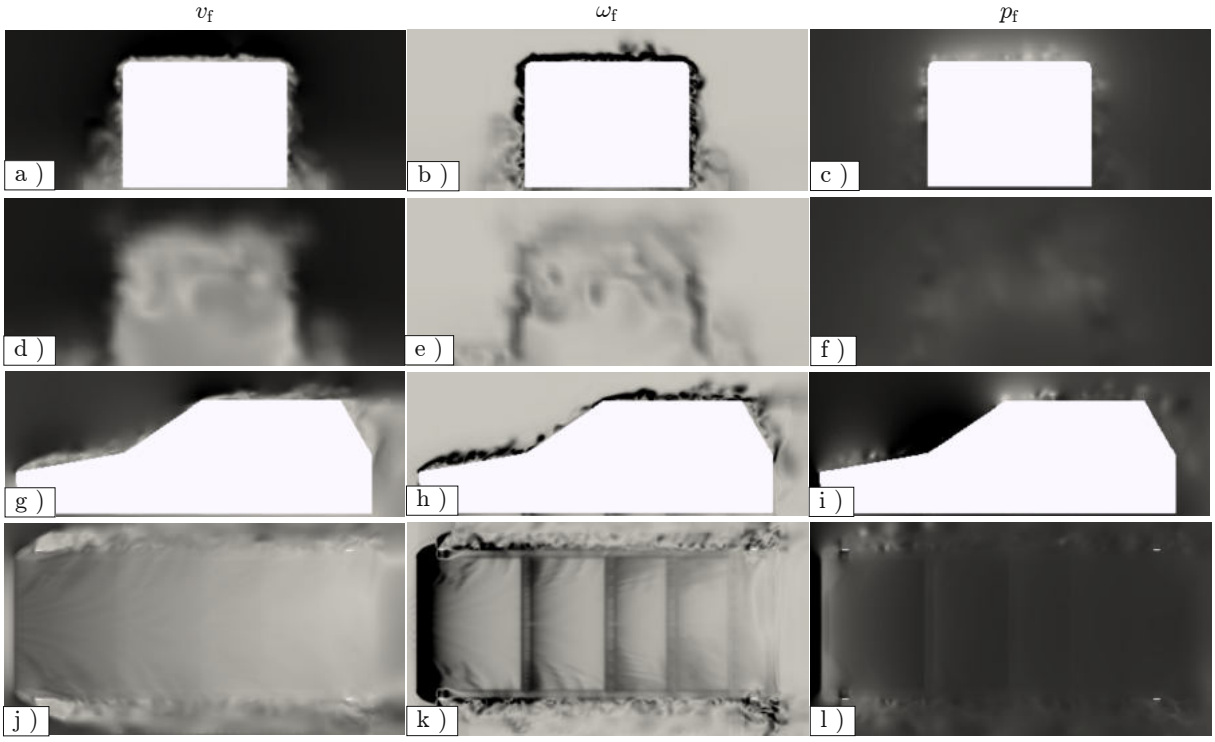

Figure 6.8: Instantaneous snapshots of velocity v_f (left column $0 - 40\,\mathrm{m/s}$), vorticity ω_f (middle column $0 - 1000\,1/\mathrm{s}$) and static pressure p_f (right column) $100633 - 101455\,\mathrm{Pa}$

the high vorticity norms in the detachment bubble at the roof as well as the high pressure fluctuations induced by it (Fig. 6.8a-c), the large-scale vortices behind the vehicle (Fig. 6.8d-f), the flow separations at the hood and the roof Fig. 6.8g-i as well as a Karmann vortex street originating at the supports and propagating to the rear of the vehicle (Fig. 6.8j-l).

6.5 Validation of wall pressure spectra

It is clear, based on the theory provided in Chap. 3, that in order to describe the effective excitation at the plates and, as a result, in order to compare the simulation results with wind channel measurements, the 5-dimensional cross-power density spectrum $\hat{S}_\mathrm{pf}(x, y, \zeta, \eta, \omega)$ at the wall should be examined. Dimensionality reduction based on the assumptions of homogenous turbulence and thus shift-invariance seems infeasible. At the same time, it is not possible to directly evaluate or interpret $\hat{S}_\mathrm{pf}(x, y, \zeta, \eta, \omega)$ and as a result, the crucial information must somehow be condensed to a limited number of plots. As a goal for the graphical evaluability and interpretability, it has been concluded that a single diagram should be sufficient to display the relevant information for each plate and case (measurement or simulation). As a result, we base our work on the metrics that can be applied to the scenario of homogeneous turbulence

and investigate the degree to which the essential assumptions do not apply. Taking into account the previously mentioned and frequently employed Corcos model, we can see that only surface pressure spectra at three positions—a reference position and a position that has been shifted in the longitudinal and lateral axes respectively—is required to obtain the model parameters. Thus, we investigate the CPSD $\hat{S}_{\mathrm{pf}}\left(x, x, \zeta, \eta, \omega\right)$ between each reference point $\boldsymbol{x}_{\mathrm{ref|i}}$ and the nearest longitudinal and lateral microphones at $(x_{\mathrm{ref|i}} + l_{\mathrm{mic}}, y_{\mathrm{ref|i}})$ and $(x_{\mathrm{ref|i}}, y_{\mathrm{ref|i}} + l_{\mathrm{mic}})$. As can be deduced from Fig. 6.2a, the in-flow pairings are AA′, BB′ and so on for all surfaces except *Side*, where the in-flow pairings are A′B′, B′C′,C′D′... and reciprocally in case of lateral pairings. As a required but not sufficient criterium for shift invariance, the APSD $\hat{S}_{\mathrm{pfc0}}(\omega)$ must agree over the surface as $\hat{S}_{\mathrm{pf}}\left(\boldsymbol{x}_{\mathrm{ref|i}}, \omega\right) = \hat{S}_{\mathrm{pf}}\left(\omega\right)$, so it is useful to examine the APSD and compare the individual APSD with an energetic average. Quantities without additional index furthermore denote arithmetic averages over the quantity itself (e.g. $\hat{S}_{\mathrm{pf}} = 1/N \sum_{n=1}^{N} \hat{S}_{\mathrm{pf|i}}$). In case of the APSD, arithmetically averaging over APSD corresponds to energetically averaging the underlying (complex) pressure spectra and hence $\hat{S}_{\mathrm{pf}}$ is referred to as energetic average. Regarding Eq. (3.41) it is clear, that the link between APSD ($\hat{S}_{\mathrm{pf|i}}$) and CPSD ($\hat{S}_{\mathrm{pf|ij}}$) in the Corcos model is the coherence $\hat{\gamma}_{\mathrm{pf}}(\zeta, \eta, \omega)$. The phase of the coherence is of special interest because it allows to deduce the convection velocity V_{c} of turbulent sources. As a result, the real part of the magnitude-squared complex coherence (MSC) $\hat{\gamma}_{\mathrm{pf|ij}}\left(\omega\right)$ defined as

$$\hat{\gamma}_{\mathrm{pf|ij}}\left(\omega\right) = \frac{\hat{S}_{\mathrm{pf|ij}}\left(\omega\right)}{\sqrt{\hat{S}_{\mathrm{pf|i}}\left(\omega\right)\hat{S}_{\mathrm{pf|j}}\left(\omega\right)}}\,. \tag{6.1}$$

is of special interest. We further denote the longitudinal magnitude-squared coherence (lonMSC) between a microphone at $\boldsymbol{x}_{\mathrm{ref|i}}$ and the neighboring longitudinally shifted microphone to $\hat{\gamma}_{\mathrm{pf}\zeta\mathrm{|i}}\left(\omega\right)$ and a laterally shifted microphone to $\hat{\gamma}_{\mathrm{pf}\eta\mathrm{|i}}\left(\omega\right)$. Finally, we are specifically interested in the low-frequency excitation, and therefore we additionally investigate the APSD of the arithmetically averaged pressure (avAPSD) given by

$$\hat{S}_{\overline{\mathrm{pf}}}(\omega) = \left|\left\{\hat{p}_{\mathrm{f|i}}(\omega)\right\}\right|^2 \tag{6.2}$$

on each surface. Note, that in contrast to the energetic mean the arithmetic mean takes phase cancellations into account. Hence a spatially uncorrelated excitation (with zero correlation length) and non-zero APSD will have zero avAPSD but non-zero energetic average. Furthermore, it must be noted that the *GRAS 40AF 1/2"* surface pressure microphone has a diameter of $d = 6.35\mathrm{mm}$, whereas a rectangular grid with edge length $l = 10\mathrm{mm}$ was used for the export of simulated pressure fluctuations. A difference in the area of the surface microphones however causes differences in the obtained APSD. This has been investigated by Corcos [161] and, based on his research, corrections can be applied. If his analytical formulas are used to examine the error due to finite microphone area, then for $U_{\mathrm{c}} = 33\mathrm{m/s}$ the relative error e in dB as $e(dB) = \hat{S}_{\mathrm{pf}}(\omega)(dB) - S_{\mathrm{pf|Real}}(\omega)(dB)$ amounts to $r_{\mathrm{l-500}} = 1.64\,\mathrm{dB}$ at $f = 500\,\mathrm{Hz}$ for the rectangular surface and to $r_{\mathrm{r-500}} = 0.9\,\mathrm{dB}$ for the circular microphone employed. Alltough rather small, the CPSD and APSD were corrected by employing the tabulated values in [161]. In conclusion, this provides us with a compact and meaningful representation of the critical and vibro-acoustically relevant statistical quantities. Although a log-log scale is useful for comparing power laws, it significantly distorts the spectrum, which is why a linear frequency axis is employed. In the detailed Figures in Fig. 6.9, 6.10, and 6.13, the APSD $\hat{S}_{\mathrm{pf|i}}(\omega)$ at each of the 14 measurement positions (red), the energetically averaged APSD $\hat{S}_{\mathrm{pf}}(\omega)$ (red with asterisks), the avAPSD $\hat{S}_{\overline{\mathrm{pf}}}$ (red with black dots), the CPSD $\hat{S}_{\mathrm{pf}\zeta\mathrm{|i}}$ and $\hat{S}_{\mathrm{pf}\eta\mathrm{|i}}$ between 7 longitudinal (green) and 6 lateral (magenta) microphone pairings, and the corresponding averaged CPSD $\hat{S}_{\mathrm{pf}\zeta}$ and $\hat{S}_{\mathrm{pf}\eta}$ (bold) are shown. In addition, the real part of the longitudinal (green) and lateral (magenta) coherence $\hat{\gamma}_{\mathrm{pf}\zeta\mathrm{|i}}$ and $\hat{\gamma}_{\mathrm{pf}\eta\mathrm{|i}}$ as well as the respective arithmetic means $\hat{\gamma}_{\mathrm{pf}\zeta}$ and $\hat{\gamma}_{\mathrm{pf}\eta}$ (bold) is shown in the upper right corner of each plot. Plots obtained from experimental data are

Frequency	Wavelength λ_c ($v_\infty = 34\,\mathrm{m/s}$)
10	0.53
25	0.21
50	0.11
100	0.05
250	0.02
500	0.01

Table 6.1: Convective wavelenght according to $\lambda_c = v_\infty/(2\pi f)$

displayed in the left column while plots from numerical data are displayed to the right. As shorthands, bracketed indices like (a) will be be used to refer to the subfigures in the corresponding section and e.g. (a&b) to denote features appearing in both (a) and (b) while (a ⅄ b) indicates differences between (a) and (b). Additionally, lonMSC and latMSC and respectively lonCPSD and latCPSD denote longitudinal and lateral MSC and CPSD.

6.5.1 Excitation by convected Turbulence

As already explained in Sec. 3.5.1 convection-dominated excitation can, in a simplified approach, be characterized by the presence of damped spatial harmonics with convection wavelength λ_c and phase velocity v_{conv} related by the dispersion relation as $\lambda_c = U_c/\omega$. For a preliminary estimate, Tab. 6.1 provides a set of wavelengths at free-field velocity v_∞ for different frequencies. By roughly comparing these bending wavelengths with those of the mode shapes in Fig. 5.7 it can already been deduced that aerodynamic coincidence does not occur. This is more likely to occur at high velocities and larger panel areas such as the side door [39]. Supposing the applicability of the Corcos model (Sec. 3.5.1), then the real part of the lonMSC between a reference position $\boldsymbol{x}_i$ and its closest in-stream neighbour (such as A′B′ at the side in Fig. 6.2) follows from Eq. (3.41) to

$$\mathrm{Re}\left\{\hat{\gamma}_{\mathrm{pf}\zeta|\mathrm{i}}(\omega)\right\} = \mathrm{Re}\left\{e^{-\gamma_{\zeta|i}|\omega\eta/V_c|}e^{ik_{conv}}\right\} = e^{-\gamma_{\zeta|\mathrm{i}}|\omega l_{mic}/V_c|}\cos\left(\omega l_{mic}/V_c\right) \tag{6.3}$$

and the latMSC between e.g. (AB in Fig. 6.2) solely reflects exponential decay as

$$\mathrm{Re}\left\{\gamma_{\mathrm{pf}\eta|\mathrm{i}}(\omega)\right\} = e^{-\gamma_{\eta|\mathrm{i}}|\omega l_{mic}/V_c|}\,. \tag{6.4}$$

A first glance on the individual plots of $\mathrm{Re}\left\{\hat{\gamma}_{\mathrm{pf}\zeta|\mathrm{i}}(\omega)\right\}$ and $\mathrm{Re}\left\{\gamma_{\mathrm{pf}\eta|\mathrm{i}}(\omega)\right\}$ in the individual upper right boxes of each realisation in Figs. 6.9, 6.10 and 6.13 shows that only the measurements at the windscreen, the roof and the side of the test body are of convective nature, i.e. show a lonMSC similar to Eq. (6.3). We note that the experimentally determined spectra are noticeably smoother than the numerical ones because of the longer time averaging of the measured data. Although the low-frequency properties of the complex vehicle flow do not satisfy the requirements given in Sec. 3.5.1 regarding the applicability of the Corcos model (no pressure gradient, homogeneous turbulence, constant APSD, etc.), the theoretical idea of reducing the WPF to the APSD plus a model consisting of only three parameters (convection velocity and lateral and longitudinal exponential decay) is however useful to investigate the overall characteristics of the excitation field. Starting with the APSD, we find that both experimental and numerical spectra fundamentally follow the overall trends shown in Fig. 3.3. Since the spectral maximum in the APSD scales with the thickness of the boundary layer δ, i.e. the correlation length of the largest vortices present, a shift to lower frequencies can be observed in the case of flow separation (and thus vortices scaling with the size of the recirculation region l_{char}). Correspondingly, the high vorticity and long correlation length

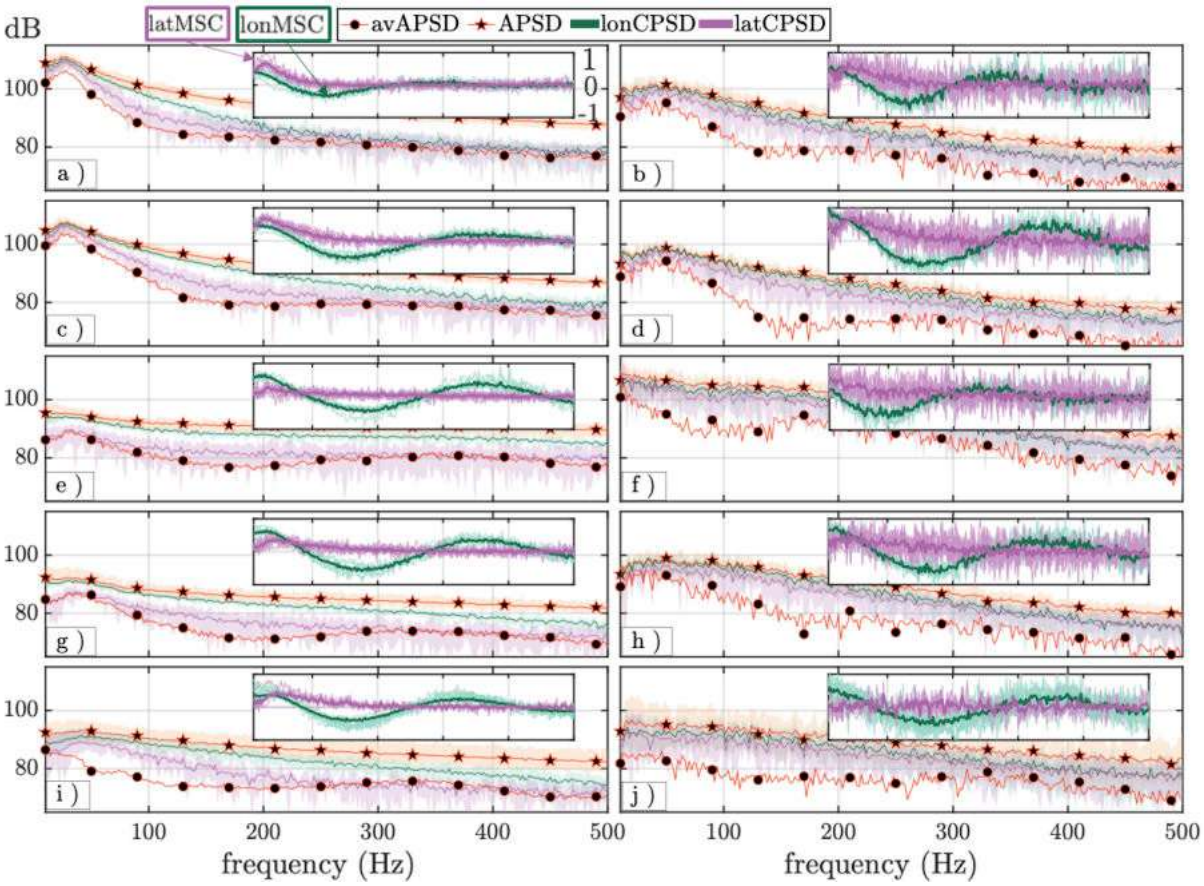

Figure 6.9: Statistical properties of WPF in convection dominated regions, left column: experimental, right column: numerical, positions according to Fig. 6.5a in regions: Windshield Low (a&b), Windshield High (c&d), Rooftop Front (e&f), Rooftop Rear (g&h), Side (i&j)

of turbulent structures cause an increase in APSD. For an exact localisation of the source terms, an experimental investigation by means of PIV (cf. [138]) is required which could not be carried out within the framework of this work. Nevertheless, based on the considerations provided in Sec. 3.5.1 and on the APSD, it can be assumed that the majority of the critical source terms are located in the logarithmic region of the turbulent boundary layer. Before delving to more detail into the various spectra, it is noted that from the different lonMSC and latMSC, the parameters of the Corcos model in Eq. (6.3) can be obtained by solving a minimisation problem that takes into account an additional scaling with $\hat{\gamma}_{\mathrm{pf|i}}(0)$, due to the condition for unity coherence at very low frequencies, which cannot be fulfilled in practice. This allows to reduce the experimental and numerical MSC to a more manageable set of parameters, specifically the phase velocity v_{conv} and the correlation parameters γ_η and γ_ζ. Hence, the lonMSC and latMSC are normalized according to $Re(\hat{\gamma}_{\mathrm{pf|i}}(\omega))/Re(\hat{\gamma}_{\mathrm{pf|i}}(0)$ and compared with the MSC of the Corcos model by defining an error function $\epsilon_{\mathrm{i}}(\omega)$ as

$$\epsilon_{\mathrm{i}}(\omega) = e^{-\gamma_{\zeta|\mathrm{i}}|\omega l_{\mathrm{mic}}/V_{\mathrm{c}}|}\cos\left(\omega l_{\mathrm{mic}}/V_{\mathrm{c}}\right) - Re(\hat{\gamma}_{\mathrm{p|ij}}(\omega))/Re(\hat{\gamma}_{\mathrm{p|ij}}(0)) \tag{6.5}$$

and to subsequently solve the nonlinear minimization problem

$$\min_{\gamma_{\zeta|\mathrm{i}}, V_{\mathrm{c}}\in\mathbb{R}} \|\epsilon_{\mathrm{i}}(\omega)\|^2 \tag{6.6}$$

	Windshield Low	*Windshield High*	*Rooftop Front*	*Rooftop Rear*	*Side*
v_{conv} *exp.*	32|26|27|26|22|20|25	29|30|30|29|28|28|28	29|36|34|31|30|30	31|32|34|34|30|30|31	24|30|29|30|29|28
v_{conv} *sim.*	24|22|20|24|22|26	30|29|27|29|29|28	20|20|20|18|18	30|26|26|23|26|27|28	30|33|28|36|34|33
γ_ζ *exp.*	0|2|3|2|2|2	3|4|4|7|3|4|3	3|3|3|4|6|3|4	7|4|4|2|5|4|5	3|3|0|0|5|4
γ_ζ *sim.*	4|5|5|4|5|3	6|9|6|8|6|5|5	4|5|5|4|3|4|4	8|5|5|4|4|4|5	2|3|3|0|3|4

Table 6.2: Corcos coefficients for the six different longitudinal microphone pairings in the upper row of *Side* (Fig. 6.2a A′B′, B′C′, C′D′, D′E′, E′F′, F′G′) and the seven longitudinal pairings at all other surfaces (Fig. 6.2a AA′, BB′, CC′, DD′, EE′, FF′, GG′).

using the Levenberg-Marquardt algorithm [194]. The Corcos model appears suitable to reproduce the longitudinal coherence, but significant deviation from the expected exponential decay occurs in the lateral direction, particularly in the low-frequency range and consequently only longitudinal parameters are utilized in the following. The parameters obtained in the curve-fitting process are shown in Tab. 6.2. Since the decay constant γ_ζ essentially describes the spatial structure of the convected turbulence, low values of γ_ζ can be interpreted as an indication of large-scale structures, and conversely, high decay indicates small-scale structures. Compared to the undisturbed incident flow velocity $v_\infty = 33\,\mathrm{m/s}$, the convection velocities at the upper windshield, the roof, and the side are within a realistic range of $U_\mathrm{c}/v_\infty \approx 0.5 - 1.1$. The convection velocities predicted by numerical simulation are underestimated, particularly at *Windshield Low* and *Rooftop Front*, indicating that the flow separation clearly apparent in Fig. 6.8 does not occur in practice. At these two surfaces, the decay constants are also significantly overestimated in the simulation, which can be explained by the fact that strong non-linear processes, i.e. decay, mixing and especially the formation of new turbulent structures, occur in the detached recirculation areas (cf. Fig. 6.7). The main differences and similarities between the simulated and measured data sets can now be compared using the condensed representation of the plots in Fig. 6.9. Considering that the APSD (red with stars) must be location-independent to allow for a shift-invariant description, it is apparent that this condition is only satisfied within a tolerance of $\approx 5\,\mathrm{dB}$ (shaded red area, a&b). However, the experimental APSD are significantly larger than numerical APSD, in a coarse estimate by $\approx 10\,\mathrm{dB}$ (a ↛ b). The disparity between the frequency maximum of the APSD at *Windshield Low* and *Windshield High* in numerical (50 Hz) and experimental (25 Hz) spectra indicates that the boundary layer thickness that is proportional to the characteristic size of turbulent structures is underestimated by a factor of two, indicating that the initial separation at the leading edge of the hood (Fig. 6.7) might also be overestimated (a ↛ b). Conversely, the APSD of *Rooftop Front* and *Rooftop Rear* are greatly overestimated by the numerical simulation by $\approx 20\,\mathrm{dB}$ (e ↛ f) and $\approx 10\,\mathrm{dB}$ (g ↛ h), furthermore supporting the conclusion that flow separation does not occur in reality. At higher frequencies all APSD in Fig. 6.9 reproduce the experimental data. Expectedly, the lonCPSD are much closer to the APSD than the latCPSD due to the convection of turbulent sources (i.e. the correlation length is much larger if the source is convected). It is apparent, that the experimental lonCPSD deviate much farther from the APSD than the numerical lonCPSD. The level difference between lonCPSD and APSD increases with frequency because of the stronger decorrelation with increasing number of phase sweeps. A major difference is visible when comparing the latCPSD. The numerical latCPSD are very close to the lonCPSD and the APSD, and interestingly the experimental latCPSD are actually a decent estimate of the arithmetically averaged spectrum avAPSD ($\hat{S}_{\overline{\mathrm{pf}}}(\omega)$,red with black circles). The reason for this cannot be clarified without detailed experimental investigation, but it seems that the lateral extent of the structures is significantly overestimated in the numerical simulation. At *Side*, the avAPSD differs significantly from the latCPSD and the APSD owing to the streamwise orientation of the array (Fig. 6.2). On the other hand, the experimental spectra can be reproduced fairly well on the side of the vehicle, both in terms of the CPSD,

the APSD and MSC Fig. 6.9i&j and the phase velocities in Tab. 6.2.

6.5.2 Excitation from leeward components

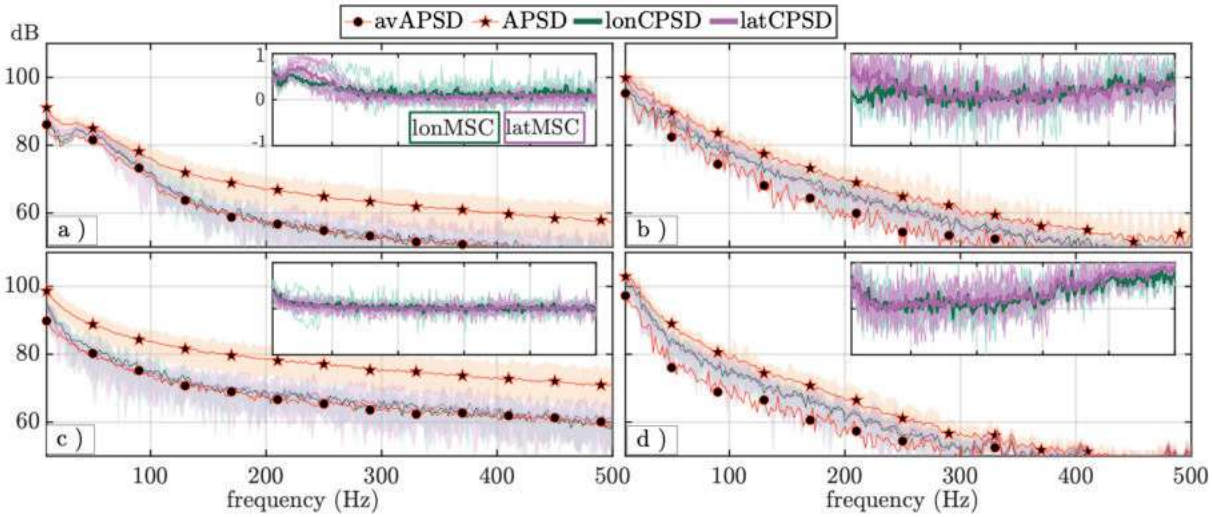

Figure 6.10: Statistical properties of WPF in wake dominated regions, left column: experimental, right column: numerical, positions according to Fig. 6.5a in regions: Trunk High (a&b), Trunk Low (c&d)

The excitation of plates facing the recirculation region behind the vehicle, i.e. *Trunk High* and *Trunk Low*, are now investigated. The abbreviations thus refer to the subplots in Fig. 6.10. In contrast to the convective spectra, neither lonMSC nor latMSC show a phase relation and therefore do not indicate a dominant convection velocity v_{conv} (a-d). Unlike the convective spectra in Fig. 6.9, that, in accordance with the theory of turbulent WFP show distinct power laws in different frequency regions, all of the statistical curves depicted here (i.e. CPSD, APSD and the avAPSD) follow the same power law (a-d). However, the logarithmic slope of (a&b&d) decreases with $\approx 10\,\text{dB/octave}$ for frequencies $f > 100\,\text{Hz}$ while in (c) the slope is only $\approx 5\,\text{dB/octave}$ (c↚d). The cause of this difference in power law scaling has not yet been identified. Although the APSD in (c) are greatly exaggerated, the vanishing MSC has minimal influence on the important avAPSD, particularly at higher frequencies. Although the experimental APSD in (c) are much higher than the numerical APSD in (d) the avAPSD are somewhat similar. This is in line with the low MSC in (c), hence there seem to be small-scale eddies in the mixing zone between the underbody and the recirculation region that are not present in the simulation results but are presumably negligible at low frequencies due to small coherence. Examining the characteristic size of the large-scale vortices in Fig. 3.1 and considering that typical Strouhal numbers for flow separation are in the range of $St \approx 0.3 - 0.5$ and that $St = fl_{\text{char}}/v_\infty$ allows to locate the corresponding frequency maximat at $f \approx 2 - 4\,\text{Hz}$ and thus, at least for the chosen velocity and the geometric scales of the test body, well below the hearing threshold. Regarding the weakly pronounced peak at $f \approx 40\,\text{Hz}$ in (a) that has not been reproduced in the simulation (a↚b), a Strouhal number of $St \approx 5$ can be calculated (as in 3.4), which is far above the usual vortex shedding frequencies . Note also that neither Zhang's [140] nor Thacker's [139] investigations display a similar peak. Nonetheless, when examining the analysis of Islam [127] for the rectangular and the sloped ($\alpha = 40°$) Ahmed body, the results reveal a comparable spectral peak at $f = v_\infty/H$, which would also suit well with the spectral peak reported here ($f = v_\infty/H = 41\,\text{Hz}$). The corresponding physical justification has not yet been found. A second spectral maximum discovered in [127] was attributed to the shear layer on the ground and is likely not discernible here owing to the low ground clearance employed. The maxima identified by Zhang [140] (Fig. 3.1) at the underbody

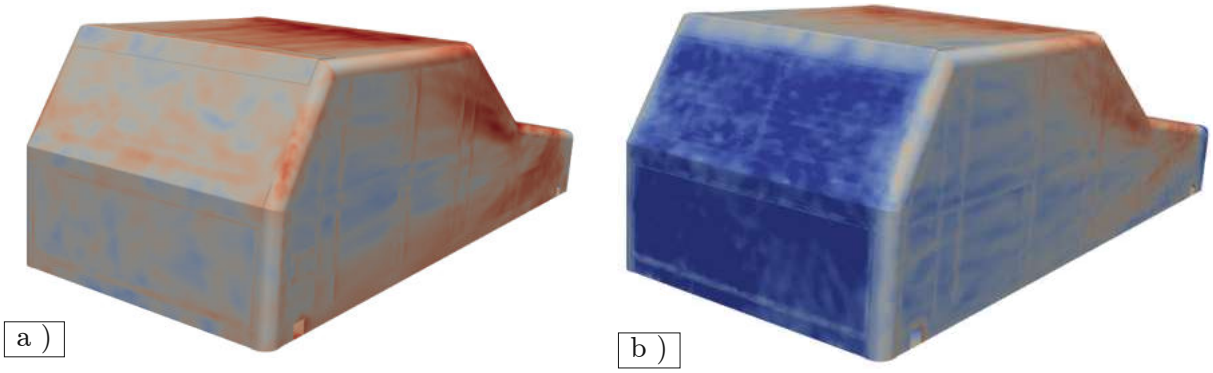

Figure 6.11: APSD at (a) 50Hz, (b) 200Hz, limits for both figures: (70 dB (blue) -110 dB (red)))

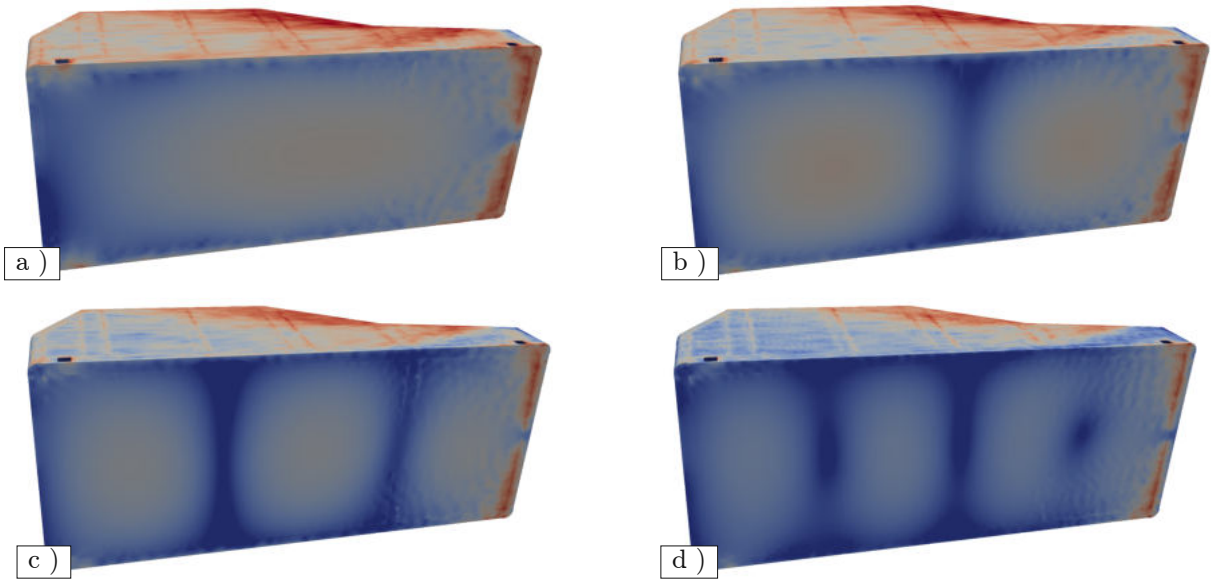

Figure 6.12: APSD at (a) 214Hz, (b) 266Hz, (b) 324Hz, (b) 404Hz, limits for both figures: (65 dB (blue) -100 dB (red))

and associated with the struts also have comparable Strouhal numbers, but convection of the underbody vortices up to the upper part of the tail seems rather implausible. The low-frequency ($f < 50\,\mathrm{Hz}$) excitation at *Trunk High* is clearly overestimated by $\approx 10\,\mathrm{dB}$ (a ⅄ b). It is further interesting to note, that the numerical MSC converge to unity at high frequencies, indicating purely acoustic excitation, while this is not the case regarding experimental MSC (a ⅄ b),(d ⅄ d). To conclude, it can be stated that the excitation from structures facing the recirculation region is limited to low frequencies.

6.5.3 Excitation from the underbody

It has been explained in detail in Sec. 3.5.3 and will now be demonstrated that acoustic modes play a dominant role in the excitation of the two underbody panels *Floor Front* and *Floor Rear*. The modal character of the acoustic underbody cavity is readily apparent in the simulated APSD in Fig. 6.13 (b&d). The corresponding spatial APSD at the resonant peaks in (b&d) are shown in Fig. 6.12. Based on the dispersion relation and the acoustic wavelengths of $\lambda_x \approx [2L, 2L/2, 2L/3, 2L/4]$ and $\lambda_y = 2B$, the acoustic natural frequencies can be estimated to be $(261, 305, 367, 439)\,\mathrm{Hz}$, which agrees reasonably well with the spectral peaks in (b&d). The dispersion relation can therefore easily be employed to obtain an initial estimate of critical acoustic resonance frequencies in aero-vibro-acoustic investigations. Two

major aerodynamic sources can be identified, being the Karmann vortex street on the vehicle's side and the high excitation at the front of the test body. Regarding the set of curves in Fig. 6.14, it is evident that all curves obtained from simulation data coincide on a uniform set of curves, while the APSD in the measured spectra is approximately 10 dB larger than the corresponding lonCPSD, latCPSD and the avAPSD. Upon further examination of the MSC, it becomes evident that the simulation results indicate a purely acoustic excitation of the underbody, whereas the experimental measurements indicate a substantial aerodynamic contribution. In spite of this, the measured data does not show a convective phase shift in the lonMSC. Thus, once again, there seem to be small-scale eddies with high decorrelation rate in the underbody that have not been resolved in the simulation. However, this excitation appears negligible at least at low frequencies because it does not contribute substantially to the CPSD and the avAPSD. The investigation of the CPSD or the avAPSD clearly highlights the dominant coherent excitation via acoustic modes at $(268, 370, 452)$ Hz which in turn demonstrates that for a physically meaningful analysis of WPF on the underbody, it is not the APSD (as investigated in [29, 33, 34, 38]) but the CPSD that must be investigated between two microphones with a reasonable distance regarding the wavelengths of the anticipated structural modes. The clearly visible narrow-band peak in (a) can be attributed to the primary mode of *Floor Rear* at 77 Hz (Fig. 5.7, see also Fig. 5.8c) and thus indicates that vibro-acoustic coupling can occur in the underbody that is not yet accounted for in the workflow pursued.

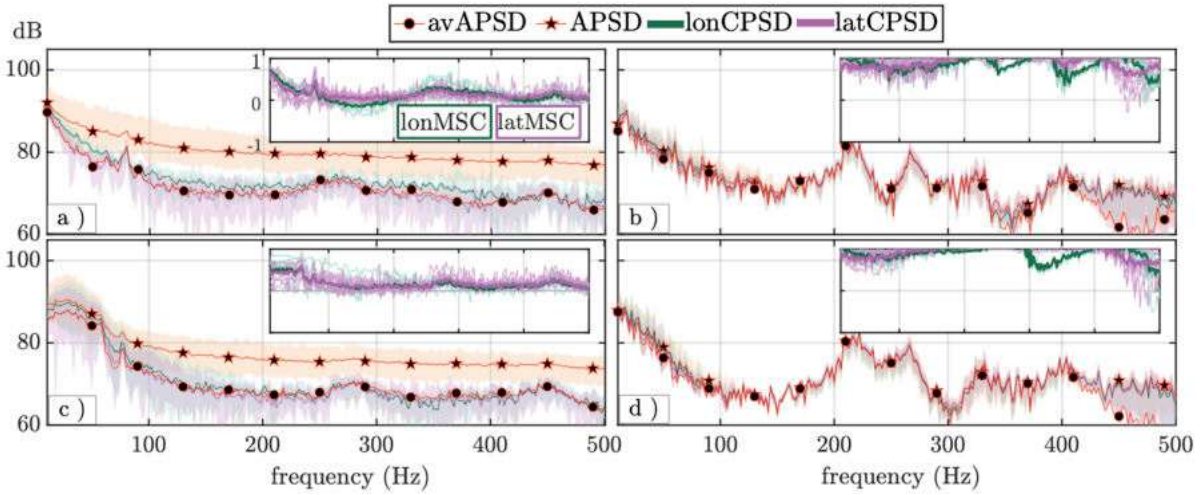

Figure 6.13: Statistical properties of WPF in underbody regions, left column: experimental, right column: numerical, positions according to Fig. 6.5a in regions: Floor Front (a&b) and Floor Rear (c&d)

6.6 Ranking of different excitations

The work carried out so far had the overall objective of reducing the complex statistical description of the WPF to a few, interpretable and comparable graphs to be able to carry out a comparison between simulated and experimental WPF regarding vibro-acoustic excitation. From the previous investigations, it is concluded that the (energy-averaged) lonCPSD $\hat{S}_{\mathrm{pf}|\zeta}$ and the avAPSD $\hat{S}_{\overline{\mathrm{pf}}}$ are highly representative. The Corcos parameter should additionally be considered in convection-dominated regions. Thus, a condensed plot can be produced to directly compare experimental and numerical spectra for both the lonCPSD and the avAPSD. These graphs are shown in Fig. 6.14 and Fig. 6.15 with the areas between the two curves shaded in color. On the roof, sides, and trunk, the avAPSD matches better than the lon-

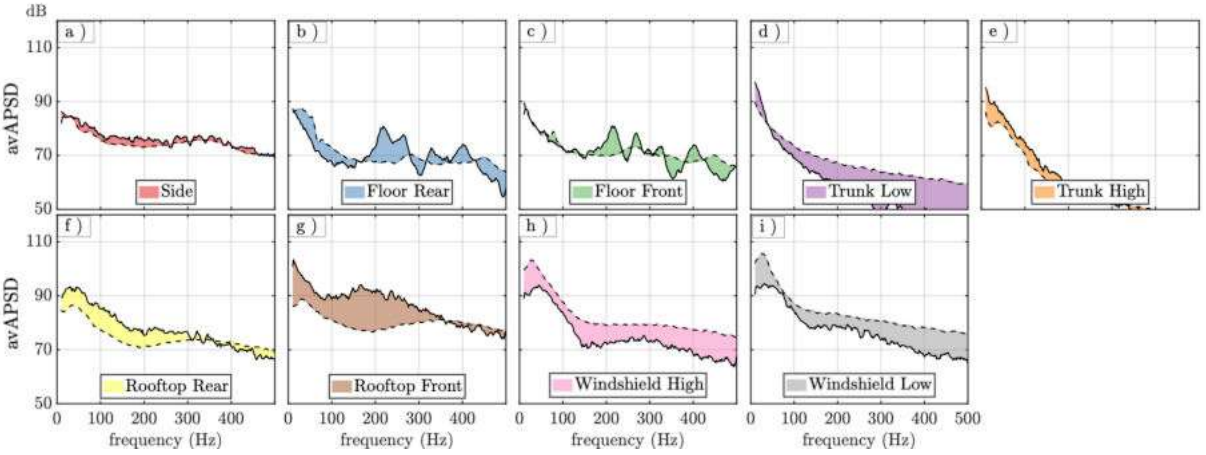

Figure 6.14: Comparison of experimental (dashed) and simulated (solid) arithmetically averaged pressure spectrum $\hat{S}_{\overline{\mathrm{pf}}}$, Errors shaded in color

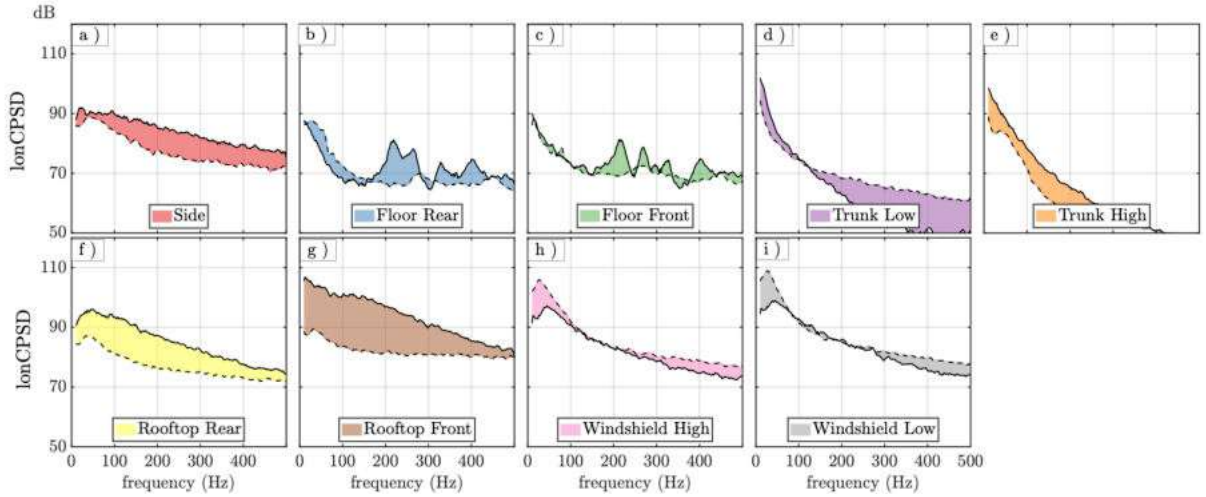

Figure 6.15: Comparison of experimental (dashed) and simulated (solid) lonCPSD ($\hat{S}_{\mathrm{pf}\zeta}$), Errors shaded in color

CPSD, while the opposite is true for the windshield. Due to the high coherence of acoustic waves in the underbody, the corresponding avAPSD and lonCPSD are fairly comparable. Substantial discrepancies can be distinguished, specifically the already mentioned underestimation of excitation at the windshield ($\approx 10\,\mathrm{dB}$) and an overestimation of excitation at the leading roof plate *Rooftop Front* ($\approx 20\,\mathrm{dB}$). For a better classification we group the spectra into four different frequency bins ($10-50\,\mathrm{Hz}$, $50-100\,\mathrm{Hz}$, $100-250\,\mathrm{Hz}$, $250-500\,\mathrm{Hz}$), calculate the respective mean in the frequency bin and rank the results (Tab. 6.3). In addition to the lonCPSD and avAPSD, the commonly used APSD (e.g., [29, 34, 38]) has been added to determine whether this most common interpretation is actually physically meaningful. It therefore makes sense to first examine only the rankings of the different experimental and numerical statistical scores. We see that especially for convectively excited regions all three measures provide a comparable ranking. At the underbody, however, the APSD is rather unsuitable for assessing experimental WPF, as the relevant acoustic component is hidden beneath the noise floor (Fig. 6.13a&c). Due to the high coherence, the lowest frequency bin displays the largest deviations, whereas at higher frequencies, all indicators are comparable. Quantitatively comparing the obtained rankings between numerical and experimental WFP reveals that the previously mentioned erroneous prediction of flow separation at the roof and the underestimation of turbulent structures convected along the windshield (Sec. 6.5.1) affects the ranking

		Side	Underbody Rear	Underbody Front	Rear Low	Rear High	Rooftop Rear	Rooftop Front	Windshield High	Windshield Low
10-50 Hz	$\hat{S}_{pf}$ (APSD, exp.)	5	7	8	4	9	6	3	2	1
	$\hat{S}_{pf\zeta}$ (lonCPSD, exp.)	7	4	8	6	9	5	3	2	1
	$\hat{S}_{\overline{pf}}$ (avAPSD, exp.)	4	5	9	6	8	7	3	2	1
	$\hat{S}_{pf}$ (APSD, sim.)	7	9	8	5	6	3	1	4	2
	$\hat{S}_{pf\zeta}$ (lonCPSD, sim.)	7	9	8	6	5	3	1	4	2
	$\hat{S}_{\overline{pf}}$ (avAPSD, sim.)	7	9	8	4	6	5	1	3	2
50-100 Hz	$\hat{S}_{pf}$ (APSD, exp.)	4	8	7	6	9	5	3	2	1
	$\hat{S}_{pf\zeta}$ (lonCPSD, exp.)	5	6	7	8	9	4	3	1	2
	$\hat{S}_{\overline{pf}}$ (avAPSD, exp.)	3	7	9	8	6	5	4	1	2
	$\hat{S}_{pf}$ (APSD, sim.)	5	9	8	7	6	3	1	4	2
	$\hat{S}_{pf\zeta}$ (lonCPSD, sim.)	5	9	7	8	6	4	1	3	2
	$\hat{S}_{\overline{pf}}$ (avAPSD, sim.)	5	9	8	7	6	3	1	4	2
100-250 Hz	$\hat{S}_{pf}$ (APSD, exp.)	4	8	6	7	9	5	3	2	1
	$\hat{S}_{pf\zeta}$ (lonCPSD, exp.)	4	8	6	7	9	5	3	2	1
	$\hat{S}_{\overline{pf}}$ (avAPSD, exp.)	4	8	6	7	9	5	3	2	1
	$\hat{S}_{pf}$ (APSD, sim.)	4	8	6	9	7	2	1	5	3
	$\hat{S}_{pf\zeta}$ (lonCPSD, sim.)	4	7	6	9	8	2	1	5	3
	$\hat{S}_{\overline{pf}}$ (avAPSD, sim.)	4	7	6	9	8	2	1	5	3
250-500 Hz	$\hat{S}_{pf}$ (APSD, exp.)	4	7	6	8	9	5	1	3	2
	$\hat{S}_{pf\zeta}$ (lonCPSD, exp.)	4	7	6	8	9	5	1	3	2
	$\hat{S}_{\overline{pf}}$ (avAPSD, exp.)	5	7	6	8	9	4	1	3	2
	$\hat{S}_{pf}$ (APSD, sim.)	2	7	6	9	8	3	1	5	4
	$\hat{S}_{pf\zeta}$ (lonCPSD, sim.)	2	7	6	9	8	3	1	5	4
	$\hat{S}_{\overline{pf}}$ (avAPSD, sim.)	2	7	6	9	8	3	1	5	4

Table 6.3: Sorted Contributions for different frequency bins and different statistic measures (1- highest, 9- lowest)

up to the point that the most dominant contributor in the experimental WPF is *Windshield Low* while in the numerical WPF it is *Rooftop Front*. The smallest contribution on the other hand does not stem from *Underbody Rear*, as supposed by numerical WPF but from *Rear High*. In line with the previous explanations, the numerical and experimental rankings agree better at higher frequencies. In summary, the extensive investigation of the measurement and simulation data revealed that the direct aerodynamic/aeroacoustic excitation of the generic test body can be grouped into three distinct categories, each with its own unique spectral properties.

7 Flow-induced noise inside the generic structure

Now, after the development of a non-conforming modal method for the hybrid treatment of aero-vibro-acoustic systems (Chap. 4), the development and validation of a generic testbody (Chap. 5) and the simulation and validation of the excitation characteristics (Chap. 6), we can turn to the final objective of this thesis, which is the calculation of wind-induced noise inside the test body. Note, that the simulation procedure has previously been performed for a simple version of the testbody with rather thick 3 mm plates and that the results have been published in [178]. However, since the induced noise was mainly transmitted through the windshield, a more challenging variant comprising a multitude of thin 1 mm plates in addition to thick 3 mm plates at the most strongly excited panels *Windshield* and *Floor Front* panels is employed for the final validation. Furthermore, it will be shown that the modal substructuring technique can handle direct excitation via leaks and openings.

7.1 Methodology and custom workflow

Based on the non-conforming modal approach presented in Chap. 4, a custom tool was developed for the efficient solution of aero-vibro-acoustic problems. The basic structure of the workflow is shown in Fig. 7.1. All computations are based on data stored in the primary data container *Storage*. This includes, on the one hand, the mechanical and acoustic modal shape matrices $\boldsymbol{\Psi}_\mathrm{s}$ and $\boldsymbol{\Psi}_\mathrm{a}$ with column-wise stored modes $\boldsymbol{\psi}_{\mathrm{s|i}}$ and $\boldsymbol{\psi}_{\mathrm{a|i}}$ with the corresponding grids and the respective eigenvalue vectors $\boldsymbol{\Lambda}_\mathrm{s}$, $\boldsymbol{\Lambda}_\mathrm{a}$ as well as the modal damping vectors $\boldsymbol{\zeta}_\mathrm{s}$, $\boldsymbol{\zeta}_\mathrm{a}$. These modes may be acquired by either FE simulation or EMA. In the case of EMA, only point clouds are available and the required grid is obtained by Delaunay triangulation. Grids are theoretically available for computational modes, but because FE models in complex simulations may contain a large number of different finite elements, it is advantageous to extract the corresponding point clouds of the inner and outer hull and reconstruct a triangular grid using Delaunay triangulation. At this point, it should be emphasized that only nodes located at the structure-acoustics or structure-flow coupling interfaces, as well as those nodes of interests for post-processing (e.g. a selection of nodes inside the cavity) are necessary for performing the modal workflow. This means that, for instance, the displacements in the engine compartment can be included in the initial FE model for deriving the modes, but they do not need to be stored, thereby significantly reducing the computational effort. The corresponding grids are then added to *Storage*. In addition, the external loads must also be stored in the form of the FFT-transformed (complex) surface pressure distribution $\hat{\boldsymbol{p}}_{\mathrm{s|i}}$ on the corresponding grid. Naturally, the consideration of other types of Loadcases, such as mechanical $\hat{\boldsymbol{f}}_{\mathrm{s|i}}$ or acoustic loads $\hat{\boldsymbol{q}}_{\mathrm{a|i}}$ is also possible. The solution of a particular aero-vibro-acoustic issue then requires the definition of the acoustic and mechanical modes involved, the coupling areas between structure and cavity $\Gamma_{\mathrm{i|s}} - \Gamma_{\mathrm{i|a}}$ or structure and flow $\Gamma_{\mathrm{i|s}} - \Gamma_{\mathrm{i|f}}$ and the choice of the correct loadcase (e.g. wind at 120 km/h). Then, using the method described in Sec. 4.2, the non-conforming coupling matrices are created between the respective coupling surfaces and the modal coupling terms are obtained by projecting each coupling matrix onto the acoustic and mechanical modes according to Eq. (4.57). For the transformation of aerodynamic pressure

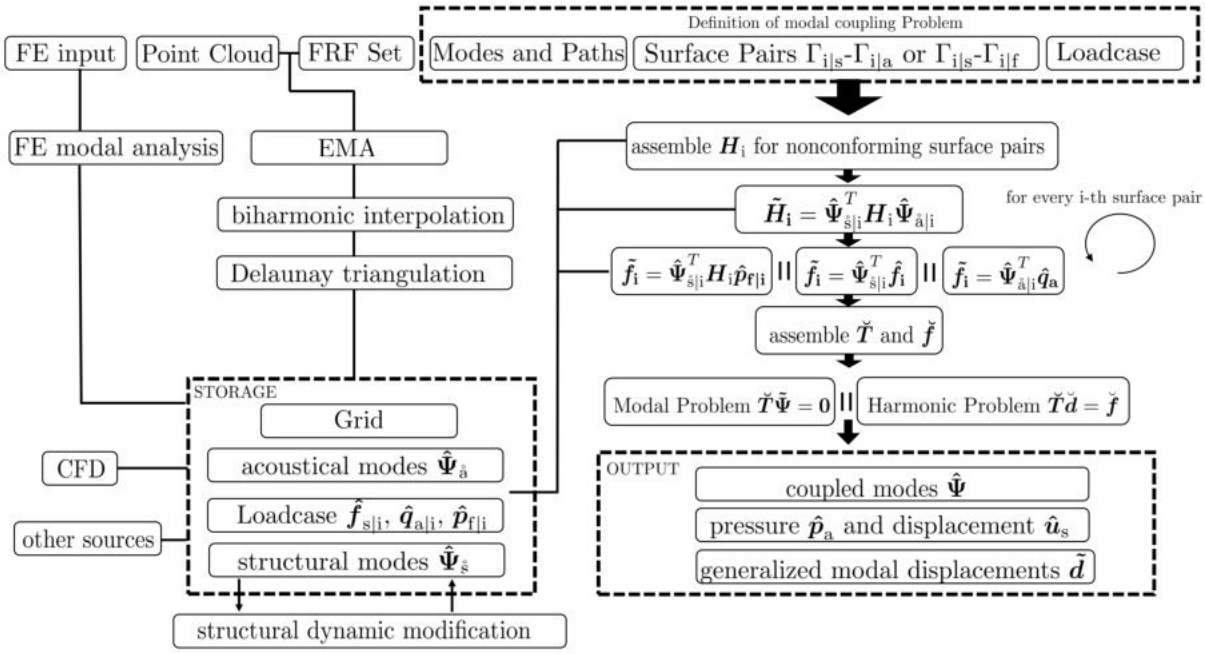

Figure 7.1: Custom tool for assessing noise inside vehicles.

loading $\hat{\boldsymbol{p}}_{s|i}$ into consistent nodal loads $\hat{\boldsymbol{f}}_{s|i}$, an additional (non-conforming) coupling matrix is required. This coupling matrix can be obtained similar to the vibro-acoustic coupling matrices (see Eq. (4.64)) and the modal loads can then be determined by projection onto the respective mechanical modes,. The modal parameter matrix $\tilde{\boldsymbol{T}}$ can then be assembled according to Eq. (4.58). The harmonic problem in Eq. (4.61) can then be solved to finally synthesize the coupled modes $\hat{\boldsymbol{\Psi}}$, the displacements $\hat{\boldsymbol{v}}_s$, and/or the acoustic pressure field $\hat{\boldsymbol{p}}_a$. The generalized modal displacements $\tilde{\boldsymbol{d}}$ can also be obtained to assess the individual contributions of different vibro-acoustic modes (Sec. 4.3.3). The averaging process described in Secs. 3.2 and 3.3 is implemented in two different ways. If, as is frequently the case, only the spectrum at a specific point at $\boldsymbol{x}_i$ (e.g. the driver's ear) is of interest, than the APSD is obtained by averaging over a set of ensemble members according to Eq .(3.33). If the full spatial APSD is of interest, averaging is performed on a modal level, as described in Eq. (3.39). Due to the $4\,s$ time frame of the simulation, the modal harmonic equation in Eq. (4.62) is solved with an initial resolution of $\delta f = 0.25\,\mathrm{Hz}$. The spectra are then transformed back into time domain and averaged over 4 blocks with an additional Hamming window to achieve a final APSD resolution of $\Delta f = 1\,\mathrm{Hz}$. In a FE formulation, the excitation of an acoustic cavity via openings can be taken into account by setting the boundary condition at the nodes according to $\hat{p}_{f|e} = \hat{p}_{a|e}$. However, having to extract the acoustical modes subject to an additional inhomogenous boundary condition at the opening would have severe negative impacts on the modal workflow presented, which is why an alternative solution is sought. The alternative solution begins by computing the acoustic modes by imposing an additional homogeneous boundary condition at the rear vent ($\hat{p}_{a|e} = 0$). Examining

Figure 7.2: Pressure distribution in Helmholtz cavity $\hat{\boldsymbol{p}}_{a|i}$.

the pressure field in the rear vent for the acoustic modes in Fig. 7.2, one finds that the rear vent behaves like a simple acoustic mass $m_h = \rho_0 l_h / A_h$ (see section 3.5.4) for all these low-order modes. We can

N_c	f_c	f_{uc}	ζ_{uc}	orig. region	orig. N_{uc}	N_c	f_c	f_{uc}	ζ_{uc}	orig. region	orig. N_{uc}
1	5.73	5.77	1.00	Cavity	1	16	127.59	127.80	0.65	Rear Low	2
2	72.10	72.39	0.52	Roof Rear	1	17	130.86	128.98	1.00	Cavity	2
3	74.56	75.00	1.31	Roof Front	1	18	131.09	131.13	2.05	Side Window (right)	1
4	76.25	76.58	2.04	Floor Rear	1	19	134.74	131.13	2.05	Side Window (left)	1
5	85.92	87.48	1.62	Floor Front	1	20	137.84	138.14	0.57	Floor Rear	5
6	90.40	91.93	1.40	Windshield	1	21	138.13	138.21	0.89	Floor Front	2
7	90.88	94.00	0.47	Roof Front	2	22	139.68	139.42	1.37	Roof Rear	4
8	96.90	97.64	0.53	Roof Rear	2	23	143.29	143.70	0.03	Side Window (right)	2
9	97.29	99.67	4.41	Rear Low	1	24	143.70	143.70	0.03	Side Window (left)	2
10	100.76	101.00	1.38	Floor Rear	2	25	143.70	143.89	0.53	Windshield	2
11	110.15	110.16	0.09	Floor Rear	3	26	145.81	145.90	0.28	Rear High	2
12	115.84	116.02	1.90	Floor Rear	4	27	146.23	146.05	1.78	Roof Rear	5
13	118.16	119.27	0.65	Roof Rear	3	28	150.97	152.44	1.60	Side Front Low (right)	1
14	119.04	119.38	0.69	Roof Front	3	29	152.10	152.44	1.60	Side Front Low (left)	1
15	119.34	119.58	0.93	Rear High	1	30	158.43	158.57	0.23	Roof Front	4

Table 7.1: Coupled and uncoupled eigenfrequencies of the generic structure. Ranking by frequency, thus coupled modes at coupled eigenfrequencies (f_c) need not necessarily be dominated by uncoupled modes with eigenfrequencies (f_{uc}) in the same row. Individual mode order denoted by N_{uc}. Coupled modes highlighted in blue are acoustically dominated modes.

thus replace the inner quantity $\hat{p}_{f|e}$ by an equivalent volume acceleration $\hat{q}_{a|i} = \hat{p}_{f|e}/(-\omega^2 m_h)$. It follows directly that increasing the acoustic mass of the rear vent m_h by increasing the length l_h or decreasing the cross section A_h directly reduces the induced volume acceleration. The equivalent modal load of the i-th acoustic mode can therefore be obtained by projecting the mean acoustic source term determined from the mean pressure at the outer nodes $\boldsymbol{x}_l$ of the rear vent onto the the acoustic modes evaluated at the inner side of the rear vent at position $\boldsymbol{x}_j$ according to $\tilde{q}_{a|i} = \hat{\Psi}_{\mathring{a}|ji} 1/(-\omega^2 m_h)(\sum_{l=1}^{N} \hat{p}_{a|l}/N)$. It is now possible to assemble the generalized modal forces as $\tilde{\boldsymbol{f}} = \left[\tilde{\boldsymbol{f}}_s; i\omega\tilde{\boldsymbol{q}}_a\right]$, to solve Eq. (4.61) and to proceed farther as explained previously.

7.2 Coupled vibro-acoustic system

Now, the uncoupled computational acoustic modes in Fig. 5.4 with estimated acoustic modal damping of $\zeta_a = 0.01$ (see Fig. 5.6) can be coupled with the experimental mechanical modes in Fig. 5.7 and the corresponding structural modal damping values ζ_{uc} in Tab. 7.1 to obtain a coupled vibro-acoustic model of the plate-cavity system. In order to reduce the coupling error and obtain a more precise mapping of the WPF, we refine the mechanical modes via the TPS interpolation presented in Sec. 4.4.1 onto an equidistant rectangular grid with discretization length of 1 cm. Then, using the modal workflow, the natural frequencies of the coupled system can be calculated and compared with the uncoupled natural frequencies. The results can be investigated either in tabular form in Tab. 7.1 or in the diagram shown in Fig. 7.3. The frequencies of the acoustically dominated coupled eigenmodes are shifted with respect to the uncoupled eigenfrequencies of the uncoupled mechanical modes (coloured in blue). In contrast to the investigations in Sec. 5.3.1, where a downward shift of the acoustic eigenfrequencies was observed, the acoustically dominated coupled eigenfrequencies are now shifted to higher frequencies. This can be explained by the fact that in the variant with 3 mm panels all modes are above the two lowest acoustic eigenmodes and the mechanical modes then act as additional mass, while in the 1 mm case in particular the vibro-acoustically important fundamental modes are below the two acoustic eigenfrequencies. These mechanical modes thus act as an additional acoustic stiffness and shift the natural frequencies upwards ($f_{a|1} = 128\,\text{Hz} \Rightarrow f_{c|19} = 135\,\text{Hz}$). The associated shifts of mechanical eigenfrequencies are small, supporting the assumption that mechanical modes can be extracted from the coupled system.

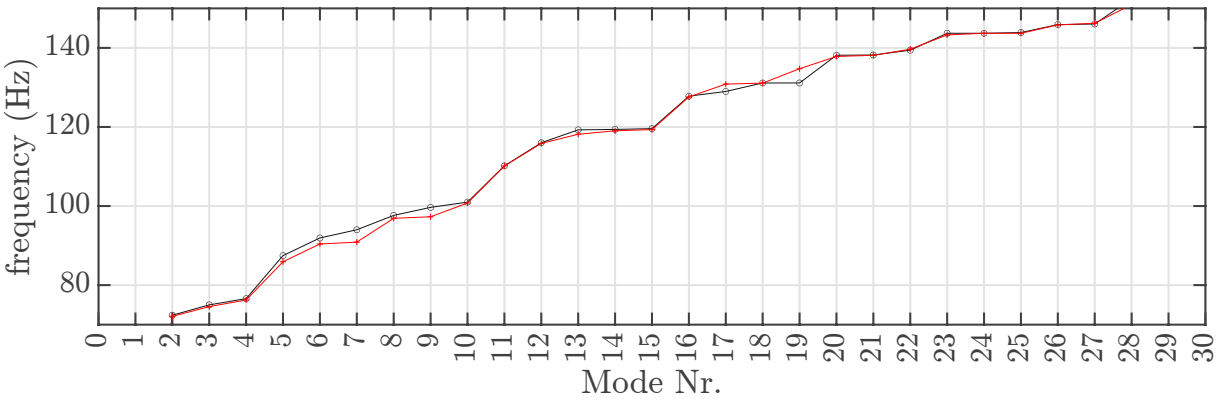

Figure 7.3: Coupled and uncoupled eigenfrequencies of the vibro-acoustic system, red (coupled), black (uncoupled).

7.3 Validation

To finally validate the hybrid aero-vibro-acoustic worflow, the WPF obtained via LB simulation and disussed in Chap. 6 are used to excite the coupled vibro-acoustic system and the results are compared to wind tunnel measurements. In a first step, the DL generated by the simulation worklow at the points shown in Fig. 5.1 are compared with accelerometer measurements. Shorthand references are furthermore associated with the subplots in Fig. 7.4. The vertical lines shown correspond to the lowest four acoustically relevant modes (more on this later). The experimental validation of the WPF in Fig. 6.14 and Fig. 6.15 as well as the energetically averaged mechanical FRFs in Fig. 5.8 should be taken into consideration when interpreting the results. For convectively excited surfaces, the acoustic feedback from the interior cavity can be ignored, but we will see later that this is not adequate for surfaces with very low excitation (here: *Trunk High*). However, it will subsequently be shown that these feedback effects are only significant in narrowband frequency ranges close to acoustically dominated eigenfrequencies. The respective acceleration spectra exhibit narrowband maxima at the mechanically dominated structural modes. The physical mechanisms are well reproduced and considering the complexity of the overall workflow, encouraging results can be achieved. The excitation at the side of the vehicle was clearly overestimated (Fig. 6.15a), causing an associated overestimation of displacement levels in (a). The displacements at the two panels in the underbody (*Floor Front (b)* and *Floor Rear (c)*) are overestimated, with displacements near the first mechanical mode $f_{c|4}$ being greatly underestimated. In line with the underestimated excitation in Fig. 6.15b and Fig. 6.13c, the DL at the underbody are underestimated as well, especially at *Floor Rear* (c). The displacements in the upper part of the trunk *Trunk High (e)* are significantly underestimated, especially in the low frequency range, although the excitation would suggest otherwise (Fig. 6.15e. and Fig. 6.14e). As a result of incorrectly predicted flow separation at the roof, the DL of convectively dominated regions at the roof (g&f) are overestimated. Interestingly, the symmetric second mode at *Rooftop Front* (g) is disproportionately excited. The reason for this could not be clarified yet, but possibly there is a connection here with the overestimated lateral correlation length in Fig. 6.9f&g. The displacement levels at the windshield (h) are equally underestimated which is once again in line with underestimated excitation in Fig. 6.14h&i, especially in the low frequency range. Hence, we can draw the essential conclusion that aerodynamic or aeroacoustic excitation might frequently outweigh the feedback effect from the cavity, and thus, high displacement levels are primarily the result of high excitation. In a next step, the sound pressure levels at the positions in Fig. 5.5 are compared with measured data (Fig. 7.5). A number of discrete, comparatively weakly attenuated maxima can be identified, as well as two, rather broadband regions around $f \approx 135, 240, 270\,\mathrm{Hz}$, which

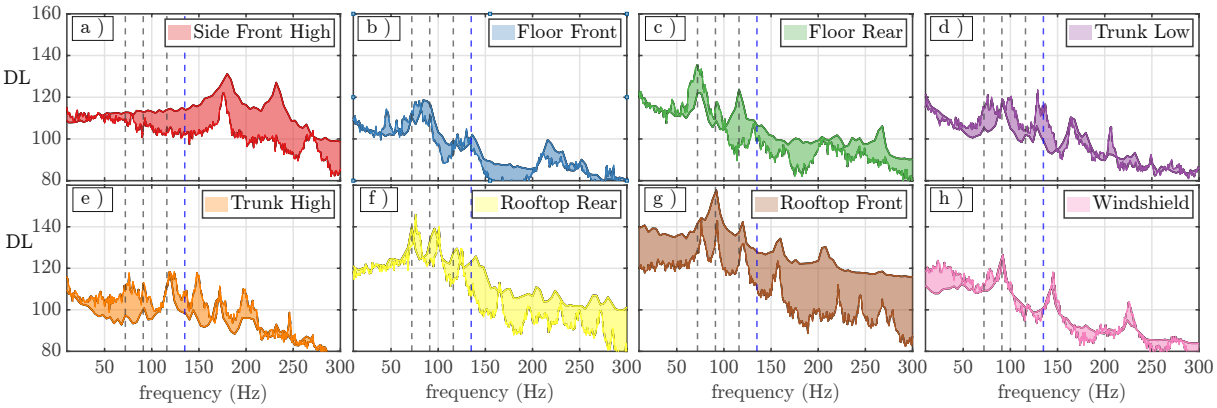

Figure 7.4: Comparison of simulated (solid) and measured (dashed) DL at the positions indicated in Fig. 2.2.

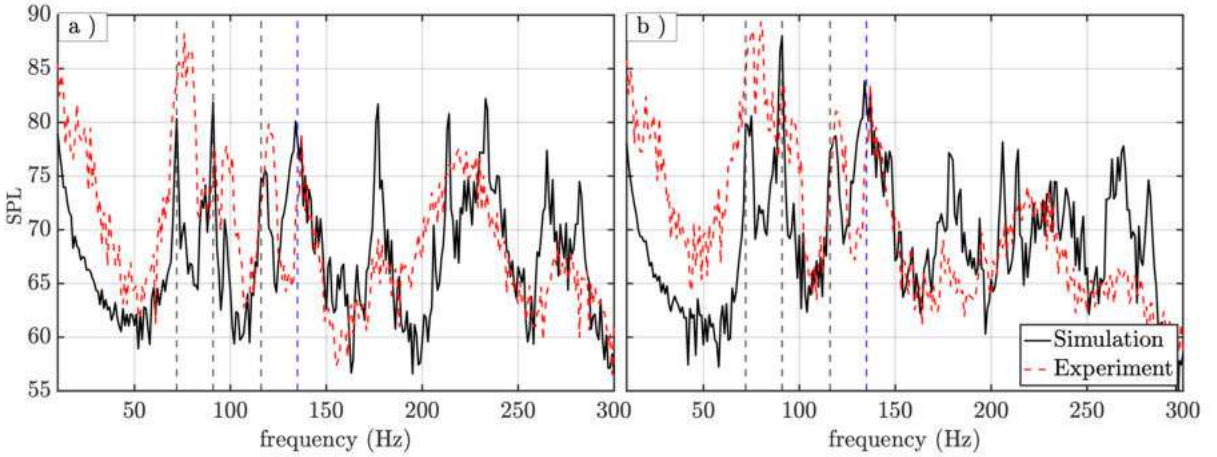

Figure 7.5: Comparison of simulated and experimental SPL at the positions indicated in Fig. 5.5 (a) Pos.1 (b) Pos. 4

(as will be shown below) can be assigned to the acoustically dominated modes. Due to the modal acoustic field, substantial deviations in the range of $\Delta dB \approx 10\,\mathrm{dB}$ between the two positions occurs in certain frequency ranges. Despite the errors in the prediction of the mechanical vibrations and especially the broadband overestimated DL at *Rooftop Front* (g) good qualitative agreement with the measured data can be achieved. Large deviations between measured and simulated results occur especially in the very low frequency range $f < 50\,\mathrm{Hz}$ dominated by direct acoustic excitation. Unfortunately, no measurement data are available for the WPF directly at the rear vent opening, the cause for these deviations is assumed to be either the underestimation of the excitation at the underbody (Fig. 6.13c ⅄ d) or the non-ideal sealing of the test body (and thus additional excitation through other openings). For a more detailed assessment of the mechanisms at stake, the contributions of individual coupled modes to the overall SPL will be analyzed similar to what was done in Sec. 4.3.3 for the rectangular plate-cavity system. More specifically, we are interested in the mechanisms related with the lowest four maxima indicated in Fig. 7.5 ($f = 72, 91, 118, 134, \mathrm{Hz}$). In a first attempt, we identify the coupled modes that contribute most to the mean SPL in the $0 - 300\,\mathrm{Hz}$ bin by ranking according to the norm of the complex coherence (see Eq. (4.67)). Clearly, this ranking pronounces broadband contributions and for a more meaningful ranking, the psychoacoustic weighting that is especially relevant in the low frequency range has to be taken into account, but this shall not be part of this thesis. The contribution of the resulting highest rank critical eigenmodes compared to the whole spectrum are shown in Fig. 7.6. It is clearly apparent, that this

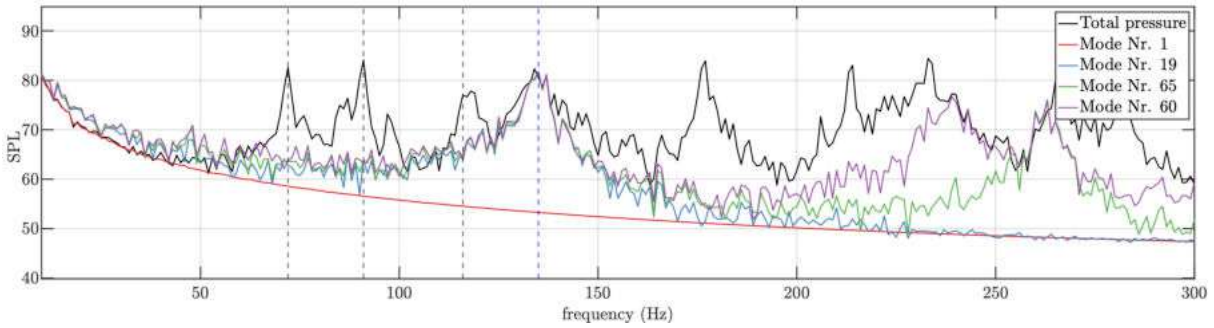

Figure 7.6: Contribution of acoustically dominated modes to overall SPL.

method allows to identify the acoustically dominated eigenmodes. The individual eigenfrequencies of the coherence-ranked modal contributions in Fig. 7.6 correspond to the Helmholtz mode at $f_{c|1} = 5.73\,\text{Hz}$, as well as the subsequent cavity modes at $f_{c|19} = 135.74\,\text{Hz}$, $f_{c|60} = 239.43\,\text{Hz}$, and $f_{c|65} = 262.44\,\text{Hz}$. Thus, modifications of the acoustic cavity (e.g. by adding holes in the package tray [11]) strongly affect the interior SPL. Therefore, the highest mode of the original selection in Fig. 7.5 has been identified as the first cavity mode (blue line). For further investigation, we choose the first three (narrowband) mechanical modes ($f_{c|2} = 72.10\,\text{Hz}$, $f_{c|7} = 90.88\,\text{Hz}$, $f_{c|13} = 118.16\,\text{Hz}$, black dashed lines) and the first acoustic cavity mode $f_{c|19}$ (blue dashed line). The coupled mode shapes of these four modes are shown in Fig. 7.7. We see that at $f_{c|2}$ (a) the first structural mode of *Rooftop Rear* couples efficiently with the first cavity mode while at $f_{c|7}$ (b) the second structural mode of *Rooftop Front* couples with both the longitudinal and the lateral lowest cavity modes (this is not so well evident in the middle-plane cut). At $f_{c|13}$ (c), the third mode of *Rooftop Rear* couples with the first acoustic cavity mode as well as the first mode of *Trunk High*. For the acoustically dominant mode $f_{c|19}$ (d), the induced acoustic pressures are so high that with the same acoustic and mechanical scaling chosen previously, only minimal displacements are discernible across all modes. Therefore, the mechanical displacements in (d) were additionally scaled by a factor $k = 25$ compared to (a-c). We see that a large number of modes are involved in the acoustically dominated mode due to efficient coupling, especially the third modes of the roof, the primary modes of *Trunk high* and *Trunk low*, and, to a lesser extent, the primary mode of *Windshield*. It is of particular importance to note, that the dominant coupled vibro-acoustic modes allow to understand the critical mechanisms that contribute to interior noise while analyzing solely the displacement field can be misleading. This may be exemplified by comparing the spatial displacement field in Fig. 7.8a, that proposes a dominant excitation by *Rooftop Front* with the coupled mode in Fig. 7.7a that rather suggests that the dominant contribution comes from *Rooftop Rear*. Clearly, the coupled modes take into account the transmission efficiency of the respective mechanical plates such that regions with high DL but, owing to e.g. low structural-acoustic coupling, low induced SPL will be ranked lower than regions with low DL but high induced SPL. For the other three modes investigated in (b&c&d) the correct mechanisms are also evident from the displacement fields. Finally, we investigate the difference between direct excitation via the rear vent and indirect excitation via the various plates. If instead of solving the modal-harmonic problem subject to $\tilde{\boldsymbol{f}} = \left[\tilde{\boldsymbol{f}}_s; i\omega\tilde{\boldsymbol{q}}_a\right]$ (Total forcing), the direct $\tilde{\boldsymbol{f}} = [\boldsymbol{0}; i\omega\tilde{\boldsymbol{q}}_a]$ (acoustic forcing) and indirect $\tilde{\boldsymbol{f}} = \left[\tilde{\boldsymbol{f}}_s; \boldsymbol{0}\right]$ (mechanical forcing) issues are solved subsequently, then their individual contributions can be compared on behalf of the synthesised SPL at Pos. 1 (Fig. 7.9). It can be shown that the acoustic Helmholtz resonance of the system dominates the SPL at very low frequencies, whereas mechanical excitation dominates at higher frequencies. The workflow in Fig. 7.1 can then be used to estimate the most promising panel for optimization measures. The excitation at the different plates in Fig. 5.1 can either be successively set to zero or the surface can be completely omitted from

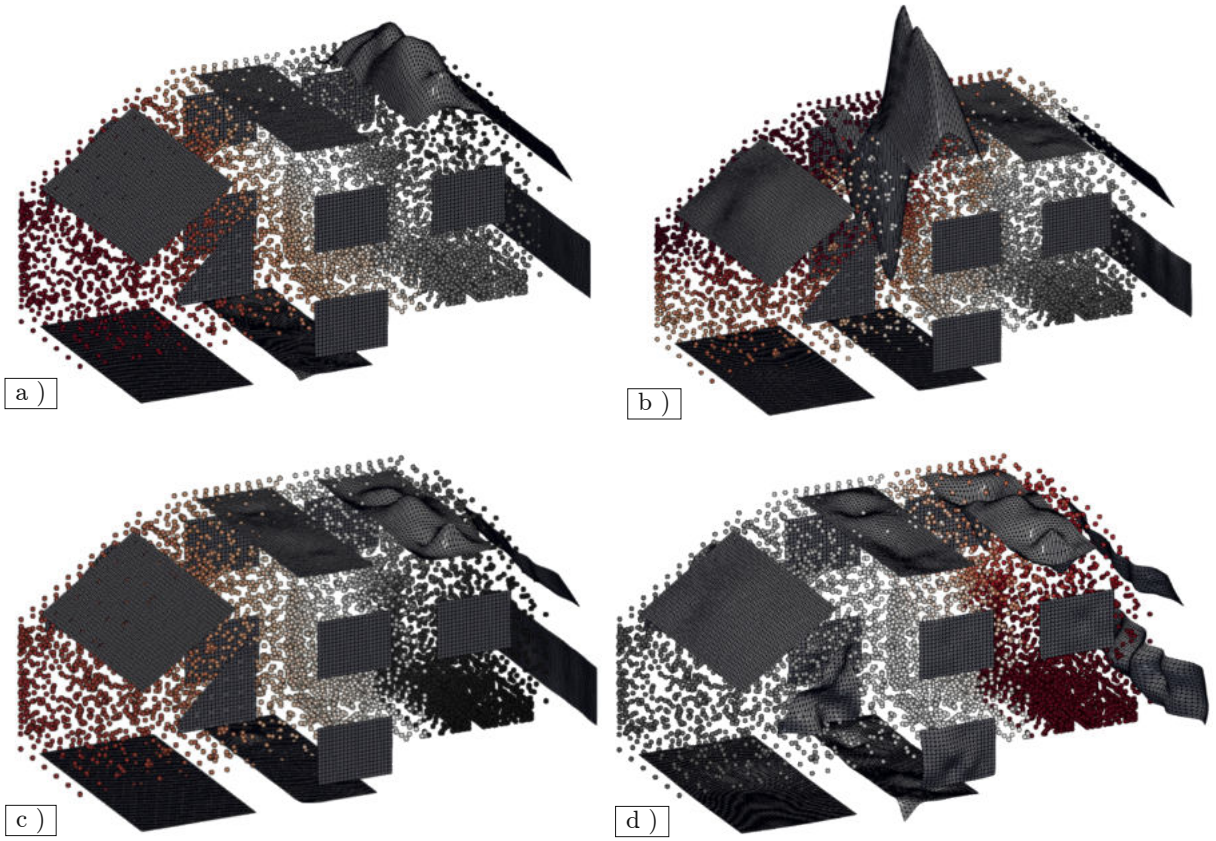

Figure 7.7: Coupled mode-shapes at (a) $f_{c|2} = 72\,\text{Hz}$ (b) $f_{c|7} = 91\,\text{Hz}$ (c) $f_{c|13} = 118\,\text{Hz}$ (d) $f_{c|19} = 134\,\text{Hz}$, mechanical displacements in (c) scaled by a factor of 25.

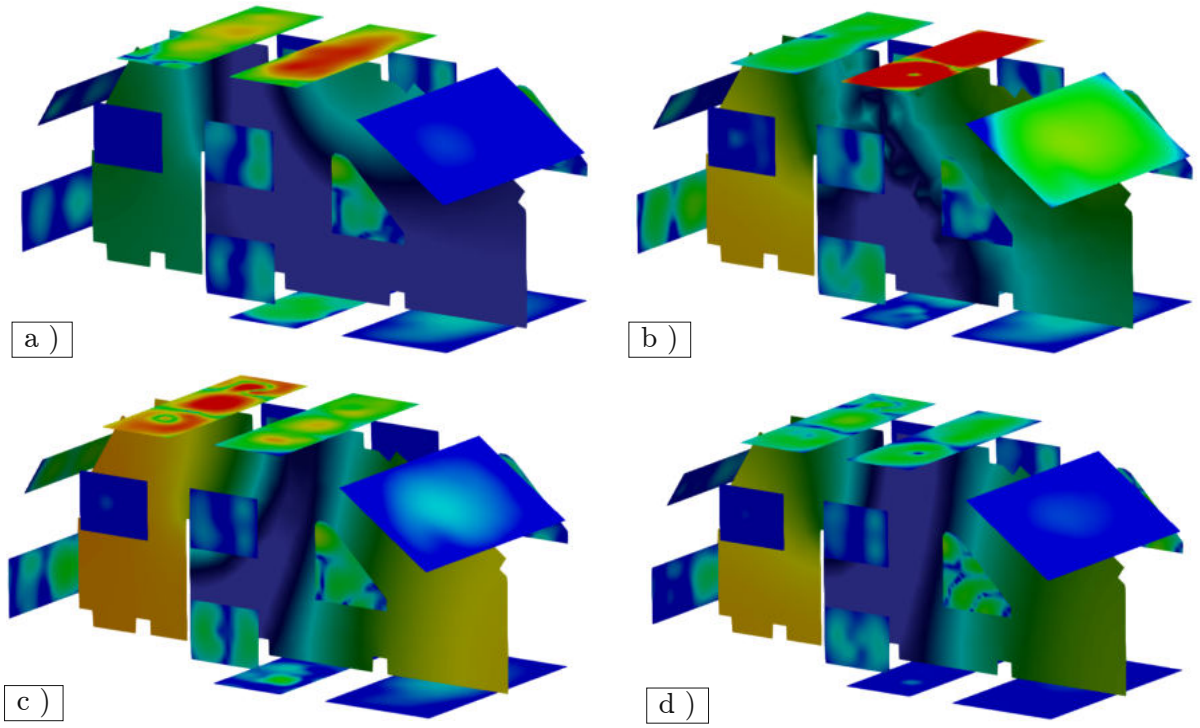

Figure 7.8: SPL and DL of synthesized fields at (a) 74 Hz, (b) 91 Hz, (c) 118 Hz, (d) 134 Hz (acou. 70 (blue)-100 dB (red), (mech. 100 (blue)-150 dB (red)

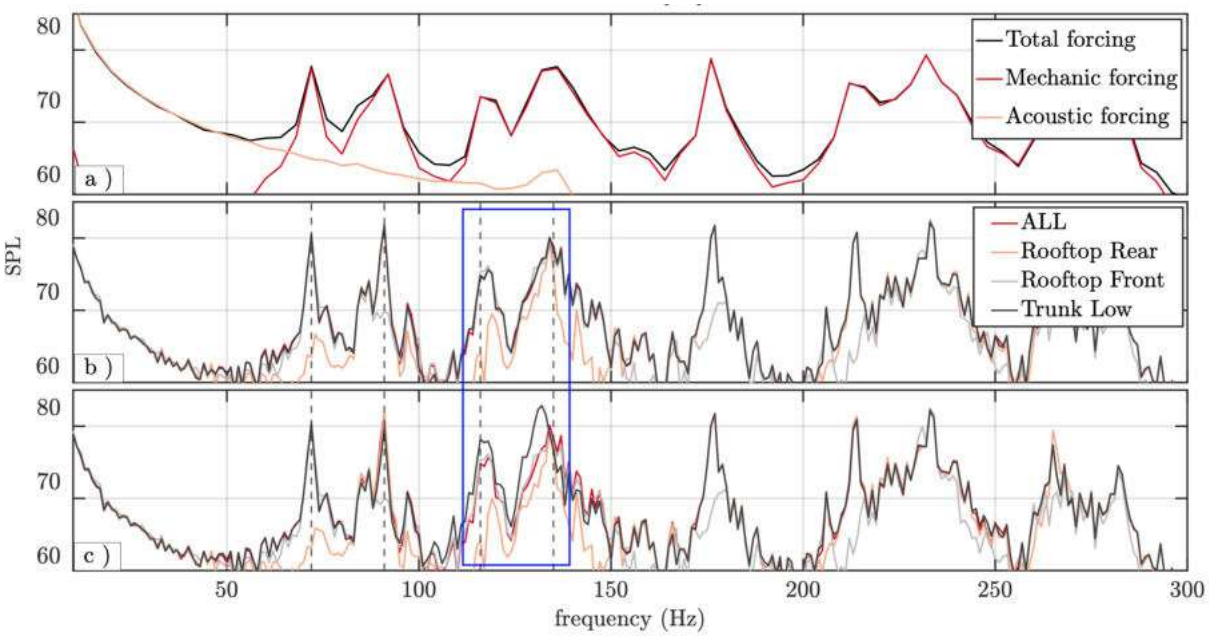

Figure 7.9: SPL at Pos. 1 induced by mechanic and acoustic forcing (b) Load case at region neglected (c) Plate assumed rigid.

the calculation process, which corresponds to an ideal rigid structure. The second variant differs from the first in that it also eliminates the coupling effects between the plate and cavity. The three plates with the largest broadband SPL reduction potential using each approach are shown in Fig. 7.9b&c (legend order represents top-down ranking). Fig. 7.9b demonstrates that due to the flow separation at the roof, modifications at *Rooftop Rear* have the highest potential for reducing the interior noise. This is interesting because, according to the ranking in Tab. 6.3, the excitation at *Rooftop Front* is even stronger, but *Rooftop Rear* has a greater influence on the measured SPL due to the stronger coupling of the structural modes with the acoustic modes (especially at $f_{\mathrm{a}|2} = 128\,\mathrm{Hz}$, Fig. 5.4). It is interesting to note that the third strongest reduction achieved by removing the load of *Trunk Low* already shows nearly indiscernible changes in the interior SPL. Thus, excitation via the roof predominates, and reductions of excitation on other panels than the critical ones have only minimal effect on the interior SPL. If, rather than ignoring the excitation, the respective panel is assumed to be rigid, the results are similar to the ones in Fig. 7.9c. Here too, *Rooftop Rear* shows the greatest potential for a reduction of the SPL. It is particularly interesting to observe that stiffening *Trunk Low* causes a significant increase in SPL in the frequency range close to the first natural frequency (blue rectangle, Fig. 7.9b↚c). However, the effect appears to be significant only for components with strong coupling and small excitation. This is confirmed by the fact that the roof plates exhibit very similar reductions when the excitation is removed versus when they are assumed to be completely rigid. To conclude, interior modifications, such as openings in the package tray, are likely to offer the greatest potential for improvement (see [11]). However, these modifications change the acoustic eigenmodes of the cavity, and as a result, there may e.g. be a significant improvement at the driver's position but a reduction of acoustic comfort in the fond. Modifications to the structure, on the other hand, don't have this drawback and can lead to improvements, particularly in the case of tonal noise. Note that increasing the dynamic stiffness of leeward components can actually cause to an increase of SPL inside the vehicle. In the very low frequency range, direct acoustic excitation via openings predominates while indirect excitation via structural transmission governs the higher frequency range.

8 Summary and Conclusion

8.1 Summary

To summarize, the fundamental objective of this thesis is to develop a theoretical framework and an experimentally validated method for understanding low-frequency wind-induced noise in vehicles. Particular emphasis is placed on experimental, numerical and hybrid methods for vibro-acoustic substructuring. After outlining relevant aerodynamic and aeroacoustic theory, it is proposed to categorize the excitation into four distinct groups; excitation by convected turbulence, excitation from leewards facing components, underbody excitation, and direct excitation via openings. A comparison of various currently available techniques for calculating flow-induced interior noise reveals that the method of Kim [44], in which experimental structural modes determined via experimental modal analysis (EMA) can be coupled with acoustic modes, exhibits the greatest potential. For the calculation of vehicle noise, the associated reduction of coupling conditions to the modal level appears possible [3, 12, 72]. The acoustic feedback effect that, in the case of light coupling, causes additional structural damping can frequently be neglected during experimental acquisition [42]. Kim's method is expanded to non-conforming grids such that vibro-acoustic issues can be assessed on behalf of arbitrarily discretised, experimental and/or computational structural and acoustic modes. The workflow is validated utilizing a simple vibro-acoustic box, and it is discovered that an additional thin-plate-spline (TPS) interpolation even permits the consideration of very coarsely discretized mechanical modes. Then, a novel generic testbody is developed for specifically investigating the low-frequency flow-induced noise if multiple flow-excited flexible panels coupled via the interior cavity are involved. This topic has not been previously discussed in literature. The mechanical modes of the different plates are extracted with experimental modal analysis and the acoustic modes are obtained via finite element simulation. Acoustic frequency response functions (FRF) are used to verify the accuracy of the acoustic simulation and it can be concluded that finite element simulations of vehicle cabins will in most cases reliably reproduce the real acoustic properties of the uncoupled acoustic system. However, real vehicles always contain flexible components that affect the acoustic mode shapes of the cavity and decoupling by blocking mechanical transmission paths is difficult to realize in practice [15]. The wall pressure fluctuations (WPF) on the surfaces are obtained via lattice Boltzmann (LB) simulation and the results are compared with experimental measurements obtained in the wind tunnel using an efficient representation that condenses all relevant information into a single plot for each panel. For surfaces excited by convected turbulence, the determination of the Corcos parameters by a least-squares fit seems particularly suitable, since differences in the phase velocity easily allow to detect differences between simulation and measurements but also to identify critical panels regarding aerodynamic coincidence [39]. At the rear of the vehicle the excitation is limited to the low frequency range whereas at the upper part of the rear a clear coherent part can be identified at $f = v_\infty/H$, which agrees with the findings of Islam [127] but could not be resolved in the flow simulation. The excitation associated with the leewards facing component remains limited to low frequencies but it is conceived possible that the shedding frequency associated with large-scale vortices in the recirculation region behind the vehicle can be shifted into the audible frequency range in small vehicles travelling at high speed. By employing the cross-power spectral density (CPSD), the important acoustic contribution at the underbody could be separated from a dominant aerodynamic

contribution in WPF measurements and distinct acoustic peaks could be distinguished and related to the underbody cavity modes postulated numerically in [29, 33, 34, 38]. Among the different statistical criteria, the averaged auto-power spectral density (APSD), the averaged longitudinal CPSD between two streamwise positions and the APSD based on the arithmetically averaged pressure over the surface are deemed most meaningful and the contributions from the different panels are grouped in frequency bins and compared. It is found that differences between the three criteria are mostly limited to the low frequency region and that they deliver similar conclusions in the high frequency region, the APSD can directly be investigated. The averaged longitudinal CPSD is deemed most suitable to estimate structural excitation in the low-frequency region and experimental and numerical WPF coincide much better on this criteria than if using the APSD. Ranking the various contributions from the different panels shows, that excitation from the windshield is most prominent in wind-tunnel measurements while excitation from the leading surface at the roof is dominant in simulation results owing to an incorrectly predicted flow separation. Having validated the excitation and the individual mechanical and acoustical subsystems, the wind-induced noise within the test body is calculated using a custom tool based on the non-conforming modal workflow. The displacement level (DL) on certain positions on the structure but also the SPL inside the vehicle are once again validated with measured data and, regarding the complexity of the workflow, encouraging results can be achieved. Finally, the optimization potential of the various panels is compared, and it is found that, due to the different coupling between mechanical and acoustic modes, the panel that vibrates the most strongly does not correspond to the panel that transmits the most noise. It is also noted that, contrary to reasoning that neglects vibro-acoustic coupling effects, the interior SPL can actually be increased if some of the weakly excited plates in the trunk region are blocked. Hence, the acoustic feedback effect, while negligible during EMA, must be considered if significant acoustic forcing via other vibrating panels is present and it is correctly reproduced by the modal workflow developed as part of this thesis.

8.2 Conclusion

It is clear that determining mechanical FRFs using impulse hammer measurements is a rather academic procedure, and significantly better results can be expected if a professional industrial process using mechanical shakers is employed. Advancements can also be anticipated with regard to the flow simulation; here, particularly, further resolution refinements and a longer simulation time should be exploited. The application of a model for the convective portion of the WPF seems possible, but a simulation will likely anyway be required to estimate low-frequency underbody excitation. Due to the special design of the test body, the mechanical coupling of flexible components via the geometry could be neglected, but in real vehicles the low frequency range is dominated mainly by global modes and it is not yet clear how efficiently these modes can be excited by the flow or how they contribute to the sound pressure in the cabin. The numerous investigations that have been conducted regarding uncertainties related to the manufacturing process indicate that this must most probably also be taken into consideration. However, this is possible on a modal level and has already been carried out in a similar way by Durand [72]. The consideration of pyschoacoustic parameters is critical for a final evaluation of passenger comfort and must therefore be additionally included in the evaluation. Thanks to the short computation time, the custom tool also allows to investigate interior SPL in the time-frequency domain via e.g. Wavelet analysis. A weighting of the relevant position in the vehicle, i.e. the positions at the passenger ears, must also be developed so that an acoustic improvement in the front does not result in a worsening of comfort in the rear. Extending the developed procedure to real vehicles is theoretically possible, but requires further development of the techniques for extracting and identifying the relevant mechanical modes. From the findings of this thesis,

some enlightening insights regarding the prevention of low-frequency noise in vehicles can be derived. Most importantly, flow separation should be avoided as far as possible which is however in line with requirements posed by aerodynamic engineers. Structural panel modes will likely result in narrow-band maxima and thus, measures to stiffen individual panels might also yield only narrow-band improvements (provided there is also significant excitation from other panels). Modifying the overall vehicle structure to modify global structural modes will likely yield broadband reductions due to the higher structural damping but this cannot be presumed on existing knowledge. Acoustic measures, on the other hand, have a rather broadband effect and therefore significant optimisation potential can be expected from measures that affect the acoustical modes, such as additional openings in the package tray, appear particularly suitable. The very low frequency contribution is dominated by the direct acoustic excitation and can most easily be reduced by increasing the acoustic mass of openings. Acoustic resonators within the cabin appear to be of little use because, in order to achieve a similar resonance frequency with a similar mass, the cavity volume must also be comparable to the volume of the vehicle. Mechanical resonators that reduce the interior SPL by coupling with the acoustic cavity however appear promising.

List of Figures

List of Tables

A Appendix: Lumped acoustical elements

This section will explain two different ways to obtain low-frequency network descriptions of acoustic systems. The difference between the two formulations originates from the differing natural boundary conditions of the one-dimensional acoustic wave equation if formulated in terms of pressure or particle velocity (and respectively volume velocity). This is of particular relevance because it is a major achievement of this thesis to describe arbitrary vibro-acoustic systems on behalf of acoustic and mechanical modes, which is only possible if the natural boundary conditions of the underlying systems are sound hard and zero stress respectively. While mechanical systems are usually described in a displacement formulation and thus satisfy this requirement, acoustical systems are more frequently employed based on mean volume acceleration because the corresponding natural boundary condition is zero pressure and this allows to easily investigate open-ended pipe systems (e.g. silencers). An alternative formulation with sound hard natural boundary conditions can be derived from continuity and mass equations by presuming that instead of the mean velocity, the mean pressure is constant over each lumped element. Explanations on the subject may also be found in [54]. Both formulations can be obtained by formulating momentum and mass equations for a one-dimensional tube with cross section A, length l, acoustic density $\rho_\mathrm{a}(t,x)$, speed of sound c_0, acoustic volume velocity $q_\mathrm{a}(t,x)$ acoustic and pressure $p_\mathrm{a}(t,x)$. Supposing both impulsive excitation via an additional pressure source p_ae and mass-like excitation via an additional volume source q_ae allows to formulate the continuity equation as

$$A\frac{\partial \rho_\mathrm{a}}{\partial t} = -\rho_0\frac{\partial q_\mathrm{a}}{\partial x} + \rho_0\frac{\partial q_\mathrm{ae}}{\partial x} \quad \text{or with } \partial p_\mathrm{a}/\partial \rho_\mathrm{a} = c_0^2 \text{ as} \tag{A.1}$$

$$A\frac{\partial p_\mathrm{a}}{\partial t} = -\rho_0 c_0^2\frac{\partial q_\mathrm{a}}{\partial x} + \rho_0 c_0^2\frac{\partial q_\mathrm{ae}}{\partial x}\,, \tag{A.2}$$

and the momentum equation as

$$\rho_0\frac{\partial q_\mathrm{a}}{\partial t} = -A\frac{\partial p_\mathrm{a}}{\partial x} - A\frac{\partial p_\mathrm{ae}}{\partial x}\,. \tag{A.3}$$

A volume-velocity based formulation can be obtained by applying a temporal derivative on Eq. (A.3) and a spatial derivative on Eq. (A.2) and by subtracting the former from the latter to arrive at

$$\rho_0\frac{\partial^2 q_\mathrm{a}}{\partial t^2} - \rho_0 c_0^2\frac{\partial^2 q_\mathrm{a}}{\partial x^2} = -A\frac{\partial^2 p_\mathrm{ae}}{\partial x \partial t} - \rho_0 c_0^2\frac{\partial^2 q_\mathrm{ae}}{\partial x^2}\,. \tag{A.4}$$

Now, by applying Fourier transformation in time and integrating in space with the boundary conditions of zero volume flux at $x = 0$ and zero pressure at $x = l$ (equivalent to $\left(\partial \hat{q}_\mathrm{a}/\partial x\right)_{x=l} = 0$) and by reducing the space-dependent quantities by single point quantities located at $x = l$ (e.g. $\hat{q}_\mathrm{a}(x,\omega) \Rightarrow \hat{q}_\mathrm{a}(\omega)$), a lumped element formulation can be obtained according to

$$\left(-\rho_0 w^2 l + \frac{\rho_0 c_0^2}{l}\right)\hat{q}_\mathrm{a} = -Ai\omega\hat{p}_\mathrm{ae} - \frac{\rho_0 c_0^2}{l}\hat{q}_\mathrm{ae}\,, \tag{A.5}$$

which can also be expressed in terms of acoustic impedance $\hat{z}_{\mathrm{av}}$ as

$$\left(\frac{i\omega\rho_0 l}{A}+\frac{\rho_0 c_0^2}{i\omega A l}\right)\hat{q}_{\mathrm{a}}=\left(i\omega m_{\mathrm{a}}+\frac{1}{i\omega}k_{\mathrm{a}}\right)\hat{q}_{\mathrm{a}}=\hat{z}_{\mathrm{av}}\hat{q}_{\mathrm{a}}=-\hat{p}_{\mathrm{ae}}-\frac{\rho_0 c_0^2}{li\omega A}\hat{q}_{\mathrm{ae}}\,. \tag{A.6}$$

Thus acoustical mass and stiffness elements are defined as $m_{\mathrm{a}}=\rho_0 l/A$ and $k_{\mathrm{a}}=\rho_0 c_0^2/(Al)$. Note once again that this formulation describes a 1D pipe element with induced pressure excitation on the left side and zero pressure (i.e. open ending) on the other side. The latter contributor on the right-hand side simply allows to define the required pressure excitation based on the induced volume velocity in the pipe. The pressure-based formulation can on the other hand be obtained by applying the time derivative to Eq. (A.2) and subtracting the space derivative of Eq. (A.3) to arrive at

$$\frac{A}{c_0^2}\frac{\partial^2 p_{\mathrm{a}}(t,x)}{\partial t^2}-A\frac{\partial^2 p_{\mathrm{a}}(t,x)}{\partial x^2}=A\frac{\partial^2 p_{\mathrm{ae}}(t,x)}{\partial x^2}+\rho_0\frac{\partial^2 q_{\mathrm{ae}}}{\partial x\partial t}\,. \tag{A.7}$$

Proceeding just as for the volume-velocity based formulation with temporal Fourier transformation, spatial integration with the reciprocal boundary conditions of zero pressure at $x=0$ and zero volume velocity at $x=l$, the lumped element formulation becomes

$$\left(\frac{-\omega^2 Al}{\rho_0 c_0^2}+\frac{A}{l\rho_0}\right)\hat{p}_{\mathrm{a}}=\frac{A\hat{p}_{\mathrm{ae}}}{\rho_0 l}+i\omega\hat{q}_{\mathrm{ae}}\,, \tag{A.8}$$

and finally the description in terms of acoustic admittance $\hat{y}_{\mathrm{av}}$ becomes

$$\left(\frac{i\omega Al}{\rho_0 c_0^2}+\frac{A}{i\omega l\rho_0}\right)\hat{p}_{\mathrm{a}}=\left(i\omega\underline{m}_{\mathrm{a}}+\frac{1}{i\omega}\underline{k}_{\mathrm{a}}\right)\hat{p}_{\mathrm{a}}=\hat{y}_{\mathrm{av}}\hat{p}_{\mathrm{a}}=\frac{A\hat{p}_{\mathrm{ae}}}{i\omega l\rho_0}+\hat{q}_{\mathrm{ae}}\,. \tag{A.9}$$

Contrary to Eq. (A.6), this formulation describes a 1D pipe element with induced volume velocity excitation on the left and zero volume velocity at the right side (i.e. sound hard). Note especially that $m_{\mathrm{a}}=1/\underline{k}_{\mathrm{a}}$ and $k_{\mathrm{a}}=1/\underline{m}_{\mathrm{a}}$ and thus the natural angular frequencies of both systems become simply $\omega_{\mathrm{a}}=\sqrt{k_{\mathrm{a}}/m_{\mathrm{a}}}=\sqrt{\underline{k}_{\mathrm{a}}/\underline{m}_{\mathrm{a}}}=2\pi c_0/l$. This reciprocal relationship however applies only on individual elements but not on the entire system description itself ($\hat{y}_{\mathrm{av}}\neq 1/\hat{z}_{\mathrm{av}}$). It is rather evident that if $\hat{z}_{\mathrm{av}}=A+B$ then $\hat{y}_{\mathrm{av}}=(1/A+1/B)/(1/A\cdot 1/B)=CD/(C+D)$ with $C=1/A$ and $D=1/B$. Hence a serial resonant circuit in volume-velocity based formulation corresponds to an equivalent parallel resonant circuit with reciprocal elements in pressure based formulation. More on the subject may be found in [57]. In the literature the relation $\rho_0 c_0^2=\kappa P_0$ is frequently exploited to obtain equivalent formulations in terms of ambient pressure P_0 and isentropic exponent κ.

B Appendix: Demonstration of modal coupling via a simple piston-cavity system

The treatment provided in this section shall serve as an introduction to coupled vibro-acoustic systems while also providing an initial treatment of eigenvalue decompositions. The reader is therefore especially invited to compare the equations that follow with the more complex formulations based on wavenumber or modal descriptions in Chap. 2. For this purpose, the most basic vibro-acoustic system reflecting the interaction of cavity with a mechanical spring-mass system excited by an external force shall be investigated. The piston shown in Fig. B.1 has mass m_s and is attached to the rigid structure with a mechanical spring with stiffness k_s. The cavity with length l and volume V_0 is filled with air at ambient pressure $P_0 = 10^5\,\mathrm{Pa}$. Using the circuit elements of the p_a-based formulation derived in A, the acoustic

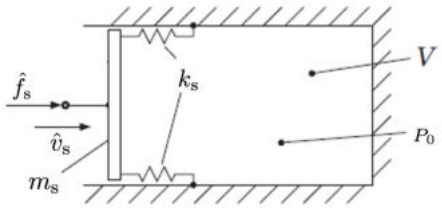

Figure B.1: A simple vibro-acoustic system composed of a piston and a cavity.

mass $\underline{m}_\mathrm{a} = Al/(\kappa P_0)$ and acoustic stiffness $\underline{k}_\mathrm{a} = A^2/V\rho_0$ can be obtained. The individual serial circuits of the uncoupled mechanical (i.e. free-displacement) and acoustical (i.e. zero volume flux) systems can thus be expressed according to

$$\hat{z}_\mathrm{sv}\hat{v}_\mathrm{s} = \hat{f}_\mathrm{s} \quad \text{with} \quad \hat{z}_\mathrm{sv} = i\omega m_\mathrm{s} + \frac{1}{i\omega}k_\mathrm{s} \quad \text{and} \tag{B.1}$$

$$\hat{y}_\mathrm{av}\hat{p}_\mathrm{a} = -\hat{q}_\mathrm{a} \quad \text{with} \quad \hat{y}_\mathrm{av} = i\omega\underline{m}_\mathrm{a} + \frac{1}{i\omega}\underline{k}_\mathrm{a}\,. \tag{B.2}$$

The force associated with the pressure in the cavity as $A\hat{p}_\mathrm{a}$ counteracts the piston movement and must thus be negative. The volume velocity $\hat{q}_\mathrm{a} = A\hat{v}_\mathrm{s}$ is however directed inwards and is therefore positive. The coupled system can thus be formulated as

$$\hat{z}_\mathrm{sv}\hat{v}_\mathrm{s} = \hat{f}_\mathrm{s} - A\hat{p}_\mathrm{a} \quad \text{and} \tag{B.3}$$

$$\hat{y}_\mathrm{av}\hat{p}_\mathrm{a} = -A\hat{v}_\mathrm{s}\,. \tag{B.4}$$

As eigenvalue decompositions are a major topic of this thesis and these eigenvalues are related to the angular frequencies as $\lambda_\mathrm{i} = \omega_\mathrm{i}^2$, it is beneficial to represent the mechanical impedance $\hat{z}_\mathrm{sv}$ in terms of mechanical dynamic stiffness $\hat{z}_\mathrm{s} = i\omega\hat{z}_\mathrm{sv}$ and the acoustic mobility $\hat{y}_\mathrm{av}$ in terms of admittance $\hat{y}_\mathrm{a} = i\omega\hat{y}_\mathrm{av}$.

Replacing $\hat{v}_\mathrm{s}$ by $i\omega\hat{u}_\mathrm{s}$ and substituting $\hat{z}_\mathrm{s}$ and $\hat{y}_\mathrm{a}$ yields

$$\hat{z}_\mathrm{s}\hat{u}_\mathrm{s} = \hat{f}_\mathrm{s} - A\hat{p}_\mathrm{a} \quad \text{and} \tag{B.5}$$

$$\hat{y}_\mathrm{a}\hat{p}_\mathrm{a} = \omega^2 A\hat{u}_\mathrm{s}\,, \tag{B.6}$$

which can be assembled in a matrix as

$$\begin{bmatrix} -\omega^2 m_\mathrm{s} + k_\mathrm{s} & A \\ -A\omega^2 & -\omega^2\underline{m}_\mathrm{a} + \underline{k}_\mathrm{a} \end{bmatrix} \begin{bmatrix} \hat{u}_\mathrm{s} \\ \hat{p}_\mathrm{a} \end{bmatrix} = \begin{bmatrix} \hat{f}_\mathrm{s} \\ 0 \end{bmatrix}. \tag{B.7}$$

By introducing the generalized system matrix $\hat{\boldsymbol{T}}$, the generalized displacement $\hat{\boldsymbol{d}} = [\hat{u}_\mathrm{s}; \hat{p}_\mathrm{a}]$ and the generalized force $\hat{\boldsymbol{f}} = [\hat{f}_\mathrm{s}; 0]$ the system can simply be written as

$$\hat{\boldsymbol{T}}\hat{\boldsymbol{d}} = \hat{\boldsymbol{f}}\,. \tag{B.8}$$

The eigenvalues λ_k and the eigenvectors $\boldsymbol{\psi}_\mathrm{k}$ shall now be obtained. For this purpose, the eigenvalue problem $(\boldsymbol{A} - \lambda_\mathrm{k}\boldsymbol{I})\boldsymbol{\psi}_\mathrm{k} = \boldsymbol{0}$ must be solved. The eigenvalues can either be obtained by zeroing the determinant of $\hat{\boldsymbol{T}}$ first to obtain the angular eigenfrequencies ω_k and in turn the eigenvalues as $\lambda_\mathrm{k} = \omega_\mathrm{k}^2$ or, equivalently, by directly replacing ω_k^2 by λ_k to arrive at a generalized eigenvalue problem of the form $(\boldsymbol{K} - \lambda_\mathrm{k}\boldsymbol{M})\boldsymbol{\psi}_\mathrm{k} = \boldsymbol{0}$ with

$$\boldsymbol{M} = \begin{bmatrix} m_\mathrm{s} & 0 \\ A & \underline{m}_\mathrm{a} \end{bmatrix} \quad \text{and} \quad \boldsymbol{K} = \begin{bmatrix} k_\mathrm{s} & A \\ 0 & \underline{k}_\mathrm{a} \end{bmatrix}. \tag{B.9}$$

The matrix $\boldsymbol{A}$ required for the general formulation can simply be obtaining according to $\boldsymbol{A} = \boldsymbol{M}^{-1}\boldsymbol{K}$. The mechanical and acoustic stiffnesses can be transformed into a normalized representation using the respective uncoupled natural frequencies as $k_\mathrm{s} = m_\mathrm{s}\omega_\mathrm{s}^2$ and $\underline{k}_\mathrm{a} = \underline{m}_\mathrm{a}\omega_\mathrm{a}^2$. The two eigenvalues of the coupled problem become

$$\det(\hat{\boldsymbol{T}}) = \underline{m}_\mathrm{a} m_\mathrm{s}(\omega_\mathrm{s}^2 - \lambda_\mathrm{k})(\omega_\mathrm{a}^2 - \lambda_\mathrm{k}) - A^2\lambda_\mathrm{k} = 0\,, \tag{B.10}$$

$$\lambda^2 - \left(\frac{A^2}{m_\mathrm{s}\underline{m}_\mathrm{a}} + \omega_\mathrm{s}^2 + \omega_\mathrm{a}^2\right)\lambda + \omega_\mathrm{s}^2\omega_\mathrm{a}^2 = 0\,, \tag{B.11}$$

and finally

$$\lambda_{1,2} = \left(\frac{\omega_\mathrm{s}^2 + \omega_\mathrm{a}^2}{2} + \frac{A^2}{2m_\mathrm{s}\underline{m}_\mathrm{a}}\right) \pm \sqrt{\left(\frac{\omega_\mathrm{s}^2 + \omega_\mathrm{a}^2}{2} + \frac{A^2}{2m_\mathrm{s}\underline{m}_\mathrm{a}}\right)^2 - \omega_\mathrm{s}^2\omega_\mathrm{a}^2}\,. \tag{B.12}$$

If the coupling surface is small ($A \ll 0$), then

$$\lambda_{1,2} = (\frac{\omega_\mathrm{s}^2 + \omega_\mathrm{a}^2}{2}) \pm \sqrt{\left(\frac{\omega_\mathrm{s}^2 + \omega_\mathrm{a}^2}{2}\right)^2 - \omega_\mathrm{s}^2\omega_\mathrm{a}^2}\,, \tag{B.13}$$

and the coupled eigenvalues then match the uncoupled ones as

$$\lambda_1 = \omega_\mathrm{s}^2 \quad \lambda_2 = \omega_\mathrm{a}^2\,. \tag{B.14}$$

Note that owing to the asymmetry of the system matrix $\hat{\boldsymbol{T}}$, there are two different sets of eigenvectors, namely the right and left eigenvectors stored column-wise in matrices $\boldsymbol{\psi}_\mathrm{k}$ and $\boldsymbol{\psi}_{\mathrm{L|k}}$. Both eigenvectors

correspond to the same eigenvalues λ_k and can be obtained by solving

$$(\boldsymbol{K} - \lambda_\mathrm{k}\boldsymbol{M})\boldsymbol{\psi} = \boldsymbol{0} \quad \text{and} \tag{B.15}$$

$$(\boldsymbol{K}^T - \lambda_\mathrm{k}\boldsymbol{M}^T)\boldsymbol{\psi}_{\mathrm{L|k}} = \boldsymbol{0}\,. \tag{B.16}$$

The right eigenvectors $\boldsymbol{\psi}_\mathrm{k}$ are thus given by

$$\begin{bmatrix} -\lambda_\mathrm{k} m_\mathrm{s} + k_\mathrm{s} & -A \\ -A\lambda_\mathrm{k} & -\lambda_\mathrm{k}\underline{m}_\mathrm{a} + \underline{k}_\mathrm{a} \end{bmatrix} \begin{bmatrix} \psi_{\mathrm{k}|1} \\ \psi_{\mathrm{k}|2} \end{bmatrix} = \boldsymbol{0}\,. \tag{B.17}$$

For the case of vanishing coupling area A, the first eigenvalue reduces to the eigenvalue of the uncoupled mechanical system and the second eigenvalue reduces to the eigenvalue of the uncoupled acoustic system (see Eq. (B.14)). Therefore, the first degree of freedom (the displacement) is set to unity at the first eigenvalue and the second degree of freedom (the pressure) is set to unity at the second eigenvalue. The resulting eigenvectors

$$\boldsymbol{\psi}_1 = \begin{bmatrix} 1 \\ \frac{A\lambda_1}{\underline{m}_\mathrm{a}(\omega_\mathrm{a}^2 - \lambda_1)} \end{bmatrix} \quad \text{and} \quad \boldsymbol{\psi}_2 = \begin{bmatrix} \frac{A}{m_\mathrm{s}(\omega_\mathrm{s}^2 - \lambda_2)} \\ 1 \end{bmatrix} \tag{B.18}$$

can then be collected in a matrix of right eigenvectors $\boldsymbol{\psi}$ as $\boldsymbol{\psi} = [\boldsymbol{\psi}_1, \boldsymbol{\psi}_2]$. Proceeding analogously for the left eigenvalue problem yields

$$\boldsymbol{\psi}_{\mathrm{L}|1} = \begin{bmatrix} 1 \\ \frac{A}{\underline{m}_\mathrm{a}(\omega_\mathrm{a}^2 - \lambda_1)} \end{bmatrix} \quad \text{and} \quad \boldsymbol{\psi}_{\mathrm{L}|2} = \begin{bmatrix} \frac{A}{m_\mathrm{s}(\omega_\mathrm{s}^2 - \lambda_2)} \\ 1/\lambda_2 \end{bmatrix}, \tag{B.19}$$

which can then be collected as $\boldsymbol{\psi}_\mathrm{L} = [\boldsymbol{\psi}_{\mathrm{L}|1}, \boldsymbol{\psi}_{\mathrm{L}|2}]$. Note that the left and right eigenvectors are related as

$$\boldsymbol{\psi}_{\mathrm{L|k}} = \begin{bmatrix} 1 & 0 \\ 0 & 1/\lambda_\mathrm{k} \end{bmatrix} \boldsymbol{\psi}_\mathrm{k}\,. \tag{B.20}$$

This relation is generally valid for linear vibro-acoustic systems [92]. It is now possible to obtain an analytic expression of the resulting displacement and pressure as a superposition of coupled vibro-acoustic modes. For this purpose, the system of equations $\hat{\boldsymbol{T}}\hat{\boldsymbol{d}} = \hat{\boldsymbol{f}}$ must be diagonalized using the previous obtained left and right eigenvectors. We shall thus presume that the generalized displacements $\hat{\boldsymbol{d}}$ can be described as modal generalized displacements $\tilde{\boldsymbol{d}}$ (also called participation factors) weighted with the matrix of the right eigenvectors $\boldsymbol{\psi}$ as

$$\hat{\boldsymbol{d}} = \boldsymbol{\psi}\tilde{\boldsymbol{d}}\,. \tag{B.21}$$

Replacing $\hat{\boldsymbol{d}}$ in Eq. (B.8) and premultiplying with $\boldsymbol{\psi}_\mathrm{L}$ gives

$$\boldsymbol{\psi}_\mathrm{L}^\mathrm{T}\hat{\boldsymbol{T}}\boldsymbol{\psi}\tilde{\boldsymbol{d}} = \boldsymbol{\psi}_\mathrm{L}^\mathrm{T}\hat{\boldsymbol{f}}\,. \tag{B.22}$$

By additionally defining a modal coupled impedance matrix $\tilde{\boldsymbol{T}} = \boldsymbol{\psi}_\mathrm{L}^\mathrm{T}\hat{\boldsymbol{T}}\boldsymbol{\psi}$ and a modal force vector $\tilde{\boldsymbol{f}} = \boldsymbol{\psi}_\mathrm{L}^\mathrm{T}\hat{\boldsymbol{f}}$, it is possible to obtain a modal (or decoupled) formulation as

$$\tilde{\boldsymbol{T}}\tilde{\boldsymbol{d}} = \tilde{\boldsymbol{f}}\,. \tag{B.23}$$

In the given case, $\tilde{\boldsymbol{T}}$ becomes

$$\tilde{\boldsymbol{T}} = \begin{bmatrix} 1 & \frac{A}{\underline{m}_\mathrm{a}(\omega_\mathrm{a}^2-\lambda_1)} \\ \frac{A\lambda_2}{m_\mathrm{s}(\omega_\mathrm{s}^2-\lambda_2)} & 1 \end{bmatrix} \begin{bmatrix} m_\mathrm{s}(s^2+\omega_\mathrm{s}^2) & -A \\ As^2 & \underline{m}_\mathrm{a}(s^2+\omega_\mathrm{a}^2) \end{bmatrix} \begin{bmatrix} 1 & \frac{A}{m_\mathrm{s}(\omega_\mathrm{s}^2-\lambda_2)} \\ \frac{A\lambda_1}{\underline{m}_\mathrm{a}(\omega_\mathrm{a}^2-\lambda_1)} & 1 \end{bmatrix}, \tag{B.24}$$

which, by defining the modal masses $\tilde{m}_1 = m_\mathrm{s} + \frac{A^2\omega_\mathrm{a}^2}{\underline{m}_\mathrm{a}(\omega_\mathrm{a}^2-\lambda_1)^2}$ and $\tilde{m}_2 = \underline{m}_\mathrm{a} + \frac{A^2\omega_\mathrm{s}^2}{m_\mathrm{s}(\omega_\mathrm{s}^2-\lambda_2)^2}$ finally results in

$$\tilde{\boldsymbol{T}} = \begin{bmatrix} \tilde{m}_1(s^2+\lambda_1) & 0 \\ 0 & \tilde{m}_2(s^2+\lambda_2) \end{bmatrix}. \tag{B.25}$$

The modal force vector becomes

$$\tilde{\boldsymbol{f}} = \begin{bmatrix} 1 & \frac{A}{\underline{m}_\mathrm{a}(\omega_\mathrm{a}^2-\lambda_1)} \\ \frac{A\lambda_2}{m_\mathrm{s}(\omega_\mathrm{s}^2-\lambda_2)} & 1 \end{bmatrix} \begin{bmatrix} \hat{f}_\mathrm{s} \\ 0 \end{bmatrix} = \begin{bmatrix} 1 \\ \frac{A\lambda_2}{m_\mathrm{s}(\omega_\mathrm{s}^2-\lambda_2)} \end{bmatrix} \hat{f}_\mathrm{s}. \tag{B.26}$$

and the generalized modal displacements result in

$$\tilde{d}_1 = \frac{\hat{f}_\mathrm{s}}{\tilde{m}_1(\lambda_1+s^2)} \tag{B.27}$$

and

$$\tilde{d}_2 = \frac{\frac{A\lambda_2}{m_\mathrm{s}(\omega_\mathrm{s}^2-\lambda_2)}\hat{f}_\mathrm{s}}{\tilde{m}_2(\lambda_2+s^2)}. \tag{B.28}$$

Acoustic pressure and mechanical displacement can then be calculated from the coupled modal displacements by superposition. This procedure is also known as modal synthesis. The modal displacements have maximum amplitude at the respective coupled natural frequency. The response to broadband excitation can thus be described by employing only a reduced set of eigenmodes. Thus, in many cases, the size of the system can be significantly reduced. In the given case, pressure $\hat{p}_\mathrm{a}$ and piston displacement $\hat{u}_\mathrm{s}$ can finally be obtained by superposition as

$$\begin{bmatrix} \hat{u}_\mathrm{s} \\ \hat{p}_\mathrm{a} \end{bmatrix} = \begin{bmatrix} \hat{u}_{\mathrm{s}|1} \\ \hat{p}_{\mathrm{a}|1} \end{bmatrix} + \begin{bmatrix} \hat{u}_{\mathrm{s}|2} \\ \hat{p}_{\mathrm{a}|2} \end{bmatrix} = \begin{bmatrix} 1 \\ \frac{A\lambda_1}{\underline{m}_\mathrm{a}(\omega_\mathrm{a}^2-\lambda_1)} \end{bmatrix} \frac{\hat{f}_\mathrm{s}}{\tilde{m}_1(\lambda_1+s^2)} + \begin{bmatrix} \frac{A}{m_\mathrm{s}(\omega_\mathrm{s}^2-\lambda_2)} \\ 1 \end{bmatrix} \frac{\frac{A\lambda_2}{m_\mathrm{s}(\omega_\mathrm{s}^2-\lambda_2)}}{\tilde{m}_2(\lambda_2+s^2)}. \tag{B.29}$$

Bibliography

[1] C. Gabriel, S. Müller, F. Ullrich, R. Lerch, Measurement of the spatial coherence of surface pressure in the wake of a car's side mirror, 19th AIAA/CEAS Aeroacoustics Conference, 2013: p. 2059.

[2] N. Broner, The effects of low frequency noise on people—A review, Journal of Sound and Vibration. 58 (1978) 483–500.

[3] D. Nefske, J. Wolf Jr, L. Howell, Structural-acoustic finite element analysis of the automobile passenger compartment: A review of current practice, Journal of Sound and Vibration. 80 (1982) 247–266.

[4] J.-F. Durand, C. Soize, L. Gagliardini, Structural-acoustic modeling of automotive vehicles in presence of uncertainties and experimental identification and validation, The Journal of the Acoustical Society of America. 124 (2008) 1513–1525.

[5] A. Guellec, M. Cabrol, J. Jacqmot, B. Van den Nieuwenhof, Optimization of trim component and reduction of the road noise transmission based on finite element methods, SAE Technical Paper, 2018.

[6] G. Lemaitre, C. Vartanian, C. Lambourg, P. Boussard, A psychoacoustical study of wind buffeting noise, Applied Acoustics. 95 (2015) 1–12. https://doi.org/10.1016/j.apacoust.2015.02.011

[7] J. Reyes, L. Gagliardini, C. Desceliers, C. Soize, Multi-frequency model reduction for uncertainty quantification in computational vibroacoustics of automobiles, SAE Technical Paper, 2020.

[8] S.A. Hambric, S.H. Sung, D.J. Nefske, Engineering vibroacoustic analysis: Methods and applications, John Wiley & Sons, 2016.

[9] K. Dammak, S. Koubaa, A. El Hami, L. Walha, M. Haddar, Numerical modelling of vibro-acoustic problem in presence of uncertainty: Application to a vehicle cabin, Applied Acoustics. 144 (2019) 113–123.

[10] E. Hills, B. Mace, N. Ferguson, Acoustic response variability in automotive vehicles, Journal of Sound and Vibration. 321 (2009) 286–304.

[11] J.W. Lee, J.M. Lee, Forced vibro-acoustical analysis for a theoretical model of a passenger compartment with a trunk—Part II: Experimental part, Journal of Sound and Vibration. 299 (2007) 918–932.

[12] D.-H. Lee, W.-S. Hwang, M.-E. Kim, Booming noise analysis in a passenger car using a hybrid-integrated approach, SAE Transactions. (2000) 1069–1075.

[13] J. Rejlek, G. Veronesi, C. Albert, E. Nijman, A. Bocquillet, A combined computational-experimental approach for modelling of coupled vibro-acoustic problems, SAE Technical Paper, 2013.

[14] M. Grialou, N. Totaro, J.-L. Guyader, A. Bocquillet, Characterization of surface impedance of vibro-acoustic subdomains with experimental measurements, Journal of Sound and Vibration. 460 (2019) 114876.

[15] G. Accardo, P. Chiariotti, B. Cornelis, M. El-Kafafy, B. Peeters, K. Janssens, M. Martarelli, Experimental acoustic modal analysis of an automotive cabin: Challenges and solutions, Journal of Physics: Conference Series, IOP Publishing, 2018: p. 012026.

[16] M. Herrmann, R. Jöst, F. Kehl, A. Özkan, S. Pless, F. Gauterin, Importance of vehicle body elements and rear axle elements for describing road booming noise, Vehicles. 2 (2020) 589–602.

[17] H. Herlufsen, H. Konstantin-Hansen, N. Moller, Operational modal analysis of a wind turbine wing using acoustical excitation, Proceedings of the Korean Society for Noise and Vibration Engineering Conference, The Korean Society for Noise; Vibration Engineering, 2002: pp. 385–1.

[18] E. Pierro, E. Mucchi, L. Soria, A. Vecchio, On the vibro-acoustical operational modal analysis of a helicopter cabin, Mechanical Systems and Signal Processing. 23 (2009) 1205–1217.

[19] M. Brandstätter, Tieffrequente Geräusche in einem Kraftfahrzeug bei Unebenheitsanregung, Dissertation, Technische Universität Berlin, 2014.

[20] F. Xue, B. Sun, Modelling and analysis of global vibroacoustic coupling characteristics of a rectangular enclosure bounded by a flexible panel, Shock and Vibration. 2018 (2018).

[21] K. Wyckaert, F. Augusztinovicz, P. Sas, Vibro-acoustical modal analysis: Reciprocity, model symmetry, and model validity, The Journal of the Acoustical Society of America. 100 (1996) 3172–3181. https://doi.org/10.1121/1.417127

[22] K. Nusser, S. Becker, Numerical investigation of the fluid structure acoustics interaction on a simplified car model, Acta Acustica. 5 (2021) 22. https://doi.org/10.1051/aacus/2021014

[23] M. Hartmann, J. Ocker, T. Lemke, A. Mutzke, V. Schwarz, H. Tokuno, R. Toppinga, P. Unterlechner, G. Wickern, Wind noise caused by the side-mirror and a-pillar of a generic vehicle model, 18th AIAA/CEAS Aeroacoustics Conference (33rd AIAA Aeroacoustics Conference), 2012: p. 2205.

[24] D. Blanchet, A. Golota, Combining modeling methods to accurately predict wind noise contribution, SAE Technical Paper, 2015.

[25] Y. He, S. Wen, Y. Liu, Z. Yang, Wind noise source characterization and transmission study through a side glass of DrivAer model based on a hybrid DES/APE method, Proceedings of the Institution of Mechanical Engineers, Part D: Journal of Automobile Engineering. 235 (2020) 095440702096955. https://doi.org/10.1177/0954407020969551

[26] Y. He, R. Wan, Y. Liu, S. Wen, Z. Yang, Transmission characteristics and mechanism study of hydrodynamic and acoustic pressure through a side window of DrivAer model based on modal analytical approach, Journal of Sound and Vibration. 501 (2021) 116058.

[27] Y. He, S. Schröder, Z. Shi, R. Blumrich, Z. Yang, J. Wiedemann, Wind noise source filtering and transmission study through a side glass of DrivAer model, Applied Acoustics. 160 (2020) 107161. https://doi.org/10.1016/j.apacoust.2019.107161

[28] Y. He, Z. Shi, Y. Wu, Z. Yang, Sound radiation analysis of a front side window glass of DrivAer model under wind excitation, Shock and Vibration. 2018 (2018).

[29] F. Schwertfirm, M. Hartmann, Acoustic-fluid-structure interaction (AFSI) in the car underbody, SAE Technical Paper, 2022.

[30] F. Van Herpe, D. d'Udekem, J. Jacqmot, R. Kouzaiha, Vibro-acoustic simulation of side windows and windshield excited by realistic CFD turbulent flows including car cavity, SAE Technical Paper, 2012.

[31] S. Senthooran, B. Crouse, S. Noelting, D. Freed, B. Duncan, G. Balasubramanian, R. Powell, Prediction of wall pressure fluctuations on an automobile side-glass using a lattice-boltzmann method, 12th AIAA/CEAS Aeroacoustics Conference (27th AIAA Aeroacoustics Conference), 2006: p. 2559.

[32] C. Glandier, M. Eiselt, O. Prill, E. Bauer, Coupling CFD with vibroacoustic FE models for vehicle interior low-frequency wind noise prediction, SAE International Journal of Passenger Cars - Mechanical Systems. 8 (2015). https://doi.org/10.4271/2015-01-2330

[33] P. Moron, A. Hazir, B. Crouse, R. Powell, B. Neuhierl, J. Wiedemann, Hybrid technique for underbody noise transmission of wind noise, SAE Technical Paper, 2011.

[34] B. Crouse, D. Freed, S. Senthooran, F. Ullrich, C. Fertl, Analysis of underbody windnoise sources on a production vehicle using a lattice boltzmann scheme, SAE Technical Paper, 2007.

[35] Y. Wang, X. Zhen, J. Wu, Z. Gu, Z. Xiao, X. Yang, Hybrid CFD/FEM-BEM simulation of cabin aerodynamic noise for vehicles traveling at high speed, Science China Technological Sciences. 56 (2013) 1697–1708.

[36] H.-D. Yao, L. Davidson, Generation of interior cavity noise due to window vibration excited by turbulent flows past a generic side-view mirror, Physics of Fluids. 30 (2018) 036104. https://doi.org/10.1063/1.5008611

[37] H. Yuan, Z. Yang, Y. Wang, Y. Fan, Y. Fang, Experimental analysis of hydrodynamic and acoustic pressure on automotive front side window, Journal of Sound and Vibration. 476 (2020) 115296. https://doi.org/10.1016/j.jsv.2020.115296

[38] Y. Wang, M. Du, C. Su, W. Wu, Numerical investigation on the contribution of underbody flow-induced noise on vehicle interior noise, Proceedings of the Institution of Mechanical Engineers, Part D: Journal of Automobile Engineering. 235 (2021) 2667–2678.

[39] A. Businger, Aerodynamisch angeregte Bauteilschwingungen, Dissertation, Universität Erlangen-Nürnberg, 2015.

[40] B. Arguillat, D. Ricot, C. Bailly, G. Robert, Measured wavenumber: Frequency spectrum associated with acoustic and aerodynamic wall pressure fluctuations, The Journal of the Acoustical Society of America. 128 (2010) 1647–1655.

[41] F. Vanherpe, L. Olivas Duarte, P. Lafon, Sound vs. Pseudo-sound contributions to the wind noise, 18th AIAA/CEAS Aeroacoustics Conference (33rd AIAA Aeroacoustics Conference), 2012: p. 2207.

[42] S. Marburg, Developments in structural-acoustic optimization for passive noise control, Archives of Computational Methods in Engineering. 9 (2002) 291–370.

[43] W.K. Blake, Mechanics of flow-induced sound and vibration. Volume 1 General concepts and elementary source. Volume 2 - Complex flow-structure interactions

[44] S.H. Kim, J.M. Lee, A Practical Method for Noise Reduction in a Vehicle Passenger Compartment

[45] M. Peichl, S. Mack, T. Indinger, F. Decker, Numerical investigation of the flow around a generic car using dynamic mode decomposition, American Society of Mechanical Engineers, Fluids Engineering Division (Publication) FEDSM. 1 (2014). https://doi.org/10.1115/FEDSM2014-21255

[46] R.F. Soares, K.P. Garry, J. Holt, Comparison of the far-field aerodynamic wake development for three drivaer model configurations using a cost-effective RANS simulation, (2017).

[47] A.I. Heft, T. Indinger, N.A. Adams, Experimental and numerical investigation of the DrivAer model, Fluids Engineering Division Summer Meeting, American Society of Mechanical Engineers, 2012: pp. 41–51.

[48] R. Engelmann, F. Toth, C. Gabriel, M. Kaltenbacher, An approach for modal coupling based on experimental and computed modes using non-conforming grids, Journal of Sound and Vibration. (2022) 117041.

[49] J.W.S.B. Rayleigh, R.B. Lindsay, The theory of sound, Dover Publications, 1945.

[50] A. Brandt, Noise and vibration analysis: Signal analysis and experimental procedures, John Wiley & Sons, 2011.

[51] B.G. Osgood, Lectures on the fourier transform and its applications, American Mathematical Society, 2019.

[52] J. Pang, Noise and vibration control in automotive bodies, John Wiley & Sons, 2018.

[53] L. Cremer, M. Heckl, B. Petersson, S.-B.S.-S. Vibrations, Sound radiation at audio frequencies, (2005).

[54] F.J. Fahy, Foundations of engineering acoustics, Academic Press, 2000.

[55] M. Kaltenbacher, Numerical simulation of mechatronic sensors and actuators: Finite elements for computational multiphysics, third edition, 2015. https://doi.org/10.1007/978-3-642-40170-1

[56] W.K. Blake, S. Temkin, Mechanics of Flow-Induced Sound and Vibration. Vol. I: General Concepts and Elementary Sources by William K. Blake

[57] R. G. Ballas, G. Pfeiffer, R. Werthschützky, Elektromechanische Systeme der Mikrotechnik und Mechatronik. Springer, Heidelberg, 2009.

[58] P. Davidsson, Structure-acoustic analysis; finite element modelling and reduction methods, PhD thesis, Lund University; Division of Structural Mechanics, Box 118; 221 00 Lund, 2004.

[59] K. Sum, J. Pan, On acoustic and structural modal cross-couplings in plate-cavity systems, The Journal of the Acoustical Society of America. 107 (2000) 2021–2038.

[60] A. Craggs, An acoustic finite element approach for studying boundary flexibility and sound transmission between irregular enclosures, Journal of Sound and Vibration. 30 (1973) 343–357.

[61] R.H. Lyon, Noise reduction of rectangular enclosures with one flexible wall, The Journal of the Acoustical Society of America. 35 (1963) 1791–1797.

[62] E. Dowell, H. Voss, The effect of a cavity on panel vibration, AIAA Journal. 1 (1963) 476–477.

[63] A. Pretlove, Free vibrations of a rectangular panel backed by a closed rectangular cavity by a closed rectangular cavity, Journal of Sound and Vibration. 2 (1965) 197–209.

[64] E.H. Dowell, G. Gorman Iii, D. Smith, Acoustoelasticity: General theory, acoustic natural modes and forced response to sinusoidal excitation, including comparisons with experiment, Journal of Sound and Vibration. 52 (1977) 519–542.

[65] J. Pan, D.A. Bies, The effect of fluid-structural coupling on sound waves in an enclosure—Theoretical part, The Journal of the Acoustical Society of America. 87 (1990) 691–707.

[66] M. Shahraeeni, R. Shakeri, S.M. Hasheminejad, An analytical solution for free and forced vibration of a piezoelectric laminated plate coupled with an acoustic enclosure, Computers & Mathematics with Applications. 69 (2015) 1329–1341.

[67] Y. Chen, G. Jin, S. Shi, Z. Liu, A general analytical method for vibroacoustic analysis of an arbitrarily restrained rectangular plate backed by a cavity with general wall impedance, Journal of Vibration and Acoustics. 136 (2014).

[68] J.T. Du, W.L. Li, H.A. Xu, Z.G. Liu, Vibro-acoustic analysis of a rectangular cavity bounded by a flexible panel with elastically restrained edges, The Journal of the Acoustical Society of America. 131 (2012) 2799–2810.

[69] Y. Wang, X. Qin, S. Huang, L. Lu, Q. Zhang, J. Feng, Structural-borne acoustics analysis and multi-objective optimization by using panel acoustic participation and response surface methodology, Applied Acoustics. 116 (2017) 139–151.

[70] Y.-H. Kim, S.-M. Kim, Solution of coupled acoustic problems: A partially opened cavity coupled with a membrane and a semi-infinite exterior field, Journal of Sound and Vibration. 254 (2002) 231–244.

[71] T. Pàmies, J. Romeu, M. Genescà, A. Balastegui, Sound radiation from an aperture in a rectangular enclosure under low modal conditions, The Journal of the Acoustical Society of America. 130 (2011) 239–248.

[72] J.-F. Durand, C. Soize, L. Gagliardini, Structural-acoustic modeling of automotive vehicles in presence of uncertainties and experimental identification and validation, The Journal of the Acoustical Society of America. 124 (2008) 1513–1525.

[73] J. Pan, S. Elliott, K.-H. Baek, Analysis of low frequency acoustic response in a damped rectangular enclosure, Journal of Sound and Vibration. 223 (1999) 543–566.

[74] S.-J. Kim, S.-K. Lee, Prediction of interior noise by excitation force of the powertrain based on hybrid transfer path analysis, International Journal of Automotive Technology. 9 (2008) 577–583.

[75] J. Plunt, Finding and fixing vehicle NVH problems with transfer path analysis, Sound and Vibration. 39 (2005) 12–17.

[76] M.S. Allen, D. Rixen, M. Van der Seijs, P. Tiso, T. Abrahamsson, R.L. Mayes, Substructuring in engineering dynamics, Springer, 2020.

[77] M. Grialou, Vibro-acoustics substructuring: Combining simulations and experimental identification of subdomains for low frequency vehicle acoustics, PhD thesis, Université de Lyon

[78] N. Contartese, E. Nijman, W. Desmet, On the physically consistent characterisation of a system for FRF-based substructuring, Journal of Sound and Vibration. 501 (2021) 116073.

[79] M.V. van der Seijs, D. de Klerk, D.J. Rixen, General framework for transfer path analysis: History, theory and classification of techniques, Mechanical Systems and Signal Processing. 68 (2016) 217–244.

[80] J. Plunt, Finding and fixing vehicle NVH problems with transfer path analysis, Sound and Vibration. 39 (2005) 12–17.

[81] S. Bi, M. Sagnard, E. Foltete, M. Ouisse, A. Jund, Identification of reduced and uncoupled models in vibroacoustical experimental modal analysis, International Conference on Noise and Vibration Engineering, 2016.

[82] A. Craggs, The transient response of a coupled plate-acoustic system using plate and acoustic finite elements, Journal of Sound and Vibration. 15 (1971) 509–528.

[83] M. Tournour, N. Atalla, Pseudostatic corrections for the forced vibroacoustic response of a structure-cavity system, The Journal of the Acoustical Society of America. 107 (2000) 2379–2386.

[84] D. Nehete, S. Modak, K. Gupta, Experimental studies in finite element model updating of vibro-acoustic cavities using coupled modal data and FRFs, Applied Acoustics. 150 (2019) 113–123.

[85] S.M. Kim, M.J. Brennan, Modelling a Structural-Acoustic Coupled System with an Equivalent Lumped Parameter Mechanical System. 1999.

[86] C.J. Cameron, P. Wennhage, P. Göransson, Prediction of NVH behaviour of trimmed body components in the frequency range 100–500Hz, Applied Acoustics. 71 (2010) 708–721. https://doi.org/10.1016/j.apacoust.2010.03.002

[87] L. Ying-jie, L. Wen-bo, P. Cheng-jian, Numerical investigation on the interior wind noise of a passenger car, International Journal of Mechanical and Industrial Engineering. 13 (2019) 744–748. https://publications.waset.org/vol/156

[88] R. Citarella, L. Federico, A. Cicatiello, Modal acoustic transfer vector approach in a FEM–BEM vibro-acoustic analysis, Engineering Analysis with Boundary Elements. 31 (2007) 248–258.

[89] K.K. Choi, I. Shim, S. Wang, Design Sensitivity Analysis of Structure-Induced Noise and Vibration. 1997.

[90] L.G. Olson, K.-J. Bathe, Analysis of fluid-structure interactions. A direct symmetric coupled formulation based on the fluid velocity potential, Computers & Structures. 21 (1985) 21–32.

[91] V. Bokil, U. Shirahatti, A technique for the modal analysis of sound-structure interaction problems, Journal of Sound and Vibration. 173 (1994) 23–41.

[92] S.A. Arjmandi, V. Lotfi, Computing mode shapes of fluid-structure systems using subspace iteration methods, Scientia Iranica. 18 (2011) 1159–1169. https://doi.org/10.1016/j.scient.2011.09.011

[93] Z.-D. Ma, I. Hagiwara, Sensitivity analysis methods for coupled acoustic-structural systems part i: Modal sensitivities, AIAA Journal. 29 (1991) 1787–1795.

[94] S. Marburg, H.-J. Beer, J. Gier, H.-J. Hardtke, R. Rennert, F. Perret, Experimental verification of structural-acoustic modelling and design optimization, Journal of Sound and Vibration. 252 (2002) 591–615.

[95] M. Xu, J. Zhang, J. Lin, P. Guo, W. He, Z. Li, Prediction and control of the structure-borne noise of a vehicle based on an optimization technique of the vehicle-body model, Proceedings of the Institution of Mechanical Engineers, Part D: Journal of Automobile Engineering. 229 (2015) 1457–1468.

[96] K. Dammak, A. El Hami, S. Koubaa, L. Walha, M. Haddar, Reliability based design optimization of coupled acoustic-structure system using generalized polynomial chaos, International Journal of Mechanical Sciences. 134 (2017) 75–84.

[97] A.S. Phani, On the necessary and sufficient conditions for the existence of classical normal modes in damped linear dynamic systems, Journal of Sound and Vibration. 264 (2003) 741–745.

[98] U. Fuellekrug, Computation of real normal modes from complex eigenvectors, Mechanical Systems and Signal Processing. 22 (2008) 57–65.

[99] A.S. Phani, J. Woodhouse, Viscous damping identification in linear vibration, Journal of Sound and Vibration. 303 (2007) 475–500.

[100] P. Avitabile, Experimental modal analysis, Sound and Vibration. 35 (2001) 20–31.

[101] M.V. van der Seijs, D. de Klerk, D.J. Rixen, General framework for transfer path analysis: History, theory and classification of techniques, Mechanical Systems and Signal Processing. 68 (2016) 217–244.

[102] D.-H. Lee, W.-S. Hwang, M.-E. Kim, Booming noise analysis in a passenger car using a hybrid-integrated approach, SAE Transactions. (2000) 1069–1075.

[103] S.-J. Kim, S.-K. Lee, Prediction of interior noise by excitation force of the powertrain based on hybrid transfer path analysis, International Journal of Automotive Technology. 9 (2008) 577–583.

[104] H. Van der Auweraer, P. Mas, S. Dom, A. Vecchio, K. Janssens, P. Van de Ponseele, Transfer path analysis in the critical path of vehicle refinement: The role of fast, hybrid and operational path analysis, SAE Technical Paper. (2007).

[105] R. Guo, S. Qiu, Q. Yu, H. Zhou, L. Zhang, Transfer path analysis and control of vehicle structure-borne noise induced by the powertrain, Proceedings of the Institution of Mechanical Engineers, Part D: Journal of Automobile Engineering. 226 (2012) 1100–1109.

[106] H. Tsuji, S. Maruyama, T. Yoshimura, E. Takahashi, Experimental method extracting dominant acoustic mode shapes for automotive interior acoustic field coupled with the body structure, SAE International Journal of Passenger Cars-Mechanical Systems. 6 (2013) 1139–1146.

[107] Y. Xu, W. Zhu, Operational modal analysis of a rectangular plate using non-contact excitation and measurement, Journal of Sound and Vibration. 332 (2013) 4927–4939.

[108] A. Brandt, M. Berardengo, S. Manzoni, A. Cigada, Scaling of mode shapes from operational modal analysis using harmonic forces, Journal of Sound and Vibration. 407 (2017) 128–143.

[109] T.C. Lim, Automotive panel noise contribution modeling based on finite element and measured structural-acoustic spectra, Applied Acoustics. 60 (2000) 505–519.

[110] S. Dhandole, S. Modak, On improving weakly coupled cavity models for vibro-acoustic predictions and design, Applied Acoustics. 71 (2010) 876–884.

[111] J. Meggitt, A. Moorhouse, Finite element model updating using in-situ experimental data, Journal of Sound and Vibration. 489 (2020) 115675.

[112] J. Plunt, Examples of using transfer path analysis (TPA) together with CAE-models to diagnose and find solutions for NVH problems late in the vehicle development process, SAE Technical Paper, 2005.

[113] X.-L. Li, D.-X. Fu, Y.-W. Ma, X. Liang, Direct numerical simulation of compressible turbulent flows, Acta Mechanica Sinica. 26 (2010) 795–806.

[114] M.J. Lighthill, On sound generated aerodynamically i. General theory, Proceedings of the Royal Society of London. Series A. Mathematical and Physical Sciences. 211 (1952) 564–587.

[115] N. Curle, The influence of solid boundaries upon aerodynamic sound, Proceedings of the Royal Society of London. Series A. Mathematical and Physical Sciences. 231 (1955) 505–514.

[116] A. Powell, Aerodynamic noise and the plane boundary, The Journal of the Acoustical Society of America. 32 (1960) 982–990.

[117] A. Powell, Theory of vortex sound, The Journal of the Acoustical Society of America. 36 (1964) 177–195.

[118] G.I. Taylor, The spectrum of turbulence, Proceedings of the Royal Society of London. Series A-Mathematical and Physical Sciences. 164 (1938) 476–490.

[119] J.E. Ffowcs Williams, D.L. Hawkings, Sound generation by turbulence and surfaces in arbitrary motion, Philosophical Transactions of the Royal Society of London. Series A, Mathematical and Physical Sciences. 264 (1969) 321–342.

[120] X. Gloerfelt, The link between wall pressure spectra and radiated sound from turbulent boundary layers, 16th AIAA/CEAS Aeroacoustics Conference, 2010: p. 3904.

[121] D.G. Crighton, A.P. Dowling, J. Ffowcs-Williams, M. Heckl, F. Leppington, J.F. Bartram, Modern methods in analytical acoustics lecture notes, (1992).

[122] E.M. Viggen, The lattice boltzmann method: Fundamentals and acoustics, PhD thesis, Norwegian University of Science; Technology, 2014.

[123] S. Succi, G. Amati, R. Benzi, Challenges in lattice boltzmann computing, Journal of Statistical Physics. 81 (1995) 5–16.

[124] A. De Rosis, C. Coreixas, Multiphysics flow simulations using D3Q19 lattice boltzmann methods based on central moments, Physics of Fluids. 32 (2020) 117101.

[125] E. Fares, Unsteady flow simulation of the ahmed reference body using a lattice boltzmann approach, Computers & Fluids. 35 (2006) 940–950.

[126] D. Forbes, G. Page, M. Passmore, A. Gaylard, Computational study of wake structure and base pressure on a generic SUV model, International Vehicle Aerodynamics Conference, 2014: pp. 67–79.

[127] A. Islam, A. Gaylard, B. Thornber, A detailed statistical study of unsteady wake dynamics from automotive bluff bodies, Journal of Wind Engineering and Industrial Aerodynamics. 171 (2017). https://doi.org/10.1016/j.jweia.2017.09.009

[128] P. Welch, The use of fast fourier transform for the estimation of power spectra: A method based on time averaging over short, modified periodograms, IEEE Transactions on Audio and Electroacoustics. 15 (1967) 70–73.

[129] S. B. Pope, Turbulent flows, Cambridge university press, 2000.

[130] G.I.Taylor, Statistical theory of turbulence-ii. Proceedings of the Royal Society of London. Series A-Mathematical and Physical Sciences. 151 (1935) 444-454.

[131] A. Businger, Berechnung aerodynamisch angeregter Bauteilschwingungen an Kraftfahrzeugen, ATZ-Automobiltechnische Zeitschrift. 118 (2016) 72-79.

[132] J. Park, L. Mongeau, T. Siegmund, An investigation of the flow-induced sound and vibration of viscoelastically supported rectangular plates: Experiments and model verification, Journal of Sound and Vibration. 275 (2004) 249–265.

[133] J. Da Rocha, A. Suleman, F. Lau, Prediction of flow-induced noise in transport vehicles: Development and validation of a coupled structural-acoustic analytical framework, Coupled Structural-Acoustic Analytical Models for the Prediction of Turbulent Boundary-Layer-Induced Noise in Aircraft Cabins. (2009) 59.

[134] A. Caiazzo, W. Desmet, others, A generalized corcos model for modelling turbulent boundary layer wall pressure fluctuations, Journal of Sound and Vibration. 372 (2016) 192–210.

[135] T. Schutz, Hucho-Aerodynamik des Automobils, Stromungsmechanik, Warmetechnik, Fahrdynamik, Komfort (Wiesbaden: Springer Vieweg, 2013), Doi. 10 (2013) 978–3.

[136] J. Katz, A. Plotkin, Low-speed aerodynamics, Cambridge university press, 2001.

[137] P. Ekman, Important factors for accurate scale-resolving simulations of automotive aerodynamics, Vol. 2068. Linköping University Electronic Press, 2020.

[138] S.S. Aleyasin, M.F. Tachie, R. Balachandar, Characteristics of flow past elongated bluff bodies with underbody gaps due to varying inflow turbulence, Physics of Fluids. 33 (2021) 125106.

[139] A. Thacker, S. Aubrun, A. Leroy, P. Devinant, Experimental characterization of flow unsteadiness in the centerline plane of an ahmed body rear slant, Experiments in Fluids. 54 (2013) 1–16.

[140] B. Zhang, Y. Zhou, S. To, Unsteady flow structures around a high-drag ahmed body, Journal of Fluid Mechanics. 777 (2015) 291–326.

[141] S.R. Ahmed, G. Ramm, G. Faltin, Some salient features of the time-averaged ground vehicle wake, SAE Transactions. (1984) 473–503.

[142] D.E. Aljure, O. Lehmkuhl, I. Rodriguez, A. Oliva, Flow and turbulent structures around simplified car models, Computers & Fluids. 96 (2014) 122–135.

[143] B. Conan, J. Anthoine, P. Planquart, Experimental aerodynamic study of a car-type bluff body, Experiments in Fluids. 50 (2011) 1273–1284.

[144] S. Krajnović, L. Davidson, Flow Around a Simplified Car, Part 2: Understanding the Flow

[145] K. Taira, S.L. Brunton, S.T. Dawson, C.W. Rowley, T. Colonius, B.J. McKeon, O.T. Schmidt, S. Gordeyev, V. Theofilis, L.S. Ukeiley, Modal analysis of fluid flows: An overview, AIAA Journal. 55 (2017) 4013–4041.

[146] S.R. Ahmed, Aerodynamic sound sources in vehicles—Prediction and control, Handbook of Noise and Vibration Control. (2007) 1072–1085.

[147] T. Tunay, B. Sahin, V. Ozbolat, Effects of rear slant angles on the flow characteristics of ahmed body, Experimental Thermal and Fluid Science. 57 (2014) 165–176.

[148] A. Spohn, P. Gilliéron, Flow separations generated by a simplified geometry of an automotive vehicle, IUTAM Symposium: Unsteady Separated Flows, Kluwer Academic, 2002.

[149] M.S.M. Ali, J. Jalasabri, A.M. Sood, S. Mansor, H. Shaharuddin, S. Muhamad, Wind noise from a-pillar and side view mirror of a realistic generic car model, DriAver, International Journal of Vehicle Noise and Vibration. 14 (2018) 38–61.

[150] M. Aucejo, Vibro-acoustique des structures immergées sous écoulement turbulent, PhD thesis, INSA de Lyon, 2010.

[151] K. Nusser, Investigation of the Fluid-Structure-Acoustics Interaction on a Simplified Car Model. Dissertation, Friedrich-Alexander-Universität Erlangen-Nürnberg (FAU), 2019 .

[152] V.P.K. Vadavalli, Un modèle numérique de l'excitation couche limite turbulente pour prédire le bruit à l'intérieur d'une automobile. 2018.

[153] M. Bull, Wall-pressure fluctuations beneath turbulent boundary layers: Some reflections on forty years of research, Journal of Sound and Vibration. 190 (1996) 299–315.

[154] A. Seifzadeh, A. Pietrzyk, P. Göransson, R. Ramakrishnan, Effect of coupling between passenger compartment and trunk of a car on coupled system natural frequencies using acoustic frequency response function, Applied Acoustics. 76 (2014) 310–318.

[155] S.-H. Shin, J.-G. Ih, T. Hashimoto, S. Hatano, Sound quality evaluation of the booming sensation for passenger cars, Applied Acoustics. 70 (2009) 309–320.

[156] G. Cerrato, Automotive sound quality–powertrain, road and wind noise, Sound and Vibration. 43 (2009) 16–24.

[157] N. Oettle, D. Sims-Williams, Automotive aeroacoustics: An overview, Proceedings of the Institution of Mechanical Engineers, Part D: Journal of Automobile Engineering. 231 (2017) 1177–1189.

[158] D. Ricot, V. Maillard, C. Bailly, Numerical simulation of the unsteady flow past a cavity and application to the sunroof buffeting, 7th AIAA/CEAS Aeroacoustics Conference and Exhibit, 2001. https://doi.org/10.2514/6.2001-2112

[159] Y. Wang, X. Yu, Study on the control of buffeting noise of a car driving with the front side window open, Forest Chemicals Review. (2021) 728–746.

[160] M. Alaoui, Coherent structures and wall-pressure fluctuations modeling in turbulent boundary layers subjected to pressure gradients, PhD thesis, Paris, ENSAM, 2016.

[161] G.M. Corcos, Resolution of pressure in turbulence, Journal of the Acoustical Society of America. 35 (1963) 192–199.

[162] W. Graham, A comparison of models for the wavenumber–frequency spectrum of turbulent boundary layer pressures, Journal of Sound and Vibration. 206 (1997) 541–565.

[163] A. Businger, S. Schimmelpfennig, G. Wickern, R. Lerch, Berechnung strö

[164] M. Smith, E. Latorre Iglesias, P. Bremner, F. Mendonca, Validation tests for flow induced excitation and noise radiation from a car window, 18th AIAA/CEAS Aeroacoustics Conference (33rd AIAA Aeroacoustics Conference), 2012: p. 2201.

[165] J. Da Rocha, A. Suleman, F. Lau, Turbulent boundary layer induced noise and vibration of a multi-panel walled acoustic enclosure, Coupled Structural-Acoustic Analytical Models for the Prediction of Turbulent Boundary-Layer-Induced Noise in Aircraft Cabins. (2010).

[166] D. Chase, The character of the turbulent wall pressure spectrum at subconvective wavenumbers and a suggested comprehensive model, Journal of Sound and Vibration. 112 (1987) 125–147.

[167] P. Winter, S. Haas, M. Wenzel, M. Weiß, R. Lerch, Der Einfluss der Grenzschichtdicke auf die aeroakustische Schallentstehung an einem generischen Heckklappenspaltmodell, DAGA 2016 Aachen, 2016.

[168] T.M. Farabee, M.J. Casarella, Spectral features of wall pressure fluctuations beneath turbulent boundary layers, Physics of Fluids A: Fluid Dynamics. 3 (1991) 2410–2420.

[169] D.H. Wood, R.V. Westphal, Measurements of the free-stream fluctuations above a turbulent boundary layer, The Physics of Fluids. 31 (1988) 2834–2840.

[170] S. Yin, Z. Gu, Y. Zong, L. Zheng, Z. Yang, T. Huang, Sound quality evaluation of automobile side-window buffeting noise based on large-eddy simulation, Journal of Low Frequency Noise, Vibration and Active Control. 38 (2019) 207–223.

[171] B.D. Duncan, R. Sengupta, S. Mallick, R. Shock, D. Sims-Williams, Numerical simulation and spectral analysis of pressure fluctuations in vehicle aerodynamic noise generation, SAE Transactions. (2002) 872–892.

[172] D.B. Sims-Williams, B.D. Duncan, The ahmed model unsteady wake: Experimental and computational analyses, SAE Transactions. (2003) 1385–1396.

[173] B. Crouse, S. Senthooran, D. Freed, G. Balasubramanian, M. Gleason, M. Puskarz, P.-T. Lew, L. Mongeau, Experimental and numerical investigation of a flow-induced cavity resonance with application to automobile buffeting, 12th AIAA/CEAS Aeroacoustics Conference (27th AIAA Aeroacoustics Conference), 2006: p. 2494.

[174] V. Sarohia, Experimental investigation of oscillations in flows over shallow cavities, Aiaa Journal. 15 (1977) 984–991.

[175] J. Lee, J. Lee, S. Kim, Acoustical analysis of multiple cavities connected by necks in series with a consideration of evanescent waves, Journal of Sound and Vibration. 273 (2004) 515–542.

[176] J.W. Lee, J.M. Lee, Forced vibro-acoustical analysis for a theoretical model of a passenger compartment with a trunk—part i: Theoretical part, Journal of Sound and Vibration. 299 (2007) 900–917.

[177] R. Engelmann, C. Gabriel, S. Schoder, M. Kaltenbacher, A generic testbody for low-frequency aeroacoustic buffeting, SAE Technical Papers. 2020 (2020). https://doi.org/10.4271/2020-01-1515

[178] R. Engelmann, C. Gabriel, F. Toth, M. Kaltenbacher, Assessing low frequency flow noise based on an experimentally validated modal substructuring strategy featuring non-conforming grids, SAE Technical Paper, 2022.

[179] B. Flemisch, M. Kaltenbacher, S. Triebenbacher, B.I. Wohlmuth, Non-matching grids for a flexible discretization in computational acoustics, Communications in Computational Physics. 11 (2012) 472–488.

[180] P.J. Frey, P.-L. George, Mesh generation: Application to finite elements, second edition, John Wiley & Sons, 2008.

[181] A. Beckert, H. Wendland, Multivariate interpolation for fluid-structure-interaction problems using radial basis functions, Aerospace Science and Technology. 5 (2001) 125–134. https://doi.org/10.1016/S1270-9638(00)01087-7

[182] H. Wendland, Piecewise polynomial, positive definite and compactly supported radial functions of minimal degree, Advances in Computational Mathematics. 4 (1995) 389–396.

[183] A. de Boer, A.H. van Zuijlen, H. Bijl, Review of coupling methods for non-matching meshes, Computer Methods in Applied Mechanics and Engineering. 196 (2007) 1515–1525. https://doi.org/10.1016/j.cma.2006.03.017

[184] D. Cinquegrana, P.L. Vitagliano, Non-linear panel instabilities at high-subsonic and low supersonic speeds solved with strongly coupled CIRA FSI framework, International Journal of Non-Linear Mechanics. 129 (2021) 103643. https://doi.org/10.1016/j.ijnonlinmec.2020.103643

[185] B.I. Wohlmuth, A mortar finite element method using dual spaces for the lagrange multiplier, SIAM Journal on Numerical Analysis. 38 (2000) 989–1012.

[186] I. Amidror, Scattered data interpolation methods for electronic imaging systems: A survey, Journal of Electronic Imaging. 11 (2002) 157–176.

[187] J.N. Reddy, Theory and analysis of elastic plates and shells, Second edition., CRC Press, an imprint of Taylor; Francis, Boca Raton, FL, 2006. https://www.taylorfrancis.com/books/9780849384165

[188] openCFS: Finite Elements for Multiphysics, www.opencfs.org

[189] M. Islam, F. Decker, M. Hartmann, A. Jaeger, T. Lemke, J. Ocker, V. Schwarz, F. Ullrich, A. Schröder, A. Heider, Investigations of sunroof buffeting in an idealised generic vehicle model-part i: Experimental results, 14th AIAA/CEAS Aeroacoustics Conference (29th AIAA Aeroacoustics Conference), 2008: p. 2900.

[190] J. Délery, Three-dimensional separated flow topology: Critical points, separation lines and vortical structures, John Wiley & Sons, 2013.

[191] J.C. Hunt, A.A. Wray, P. Moin, Eddies, streams, and convergence zones in turbulent flows, Studying Turbulence Using Numerical Simulation Databases, 2. Proceedings of the 1988 Summer Program. (1988).

[192] C. Bailly, G. Comte-Bellot, Turbulence, Springer International Publishing, 2015.

[193] S.K. Robinson, Coherent motions in the turbulent boundary layer, Annual Review of Fluid Mechanics. 23 (1991) 601–639.

[194] D.W. Marquardt, An algorithm for least-squares estimation of nonlinear parameters, Journal of the Society for Industrial and Applied Mathematics. 11 (1963) 431–441.